

SKB

**TECHNICAL
REPORT**

92-07

**Discrete fracture modelling of the
Finnsjön rock mass: Phase 2**

J E Geier, C-L Axelsson, L Hässler,
A Benabderrahmane

Golder Geosystem AB, Uppsala, Sweden

April 1992

SVENSK KÄRNBRÄNSLEHANTERING AB

SWEDISH NUCLEAR FUEL AND WASTE MANAGEMENT CO

BOX 5864 S-102 48 STOCKHOLM

TEL 08-665 28 00 TELEX 13108 SKB S

TELEFAX 08-661 57 19

DISCRETE FRACTURE MODELLING OF THE FINNSJÖN ROCK
MASS: PHASE 2

J E Geier, C-L Axelsson, L Hässler,
A Benabderrahmane

Golder Geosystem AB, Uppsala, Sweden

April 1992

This report concerns a study which was conducted for SKB. The conclusions and viewpoints presented in the report are those of the author(s) and do not necessarily coincide with those of the client.

Information on SKB technical reports from 1977-1978 (TR 121), 1979 (TR 79-28), 1980 (TR 80-26), 1981 (TR 81-17), 1982 (TR 82-28), 1983 (TR 83-77), 1984 (TR 85-01), 1985 (TR 85-20), 1986 (TR 86-31), 1987 (TR 87-33), 1988 (TR 88-32), 1989 (TR 89-40) and 1990 (TR 90-46) is available through SKB.

DISCRETE FRACTURE MODELLING
OF THE FINNSJÖN ROCK MASS: PHASE 2

J.E. Geier
C.-L. Axelsson
L. Hässler
A. Benabderrahmane

Golder Geosystem AB
Uppsala, Sweden

For

Svensk Kärnbränslehantering AB
Swedish Nuclear Fuel and Waste Management Company
Stockholm

April 28, 1992

This report concerns a study which was conducted for SKB. The conclusions and viewpoints presented in the report are those of the authors and do not necessarily coincide with those of the client.

A list of other reports published in this series is attached at the end of the report. Information on previous reports is available through SKB.

ABSTRACT

A discrete fracture network (DFN) model of the Finnsjön site was derived from field data, and used to predict block-scale flow and transport properties.

The DFN model was based on a compound Poisson process, with stochastic fracture zones, and individual fractures concentrated around the fracture zones. This formulation was used to represent the multitude of fracture zones at the site which could be observed on lineament maps and in boreholes, but were not the focus of detailed characterization efforts. Due to a shortage of data for fracture geometry at depth, distributions of fracture orientation and size were assumed to be uniform throughout the site. Transmissivity within individual fracture planes was assumed to vary according to a fractal model.

Constant-head packer tests were simulated with the model, and the observed transient responses were compared with actual tests in terms of distributions of interpreted transmissivity and flow dimension, to partially validate the model. Both simulated and actual tests showed a range of flow dimension from sublinear to spherical, indicating local variations in the connectivity of the fracture population.

A methodology was developed for estimation of an effective stochastic continuum from the DFN model, but this was only partly demonstrated. Directional conductivities for 40 m blocks were estimated using the DFN model. These show extremely poor correlation with results of multiple packer tests in the same blocks, indicating possible limitations of small-scale packer tests for predicting block-scale properties.

Estimates are given of effective flow porosity and flow wetted surface, based on the block-scale flow fields calculated by the DFN model, and probabilistic models for the relationships among local fracture transmissivity, void space, and specific surface. The database for constructing these models is extremely limited. A review is given of the existing database for single fracture hydrologic properties.

TABLE OF CONTENTS**SUMMARY****ABSTRACT**

1.	INTRODUCTION	1
2.	BACKGROUND	4
	2.1 Definitions	4
	2.1.1 Geological terms	4
	2.1.2 Fracture geometry	5
	2.1.3 Fracture hydrologic properties	6
	2.1.4 Rock mass hydrologic properties	9
	2.1.5 Packer testing terminology	9
	2.2 Site description	13
	2.2.1 Major Features	15
	2.2.2 Fractures	22
	2.2.3 <i>In situ</i> stresses	25
	2.2.4 Hydrologic measurements	27
	2.2.4.1 Single-hole packer test results	28
	2.2.4.2 Cross-hole flow and tracer test data	35
	2.3 Review of models for fractured, crystalline rock	36
	2.3.1 Discrete fracture network (DFN) model	39
	2.3.2 Stochastic continuum (SC) model	41
	2.3.3 Channel network (CN) model	44
	2.3.4 Dual-porosity streamtube (DPST) models	46
3.	PROPERTIES OF SINGLE FRACTURES	49
	3.1 Aperture variation	49
	3.1.1 Single-fracture flow experiments	50
	3.1.2 Aperture estimated from surface profiles	55
	3.1.3 Direct measurements of fracture aperture	55
	3.1.4 Models for fracture aperture	57
	3.2 Hydromechanical effects	62
	3.2.1 Normal stress and transmissivity	62

3.2.2	Shear stress and transmissivity	66
3.2.3	Normal stress and storativity	68
3.3	Fracture infilling	70
3.3.1	Types of infilling in Fennoscandian granitic rock	70
3.3.2	Infilling type and transmissivity	71
3.3.2.1	Observations in tunnels	71
3.3.2.2	Analyses of borehole data	73
3.3.3	Infilling type and transport properties	74
3.3.3.1	Sealed fractures	74
3.3.3.2	Coated fractures	77
3.3.3.3	Fractured or crushed infilling	78
3.4	Effective Transport Parameters	79
3.4.1	Porosity	79
3.4.2	Wetted Surface	83
4	MODELLING APPROACH	84
4.1	Objectives	84
4.1.1	Existence of a conductivity tensor for SC models	84
4.1.2	Average conductivity tensor, variability, and anisotropy	85
4.1.3	Spatial structure of effective or equivalent conductivity	86
4.1.4	Relation of packer tests to block-scale conductivity	86
4.1.5	Transport parameters for ST and CN models	87
4.2	Major considerations for the DFN model	87
4.2.1	Characteristics of major features	87
4.2.2	Characteristics of fracture population	88
4.2.3	Preliminary results from the feasibility study	89
4.3	Conceptual model definition	90
4.3.1	Comparison of alternative models	90
4.3.1.1	Ability to reproduce heterogeneity	92
4.3.1.2	"Hard" data requirements	92
4.3.1.3	"Soft" data utilization	92
4.3.1.4	Feasibility of DFN/SC interface	93
4.3.2	Description of conceptual model	94

4.4	Modelling Methodology	99
4.4.1	Derivation of parameters	99
4.4.2	Simulation	102
4.4.3	Validation approach	102
4.4.4	Prediction	103
4.5	Interface to the stochastic continuum model	103
4.5.1	Basic definitions and assumptions	104
4.5.2	Generation of independent realizations of the DFN model	106
4.5.3	Estimation of the conductivity tensor	107
4.5.4	Packer test simulations	109
4.5.5	Covariance matrix function estimation	109
4.6	Interface to the streamtube model	112
4.6.1	Porosity	113
4.6.2	Wetted surface	114
5	DATA ANALYSIS FOR THE FRACTURE NETWORK MODEL	115
5.1	Statistical homogeneity	115
5.1.1	Dip angle data	115
5.1.2	Fracture frequency data	117
5.2	Size distribution for major and minor features	119
5.3	Geometry of major features	121
5.3.1	Orientation distribution	121
5.3.2	Termination measures	123
5.3.3	Intensity	124
5.4	Geometry of minor features (fractures)	127
5.4.1	Location	127
5.4.2	Orientation	130
5.4.3	Termination	132
5.5	Single fracture aperture variation	132
5.5.1	Fractal dimension for surface roughness	132
5.5.2	Variance of physical aperture	134

5.6	Steady-state packer test data interpretation	134
5.6.1	At-borehole <i>vs.</i> cross-fracture transmissivity	137
5.6.2	Simultaneous estimation of fracture transmissivity distribution, conductive fracture frequency, and depth-transmissivity dependence	137
5.6.3	Network effects and non-uniqueness in the estimation of transmissivity parameters	143
5.6.4	Conductive fracture intensity	146
5.7	Transient packer test reinterpretation	146
5.7.1	Transmissivity and dimensionality	148
5.7.2	Storativity <i>vs.</i> transmissivity	151
5.8	Detailed fracture properties	153
5.8.1	Fracture infilling	153
5.8.2	Porosity	155
5.8.3	Wetted surface	155
6	MODEL VALIDATION AND CALIBRATION	158
6.1	Conceptual model dataset	158
6.2	Packer test simulations	158
6.3	Results of validation exercise	163
7	ESTIMATION OF PARAMETERS FOR THE STOCHASTIC CONTINUUM MODEL	167
8	ESTIMATION OF TRANSPORT PARAMETERS	173
8.1	Flow porosity	174
8.2	Specific wetted surface	178
9	DISCUSSION OF RESULTS	184
9.1	Limitations of the DFN model	184
9.2	Computational limitations	185
9.3	Estimates transport parameters	185

10	CONCLUSIONS	187
	10.1 Site characteristics	187
	10.2 Discrete fracture network model	188
	10.3 Effective block-scale conductivity	188
	10.4 Effective transport parameters	189
	10.5 Methodology	189
	10.6 Recommendations for further study	190
11	ACKNOWLEDGEMENTS	191
12	REFERENCES	192
13	NOTATION	205
	APPENDICES	

LIST OF FIGURES**Page No.**

1.	INTRODUCTION	
1-1	Location of the Finnsjön site	3
2.	BACKGROUND	
2-1	Definitions of fracture aperture	8
2-2	Flow dimension in packer testing	11
2-3	The Finnsjön rock block	14
2-4	Location of major fracture zones at the site	17
2-5	Interpreted 3-D view of fracture zones	18
2-6	Schematic cross-section of Zone 2	20
2-7	Local-scale lineament map	21
2-8	Cell mapping near Borehole KFI 11	24
2-9	Scale effects in fracture trace and lineament length data	26
2-10	Comparison of conductivity estimates based on Moyes' formula and generalised radial flow analysis	29
2-11	Hydraulic conductivity profiles - Boreholes KFI 01 & 02	33
2-12	Hydraulic conductivity profiles - Boreholes KFI 03 & 06	34
2-13	Comparison of DFN, SC, and CN models	37
2-14	Dual-porosity streamtube model	38
3.	PROPERTIES OF SINGLE FRACTURES	
3-1	Cross-hole flow response in a single fracture - Stripa Channeling Experiment	53
3-2	Cross-hole tracer response in a single fracture - Stripa Channeling Experiment	54
3-3	Distributions of mechanical aperture based on joint surface profiles	56
3-4	In-situ aperture measurements - Stripa Channeling Experiment	58
3-5	Examples of aperture distribution produced by Brown's fractal model	60
3-6	Experimental measurements of effects of normal stress on fracture transmissivity	63
3-7	Compilation of data for effects of normal stress on fracture transmissivity	65
3-8	Effects of shear displacement on fracture transmissivity	67
3-9	Storativity vs. transmissivity for the Bandis-Barton model	69
3-10	Types of infilling structure	76
3-11	Theoretical and experimental estimates of hydraulic vs. void aperture relationship	80
4.	MODELLING APPROACH	
4-1	Single-domain and multi-domain DFN models	91
4-2	Conceptual model for fracture system	95

4-3	Conceptual model for spatial correlation among blocks	97
4-4	Simulations of packer tests and block-scale flow	98
4-5	FracMan/MAFIC Discrete Feature Modeling Package	100
4-6	Outline of modelling approach	101
4-7	Nested simulation scheme for fracture generation	108
5.	DATA ANALYSIS FOR THE FRACTURE NETWORK MODEL	
5-1	Estimation of optimum fit for size distribution parameters	120
5-2	Identification of fracture zones based on "Fracture Zone Index"	126
5-3	Estimation of Nearest Neighbor statistic	128
5-4	Analysis of fracture spacing distribution	129
5-5	Dataset for fracture orientation	131
5-6	Fracture aperture variability	133
5-7	OxFILZ packer test interpretation algorithm	136
5-8	Boundary conditions for estimation of cross-fracture vs. at-borehole transmissivity	138
5-9	Estimated at-borehole vs. cross-fracture transmissivity	139
5-10	Examples of conductivity profiles from a single OxFILZ simulation	141
5-11	OxFILZ estimate of fracture transmissivity distribution	142
5-12	Effect of network length on estimation of fracture transmissivity distribution	145
5-13	Distributions of flow and transmissivity from GRF analysis of packer tests	149
5-14	Flow dimension vs. GRF conductivity and transmissivity	150
5-15	Estimation of storativity vs. transmissivity relation	152
5-15	Empirical relationship for void aperture as a function of hydraulic aperture	156
6.	MODEL CALIBRATION AND VALIDATION	
6-1	Statistical description of the DFN conceptual model	159
6-2	Single realization of the DFN model	160
6-3	Geometry for packer test simulations	151
6-4	Distributions of flow dimension and transmissivity for the DFN model	165
7.	ESTIMATION OF PARAMETERS FOR THE STOCHASTIC CONTINUUM MODEL	
7-1	Equivalent conductivity for 40 m blocks at 500 m depth	168
7-2	Trends in block-scale conductivity with depth	171
7-3	Correlation of block-scale conductivity to multiple packer test measurements	172
8.	ESTIMATION OF TRANSPORT PARAMETERS	
8-1	Flux-weighted estimates of flow porosity	175
8-2	Porosity as a function of flux magnitude	177
8-3	Flux-weighted estimates rock-mass specific wetted surface	179
8-4	Rock-mass specific wetted surface as a function of flux magnitude	180
8-5	Flux-weighted estimates of flow specific wetted surface	181

8-6	Flow specific wetted surface as a function of flux magnitude	182
8-7	Correlation between porosity and flow specific wetted surface	183

1. INTRODUCTION

This report describes data analysis and discrete-fracture network (DFN) modelling performed by Golder Geosystem AB (GGAB) in conjunction with the SKB 91 safety assessment study, which is being performed by the Swedish Nuclear Fuel and Waste Management Co. (SKB) for a generic repository located at the Finnsjön site in Sweden (Figure 1-1).

The goals of the SKB 91 study have been described by Papp *et al.* (1990). A main objective is to evaluate the influence of site-specific parameters on probabilistic predictions of radionuclide migration from a KBS-3 type repository to the biosphere.

Radionuclide migration is modelled by combining mathematical submodels for each of the various aspects of the migration process. Uncertainty in input parameters for the submodels is estimated and propagated by Monte Carlo methods, to estimate the consequent uncertainty in the predicted radionuclide arrival-time distributions.

The Monte Carlo method involves repeated calculations of model outcomes, for random combinations of possible input parameter values. Practical limits on computation resources require either that the mathematical submodels be very simple, or that very fast numerical algorithms be used (Lovius *et al.*, 1990). Therefore the full complexity of geological systems cannot be represented in the submodels. Instead, simplified geological models are used. Simplified models are also used to interpret *in situ* measurements, to estimate model parameters such as hydraulic conductivity (Doe and Geier, 1990).

These simplifications lead to uncertainty which is difficult to account for within the Monte Carlo approach. One way to evaluate this uncertainty is to compare aspects of the main model with predictions of a more physically realistic approach.

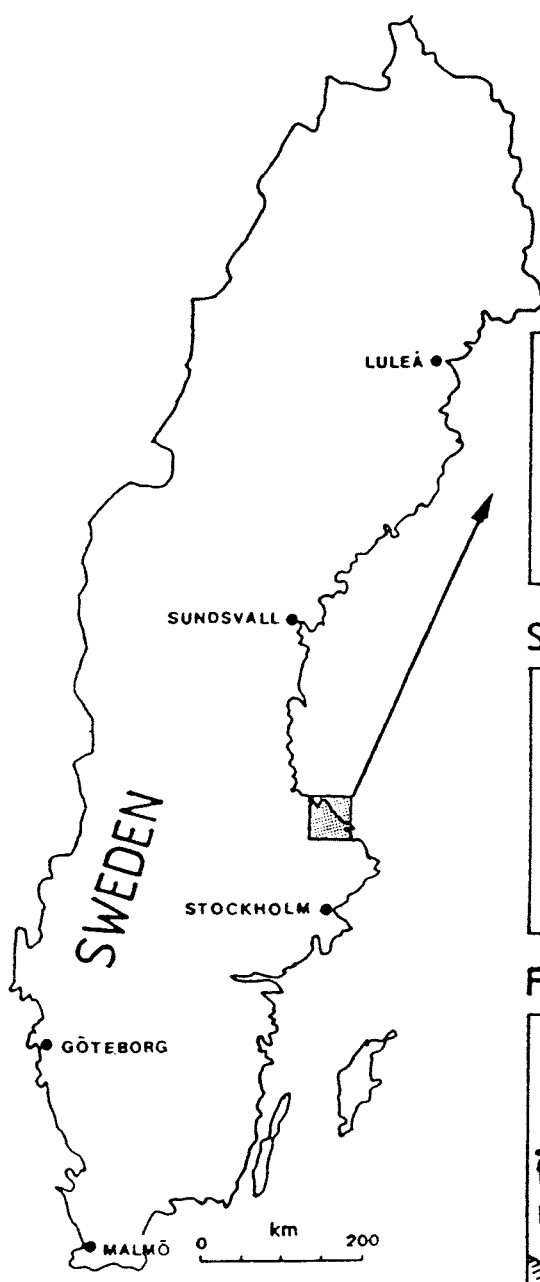
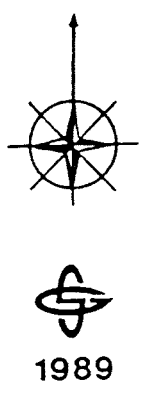
This report describes the use of an alternative approach, based on discrete-fracture network modelling, to estimate hydrologic and transport properties of the rock at the Finnsjön site. A DFN model is developed which provides a basis for appraising continuum-based models of the site. The predictions of this model can be used to evaluate a few assumptions of the main-line SKB 91 modelling approach.

In particular, this report addresses the following questions regarding the rock at Finnsjön:

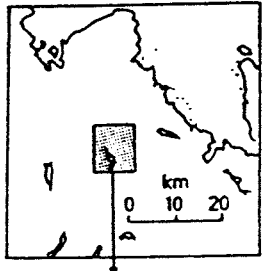
- How much do packer tests tell about large-scale hydrologic properties?
- Does the rock behave as a stochastic continuum on any practical scale?
- What are reasonable values for transport parameters?

The DFN approach provides a method for investigating these questions. This method (like other models presently available for modelling fractured rock) involves assumptions and simplifications. While most assumptions are well-founded on the available data, the current state of ignorance as to how water moves within fractured rock requires making a number of assumptions based on limited and/or indirect measurements of physical parameters. Nevertheless, the DFN approach is valuable because it explicitly represents the discontinuous

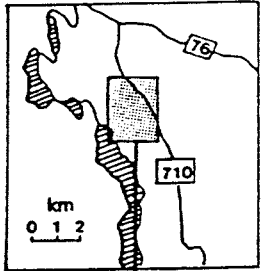
nature of flow in fractured rock, based upon observations of fracture geometry which cannot be utilized in other types of models.



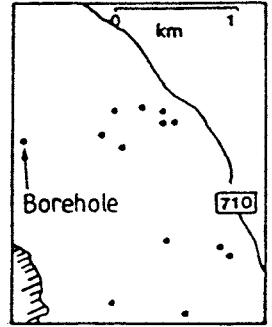
REGIONAL AREA



SEMI-REGIONAL AREA



FINNSJÖN SITE



(Andersson et al., 1991)

FIGURE 1-1
LOCATION OF THE FINNSJÖN SITE
SKB-91/DFNST

2. BACKGROUND

The DFN model of the Finnsjön site provides an interface between (1) the geological description of the site in terms of fractures and fracture zones, and (2) several simplified models of hydrogeological processes at the site. A description of the formulation and application of this model requires discussion of a wide span of topics, ranging from site-specific geology to the mathematics of the various models.

This chapter gives background information on concepts which are necessary for the later exposition. §2.1 gives definitions of terminology for the DFN model and other models. §2.2 gives a summary of site characterization activities which are relevant to development of the DFN model. §2.3 describes the different types of models for fractured rock that are related to this work, and summarizes the major strengths and weaknesses of the different methods.

2.1 DEFINITIONS

2.1.1 Geological terms

A *fracture* is any mechanical discontinuity or break in the rock.

A *joint* is a fracture for which there is little or no relative displacement between the opposing surfaces.

A *zone* is an approximately tabular region of the rock.

A *fracture zone* is a zone distinguished by a high fracture intensity (defined as in §2.1.2) relative to the surrounding rock. Strictly speaking this term should be applied only to zones with a fracture intensity at least one order of magnitude greater than in the surrounding rock (Gustafson, 1990). This report does not apply the further restriction (Carlsson and Gidlund, 1983) that the fractures within a zone should be subparallel.

This definition is clearly dependent on the scale of observation. Tirén (1989) gives sketches of connections between ends of single fractures on the scale of roughly 1 m. These complex interconnections on a fine scale may also be called "fracture zones," but in general the term will be applied only to zones with thickness ≥ 1 m.

A *fracture swarm* is a zone with relatively high fracture intensity, but not so high as a proper fracture zone (Gustafson, 1990).

A *lineament* is a chartable formation in a surface. The parts of a lineament are aligned in a straight or slightly curved line, which "deviates markedly from the pattern of surrounding formations and probably reflects a subterranean condition" (O'Leary, Friedman and Pohn, 1976, as quoted by Carlsson and Gidlund, 1983). In the present study, a lineament is commonly taken as evidence for a fracture zone.

A *hydrologic zone* is a tabular zone which is generally more permeable than the surrounding rock.

2.1.2 Fracture geometry

This section defines terminology for fracture geometry on the scale of a fracture network (as defined below). This terminology is based mainly on the system of Dershowitz and Einstein (1989).

Fracture *location* refers to the 3-D coordinates of the centroid of a fracture.

The *shape* of a fracture is its 2-D appearance when viewed from the direction in which the projected area is a maximum. The shape of a fracture may be polygonal, circular, elliptical, or "irregular." The present study treats all fractures as being polygonal. This allows approximate representation of most fracture shapes.

The *planarity* of a fracture is its character as related to an ideal plane. Most fractures are not perfectly planar, but rather curved, wavy, rough, or stepped. However, for large-scale modelling the effects of non-planarity may be minor, compared with connectivity effects. The present study treats all fractures as approximately planar.

Fracture *size* refers to the extent of a fracture. In the present report fracture size is described quantitatively as the *effective radius*, r_e . This is the radius of a circle with area equal to that of the polygonal fracture.

Fracture *orientation* is the direction of a vector perpendicular to the fracture plane. This may be described in polar or rectilinear coordinates.

Above the scale of a single fracture, some additional terminology is useful to describe characteristics of groups of fractures:

A *fracture network* is any group of one or more fractures, every member of which is connected to every other member, either directly or via other fractures in the group.

A *fracture population* is the aggregate of all fractures present in a given unit of the rock.

A *fracture set* is a distinctive subset of a fracture population. Commonly fracture sets are classified by orientations, but other characteristics such as mineralization, or hypotheses of fracture genesis may also provide a basis for classification.

Fracture intensity can be defined in various ways, but within this report this term refers always to the P_{32} intensity (Dershowitz, 1985; Dershowitz and Herda, 1992), which is the total fracture area per unit volume of rock.

Fracture frequency is the number of fractures intersected per unit length of a line sample (e.g. a borehole or scanline). This is the inverse of *mean fracture spacing*, which is the mean value of *fracture spacing* (the distance between fractures along a line) for a given sample length.

2.1.3 Fracture hydrologic properties

This study is concerned exclusively with saturated flow of fresh water through fracture systems. Therefore, for the purposes of this study, the terms *fluid density* (ρ_f) and *fluid viscosity* (μ_f) can be considered to be synonymous with *water density* (ρ_w) and *water viscosity* (μ_w). However, the distinction is observed in the notation used, and so ρ_f and μ_f are used only in expressions of general validity. The distinction could be relevant, for instance, if the results are applied to model saltwater flow at the Finnsjön site.

Hydraulic head is always taken to mean the total head:

where:

p	= absolute fluid pressure	[M/LT ²]
g	= gravitational acceleration	[L/T ²]
z	= elevation above some datum	[L]

Transmissivity is a constant of proportionality between flux density and the gradient of head for 2-D, steady flow in the plane of the fracture:

$$q_i = -T(\xi) \frac{dh}{d\xi_i} \quad (2-2)$$

where:

q_i	= flux per unit width of fracture plane in the direction ξ_i	[L ² /T]
$T(\xi)$	= transmissivity of the point ξ in the fracture plane	[L ² /T]
ξ_i	= i th component of the local coordinate vector ξ	[L]

No particular relationship between T and mechanical aperture (defined below) is assumed to hold. This definition is applicable to fractures with or without infilling. T is assumed to be locally isotropic in the plane, and independent of ∇h . The latter assumption may not be strictly true in fractures subject to high gradients, where turbulent flow may occur (Elsworth and Doe, 1986).

In the simplest case, T is assumed to be uniform within each fracture. For large-scale network flow, this assumption *may* be adequate, but is almost certainly invalid on the scale of a single fracture (Abelin *et al.*, 1985). Alternative assumptions are discussed in §3.1.

Cross-fracture transmissivity (T_f) is the macroscopic, effective T for flow across a section of a fracture. T_f is assumed to be isotropic within the plane of the fracture.

At-borehole transmissivity (T_b) is the effective T for flow from a borehole into a fracture, as measured by a packer test. Local variations may dominate T_b .

Storativity describes the increase in the weight of water in the fracture, per unit area of the fracture, in response to a unit increase in pressure:

$$S(\xi) = \lim_{A \rightarrow 0} \left(\frac{1}{A} \frac{\partial [\rho_w g V_w(\xi)]}{\partial p(\xi)} \right) \quad (2-3)$$

where:

A	= element of area in the fracture plane	[L ²]
$S(\xi)$	= storativity at a point ξ on a fracture	[-]
$V_w(\xi)$	= volume of water between the two faces of the fracture, within A around the point ξ .	[L ³]

The storativity is related to the fracture deformability (possibly including infilling deformability) and fluid compressibility, as discussed in §3.2.3.

The above definitions are often adequate for modelling large-scale DFN flow. To discuss the detailed-scale behavior, some additional definitions are useful (Figure 2-1):

Mechanical aperture ϵ_m is the separation between the two surfaces of a fracture.

Hydraulic aperture ϵ_h is an "effective" aperture related to T by the cubic law:

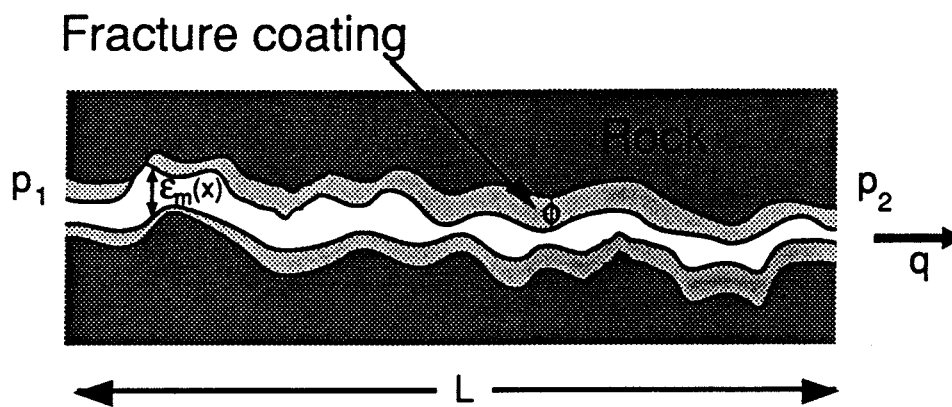
$$T = \frac{\epsilon_h^3 \rho_w g}{12\mu_w} \quad (2-4)$$

This definition is based on the solution for laminar flow between smooth, parallel plates. Due to fracture roughness and aperture variation, generally $\epsilon_h < \epsilon_m$.

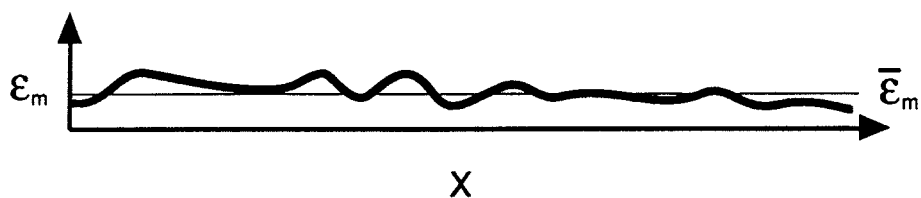
Void aperture ϵ_v is the accessible void volume contained per unit area of a fracture. For unfilled fractures this is simply the average mechanical aperture $\bar{\epsilon}_m$, but for a fracture with permeable infilling $\epsilon_v < \bar{\epsilon}_m$, due to the porosity of the infilling.

Transport aperture ϵ_T denotes the effective void aperture of a fracture for transport, e.g. as estimated from a tracer experiment. Theoretically $\epsilon_T \approx \epsilon_v$.

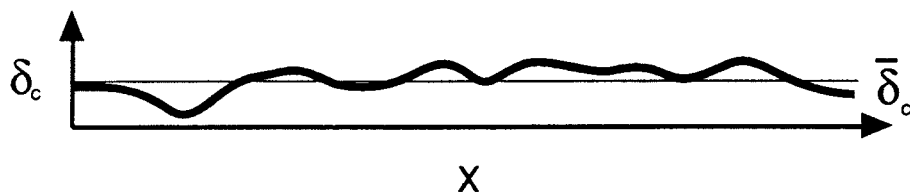
Fracture specific wetted surface (s_w) is the total surface area accessible to fluid within a saturated fracture, per unit area of the fracture plane.



Mechanical aperture



Coating thickness



Hydraulic aperture $\epsilon_h = \sqrt[3]{\frac{12\mu_w q L}{p_1 - p_2}}$

Void aperture $\epsilon_v = \bar{\epsilon}_m + \phi \bar{\delta}_c$

FIGURE 2-1
DEFINITIONS OF
FRACTURE APERTURE
SKB-91/DFNST

2.1.4 Rock mass hydrologic properties

The term "*unfractured*" rock refers to blocks of rock which, for practical purposes, can be said to contain no fractures. There is probably no such thing as a piece of rock which is unfractured, in absolute terms, above the scale of a single crystal, since polycrystalline rocks normally contain myriads of microfractures (Jaeger and Cook, 1979). However, for fluid flow calculations the smallest fractures can often be neglected.

Matrix conductivity (or *primary conductivity*) refers to the hydraulic conductivity of a piece of "unfractured" rock. For the purposes of this report, matrix conductivity is regarded as negligible. Non-zero matrix conductivity may be important for transport by matrix diffusion (Neretnieks, 1991), which is not considered in the present study.

Equivalent hydraulic conductivity (\hat{K}_e) for a volume of rock is the macroscopic, apparent conductivity tensor for the volume which acts for a particular set of boundary conditions.

Effective hydraulic conductivity (K_e) for a volume of rock is the macroscopic conductivity tensor (if one exists) for the volume which acts for any given set of boundary conditions.

The *total porosity* ϕ of a bulk volume of rock V_B is defined as:

$$\phi = \frac{V_v}{V_B} \quad (2-5)$$

where V_v the volume of void space within the volume V_B . For hydrologic purposes, usually ϕ includes some voids which are inaccessible to the moving fluid, so it is more appropriate to speak of a *flow porosity* ϕ_w which excludes inaccessible voids. For fractured rock with an impermeable matrix, ϕ_w includes the void space within all fractures contained in networks that connect to the hydrological boundaries. This may include pore space within permeable fracture infillings.

Specific wetted surface is defined in several ways within this report. *Rock-mass specific wetted surface*, S_b , is the total wetted surface area per unit volume of the rock mass (bulk volume). *Void-space specific wetted surface*, $S_v = \phi S_b$, is the wetted surface area per unit pore volume. *Flow specific wetted surface*, $S_w = \phi_w S_b$, is the total wetted surface area per unit volume of flowing water.

2.1.5 Packer testing terminology

Most of the packer test data considered herein are *single-hole packer tests*, as opposed to *cross-hole packer tests*. Single-hole tests can be interpreted either by steady-state or transient analysis.

The *flow dimension*, D_f , is of fundamental importance for both types of interpretation. This is defined by Barker (1988) as D_f where:

$$A_c \propto r^{D_F - 1} \quad (2-6)$$

describes the power at which the conductive cross-sectional area, A_c , increases with distance r from the borehole, for constant conduit conductivity K_c . For single-hole tests, the observed D_F will be the same whenever (Doe and Geier, 1990):

$$A_c K_c \propto r^{D_F - 1} \quad (2-7)$$

Figure 2-2 illustrates cases of *integral dimension flow*, including:

- a) *linear flow* ($D_F = 1$),
- b) *radial or cylindrical flow* ($D_F = 2$), and
- c) *spherical flow* ($D_F = 3$) for constant K_c .

As depicted, the conduits need not be "space-filling."

Fractional dimension flow refers to any flow dimension intermediate between the integral cases. Figure 2-2d shows an example for $D_F \approx 1.5$. The following terms are useful:

<i>sublinear flow</i>	$0 < D_F < 1$
<i>subradial flow</i>	$1 < D_F < 2$
<i>subspherical flow</i>	$2 < D_F < 3$
<i>hyperspherical flow</i>	$3 < D_F$

The general class of all flow dimensions, including integral and fractional D_F , is referred to as *generalized radial flow* (GRF). Further discussion is given by Barker (1988), and by Doe and Geier (1990), who give examples of GRF analysis for constant-pressure tests. Any conductivity value estimated by this theory shall be referred to herein as *GRF conductivity*, K_{GRF} . GRF estimates of transmissivity and storativity are denoted T_{GRF} and S_{GRF} , respectively.

POROUS
CONTINUUM

FRACTURED AND/OR CHANNELED
DISCONTINUUM

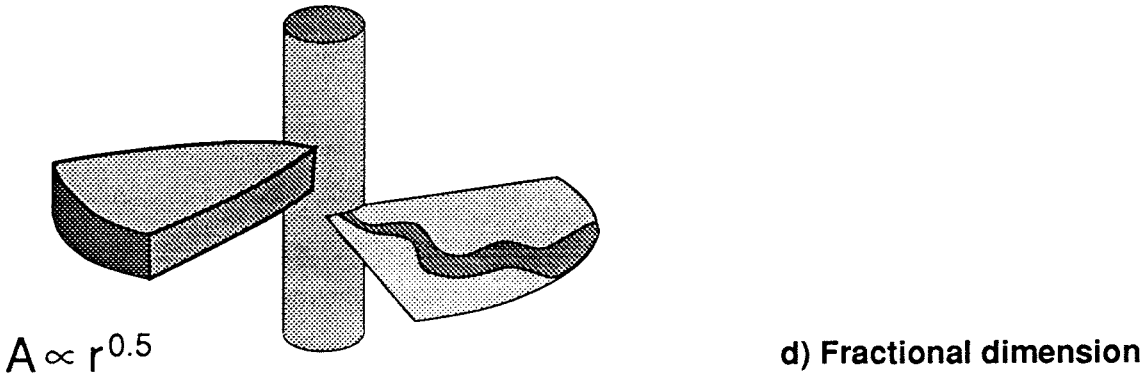
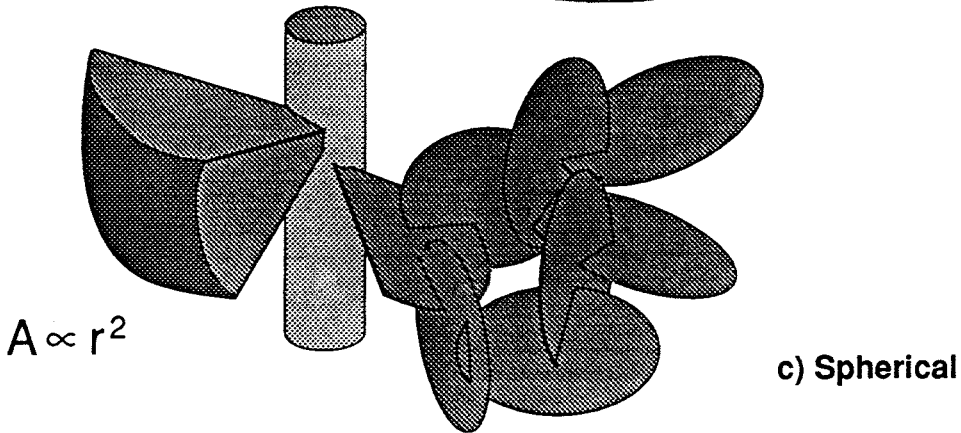
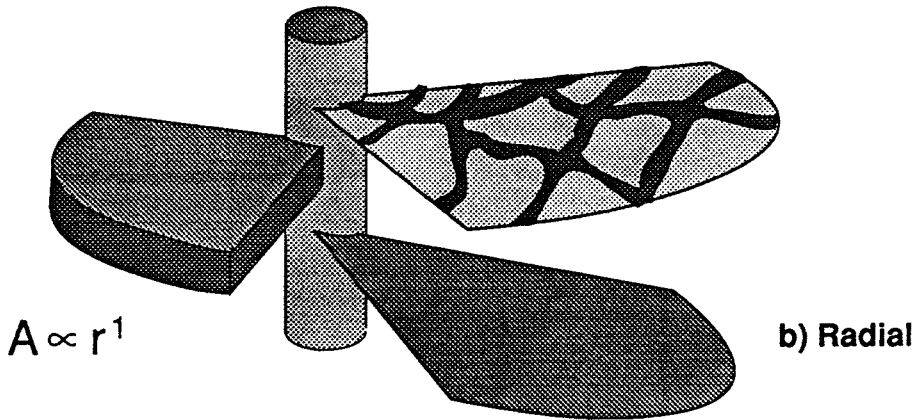
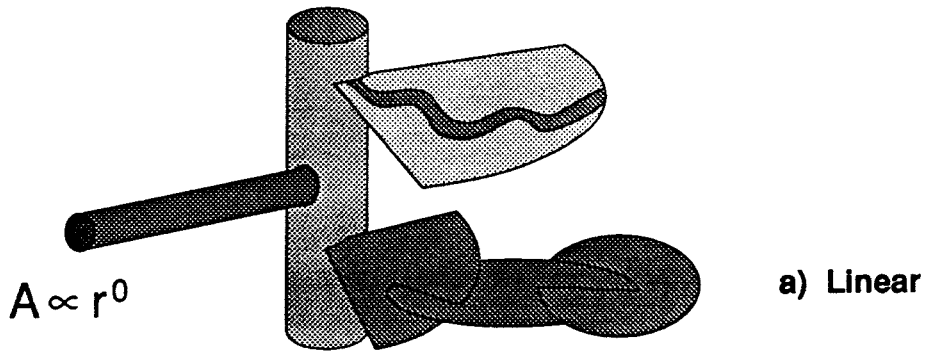


FIGURE 2-2
FLOW DIMENSION IN
PACKER TESTING
SKB-91/DFNST

Moyes-formula conductivity is a conductivity estimated from the assumed steady-flow the end of a constant-pressure packer test, using the formula of Moyes (1967):

$$K_{Moyes} = \frac{\rho_f g Q_f}{2\pi(p_w - p_i)} \left[1 + \ln\left(\frac{b_w}{2r_w}\right) \right] \quad (2-8)$$

where:

Q_f	= final flowrate measured at end of test	[L ³ /T]
p_w	= wellbore pressure during test	[M/LT ²]
p_i	= fluid pressure in rock prior to test	[M/LT ²]
b_w	= interval length (packer spacing)	[L]
r_w	= wellbore radius	[L]

This formula is based on an assumption that the flow is initially cylindrical, but becomes effectively spherical at a distance $r = 2b_w$ from the center of the section. The applicability of this formula is questionable for fractured, crystalline rock.

Packer test conductivity, K_p , is a generic term for a conductivity value estimated from a packer test by any method. Similarly, packer-test estimates of transmissivity and storativity are denoted T_p and S_p when referred to in a generic sense.

2.2 Site Description

The Finnsjön site (Figure 1-1) is located in northeastern Uppland in east-central Sweden. A geological description of the site is given by Ahlbom and Tirén (1991). The site is located within a granodiorite intrusion in earlier basic rocks. Lineaments indicate shear on a regional scale. The site is situated in the western wedge of a NW-trending shear lens, which is bounded by the Gräsbo and Giboda regional shear zones. This lens is subdivided into blocks by three sets of fracture zones:

- NW trending shear zones conforming to the regional zones
- NE trending, extensive shear zones which intersect the lens
- N-S trending, less extensive fracture zones

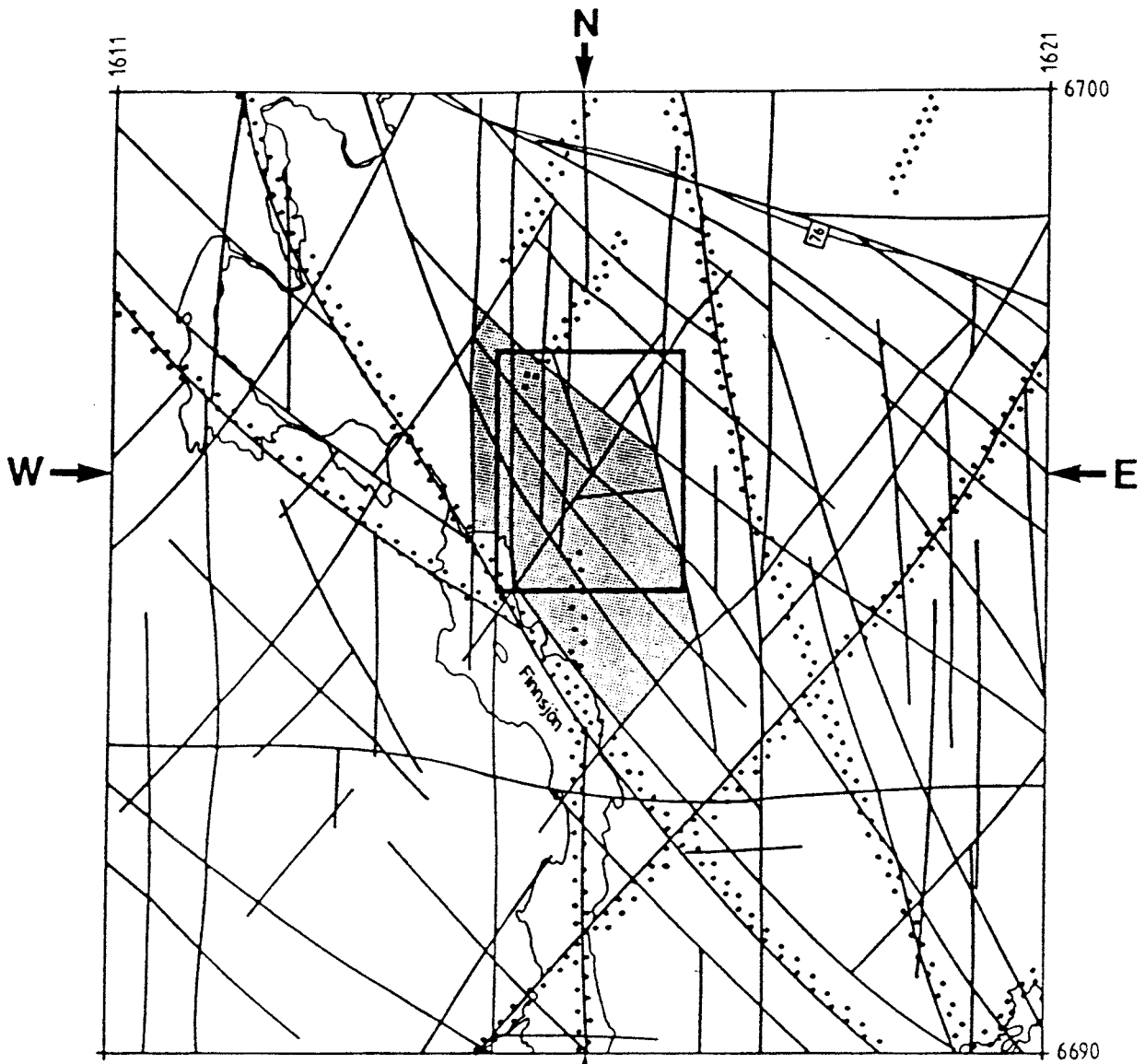
The Finnsjön site lies within one of these blocks, the Finnsjön Rock Block (Figure 2-3). The NE-trending, Brändan fracture zone divides this block into northern and southern blocks.

Detailed site investigations have been conducted to describe the geologic and hydrogeologic conditions in the Finnsjön area. The findings have been summarized by Andersson *et al.* (1991), who proposed conceptual models of the Finnsjön area for three different scales:

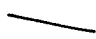


- Semiregional
- Local (site)
- Detailed

The semiregional model is used to estimate hydrologic boundary conditions for the local and detailed-scale areas. The local-scale ("far-field") model is used to predict transport of radionuclides from the hypothetical repository. The detailed-scale ("near-field") model considers transport in the immediate vicinity of the repository. The areas considered in the semiregional and local-scale model are shown in Figure 1-1. The boundaries of the models are delimited by sets of fracture zones which are thought to dominate groundwater flow within the respective regions.

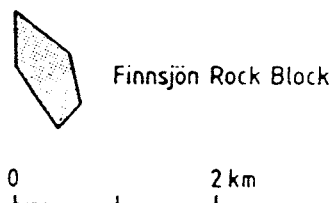
The present study is mainly concerned with characterization of the rock within the local-scale model. This section summarizes aspects of the site investigations which are of particular interest for DFN modelling on this scale.



ROCK BLOCK MAP , GÅVASTBO AREA
SEMI-REGIONAL AREA

-  Rock block boundary
-  Position of lineaments interpreted on regional scale
-  Finnsjön site

The glacial striation is north-south



Division of Engineering Geology
S A TIRÉN, Uppsala 1989

Rock block map of the Gåvastbo area, semi-regional area.

2.2.1 Major features

Fourteen major fracture zones have been identified at Finnsjön by synthesis of geologic, hydrogeologic and geophysical investigations (Ahlbom and Tirén, 1991; Andersson *et al.*, 1991). The zones were identified based on characteristics such as high K_f values and high fracture frequency, plus geological judgement taking into account fracture orientations and fracture coatings (Andersson *et al.*, 1991).

The major zones occur in four sets. The three subvertical sets mentioned in §2.2 are seen as lineaments. A subhorizontal set is inferred mainly from borehole data. A detailed geological description of the major zones is given by Ahlbom and Tirén. Figure 2-4 shows the lineaments identified as zones. Figure 2-5 shows a 3-D interpretation of the zones, including the subhorizontal Zone 2, which does not outcrop.

The reliability of this interpretation is discussed by Ahlbom and Tirén (1991), who state that "the only zones that can be regarded as well established, with respect to location and character, are Zone 1 and Zone 2. Other interpreted fracture zones must be regarded as more or less uncertain." Table 2-1 summarizes the evidence for the identified zones. For 10 of the 14 zones, the primary evidence comes from lineament maps and, at most, one borehole. The lineament maps give only limited information regarding degree of fracturing or dip (Ahlbom and Tirén, 1991). When only a single borehole intercepts a zone, several different interpretations may be possible (*op cit.*). Therefore most of the zone orientations may be regarded as uncertain. Interpretations are strengthened when more than one borehole intersects a zone and similarities in geological characteristics, such as fracture coatings, can be seen between boreholes. Ahlbom and Tirén suggest that further work, including new boreholes and trenches across fracture zones, could increase the reliability of the interpretation, but could also lead to identification of new zones.

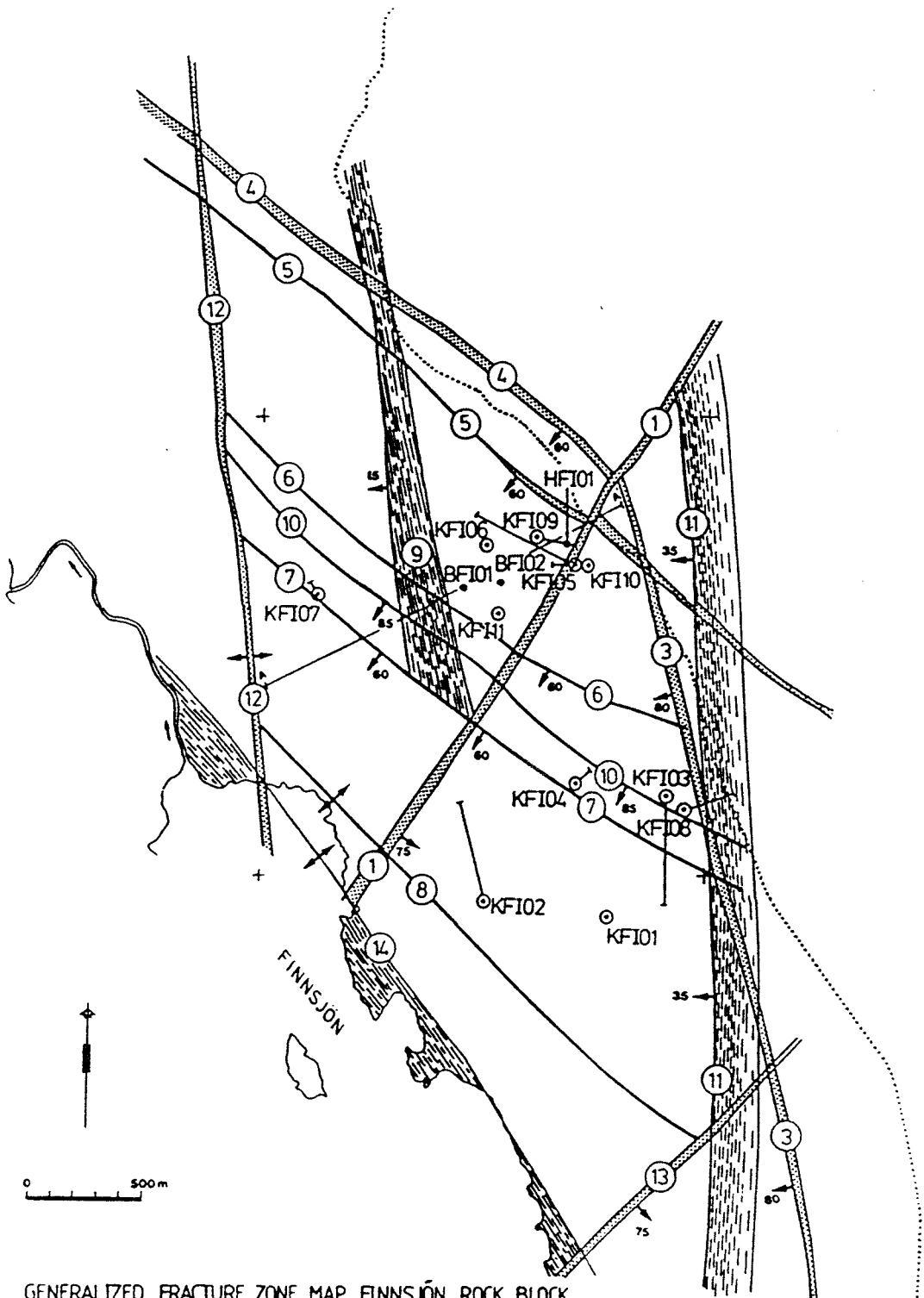
Thus with regard to characterization of the "major" fracture zones at the site, two problems are evident:

- Orientation and fracturing character of most of the major zones are uncertain.
- Unidentified zones, comparable in scale to the identified "major" zones (excluding perhaps Zone 2) may exist within the site.

The relevance of these observations for hydrologic modelling is discussed in §4.2.

Zone	Lineament evidence	Boreholes penetrating interpreted zone	Supplementary evidence
1	Yes	KFI05, 10	Resistivity maps. High K_p .
2	No	BFI01-02, HFI01, KFI05-07, 09-11	Alteration, mylonites. Crosshole hydrologic connections and high K_p in subzones. No anomaly in seismic reflection survey. Little displacement of intersecting structures seen with borehole radar.
3	Yes	KFI08	Geophysical logging and radar.
4	Yes	—	Dip inferred from proximity to Zone 5.
5	Yes	KFI05, 06, 09	High borehole conductivity.
6	"Poor"	KFI07	Geophysical measurements at surface.
7	Yes	—	—
8	Yes	—	—
9	Low relief	KFI07	No significant increase in K_p .
10	Yes	KFI03	—
11	Low relief	KFI01, 03, 04, 08	Borehole geophysics.
12	Yes	—	—
13	Yes	—	—
14	Yes	—	—

The most detailed characterization efforts have been focused on Zone 2. This is a "more or less altered" zone about 100 m thick, with a generally low fracture frequency except for 2-3 narrow (2-30 m) sections in each borehole (Ahlbom and Tirén, 1991). Zone 2 is considered to have been formed by ductile shear, with subsequent minor reactivation, mainly along the upper boundary.



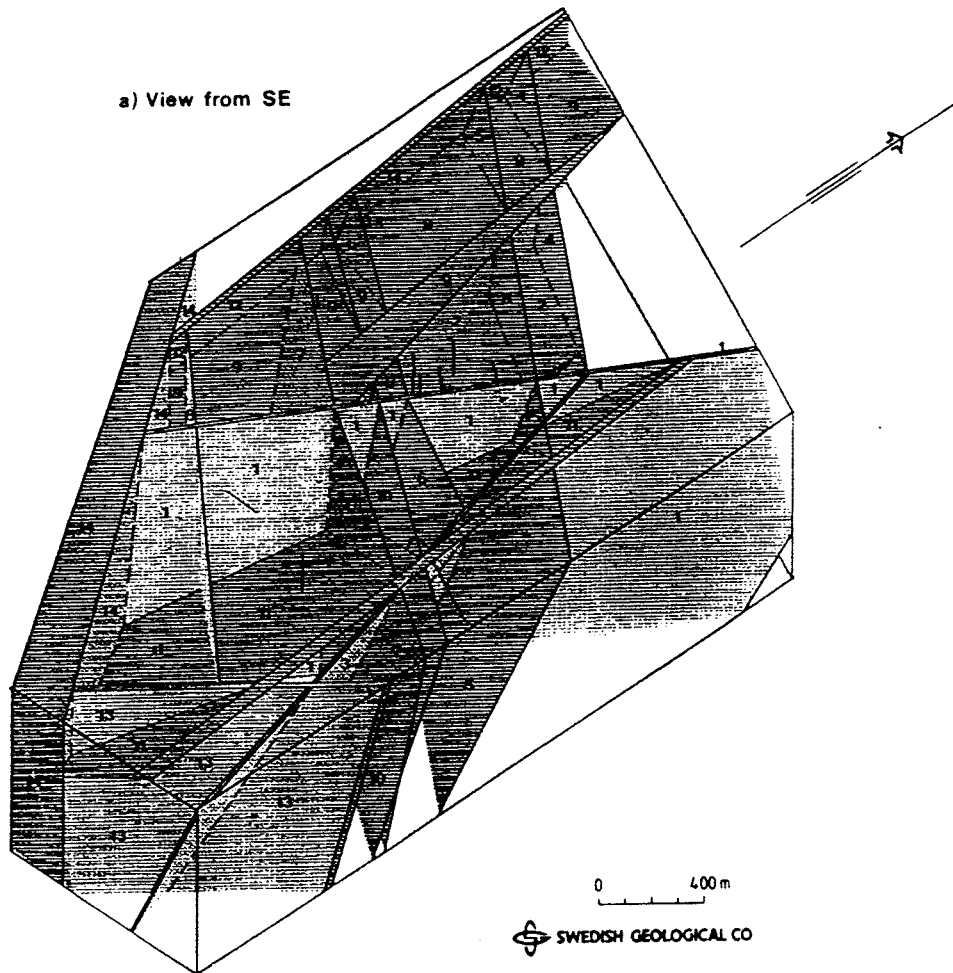
GENERALIZED FRACTURE ZONE MAP, FINNSJÖN ROCK BLOCK

- FRACTURE ZONES
- DIP, 60° AND VERTICAL
- CORE BOREHOLE
- PERCUSSION BOREHOLE

DIVISION OF ENGINEERING GEOLOGY
 S.A. Tinén, Uppsala
 1989

FIGURE **2-4**
LOCATION OF MAJOR FRACTURE ZONES AND BOREHOLES
 SKB-91/DFNST

(Anderson et al., 1991)



3D-model of the Finnsjön Rock Block. The view of the model is inclined 40°

(Anderson et al., 1991)

FIGURE 2-5
**INTERPRETED 3-D VIEW
 OF MAJOR FRACTURE ZONES**
 SKB-91/DFNST

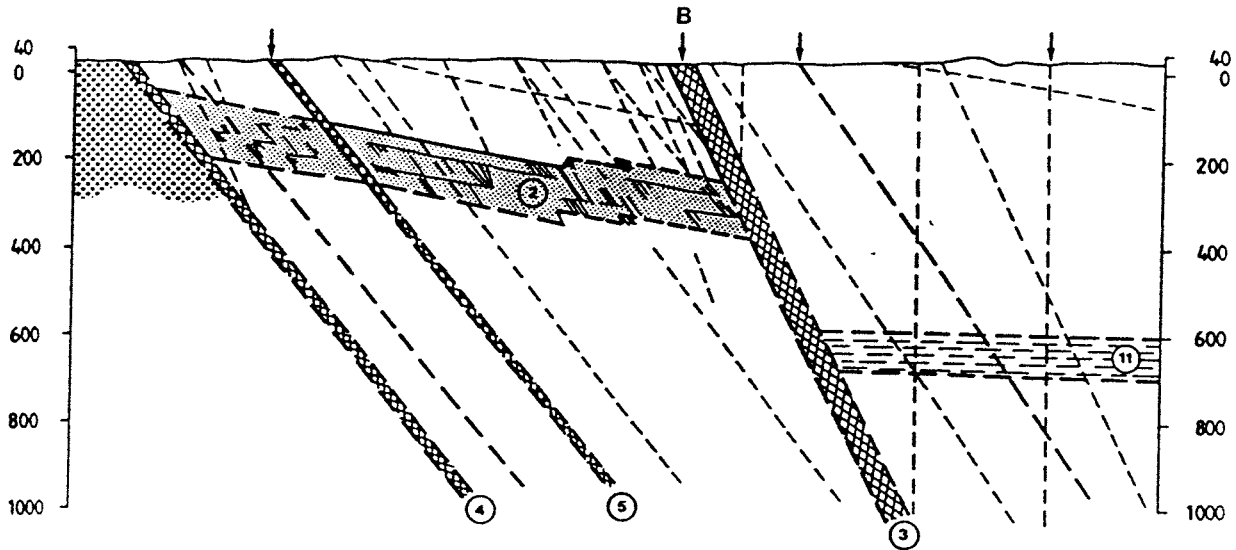
Zone 2 apparently does not form a continuous planar surface, but rather is interpreted as a compound fault (Figure 2-6). The zone was not detected by a reflection seismic survey (Ahlbom and Tirén, 1991), so there is some doubt about its structure away from boreholes. Evidence for interpolation of the zone between boreholes includes (1) frequent occurrence of mylonites, cataclastic rocks, and a high frequency of sealed fractures (Ahlbom and Tirén, 1991), and (2) its distinctive hydrologic character (§2.2.4) showing strong lateral connections.

Besides major zones, the site contains many subvertical, "minor" zones (Ahlbom and Tirén, 1991). These are seen on the local-scale lineament map (Figure 2-7). A N60W striking set has spacings of 40-400 m, with extents of several hundred meters and thicknesses commonly 1-5 m (up to 20 m). Within these minor zones, fracture frequencies range from 0.5-5 m⁻¹, and fractures are predominantly subparallel to the zones. A few minor zones with a NE orientation have also been mapped at surface.

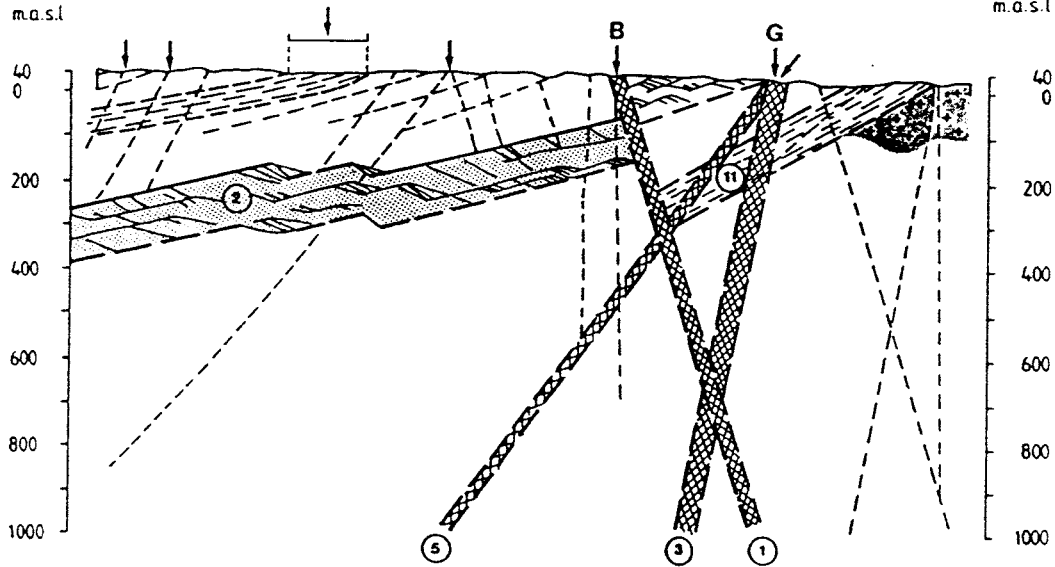
Below surface, the frequency of minor zones can be inferred from borehole radar reflections. The radar reflectors may be interpreted as "minor fracture zones" or, in some cases, lithological contacts. Table 2-2 gives the frequency of minor reflectors in 10 of the 14 deep boreholes. These data indicate a mean zone spacing of about 20 m. Estimates of the extents of the features that produce the reflection are only approximate. However, inspection of radar maps suggests that a feature must extend more than 20 to 25 m to be distinguished, for the radar wavelengths used.

The minor zones may be significant for radionuclide transport. If the hypothetical repository is situated within a block bounded by major zones, then the most conductive pathway to a major zone could well follow minor zones within the block. Feasibility of modelling the minor zones with DFN and other models is discussed in §2.3.

N (6694740, 1616075) S (6694750, 1616075)
 m.a.s.l. m.a.s.l.



W (6693340, 1615150) E (6693340, 1617150)
 m.a.s.l. m.a.s.l.

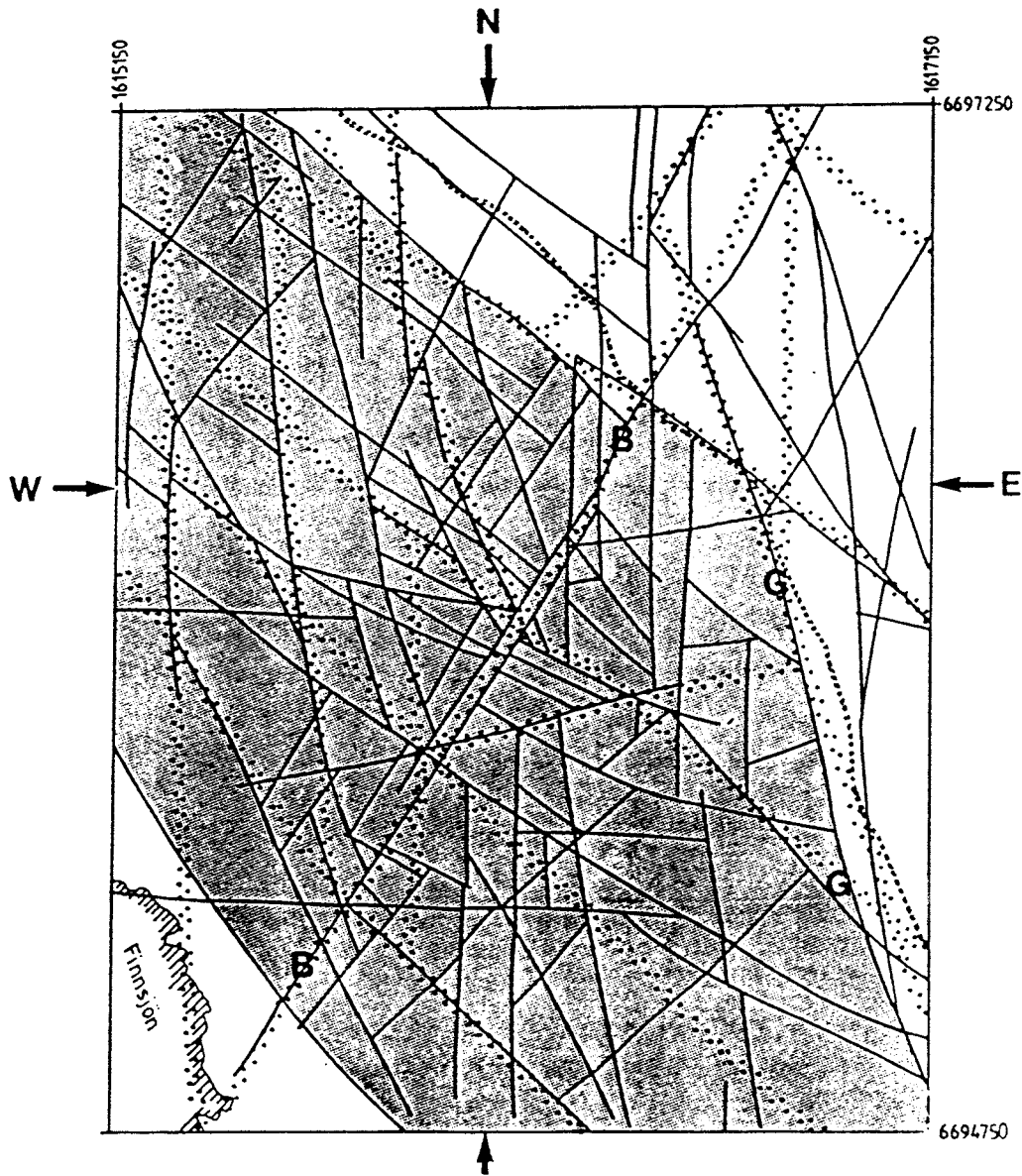


- YOUNGER GRANITE, USUALLY UNFOLIATED
- FOLIATED GRANODIORITE
- GREENSTONE

Tentative geological vertical cross-sections in N-S and E-W through the Finnsjön site. The numbers at fracture zones refer to their identification (c.f. Chapter 6). Arrows mark lineaments identified on the semi-regional scale map.

FIGURE 2-6
 SCHEMATIC CROSS-SECTION
 OF ZONE 2
 SKB-91/DFNST

(Ahlbom and Tiren, 1991)



ROCK BLOCK MAP, FINNSJÖN SITE

LOCAL AREA

— Rock block boundary

⋯ Position of rockblock boundaries interpreted on semi-regional scale

The glacial striation is north-south



Finnsjön Rock Block

0 500m



Division of Engineering Geology
S.A. TIRÉN, Uppsala 1989

(Anderson et al., 1991)

FIGURE 2-7
LOCAL-SCALE LINEAMENT MAP
SKB-91/DFNST

Table 2-2 Frequency of radar reflectors in boreholes at the Finnsjön site.

Borehole	Surveyed Length (m)	Number of Reflectors	Frequency of Reflectors (m ⁻¹)	References
BFI 01	450	23	0.051	Niva, 1987
BFI 02	260	20 (1)	0.077	Andersson and Carlsten, 1987
HFI 01	110	5 (2)	0.045	Ahlbom <i>et al.</i> , 1986
KFI 05	530	31	0.058	Ahlbom <i>et al.</i> , 1986
KFI 06	510	22	0.043	Ahlbom <i>et al.</i> , 1986
KFI 07	500	15	0.030	Ahlbom <i>et al.</i> , 1987
KFI 08	170	4	0.024	Ahlbom <i>et al.</i> , 1987
KFI 09	350	22 (2)	0.063	Ahlbom <i>et al.</i> , 1986
KFI 10	240	9 (2)	0.038	Ahlbom <i>et al.</i> , 1986
KFI 11	380	20	0.053	Ahlbom <i>et al.</i> , 1987
All HIs	3500	171	0.049	

(1) Excludes parallel reflectors.

(2) Excludes reflectors projected to intersect beyond ends of hole

2.2.2 Fractures

Ahlbom and Tirén (1991) have classified the fractures at the site into two steeply dipping sets (NE trending and NW trending) and a set of flat-lying fractures. The following is a summary of their observations regarding these sets:

The NE (N10-70E) set is the most frequent. These fractures dip steeply SE, and often occur *en echelon*. The set seems to have been formed by a regional ENE, left-lateral shearing with a NNE compressive component.

The NW (N25-80W) set dips steeply SW, and are commonly more extensive in outcrops.

The flat-lying set is scarce in outcrops. Most of the mapped fractures in this set dip toward SW. Wall-rock alteration in some of these indicates that the flat-lying fractures have been connected with the NE trending fractures.

The fracture frequency measurements along outcrop scanlines and in core are similar (Ahlbom and Tirén, 1991). The average fracture frequency in the upper 100 m of boreholes KFI 03, 04, and 05 is 3.0 m⁻¹ excluding crushed sections. Ahlbom and Tirén observed that no decrease is seen in fracture frequency with depth.

Fracture surveys in the northern (Brändan) block show a lower fracture frequency (1.5 m^{-1}) than in the southern (Gåvastbo) block (2.9 m^{-1}). This lower frequency is also seen in KFI11, in the northern block (Ahlbom and Tirén, 1991). Other differences between blocks include:

- NE-trending fractures in the southern block containing pink coatings of laumontite and hematite, which are rare in the northern block.
- A resistivity contrast across the Brändan zone which indicates lesser fracturing in the northern block.

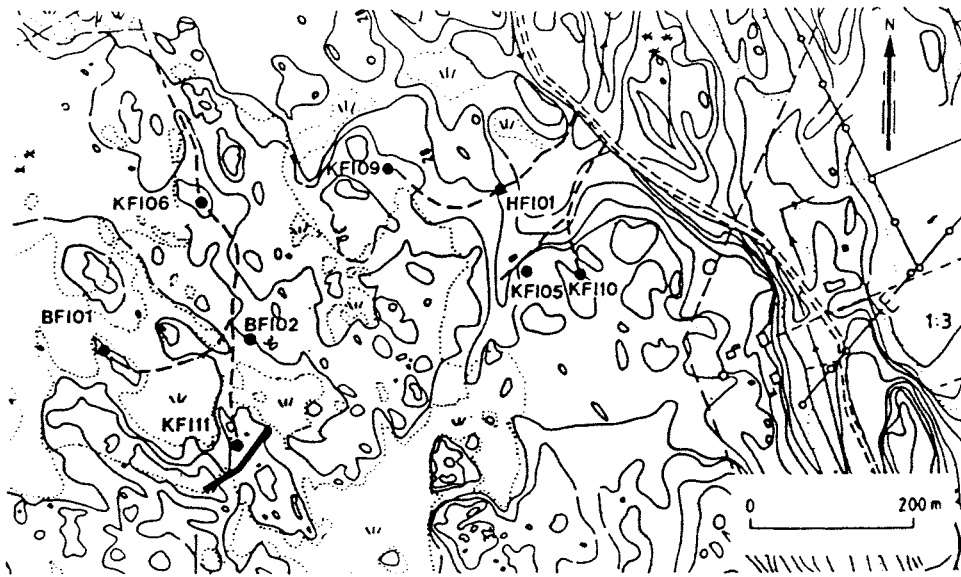
The dataset for fracture geometry at the Finnsjön site consists of:

- Detailed cell mapping of a 48 m long by 1 m wide section of a trench (Tirén, 1990), in which fracture trace lengths and fracture orientations (strikes and dips) were recorded for all traces longer than about 0.1 m. The trench was located close to KFI 11 (Figure 2-8).
- Scanline mapping of another section of the same trench, 40 m long, in which strikes and dips were recorded (Tirén, 1990).
- Scanline mapping for the PROF study (Andersson *et al.*, 1991) in which fracture strike was recorded, but dips and trace lengths were not determined for most fractures.
- Unoriented core from the KFI boreholes, which gives information on fracture spacing and incomplete information about fracture orientation. Core from vertical holes gives true dip angles, which were analyzed in the present study (§5.1).

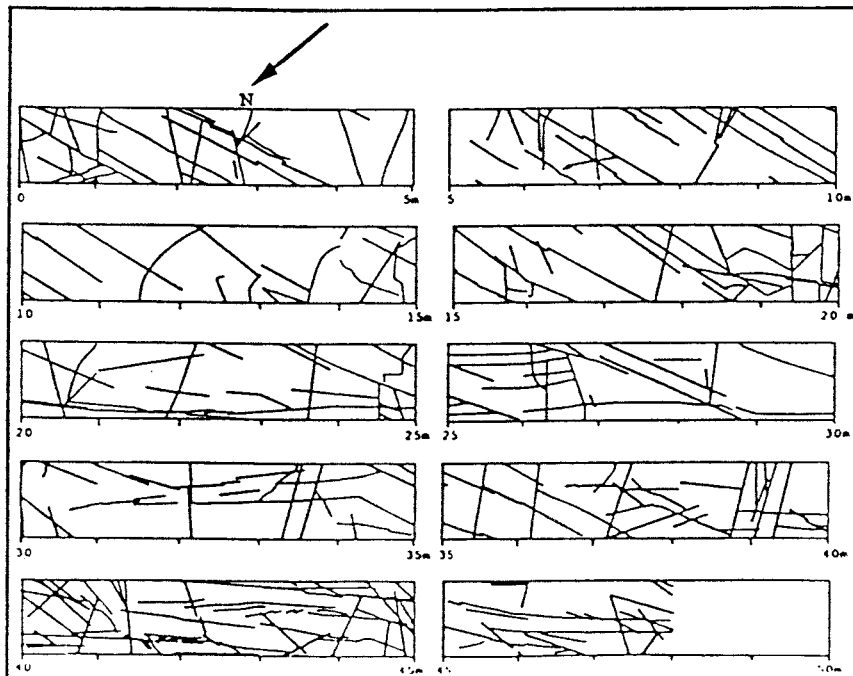
There are virtually no data regarding fracture size from subsurface. The cores are unoriented, so fracture orientations cannot be uniquely determined. Therefore extrapolation of fracture geometric data to depth is questionable. Evidence which can be examined to consider whether extrapolation is justified includes:

- Dip angles in vertical core (evidence of a homogeneous distribution with respect to depth).
- Fracture tracelength and lineament data (evidence for a common size distribution valid over a wide range of scales).
- Fracture frequency in core (evidence of a change in fracturing intensity).
- Other data such as similarities in infilling and rock type.

A preliminary analysis of fracture dip angle was given by Geier and Axelsson (1991), to examine possible similarity between the fracture population at the surface and at depth. This was based on qualitative comparisons between Terzaghi-corrected distributions for dip angle from cell maps, scanlines, and vertical boreholes. The comparison was crude, and no test was made of the statistical significance of the similarities. Major problems are that the cellmap data are considered to be atypical due to an unusually high percentage of NE trending fractures



Location of excavated trench, just SE of borehole KFI11 (KFIxx, BFIxx and HFIxx are different types of boreholes).



Fracture map of the 1 x 48 m cell.

FIGURE 2-8
**DETAILED-SCALE MAPPING
 NEAR BOREHOLE KFI 11**
 SKB-91/DFNST

(Anderson et al., 1991)

(personal communication, S. Tirén, 1991) and the large number of scanline fractures with no dip measurement, which may be subvertical. These problems make comparisons between borehole and surface data unreasonable, and therefore in the present study (§5.1) comparison is restricted to dips in core at different depths.

Geier and Axelsson (1991) also gave preliminary analysis of the fracture size distribution. They observed that both fracture tracelengths and lineaments roughly followed a common, power law distribution:

$$f_{\lambda}(\lambda) \propto \lambda^{-B} \quad (2-9)$$

where $B \approx 3$, as indicated in Figure 2-9.

2.2.3 In-situ stresses

The stresses in the rock at Finnsjön have been measured by hydraulic fracturing in the vertical borehole KFI 06 (Bjarneson and Stephansson, 1988). Regression analysis by Bjarneson and Stephansson gives a linear model for the stress variation with depth as:

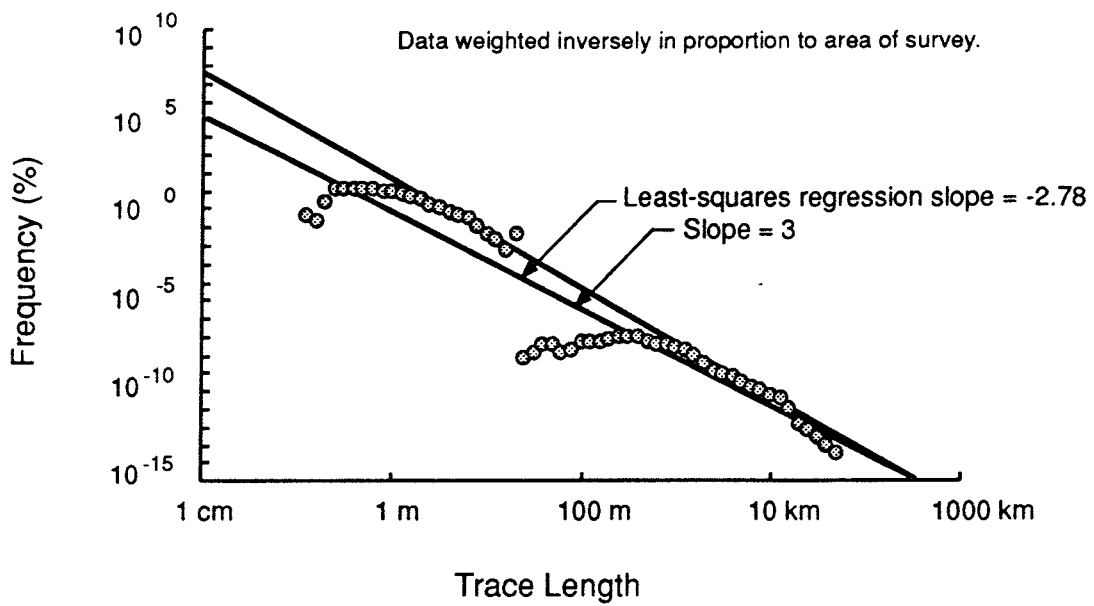
$$\begin{aligned} \sigma_v &= \left(0.0265 \frac{\text{MPa}}{\text{m}}\right) Z \\ \sigma_h &= 2.6 \text{ MPa} + \left(0.0237 \frac{\text{MPa}}{\text{m}}\right) Z \\ \sigma_{H(1)} &= 6.2 \text{ MPa} + \left(0.0416 \frac{\text{MPa}}{\text{m}}\right) Z \\ \sigma_{H(2)} &= 2.4 \text{ MPa} + \left(0.0412 \frac{\text{MPa}}{\text{m}}\right) Z \end{aligned} \quad (2-10)$$

where:

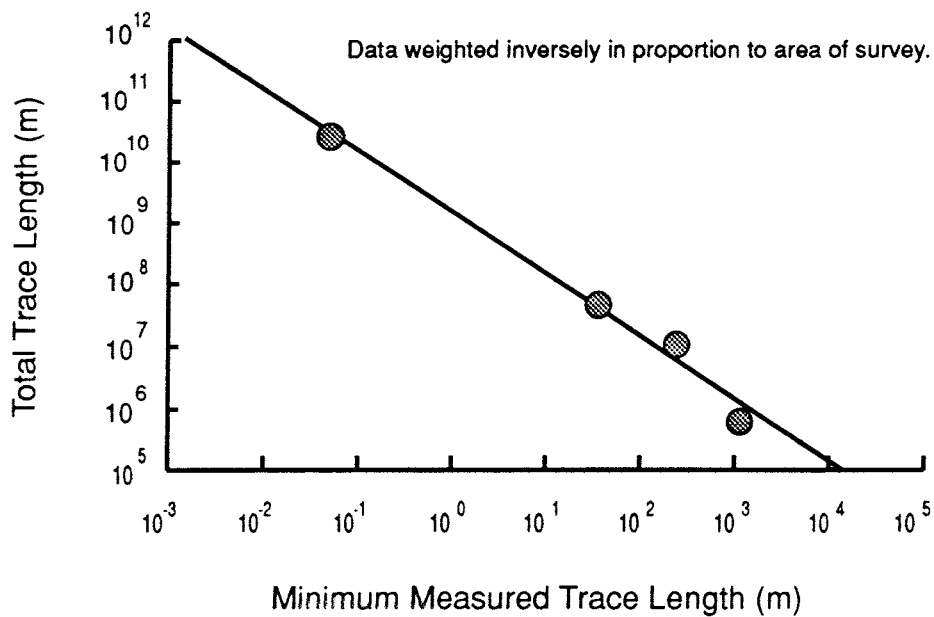
σ_v	= vertical stress	[MT ² /L]
σ_h	= minimum horizontal stress	[MT ² /L]
$\sigma_{H(1)}$	= maximum horizontal stress by 1st breakdown method	[MT ² /L]
$\sigma_{H(2)}$	= maximum horizontal stress by 2nd breakdown method	[MT ² /L]

The regression indicates that the vertical stress is the minimum principal stress down to depths of about 500 m. The analysis indicated a slight discontinuity in σ_h of about 3 MPa across Zone 2, but the data were inconclusive for σ_H . Strikes of vertical hydrofractures were consistently NW-SE, giving the direction of σ_H as N45°W above and N53°W below Zone 2.

The stress field is expected to have important effects on fracture conductivities, based on experimental evidence described in §3.2. A possible effect is that subhorizontal fractures will tend to be more conductive than subvertical fractures.



a) Distribution of fracture trace and lineament lengths.



b) Total observed tracelength as a function of survey resolution.

FIGURE 2-9
**SCALE EFFECTS IN FRACTURE TRACE
 AND LINEAMENT LENGTH DATA**
 SKB/SKB91 DFNST

(from Geier and Axelsson, 1990)

2.2.4 Hydrologic measurements

Small-scale hydrologic measurements of the rock at Finnsjön have been obtained by single-hole water injection tests in boreholes. Table 2-3 summarizes the dataset for 2 m and 3 m packer tests at Finnsjön.

Table 2-3 Single-hole injection tests at the Finnsjön site, 2 m and 3 m section lengths (from GEOTAB database).				
Borehole	Nominal Section Length (m)	Number of Sections	Estimated Minimum Measurable Conductivity (m/s)	Type of analysis
KFI06	2	3	7.5×10^{-10}	Transient
KFI07	2	4	7.5×10^{-10}	Transient
KFI09	2	2	4.0×10^{-11}	Transient
KFI10	2	9	1.0×10^{-10}	Transient
BFI01	2	115	1.0×10^{-10}	Steady-state
BFI02	2	42	1.0×10^{-10}	Steady-state
HFI01	2	10	5.0×10^{-10}	Steady-state
KFI01	2	240	2.4×10^{-9}	Steady-state
KFI02	3	220	2.0×10^{-9}	Steady-state
KFI03	3	223	3.0×10^{-9}	Steady-state
KFI04	3	181	1.9×10^{-10}	Steady-state
KFI05	2	108	7.5×10^{-10}	Steady-state
KFI05	3	231	1.9×10^{-10}	Steady-state
KFI06	2	48	7.5×10^{-10}	Steady-state
KFI06	3	206	1.9×10^{-10}	Steady-state
KFI07	2	50	7.5×10^{-10}	Steady-state
KFI07	3	175	1.9×10^{-10}	Steady-state
KFI08	3	139	1.6×10^{-10}	Steady-state
KFI09	2	74	1.0×10^{-10}	Steady-state
KFI10	2	81	1.0×10^{-10}	Steady-state
KFI11	2	75	1.0×10^{-10}	Steady-state

The table also indicates the type of analysis that was used for each set of tests. The "steady-state" tests were interpreted using Moyes' formula (Andersson *et al.*, 1991). Only a few transient interpretations have been produced. However, some of the steady-state tests produced transient flowrate and pressure data which allows evaluation of the flow geometry for the tests.

A limited program of crosshole packer testing has also been performed at the site (Andersson *et al.*, 1989a; Andersson *et al.*, 1991). This program was focused almost exclusively on Zone 2. A number of cross-hole tracer tests were also performed.

2.2.4.1 Single-hole packer test results

The GEOTAB database includes K_{Moyes} estimates from steady-state tests. The accuracy of Moyes' formula (§2.1.4) is questionable, due to assumptions about flow dimension which are not generally valid in fractured crystalline rock (Karasaki, 1986; Doe and Geier, 1990).

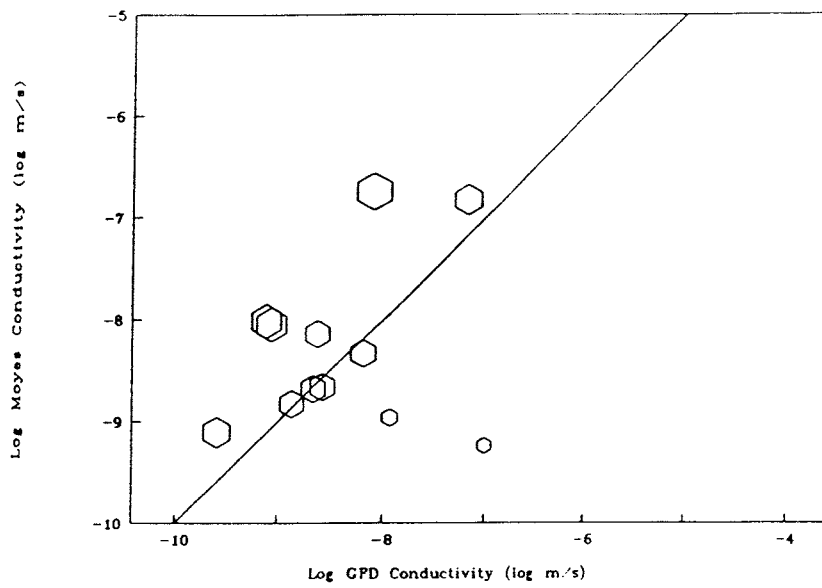
Preliminary GRF analysis of a limited dataset (Geier and Axelsson, 1991) suggests that the errors in estimates of mean K may be small, but the variance in K may be underestimated. Figure 2-10 compares estimated K_{GRF} values with K_{Moyes} . For $2 \leq D_f \leq 3$ the estimates agree within 1 or 2 orders of magnitude, but for subradial flow the disagreement can be larger.^[1] The data set may have been biased toward more conductive intervals. §5.6 presents an extension of the GRF analysis to all 2 m test data from BFI 01, BFI 02, and KFI 11.

Due to the uncertain flow geometry, the most defensible use of the K_{Moyes} data is as a rough indication of trends and anomalies in the rock. In the SKB 91 study, the K_{Moyes} data have been used to identify the hydrologically important fracture zones (Andersson *et al.*, 1991), and to estimate the hydrological properties of these zones. Table 2-4 gives estimated zone transmissivities T_z for the major zones from Andersson *et al.*, for each borehole intersecting the zones.

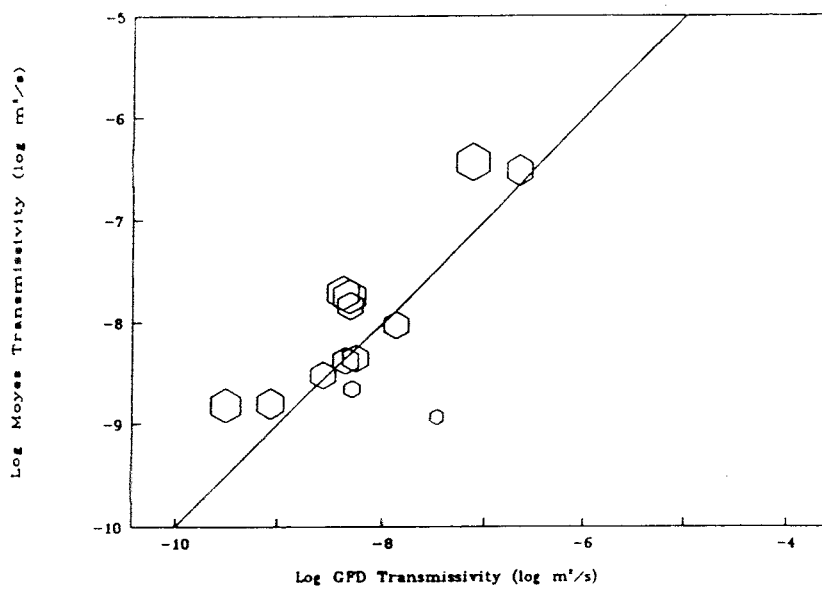
These data give some indication of heterogeneity within the major zones. For upper and lower parts of Zone 2, estimates of T_z vary by only an order of magnitude or so between boreholes, but for the other zones (where comparison is possible) the variation is 2-3 orders of magnitude.^[2]

¹ GRF analysis is also subject to limitations, mainly related to the uncertainty about conduit cross-section at the borehole. Therefore the K_{GRF} estimates should be viewed as "alternative" rather than "correct" estimates, although major errors due to inappropriate assumptions about D_f are hopefully eliminated by treating D_f as a parameter to be estimated.

² The fact that large variability is seen within a limited number of packer sections within a zone underscores the relevance of the observed heterogeneity. Including additional sections from the surrounding rock would not change the estimated T_z by much, since the sections classified as zones have higher K_{Moyes} by orders of magnitude, than the surrounding rock.



a) Conductivity



b) Transmissivity

○ Dimension = 1

⬡ Dimension = 3

FIGURE 2-10
 COMPARISON OF CONDUCTIVITY
 ESTIMATES BASED ON MOYE'S FORMULA
 AND GENERALIZED RADIAL FLOW ANALYSIS

SKB-91/DFNST

(Geier and Axelsson, 1991)

There is also great variation in zone properties, within a single borehole. Based on ratios of maximum T_p to total T_z as calculated by Andersson *et al.* (1991), typically the major portion of T_z is due to a single packer interval, although in a few places (Zone 3, Zone 5 where intercepted by KFI 05, and Zone 11 where intercepted by KFI 01 and 08) the T_z is well distributed. Based on inspection of K_{Moyes} profiles, Geier and Axelsson (1991) noted that the variations within a single zone, in places, may exceed the difference between the zone and the "rock mass" taken as a whole. This suggests the possibility of treating the major fracture zones as expressions of the ordinary variability in the rock mass. This is discussed further in §4.2.

Table 2-4 Estimated transmissivities of major zones at Finnsjön (from Andersson *et al.*, 1991).

Fracture Zone	Borehole	Packer Spacing (m)	Length Tested (m)	Estimated Transmissivity (m ² /s)
1	KFI 10	20	40	2.6×10 ⁻⁴
	KFI 10	2	28	2.1×10 ⁻⁴
2 (upper)*	BFI 01**	2	20	1.3×10 ⁻³
	BFI 02	2	24	1.7×10 ⁻³
	HFI 01	2	47	4.6×10 ⁻⁴
	KFI 05	2	26	1.2×10 ⁻³
	KFI 06	2	25	5.6×10 ⁻⁴
	KFI 09	2	32	1.0×10 ⁻³
	KFI 10	2	19	1.2×10 ⁻⁴
	KFI 11	2	23	3.7×10 ⁻⁴
2 (middle)*	KFI 05	2	13	4.2×10 ⁻³
	KFI 09	2	36	5.8×10 ⁻⁴
	KFI 10	2	34	7.6×10 ⁻⁵
2 (lower)*	BFI 01	2	19	1.1×10 ⁻⁴
	BFI 02	2	24	8.3×10 ⁻⁴
	KFI 05	2	55	2.6×10 ⁻⁴
	KFI 06**	2	27	6.7×10 ⁻⁴
	KFI 09	2	41	1.2×10 ⁻⁴
	KFI 10	2	31	2.2×10 ⁻⁴
	KFI 11**	2	32	1.7×10 ⁻⁵
3	KFI 08	3	111	1.0×10 ⁻⁴
5	KFI 05	3	42	1.6×10 ⁻⁵
	KFI 06	3	3	1.4×10 ⁻⁶
	KFI 09	2	4	2.9×10 ⁻⁵
	KFI 09	20	20	1.2×10 ⁻⁴
6	KFI 07	3	6	2.9×10 ⁻⁸
9	KFI 07	3	54	2.5×10 ⁻⁶
10	KFI 03	3	6	2.8×10 ⁻⁸
11	KFI 01	2	56	5.9×10 ⁻⁷
	KFI 03	3	168	6.6×10 ⁻⁴
	KFI 04	3	30	1.7×10 ⁻⁴
	KFI 08	3	99	1.1×10 ⁻⁴

* Data for single-hole test sections corresponding to interference sections as given in Table 4.7 of Andersson *et al.* (1991)

** Values for two subsections of zone section have been summed. Subsections are not contiguous in some cases.

A second use of the K_{Moyes} data, within the SKB 91 project, has been to estimate the hydrological properties of the rock mass, including the evaluation of trends with depth. Plots of the K_{Moyes} data from Finnsjön as a function of depth indicate that, on average, hydraulic conductivity decreases with depth. This has been described by Andersson *et al.* (1989a), in terms of a regression model which gave:

$$K_{Moyes} = (1.04 \times 10^{-6}) z^{-1.10} \quad [\text{m/s}] \quad (2-11)$$

for the southern block and:

$$K_{Moyes} = (3.90 \times 10^{-5}) z^{-1.53} \quad [\text{m/s}] \quad (2-12)$$

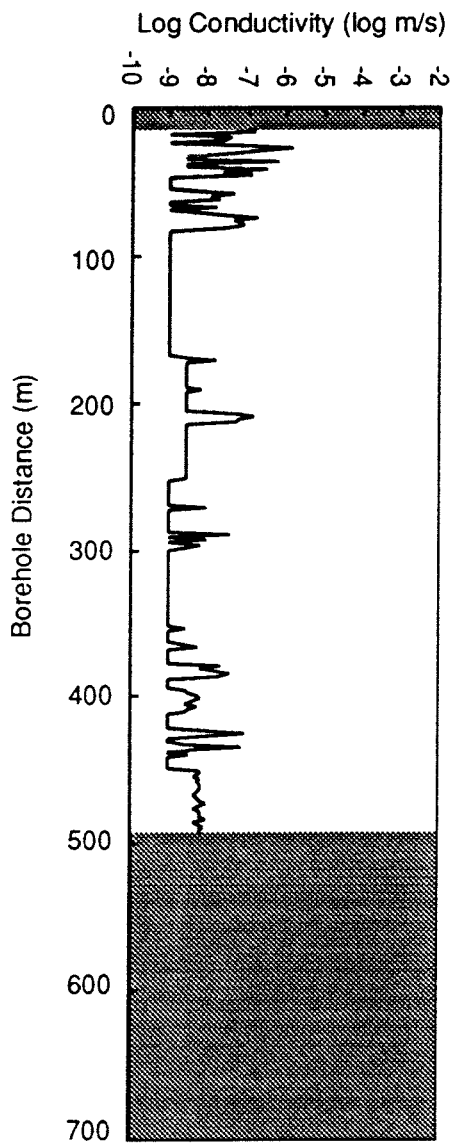
for the northern block, where:

$$Z = \text{depth [m]}$$

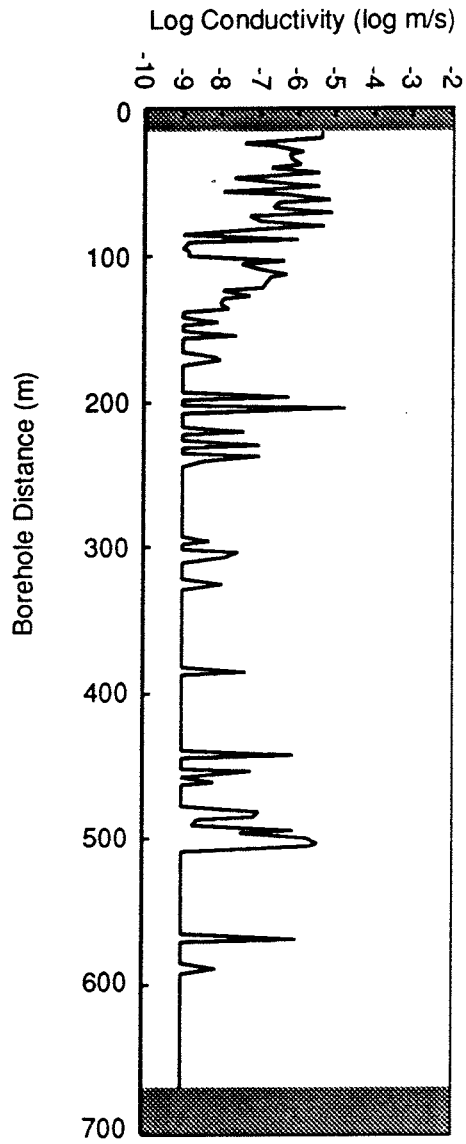
The validity of this model is questionable for numerous reasons:

- The transmissivities for many of the packer intervals are below the transmissivity measurement limits ($T_{\text{threshold}}$) for the test equipment. The data therefore represent upper bound estimates. This may affect estimation of a trend.
- KFI 01 and 02 have been excluded due to a higher $T_{\text{threshold}}$. Profiles of these data (Figure 2-11) show little variation for $Z > 100$ m.
- The model does not consider possible lateral heterogeneity, which may be as strong as any trend in the vertical direction. Figure 2-12 shows K_{Moyes} profiles from boreholes KFI03 and KFI06, which exhibit trends quite different from the above models.
- Near-surface ($Z < 200$ m) data dominate the regression, partly because there are more data at the surface. For $Z > 200$ m, the model predicts a stronger trend than is seen when only data from $Z > 200$ m are considered.

Andersson *et al.* (1991) analyzed the data from $Z > 200$ m separately. The estimated 95% confidence intervals were $\{-1.00 \leq b \leq 0.31\}$ for the southern block, and $\{-1.03 \leq b \leq 0.17\}$ for the northern block. Thus the evidence of a trend at depth is poor.



a) KFI 01



b) KFI 02


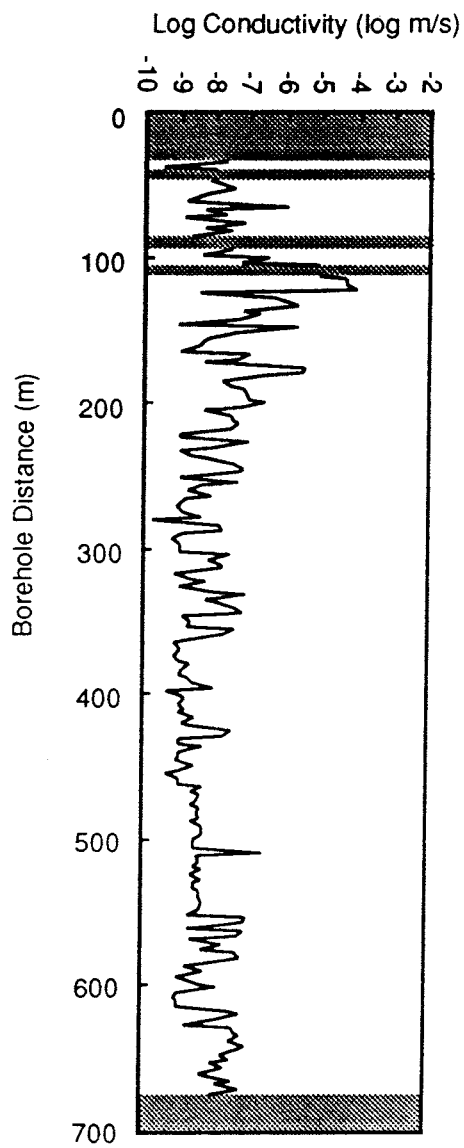
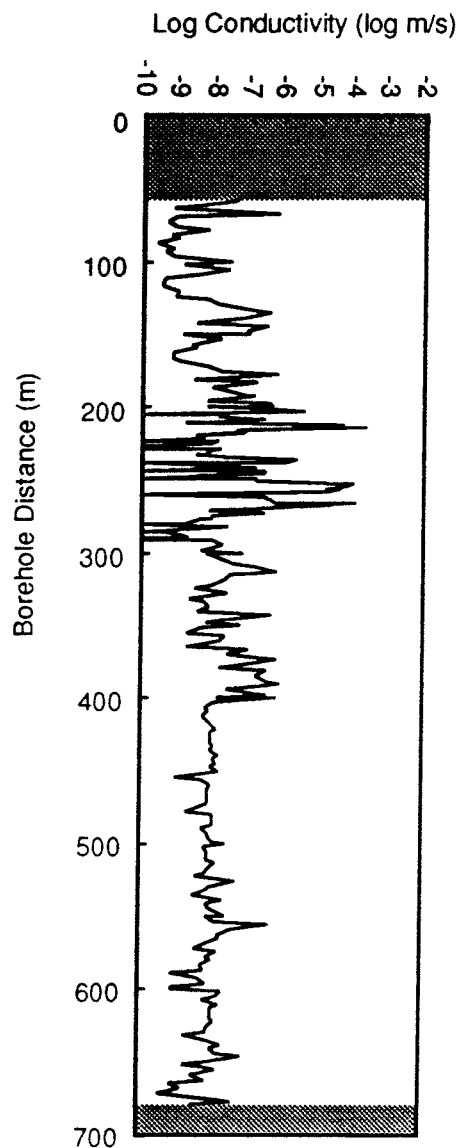
 No data for interval

FIGURE **2-11**
HYDRAULIC CONDUCTIVITY PROFILES
BOREHOLES KFI 01 & 02
 SKB-91/DFNST



a) KFI 03



b) KFI 06

 No data for interval

FIGURE **2-12**
HYDRAULIC CONDUCTIVITY PROFILES
BOREHOLES KFI 03 & 06
 SKB-91/DFNST

Because of the above limitations, the regression models (Eq. 2-11 and 2-12) for K_{Moyes} were not used directly in developing the DFN model. However, physical mechanisms which could produce similar effects were considered (§4.2). Interval transmissivity estimates calculated from the K_{Moyes} data were used in estimating the distribution of T_f for the fracture population (§5.6.3) but the behavior of the resulting model was compared with GRF analyses of transient test data to ensure that the model reproduces the distribution of D_f seen at the site (§6.3).

2.2.4.2 Cross-hole flow and tracer test data

Andersson *et al.* (1989a) conducted cross-hole flow and tracer tests at the Finnsjön site. Tests included hydraulic interference tests with multiple observation intervals, and pulse injection tracer tests. All injection and most monitoring intervals were located within Zone 2. Additional indications of the crosshole response outside of Zone 2 are given by monitoring in HFI 01 of tracer from the drilling fluid for borehole KFI 11.

The test results within Zone 2 indicate strong local heterogeneity. In some cases, better connections were seen between boreholes for sections in the same horizon of the zone, than sections which were in the same borehole but in different horizons (Andersson *et al.*, 1991). This suggests that Zone 2 consists of distinct, laterally extensive subzones. This is consistent with the structural interpretation of Tirén (1990). The tests also indicated anisotropy within the plane of the zone. The conductivity in the strike direction appears to be higher than in the dip direction. Andersson *et al.* speculate that this may be due to a second, intersecting zone.

Hydraulic conductivities estimated from interference tests in Zone 2 over several hundred meters were typically 3 to 30 times higher than the K_p estimates from single-hole tests in the same sections. For BFI 02 the estimates from interference tests were 750 times higher than the single-hole K_p .

The tracer test results were analyzed in terms of an equivalent, single fracture (Andersson *et al.*, 1991), to estimate transport parameters. The estimated zone conductivities K_z from tracer residence times was roughly 0.1 to 1 m/s, several orders of magnitude higher than the estimated K_z in Table 2-3. Comparison in terms of transmissivity (Andersson *et al.*, 1991) showed much better agreement. This indicates that the hydraulically most-active part of the zone is only a small fraction of the tested thickness. The tracer data showed multiple arrival peaks, indicating numerous flow paths.

The cross-hole tests and tracer tests provide data suitable for validation and/or calibration of a DFN model. This has been done in modelling for the Stripa SCV experiment (Dershowitz *et al.*, 1991ab). Although such simulations could be carried out using FracMan, this possibility was beyond the scope of the study. Therefore the main value of these data for DFN modelling is as "soft" data for development of a conceptual model.

2.3 Hydrogeologic Models for Fractured, Crystalline Rock

The rock at Finnsjön is mainly granitic. Unfractured blocks of crystalline rock such as granite typically have very low hydraulic conductivities. However, large volumes typically contain numerous fractures. Such fractures can be expected to form the main pathways for fluid flow through the rock mass at Finnsjön.

The transmissivity of fractures in granitic rock can vary over many orders of magnitude. Interconnection of the fractures is often irregular. For these reasons, the hydrologic properties of this rock may be, on a local scale, extremely heterogeneous. Therefore it is questionable whether homogeneous continuum concepts are suitable for evaluation small-scale hydrologic tests, or for extrapolation from these tests to predict large-scale behavior.

Investigations in granitic rock adjacent to the Stripa mine in Sweden have demonstrated two further complications in this view of fractured rock:

- Fractures are not uniformly distributed through the rock mass, but rather they are concentrated in zones (Olsson *et al.*, 1989).
- Fracture roughness and variability in mineralization may cause flow heterogeneity even within single fractures (Abelin *et al.*, 1985).

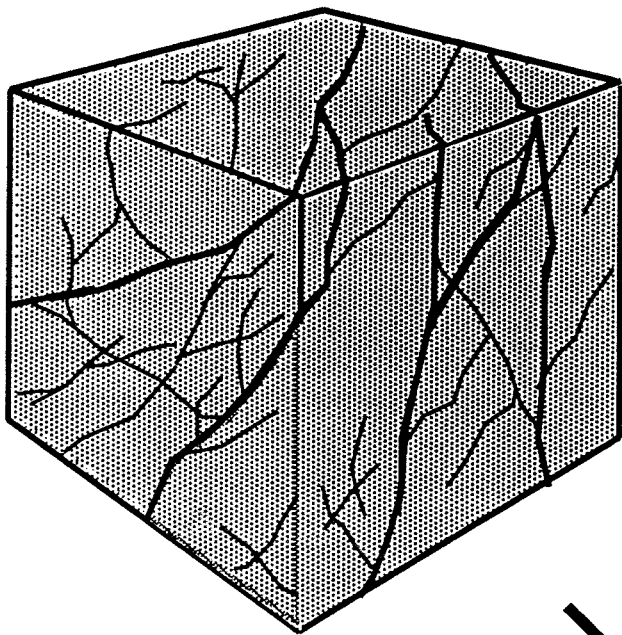
In recent years, techniques for characterizing fracture zones have seen considerable development. However, even a state-of-the-art investigation cannot guarantee detection of all fracture zones in the vicinity of a repository, although there is in general an increasing probability of detection for larger, closer and/or more hydraulically conductive features (Dershowitz and Roberds, 1990). Channeling in fracture networks may cause even greater difficulties, since one-dimensional conductive structures are more likely to escape detection than planar conductive structures.

This section describes briefly four types of models which have been used to simulate groundwater flow and transport in fractured crystalline rock:

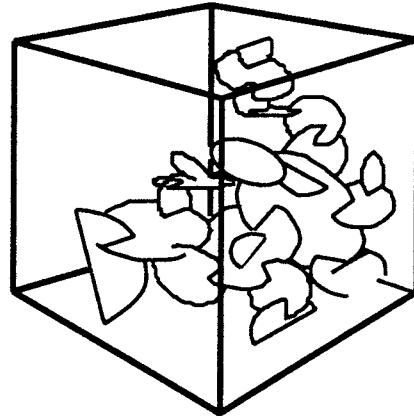
- Discrete fracture network (DFN) models
- Stochastic continuum (SC) models
- Channel network (CN) models
- Dual-porosity streamtube (DPST) models

These models represent four different idealizations of the processes of water flow and chemical transport through fractured rock. The DFN, SC, and CN models, as depicted in Figure 2-13, attempt to represent the irregularity of fluid pathways through the fractured rock. The last type of model, DPST (Figure 2-14), is used to calculate essentially one-dimensional transport within a "streamtube," defined by the streamlines of a potential field. The streamtube boundaries and appropriate, average hydrogeologic properties within the streamtubes must be estimated by one of the more detailed models.

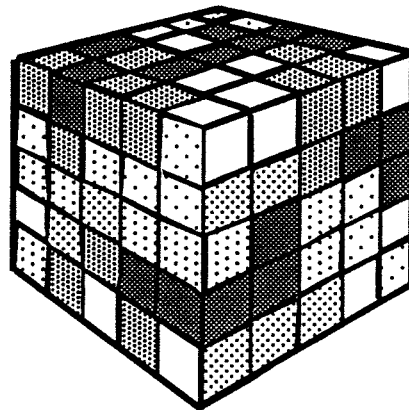
Each type of model has particular advantages and disadvantages for modelling fractured rock masses. Within the SKB 91 project, the different types of models have been applied in complementary fashion. The DFN model, in particular, has been used to provide possible input



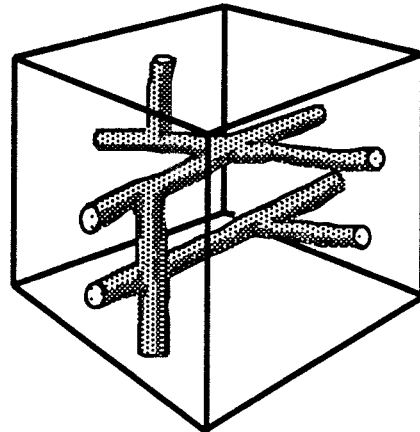
ROCK MASS



DISCRETE FRACTURE NETWORK MODELS



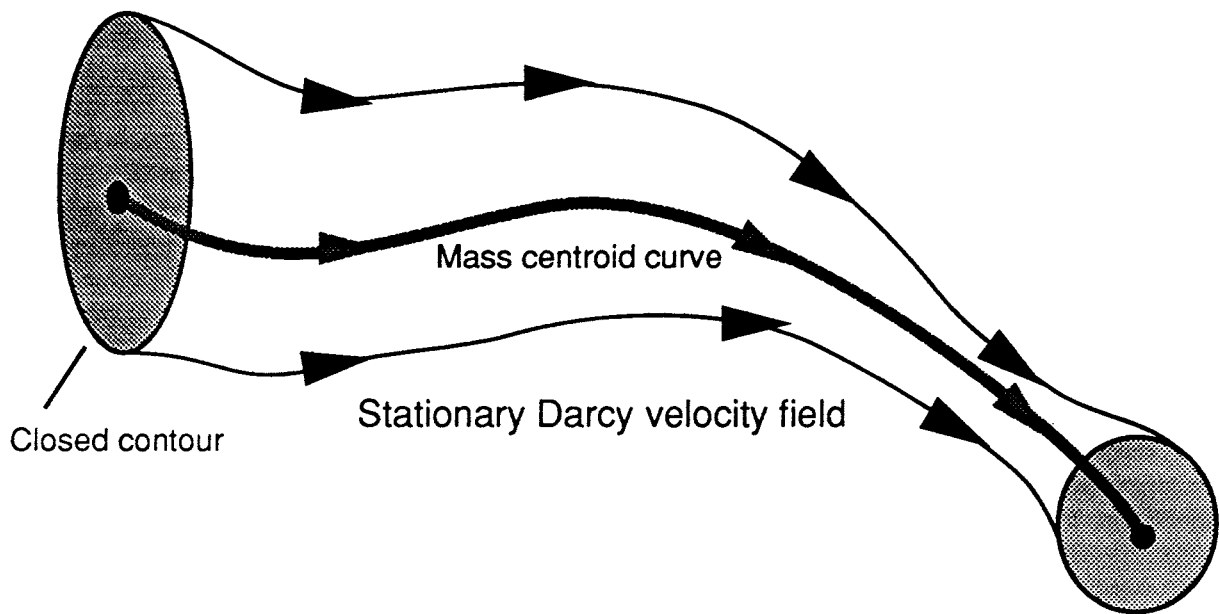
STOCHASTIC CONTINUUM MODELS



CHANNEL NETWORK MODELS

FIGURE 2-13
COMPARISON OF DFN, SC AND CN
MODELLING APPROACHES

SKB/SKB91 DFNST



(from Norman and Kjellbert, 1991)

FIGURE **2-14**
DUAL POROSITY STREAMTUBE MODEL
 SKB-91/DFNST

data for the SC, CN, and DPST models, and as an alternative model for comparison. §2.3.1-4 describe these models. The descriptions of the models are not intended to be comprehensive. For the SC, CN, and DPST models, emphasis is placed on their relation to the DFN model.

2.3.1 Discrete-Fracture-Network (DFN) Model

A discrete fracture network model is built up from a statistical description of fracture geometric and hydraulic properties. Statistics that describe distributions of the following fracture properties are required:

- Location and spatial structure
- Size (*i.e.*, radius or extent)
- Orientation
- Transmissivity (or hydraulic aperture)
- Intensity (expressed as P_{32} total fracture area per unit volume of rock)

Fracture populations are simulated based on these statistics. The primary flow paths are assumed to result from networks of interconnecting fractures.

Simultaneous flow through fractures and the rock matrix may also be modelled in MAFIC using a fully discretized 3-D model (Miller, 1990). However, the problem of simultaneously discretizing both fractures and matrix in 3-D is formidable, and thus far practical modelling of fracture-matrix flow has been limited either to 2-D models (*e.g.* Karasaki *et al.*, 1985), or to 3-D models (Doe *et al.*, 1990) in which fluid storage in the matrix is coupled with flow in the fracture flow, but the matrix does not provide connection between non-intersecting fractures.

Strictly speaking, valid DFN models are restricted to the simulation of regions composed of domains within which the fracture population is *statistically homogeneous*. Most theoretical developments and applications to date have defined statistical homogeneity in very strict terms of spatially uniform distributions of fracture properties, either univariate (*e.g.* size) or bivariate (*e.g.* orientation). When this narrow definition of statistical homogeneity is applied, field studies suggest that fracture populations are often not "statistically homogeneous" over any practical modelling scale. For example, in a recent study of a 36 m section of tunnel in the Stripa mine (Kutilake *et al.*, 1990), the largest "statistically homogeneous" region found was 10 m long. Since access to the rock is limited, and not every 10 m block in a site can be mapped, clearly site-scale DFN modelling is impossible if this very limited definition of statistical homogeneity is applied.

Practical DFN modelling requires a broader definition of statistical homogeneity, based on a statistical description of heterogeneity in the fracture population. The simplest possibility is non-uniform expectations for fracture intensity. The FracMan model (Dershowitz *et al.*, 1991a) includes four conceptual models with non-uniform spatial intensity--Levy-Lee fractal, Nearest-Neighbor, Baecher Revised Termination (BART), and probabilistic War Zone models. More general models allow heterogeneity of all fracture properties. A 2-D example of this is the Parent-Daughter model (Long and Billaux, 1986), which uses a geostatistical description of fracture population heterogeneity. Modelling of multi-domain regions, in which each region is characterized by a distinct set of statistics, is possible using the deterministic War Zone Model (Dershowitz *et al.*, 1991a).

The major advantages of DFN models are:

- Explicit representation of the geometry and physical properties of fractures and fracture zones.
- Ability to incorporate fracture geometry data in the model, and thus give a basis for extrapolating from packer tests of uncertain flow geometry.
- Possibility to model fracture zones of various scales, including undetected zones, and other heterogeneity, based on observations of structural patterns.

For the Finnsjön site the last point is particularly important, because minor zones are too numerous for full detailed characterization, and cannot be represented explicitly in the site-scale, continuum models. A non-uniform model such as the Nearest-Neighbor model (Dershowitz *et al.*, 1991a) allows stochastic generation of zones based on the statistical properties of observed zones, and subsequent generation of the fracture population with higher concentration around the defined zones.

Problems with the DFN approach include:

- Need for fracture geometric data at sampling locations distributed throughout the region to be modelled, including data from at depth. When sampling locations are not well-distributed, extrapolation is required.
- Need to simplify fracture patterns and/or restrict the range of fracture transmissivity T_f modelled, to simulate large-scale regions.
- Need for further theoretical and code development to produce more realistic fracture patterns and incorporate more structural information.

The possible roles of the DFN approach in repository safety assessment include:

- **Preprocessor:** Synthesis of geometric data and hydrological data to estimate appropriate parameters for the other models.
- **Alternative conceptual model:** Testing assumptions used within the other modelling approaches.
- **DFN safety assessment model:** Modelling of flow and transport at canister, repository, and site-scales, with increasingly simplified representation of the fracture population at the larger scales.
- **Coupled DFN/SC model:** Direct coupling of a DFN model in the near-field to a SC model in the far-field, possibly with discrete, "fast paths" in the matrix.

The last two approaches are feasible with existing DFN flow equation solvers, but have not been tested. In the SKB 91 Project, the DFN model has been used for the first and second purposes only.

2.3.2 Stochastic-Continuum (SC) Models

A major goal of the present study was to develop a method for deriving a SC model from a DFN interpretation of site data. The SC approach for modelling groundwater flow in heterogeneous formations is based on the idea that a formation can be described in terms of physical parameters (conductivity, specific storage, *etc.*) that vary in space according to spatially random functions. Among other uses, SC models have been used as the basis for channeling models of single fractures (*e.g.* Abelin *et al.*, 1990).

The advantages of SC models include:

- Extensive theory and statistical procedures for analysis.
- Procedures for derivation which are solely based on packer test data.
- Ability to model site-scale regions.
- Possibility of conditional simulations.
- Tendency to produce more structure than a purely random K field.

Disadvantages of the SC method, for fractured crystalline rock, are mainly related to:

- The simplistic structure of the conductivity fields produced by these models.
- Uncertain relation of model parameters to packer test data.
- Inability to model discrete, heterogeneous connections.

These issues are discussed below. Questions about suitability of SC models for modelling transport (Dverstorp and Andersson, 1990) are not considered here because, within the SKB 91 study, a SC model is used only for Monte Carlo prediction of the groundwater flow field (head gradients, velocities, and streamlines) for input to a DPST model, which is used for the actual transport predictions.

The present study is concerned with SC descriptions of the conductivity tensor K . Usually it is assumed that, on some suitable averaging scale s , an *effective hydraulic conductivity* tensor K_s exists which forms a continuous, random tensor field, *i.e.*:

$$K_s = K_s(x) \quad (2-13)$$

where:

x = a coordinate vector of appropriate dimension.

Assuming existence, the field $K_s(x)$ is described in terms of statistics for the expected value, variance, covariance function, and possible trends in the conductivity field. A site-specific model is constructed by dividing the region into blocks, and producing multiple realizations of the conductivity field. In each simulation, each block is assigned a random value of K_s from a population based on the estimated statistics.

Usually the statistics are estimated for some transformation of the conductivity field:

$$Y(x) = f[K_s(x), x] \quad (2-14)$$

The transformation is chosen so that $Y(x)$ satisfies conditions such as stationarity and Gaussian behavior, which may be required for analysis and simulation. In generating realizations of the random conductivity field, first the field $Y(x)$ is generated, and then the inverse transformation f^{-1} is applied to give the simulated field $K_s(x)$.

In the simplest case, K_s is assumed to be locally isotropic at each point, and the method is concerned only with a scalar field:

$$Y(x) = f[K_s(x), x] \quad (2-15)$$

This assumption is usually adopted, and is assumed in the following discussion for the sake of simplicity. §4.5 describes treatment of the fully anisotropic case.

Assuming that the transformation is chosen so that $E[Y(x)] = 0$, and that the $Y(x)$ is second-order stationary (see, e.g., Mantuoglu and Wilson, 1982), the covariance function is:

$$C_Y(h) = E[Y(x)Y(x+h)] \quad (2-16)$$

where:

h = the lag vector (vector between two points in the field).

$C_Y(h)$ is a statistical way of describing the spatial structure of a field. Many types of structured conductivity fields can show similar $C_Y(h)$, particularly when data are limited. A simulation based on a particular function $C_Y(h)$ will not necessarily tend to contain structures similar to those in the real conductivity field. However, the estimate of $C_Y(h)$ is a stricter constraint on a model than just a mean and a variance. Therefore simulations based on an estimated $C_Y(h)$ should, in a mathematically defined way, resemble the real conductivity field (assuming one exists) more closely than an uncorrelated field.

If a suitably simple (though not necessarily geologically realistic) form is assumed for $C(h)$, the parameters can be estimated uniquely from field data. A common assumption is *isotropic covariance*, meaning that $C(h)$ depends only on $|h|$. Somewhat more realistic models may be developed based on linear combinations of several fields with strongly anisotropic covariance, but unique estimation of the parameters from packer test data is difficult or impossible. Prior to estimating the statistics of $K_s(x)$ from packer test conductivities $K_p(x)$, usually the $K_p(x)$ are *regularized* by taking a moving average (see Matheron, 1971), often a harmonic mean. Regularization methods which have been developed for harmonically-averaging quantities may not be appropriate for conductivity data (Winberg *et al.*, 1990).

Various methods are available for simulation (see Mantuoglu and Wilson, 1982). Within the SKB 91 study, several different SC simulation methods have been considered, including "parametric" (Norman, 1991; Winberg *et al.*, 1990) and "nonparametric" (Winberg *et al.*, 1990) approaches. The nonparametric approach differs from the above description in that covariance functions are estimated for each of several threshold values of conductivity.

In the present study, a DFN methodology was developed which can be used to provide a basis for simulations using the HYDRASTAR code (Norman, 1991). HYDRASTAR produces conditional simulations of the 3-D $K_s(x)$, *i.e.* the simulated $K_s(x)$ are constrained to match the regularized measurements.

The advantages of the SC method make it computationally feasible for modelling the Finnsjön site. However, the simulations must contend with some general difficulties for modelling fractured crystalline rock, including:

- There is great uncertainty as to what the "hard" data (*i.e.*, the K_p values) are measurements of, due to uncertain flow geometry. It is very unlikely that these values can be interpreted as direct measurements of SC properties.
- The basic assumption of porous media behavior with an equivalent K , may not apply on a scale suitable for modelling, and possibly not at any scale (Long and Witherspoon, 1985) in certain fracture populations.
- The use of fairly simple forms for $C_Y(h)$ (to allow derivation of model parameters) results in models with limited ability to reproduce extensive, thin, high-conductivity structures similar to fractures, channels, or thin fracture zones.^{3]}
- Theoretical scaling-up procedures may not be valid for media controlled by extensive, thin structures (Durlofsky, 1991).
- Regularization methods are virtually all based on assumptions about the magnitude of variance in K , or the form of correlation of K (Durlofsky, 1991), or an assumption that the rock acts as a continuum at the packer test scale.

A specific problem for the Finnsjön site is that:

- If the minor zones have higher average K than the rock mass, this may produce a heterogeneous, anisotropic $C_Y(h)$ on a scale comparable to the minor zones. Whether this could be described by anisotropic K on a larger scale is not clear.

A main purpose of the DFN model was to answer the questions:

- Can the rock at Finnsjön be described as an equivalent porous medium on some practical scale?

³ Planar structures may be produced by conditioning, if the borehole spacing is less than the correlation length, or by strongly anisotropic covariance functions. The former is not usually the case over a site. The latter works only if all of the structures are roughly parallel, unless linear combinations are used, but estimation of parameters is a problem, as mentioned above. More complex stochastic continua with "nested" covariance structures have been proposed (Neumann, 1990) but apparently have not been implemented in numerical models capable of site-scale simulations.

- Are the methods for deriving a SC model from packer test K_p valid for fractured rock similar to that at Finnsjön? If not, can alternative scaling laws be developed based on a DFN model?
- Are the forms of $C_v(h)$ assumed in derivation of SC models reasonable for fractured rock similar to that at Finnsjön?
- Does the DFN model predict a single function $C_v(h)$ throughout a geologically-defined region of the model?

Methods for investigating these issues are discussed in §4.5.

2.3.3 Channel-Network (CN) Models

As part of the present study, DFN analysis methods and simulations were used to estimate parameters of a channel-network (CN) model. The basic concept of a CN model is that flow within a fracture network is confined to discrete, effectively one-dimensional pathways known as *channels*, which intersect at various interval. Examples of CN models include transport models derived from DFN models for use in transport simulations (Cacas *et al.*, 1990b; Dverstorp and Andersson, 1990). The channel properties may also be derived directly from field data.

The CN model of Moreno and Neretnieks (1991), which is used as an alternative conceptual model in the SKB 91 study, is based on channel statistics properties estimated directly from observations in boreholes and tunnels. The equivalent-conductor-grid model used in the Stripa Project by Long *et al.* (1991) derives a channel network by inversion of hydrologic and geophysical measurements, by forward modelling combined with a simulated-annealing, optimization algorithm.

CN models are similar to DFN models in their recognition of the discrete nature of the fracture pathways. However, they have a number of advantages including:

- Use of a network composed of effectively 1-D elements can reduce the computational difficulty, and thus simplifies modelling of complex processes such as transport of sorbing species (Moreno and Neretnieks, 1991) and flow of non-Newtonian fluids such as grouts (Hässler, 1991).
- Possibility to consider channels as distinct features with autocorrelation of properties over multiple fractures, due to processes such as non-uniform erosion, clogging, precipitation and/or dissolution within fracture planes (Moreno and Neretnieks, 1991).⁴

Relative to SC models, CN models have an advantage that network dispersion effects can be modelled without resort to scale-dependent dispersion coefficients.

⁴ Recent developments in the FracMan/MAFIC package allow auto-correlation of aperture over multiple fracture planes.

For the direct approach used by Moreno and Neretnieks (1991), the data requirements for the CN model are somewhat less than for a DFN model, because the specifics of fracture geometry are ignored. This model uses a network of channels which is topologically equivalent to a regular, cubic lattice. Properties including:

- Channel "conductance" (here meaning the ratio of flowrate to pressure difference between the two ends of a channel)
- Channel volume
- Wetted surface area

are assumed, in effect, to be uniformly distributed along each channel, and randomly distributed or constant for the channel population. Methods for estimating these properties are described by Moreno and Neretnieks. Demonstration simulations (*op cit.*) indicate that calibration of a CN model to field data is straightforward, and observed behavior such as long tails and plateaus in breakthrough curves are reproduced.

A few problems with the method are that:

- Field data that provide the observational basis for the model are limited to a few experiments in relatively low-transmissivity, single fractures (see §3.1.1), and observations in tunnels which may reflect strongly disturbed flow fields.
- Estimation of channel frequencies and length distributions requires simplistic assumptions about channel geometry (width and tortuosity), the validity of which is difficult to appraise, due to limited field data.
- For moderately well-connected rock such as the Finnsjön site, the distance between channel intersections may be so small that packer tests measure the properties of multiple channels (in series and/or in parallel), which means that deconvolution of the data is necessary to obtain the required properties.
- When a large fraction of the packer tests display radial to spherical flow, problems of non-uniqueness can be expected in the derivation of CN model parameters. In such cases the *need for* and even the *validity of* a CN model may be questioned (although a dense channel network could very plausibly reproduce this type of behavior).^[5] An important question in such cases is whether the more conductive packer test intervals tend to display low flow dimension.

⁵ The same comment can be applied to DFN models, for the case when packer test flow dimensions are predominantly near-spherical.

A problem which is common to all modelling approaches for strongly heterogeneous rock, but which is most plainly evident in the CN model of Moreno and Neretnieks (1991), due to the simplicity of the conceptual model, is that:

- **The spatial intensity of occurrence of the most transmissive features (channels, fractures, or zones) may not be adequately characterized, due precisely to the infrequency of their occurrence and the low probability of their intersecting a borehole.**

Because of the overwhelming significance of the most transmissive features, the possibility of large errors in their estimated spatial intensity cannot be overlooked.

The present study included, as a subtask, an estimation of the significance (with regard to this particular CN model) of the fact that only a finite number of packer test transmissivity measurements T_p are available. The results, as given in Appendix 1, show that the *probable* error in characterization of the the most transmissive conduits is significant, for the Finnsjön T_p dataset. Appendix 1 also gives an evaluation of a simplifying assumption used in the CN model derivation, that a maximum of one channel intersects any given packer interval. The analysis indicates that this assumption does not introduce significant errors for the CN model of Moreno and Neretnieks (1991).

2.3.4 Dual-Porosity Streamtube (DPST) Models

A major goal of the present study was to use the DFN approach to estimate parameters for the dual-porosity streamtube model (DPST) developed by Norman and Kjellbert (1990). The estimates were used as alternatives to tracer test interpretations, which are subject to great uncertainty as discussed below.

The streamtube concept is a method for transforming the problem of 3-D solute migration in inhomogeneous flow fields into a set of realizations of a 1-D transport model.

The basic idea is to partition to flow field predicted by a given groundwater model into flow paths contained within **stream tubes**. A stream tube is defined (Norman and Kjellbert, 1990) as the surface composed of all streamlines passing through a closed contour⁶ (Figure 2-14). The **mass centroid curve** for a stream tube is defined by the set of mass centroids for every cross section through the stream tube (where "cross section" is taken to mean the intersection of an equipotential surface with the volume contained by the streamtube). Transport is defined solely in terms of distance along the mass centroid curve, resulting in a 1-D equation describing transport within the streamtube. Distributed values of properties such as porosity are replaced by appropriate averages over each cross section.

The SKB 91 study uses a dual-porosity formulation of the stream tube concept, FARF31 (Norman and Kjellbert, 1990) to predict travel times and concentrations for radionuclides migrating to the biosphere. FARF31 incorporates longitudinal dispersion, matrix diffusion,

⁶ The contour is most sensibly chosen to lie within an equipotential surface defined by the flow model.

decay, and possible sorption for each radionuclide species modelled. Matrix diffusion is implemented as 1-D diffusion between the "flow" porosity and the "matrix" porosity (Norman and Kjellbert). It is understood that the distinction between "flow" and "matrix" porosity involves a somewhat arbitrary division between "fissures" and "microfissures" in the fractured granite.

The advantages of the DPST approach arise from the enormous simplification in the effective geometry of the transport equations, which allows more detailed mathematical models for the transport aspects, and facilitates Monte Carlo modelling which requires a large number of simulations.

Some fundamental problems with the approach follow directly from the simplifying assumptions:

- Individual stream tubes are modelled independently of each other. Together with the fact that transverse dispersion is neglected, this means that there is no chance for radionuclides to move between stream tubes. On a small scale the importance of this may be negligible, but as observed by Dverstorp and Andersson (1990) in fractured granite the apparent lateral dispersion tends to increase with distance due to network effects.
- Pore velocity and porosity are replaced by averages over each cross section, based on the assumption that the stream tube is sufficiently narrow for velocity and porosity variations to be negligible. This assumption may not hold if multiple channels or discrete-fracture flow paths pass through a typical stream-tube cross section. Observations of multiple plateaus in arrival curves for tracer experiments in fractured granite (see Neretnieks, 1990) would imply that this will commonly be the case for transport on the scale of tens to hundreds of meters.^[7]

The significance of these weaknesses is not well understood. This is a basic motivation for the use of alternative conceptual models such as the CN and DFN models. Additional problems relate to the difficulty of obtaining suitable "average" parameters for the model:

- Flow porosity can be estimated from tracer experiments, but is subject to uncertainty due to the unknown geometry of the active flowpaths in these experiments. Furthermore, the number of such experiments is limited, particularly in the rock mass, for Finnsjön.
- Flow wetted surface is even more difficult to estimate from tracer experiments, since this is available only by (1) analysis of experiments using sorbing tracers, or (2) model fitting for matrix diffusion effects (*e.g.* Abelin *et al.*, 1987).

⁷ Presumably arrival curves for a single sampling point must reflect flow through a single stream tube, by definition -- unless they reflect the effects of transverse dispersion across stream-tube boundaries.

Within the SKB 91 project, use of the DFN model to support the DPST modelling was limited to estimation of porosity and specific wetted surface directly from fracture geometric models and flow simulations, for comparison with estimates from tracer tests. A second possibility, back-analysis of the tracer tests at Finnsjön by calibration of the DFN model, was not within the scope of the present study. The software and methods needed for the back-analysis approach have been demonstrated for the Stripa site by Dershowitz *et al.* (1991b), but the approach would have required large-scale modelling and deterministic inclusion of major features. Due to the limited time frame of the project, the simpler approach was followed, mainly because it gave the possibility to simultaneously produce data for the SC model.

3 HYDROLOGIC PROPERTIES OF SINGLE FRACTURES

The scope of this project exceeds the scope of most previous applications of DFN models in two respects:

- [1] The domain of the model extends from surface rock to a depth of several hundred meters. Packer test data (§2.4.1) show indications of a decrease in K_p with depth, in the upper part of the domain, but no change is seen in the fracture frequency with depth. Therefore some other explanation (such as stress) is needed to explain the changes in fracture hydrologic properties with depth.
- [2] The goal of estimating effective porosity and wetted surface for transport prediction means that the detailed-scale properties of the fractures are more important than for a prediction of bulk flux.

To fulfill the scope, adequate models are needed for the detailed hydrologic behavior of single fractures within a fracture network. Properties of importance include the following:

- **Aperture variability or channelling:** Variations in fracture aperture can affect the geometry of flow paths, with profound effects on transport properties.
- **Hydromechanical effects:** Fracture deformation due to *in situ* stresses can affect the hydrologic properties of the fractures.
- **Coatings and infilling:** Mineral coatings or infilling within a fracture may strongly affect its mechanical, hydrologic and transport properties, and their interrelationships.

Findings of a review of these subjects are described in §3.1 - 3.3.

3.1 Aperture variation

Most 3-D DFN modelling performed to date has assumed uniform aperture (or transmissivity) throughout the fracture plane (*e.g.* Long *et al.*, 1982, Herbert and Splawski, 1990, Geier *et al.*, 1990, Dershowitz *et al.*, 1991b). However, it is widely recognized that flow is non-uniformly distributed within individual fractures (Neretnieks, 1990). This is clear from observations of inflow to tunnels (*e.g.* Palmqvist and Lindström, 1991).

The use of a uniform transmissivity (rather than uniform aperture) throughout the fracture plane (*e.g.* Dershowitz *et al.*, 1991b) may be sufficient for flow (and some transport) predictions where only the effective, cross-fracture transmissivity is important. However, theoretical calculations and experimental observations (Gelhar, 1987; Neretnieks, 1990) indicate that the inhomogeneous distribution of flow within a single fracture may be significant for radionuclide transport, in some cases.

Despite the widespread recognition of nonuniform flow within fracture planes, there are few data from controlled experiments, on which non-uniform flow models can be based.

Experiments to address the question of channeling within single fractures have been performed (§3.1.1), but the possibilities of correlations *between* fracture planes, or distinct channels at the intersections between fractures, have been investigated in only a few instances (Abelin *et al.* 1985, 1990).^[8]

Since one goal of this project is to estimate transport parameters (flow porosity and wetted surface) from the DFN model, a reasonable model is needed for the variation of ϵ_m . For this purpose, the experimental evidence for various models of ϵ_m was reviewed. Observations, theoretical models, and simulation studies of the behavior of different models are discussed in §3.1.1-4.

3.1.1 Single-fracture flow experiments

Experimental evidence of inhomogeneous flow within a single fracture includes both laboratory studies and *in situ* experiments. Early laboratory studies using natural fractures (Sharp, 1970; Iwai, 1976) were concerned mainly with the effective transmissivity of fractures with variable ϵ_m , and did not explicitly consider the distribution of flow within the fracture.

More recent experiments have focused on the distribution of flow and transport within the fractures. Neretnieks *et al.* (1982) performed tracer tests in a natural fracture from the Stripa mine. The area of fracture tested was roughly 0.06 m². The breakthrough curves for two non-sorbing tracers showed plateaus, which were interpreted as the superposed effect of two distinct transport paths with different flow velocities.

Hakami (1989) produced clear plastic replicas of five fractures, and mapped the flow velocity distribution by injecting colored dye to indicate the streamlines. The areas of the fractures tested ranged from 0.008 to 0.03 m². The channeling character differed among samples. The fraction of fracture area through which 75% of the flow passed ranged from roughly 30 to 70% of the total fracture surface area. Estimated velocities varied within a single sample by up to a factor of 20.

Piggott and Elsworth (1990) measured pore volume, pneumatic, hydraulic, and electrical conductivity, and tracer transport characteristics of a 0.06 m² natural fracture in granite, first in a mated configuration, and then after shifting one surface of the fracture slightly to produce a dilation of 1 mm. A grid of probes measured variations in the induced fields, and showed that these were more uniform for the fracture after "shearing." This suggests that a small shear displacement and dilation may produce a reduction in aperture variance. However, the variation within the fracture tested was very small, and effective apertures from all measurement techniques were within a factor of 4 of ϵ_p .

⁸ The observations of inflows to a tunnel (Palmqvist and Lindström, 1991) contain semiquantitative information about flow through fracture intersections, but have not been analyzed in this respect. Interpretations of these observations may not be straightforward because of uncertain stress and boundary effects, and the somewhat qualitative way of measuring flowrates.

The applicability of the laboratory results is limited by two considerations:

- The scale is extremely small relative to the fractures of $A > 1 \text{ m}^2$ which are considered in DFN models.
- The fractures have been disturbed, and the ϵ_m distribution may be quite different from *in situ*, due to stress relief, possible mismatch of the fracture surfaces, and disruption of infilling in weakly sealed parts of the fractures.

In situ experiments give data on a larger scale, with less disturbance of the fractures.

Novakowski *et al.* (1985) analyzed injection-withdrawal flow and tracer tests in a single fracture in monzonitic gneiss at the Chalk River site in Canada. Interpreted ϵ_s was $60 \mu\text{m}$, compared with a ϵ_T estimate of $510 \mu\text{m}$. This difference seems to indicate the presence of "stagnant pools" of water adjacent to the flow paths.

Raven *et al.* (1986) analyzed four injection-withdrawal tests and one radially converging test in a single fracture at the same site. A "transient solute storage model" was used to analyze the results. For the tests with a distance of 12.7 m from injection to withdrawal point, good fits were obtained by assuming there was no "stagnant" water. For tests over a longer distance of 29.8 m and much longer residence times, good fits were obtained by assuming that 35 to 65% of the water volume was stagnant.

Shapiro (1988) conducted radially convergent NaCl tracer tests in an areally extensive, horizontal fracture in dolomite. The scale of the tests was about 20m. Transmissivity and storativity for the fracture tested by Shapiro (1988) were estimated as $1.9 \times 10^{-2} \text{ m}^2/\text{s}$ and 2.7×10^{-5} to 9.7×10^{-5} , respectively (Nicholas, 1988). The product $\epsilon_s \phi$ and longitudinal dispersivity α were estimated by fitting to the first and second moments of the mass arrival curves. Estimated values of $\epsilon_s \phi$ were 8.5 mm, 8.7 mm, and 10.1 mm in three tests. Effective longitudinal dispersivity estimates were 2.0 m, 2.7 m, and 11.0 m. Different values of longitudinal dispersivity were measured in different directions, although hydraulic tests showed no anisotropy in the horizontal plane. Simulations of the tracer test using these parameters and a finite-difference approximation gave mass arrival curves that had much a less steep initial rise in the mass arrival curves.

Abelin *et al.* (1985) describe tracer migration experiments over distances of 5 to 10 m in a single fracture in the Stripa mine. Based on pressure pulse testing in one intersecting borehole, H2, they estimate $T_b = 2.8\text{-}6.5 \times 10^{-10} \text{ m}^2/\text{s}$ and $S = 3.6\text{-}7.5 \times 10^{-8}$ for the fracture. Testing in four other boreholes that intersected the fracture gave $T_b \leq 4 \times 10^{-11}$. Thus the range in T_b was at least an order of magnitude. Hydraulic diffusivities estimated from small-scale crosshole tests ranged from 1.3×10^{-4} to $6.1 \times 10^{-2} \text{ m}^2/\text{s}$ (Abelin *et al.* suggest that these may be underestimated due to possibly high wellbore storage effects). More than 90% of the water flowing into the drift from the fracture came in through 5 of 27 measurement sections. The four highest-flow sections were localized in one side of the drift cross-section. However, high head gradients in the rock around the drift, due to nearby mine openings, complicate interpretation of the observed irregularity in the inflow distribution.

A recent set of experiments by Abelin *et al.* (1990) to investigate channeling in a single fracture provides the most detailed information to date regarding distribution of flow and ϵ_m in a single

fracture *in situ*. In these experiments, pairs of boreholes were drilled along single fracture "planes." Detailed observations of ϵ_m and fracture infilling thickness variation were made (see §3.1.3). Multiple crosshole flow and tracer tests were performed, using "multipede" packers to isolate 5 cm sections of the fractures. The crosshole flow tests showed an uneven distribution of responses along the length of the monitoring holes (Figure 3-1). Tracer tests between holes indicate an increase in the unevenness for transport (Figure 3-2). Some tracer disappears into the fracture or possibly into other, intersecting fractures. Abelin *et al.* concluded that there were dead-end channels in the fracture planes studied.

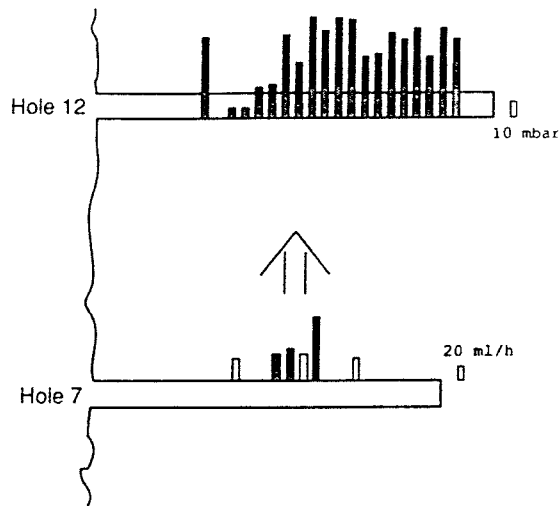
Other experiments in granitic rock at Cornwall, England (Heath, 1984; Bourke, 1987) showed highly variable cross-hole connections for boreholes intersecting single fractures at different points. In the single-fracture experiment described by Bourke, the flow was interpreted as being restricted to a few channels occupying approximately 10% of the fracture area.

Taken together, the results of the *in situ* experiments indicate that:

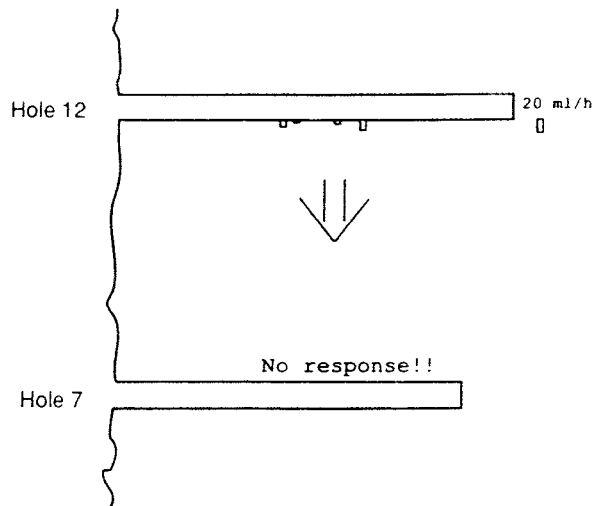
- The transmissivity (or ϵ_m) is not uniform at the mm to dm scale within fracture planes.
- The flow distribution in single fractures is not uniform.
- The main pathways for flow occupy a small fraction (less than 20 percent) of the fracture plane.
- There are stagnant volumes of water even in fracture planes subjected to high gradients.
- Hydraulic connections between different parts of a fracture are irregular.

Beyond these basic observations, a variety of interpretations are possible due to effects of intersecting fractures. The local ϵ_m within the fractures is known only at a few points or along a few profiles. Possibly many different models for how ϵ_m varies in unobserved locations could match the observed flow and transport responses.

However, these experiments, particularly the Stripa Channeling experiment, provide datasets that can be used at least to decide which models for ϵ_m variation are invalid and should be rejected. For an indication of which models *might* be valid, the direct measurements of fracture surface roughness and ϵ_m for granitic rock types must be considered.



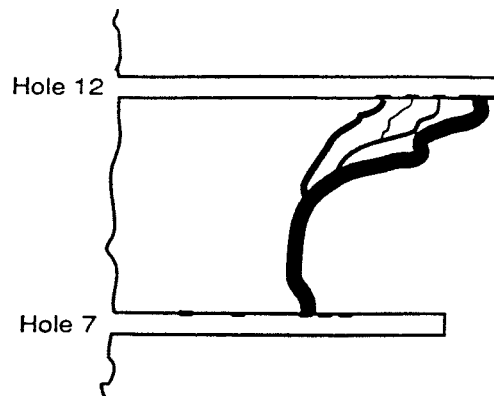
a) Compiled results from all injection tests in Hole 7; monitoring in Hole 12.



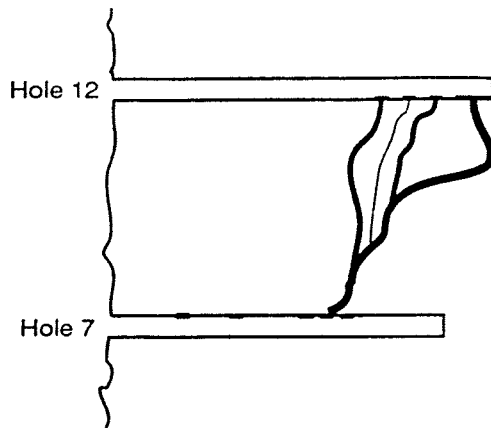
b) Compiled results from all injection tests in Hole 12; monitoring in Hole 7.

(Abelin et al., 1990)

FIGURE **3-1**
CROSSHOLE FLOW REPOSE
IN A SINGLE FRACTURE
STRIPA CHANNELING EXPERIMENT
 SKB-91/DFNST



a) Injection of Uranin tracer in Hole 7; collection in Hole 12.



b) Injection of Duasyn tracer in Hole 7; collection in Hole 12.

(Abelin et al., 1990)

FIGURE **3-2**
CROSSHOLE TRACER REPOSE
IN A SINGLE FRACTURE
STRIPA CHANNELING EXPERIMENT
 SKB-91/DFNST

3.1.2 Aperture estimates from surface profiles

Most data on the variation of ϵ_m within a single fracture are based on fracture surface height profiles.

Bandis *et al.* (1981) measured fracture surface profiles in various sedimentary rocks. Tsang and Witherspoon (1983) used a profile from Bandis *et al.* to generate synthetic ϵ_m profiles, by shifting a mirror image of the profile laterally along the original profile. For a very small displacement, the distribution of ϵ_m was roughly normal, but for increasing displacements it became multimodal.

Gentier (1986) constructed ϵ_m profiles for a natural joint in granite, by combining surface profiles from opposite sides of the fracture. Figure 3-3 shows distributions of ϵ_m obtained from measurements along profiles in two orthogonal directions.

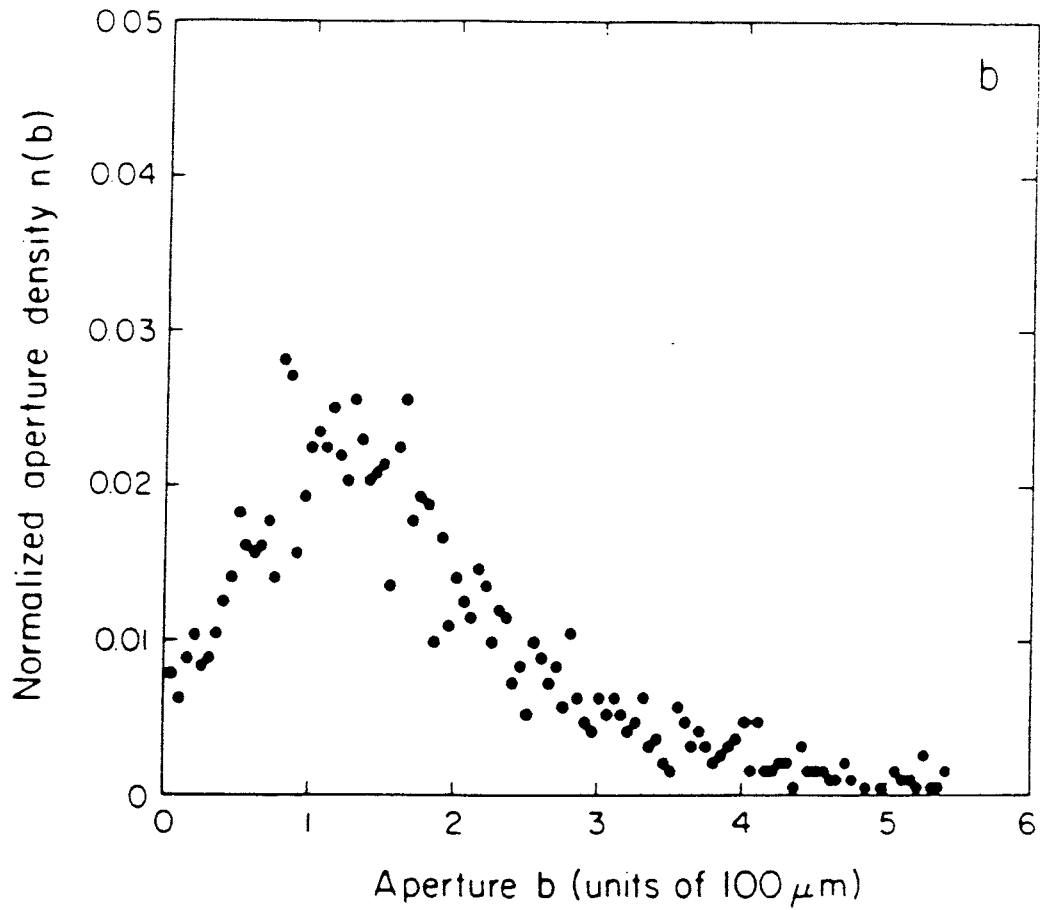
Brown and Scholz (1985) measured fracture roughness along multiple, perpendicular directions on single fracture surfaces in sedimentary and crystalline rock (columnar cooling joints in diabase). Measurement scales ranged from 1 μm to 1 m. Brown and Scholz characterized fractures in terms of power spectral densities, as a function of roughness wavelength, and related this to a fractal dimension for surface height variation, which appeared to vary with scale. For the larger-scale wavelengths, they estimated an apparent fractal dimension $D_p = 1.18\text{--}1.26$. Brown (1987) used these measurements to simulate ϵ_m variation between uncorrelated fractal surfaces with a specified mean ϵ_m (see §3.1.4).

Brown *et al.* (1986) investigated correlation between fracture surfaces by taking surface profiles from opposite faces of joints in granodiorite, and combining the profiles to estimate ϵ_m after the method of Gentier (1986). The joints were well-mated (with correlation lengths for ϵ_m from 0.5 to 5 mm) and were coated with chlorite and epidote.

Estimates of ϵ_m derived from surface profiles, by any of the above methods, are questionable. Studies of fractures with shear displacements are lacking, although other research (§3.2.2) indicates small shear displacements may increase fracture transmissivity by dilation. The composite-profile measurements have been limited to very well-mated joints. Furthermore, because uncertainties about the precise relative position of the opposing profiles are resolved by optimizing the match, the degree of mating may be overestimated (Brown, 1987). Simulation of shear displacement, by shifting surfaces, is unsatisfactory because processes such as normal stress, shearing of asperities and precipitation of infilling cannot be taken into account. These questions can only be examined by direct measurements of ϵ_m .

3.1.3 Direct measurements of fracture aperture

The simplest direct method for measuring ϵ_m variation is to take a profile along a cross-section of a fracture. Gale (1987) injected epoxy resin into fractures in Stripa granite, under normal stress. After the resin hardened, the rock was sectioned and the resin thickness was measured. The distribution of ϵ_m was approximately lognormal, or left-skewed, in contrast to the right-skewed distributions (Figure 3-3) obtained by Gentier (1986), based on surface profiles. The mean ϵ_m was 4 to 5 times ϵ_n measured under normal load.



(after Gentier, 1986)

FIGURE **3-3**
**DISTRIBUTIONS OF MECHANICAL
 APERTURE BASED ON JOINT
 SURFACE PROFILES**
 SKB-91/DFNST

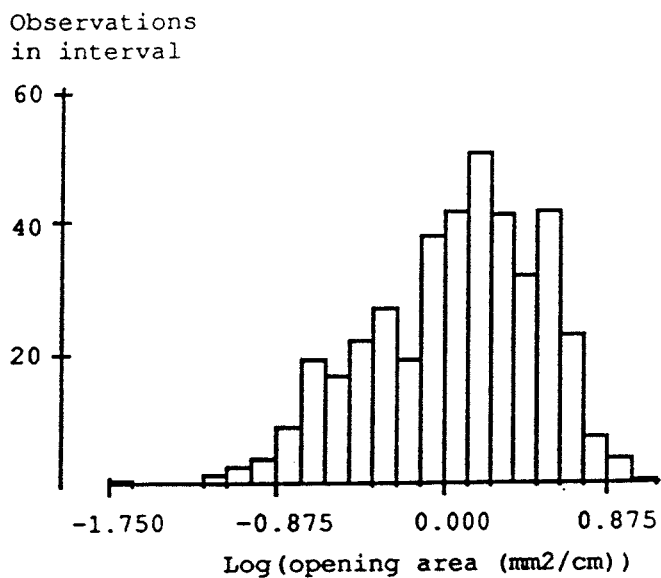
In situ profiles of ϵ_m in Stripa granite were produced by Abelin *et al.* (1990), by photography in boreholes drilled along fracture planes. The cross-sectional areas of infilling and void space were measured on photographs for 5 cm sections of the fractures. The average ϵ_m for each section was calculated as the void area divided by the length. Example histograms and variograms for ϵ_m are shown in Figure 3-4.

A few researchers have measured two-dimensional variations in ϵ_m by producing casts of fractures. Pyrak-Nolte *et al.* (1985) produced Wood's metal casts of fractures in Stripa granite (52 mm diameter) under stress. Pyrak-Nolte *et al.* (1988) analyzed these to determine the pattern of contact areas and voids. The measurements were binary (contact or void) but by use of a fractal, stratified-continuum percolation model, a distribution of ϵ_m was produced. Gentier *et al.* (1989) produced casts of fractures (12.5 cm diameter) under normal stress using a silicone polymer resin which absorbs light in (nonlinear) proportion to its thickness. Gray-scale images produced by illuminating the resin cast from below give a two-dimensional characterization of ϵ_m . Hakami (1989), in the study described in §3.1.1, produced maps of ϵ_m by placing measured drops of fluid at evenly spaced points, between clear plastic replicas of fracture surfaces. The distribution of ϵ_m in each of the fractures was approximately lognormal. The distributions became increasingly left-skewed with increasing normal load.

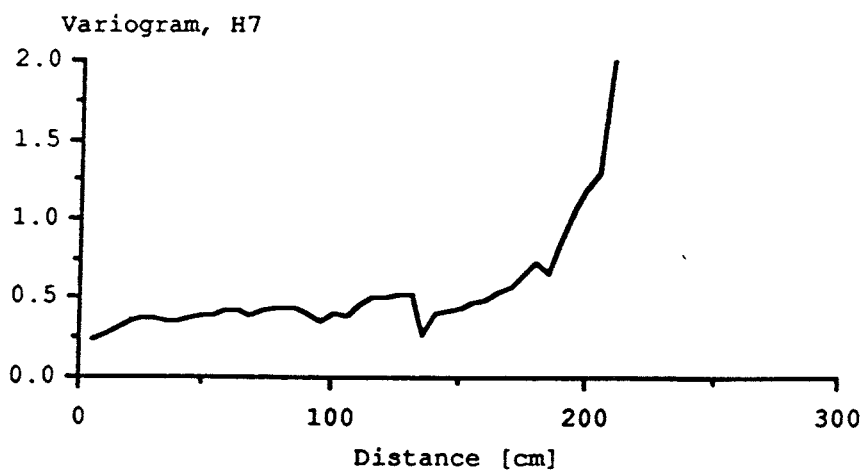
Of the work cited, only the *in situ* profiles of Abelin *et al.* (1990) give direct measurements on a scale comparable to fractures in DFN models. As a group, the direct measurements of ϵ_m give results similar to data from surface profiles. However, the direct measurements show strong effects of normal stress on ϵ_m . This implies surface profile data cannot be applied without making a theoretical compensation for rough fracture deformation. Current research is directed toward such a theory (§3.2), but so far a comprehensive, validated theory is lacking. Therefore the data of Abelin *et al.* (1990) are the most useful data for this study.

3.1.4 Models for fracture aperture

Early models for variation of ϵ_m within a single fracture were based on spatially uncorrelated, random distributions of ϵ_m . Neuzil and Tracy (1981) proposed a lognormal distribution for ϵ_m . Tsang (1984) modelled the data of Gentier (1986) as a normal distribution, truncated at zero. Tsang also suggested a right-skewed distributional form based on ϵ_m distributions derived from load-displacement data for granites and basalts, according to the theory of Tsang and Witherspoon (1981). These models tend not to produce high-conductivity channels, due to the absence of spatial correlation.



a) Distribution of log opening areas, Hole 7.



b) Variograms calculated on the mean of the visual apertures over 5 cm intervals, Hole 7.

(Abelin et al., 1990)

FIGURE 3-4
IN -SITU APERTURE MEASUREMENTS
STRIPA CHANNELING EXPERIMENT
 SKB-91/DFNST

Recent models that tend to produce channel-like structures include 2-D SC (geostatistical) models (Tsang and Tsang, 1987; Moreno *et al.*, 1988; Stratford *et al.*, 1990) and two types of fractal models: a stratified continuum percolation model (Pyrak-Nolte *et al.*, 1988), and composite topography models (Brown, 1987; Wang *et al.*, 1988). Wang *et al.* noted a correspondence between their model and a geostatistical model with isotropic covariance.

All of these models provide methods for extrapolating from ϵ_m profiles to ϵ_m variation within the fracture plane. None of the models accounts for possible correlations between fracture planes, or distinct channels at the intersections between fractures.^{9]}

Stratford *et al.* (1990) applied the model of Moreno *et al.* (1988) to fractures in a network, with no correlation between channeling in intersecting fractures. They observed that, in this model, channeling is a local effect, and persistence of dominant pathways over several fracture planes depends mainly on the T_f of the interconnecting fractures. The validity of this aspect of the model cannot be tested with the currently available data.

Simulation of variable ϵ_m fractures, based on the various models, have been presented by the authors cited above. With suitable parameter values, all of the models reproduce the qualitative characteristics of single fractures, as deduced from the field experiments cited in §3.1.1. Abelin *et al.* (1990) compared their experimental results directly to the model of Moreno *et al.* (1988), showing reasonably good quantitative agreement.

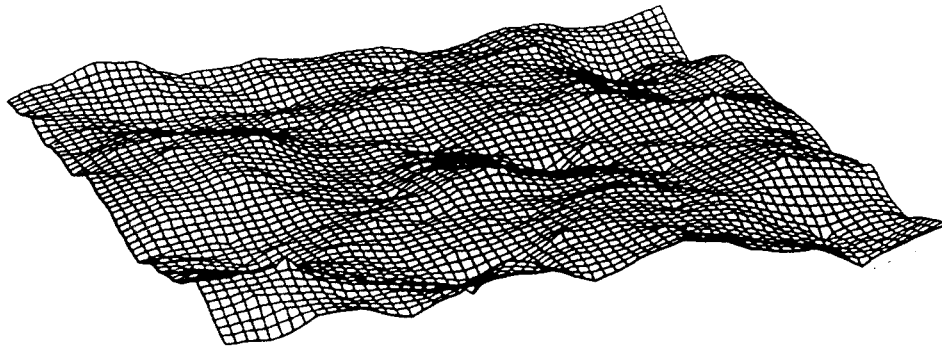
The present study considered primarily the composite topography models of Brown (1987) and of Wang *et al.* (1988), which are particularly simple to implement, by the fractal interpolation algorithm of Fournier *et al.* (1982).

Brown (1987) superposed two uncorrelated surfaces with the same fractal dimension D_s . This can be calculated from the fractal dimension of a surface profile as (Brown, 1987):

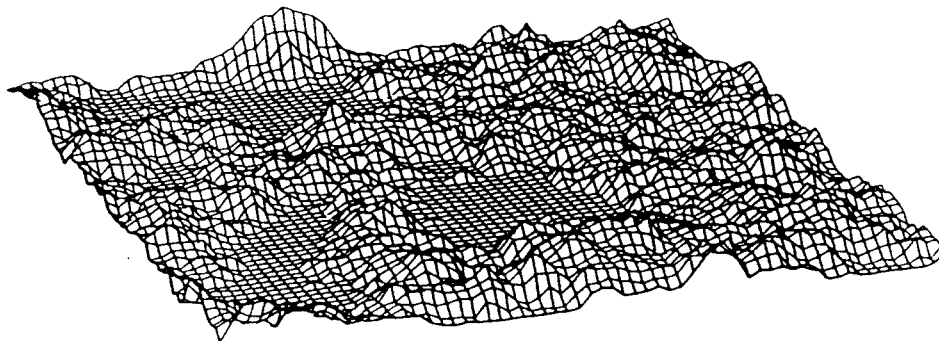
$$D_s = D_p + 1 \quad (3-1)$$

The surfaces were placed a fixed distance $\bar{\epsilon}_m$ apart. For small $\bar{\epsilon}_m$ the surfaces may overlap. In these cases, Brown ignored deformation mechanisms and assumed $\epsilon_m = 0$ in the regions of overlap. Figure 3-5 shows aperture maps for two fractures simulated by this method. Hakami (1989) compared direct flow measurements with results from Brown's model, and reported good qualitative agreement in terms of tortuosity and velocity variation.

⁹ Tsang and Tsang (1987) discussed the possibilities of spatial correlation between planes but their mathematical formulation did not account for this.



a) Topography of a fracture surface.



b) Aperture distribution produced by combining two uncorrelated fractal surfaces.

(from Brown, 1987)

FIGURE **3-5**
**EXAMPLE OF APERTURE DISTRIBUTION
PRODUCED BY BROWN'S FRACTAL MODEL**
SKB-91/DFNST

Brown's model has several weaknesses, mainly the assumption of uncorrelated surfaces, and the simplistic removal of overlapping regions. Also, derivation of model parameters directly from ϵ_m measurements is preferable to the use of surface height profiles (§3.1.2).

An improved version of the model (Wang *et al.*, 1988) consists of two initially mated surfaces, both of fractal dimension D_s . One of the surfaces is shifted by a vector displacement within the plane of the fracture. Wang *et al.* derived an expression for the isotropic variogram of ϵ_m :

$$\gamma_f(x, y) = \frac{1}{2} \left\langle \left[\epsilon_m(x_o+x, y_o+y) - \epsilon_m(x_o, y_o) \right]^2 \right\rangle_{x_o, y_o} \quad (3-2)$$

for a relative shear displacement (x_c, y_c) . The expression for the variogram is:

$$\gamma_f(r) = \sigma_{\epsilon_m}^2 \left[1 + \frac{r^{6-2D_s}}{r_c^{6-2D_s}} - \frac{r_{>}^{6-2D_s}}{r_c^{6-2D_s}} F\left(D_s-3, D_s-3, 1; \frac{r_{<}^2}{r_{>}^2}\right) \right] \quad (3-3)$$

where

$F[\alpha, \beta, \gamma; \zeta]$ = the hypergeometric function (see §13)

$$r = \sqrt{x^2 + y^2} = \text{the magnitude of separation} \quad [L]$$

$$r_c = \sqrt{x_c^2 + y_c^2} = \text{the magnitude of shear displacement} \quad [L]$$

$$r_{<} = \begin{cases} r, & r < r_c \\ r_c, & r > r_c \end{cases}$$

$$r_{>} = \begin{cases} r_c, & r < r_c \\ r, & r > r_c \end{cases}$$

This model accounts for possible correlation of the fracture surfaces. Since the parameters are obtained directly from ϵ_m profiles, the simplifying assumptions about contact regions are less of a problem. Wang and Narasimhan (1988) suggested a type-curve matching approach to estimate the parameters r_c and D_s from log-log variograms of ϵ_m . This method was applied in the present project (§5.5).

It should be noted that, although the models of Brown (1987) and of Wang *et al.* (1988) both assume that the fracture surfaces themselves are fractal, the resulting aperture structures are not necessarily fractal.

3.2 Hydromechanical effects

The term "hydromechanical effects," for a single fracture, refers to the interrelationships of rock stress, fluid pressure, and flow within the fracture. Effects include:

- Reduced transmissivity due to closure under normal stress.
- Changes in transmissivity due to shear stress and displacements.
- Changes in fluid storage due to changes in pressure and state of stress.

These effects are discussed in §3.2.1 - 3.2.3.

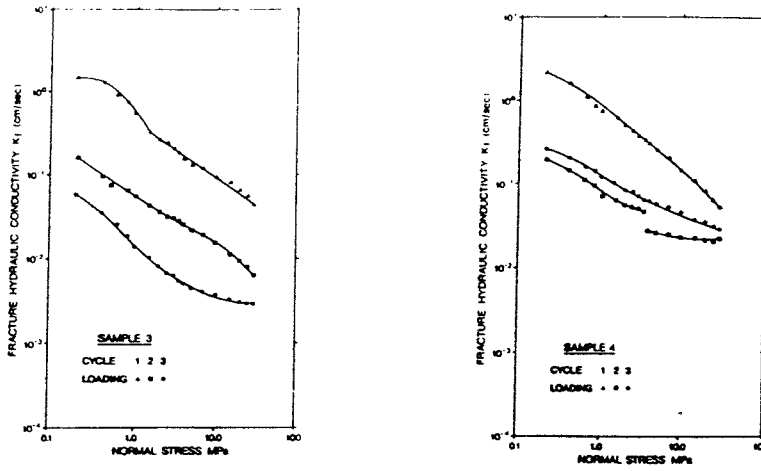
3.2.1 Normal stress and transmissivity

The effects of normal stress σ_n on cross-fracture transmissivity T_f have been studied over a range of measurement scales, from laboratory studies on a 0.15 m scale (Iwai, 1976) to *in situ* experiments on scales above 1 m (Carlsson and Olsson, 1986; Makurat *et al.*, 1990b). From these it is clear that increasing σ_n causes fracture closure and hence decreasing T_f .

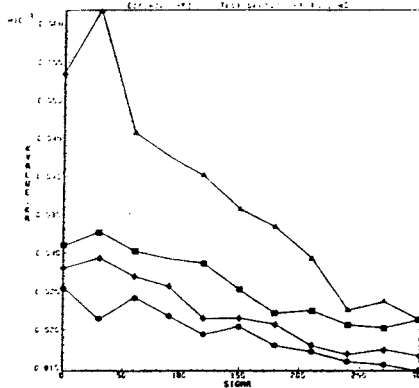
However, there are difficulties in interpreting both laboratory and field experiments, due to uncertainty as to the "correct" initial conditions for the tests. Figure 3-6a shows data from tests on core by Gale and Raven (1980). Figures 3-6b and 3-6c show results of *in situ* tests by Carlsson and Olsson (1986) and by Makurat *et al.* (1990b), respectively. In these experiments, the normal load is increased and decreased in several cycles.

All of the tests show hysteresis, particularly for the initial loading cycle. The later cycles usually show less hysteresis. An interpretation of this behavior is that the initial condition of the joint is disturbed, producing a slight shift from "mated" conditions.^{10]} The initial loading cycles are presumed to correct for this mismatch by non-elastic deformation around the contacting asperities. The later cycles are therefore considered to be more similar to undisturbed *in situ* conditions.

¹⁰ Fractures in laboratory samples are undoubtedly disturbed, but fractures *in situ* may also be disturbed by slight shear movements due to excavation of the site (Witherspoon *et al.*, 1979).

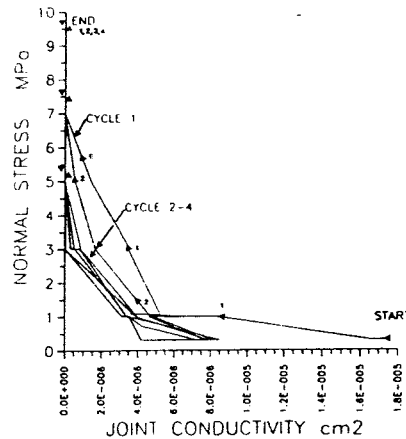


a) Results of tests on core by Gale and Raven, 1980.



Test No.4. Hydraulic conductivity as a function of load for different values of the injection pressure.

b) Results of in-situ tests by Carlsson and Olsson (1986).



c) Results of in-situ tests by Makurat et al. (1990).

FIGURE 3-6
EXPERIMENTAL MEASUREMENTS
OF EFFECTS OF NORMAL STRESS
ON FRACTURE TRANSMISSIVITY

SKB-91/DFNST

A rough pattern is seen of a log-log relation between T_f and σ_n , expressed as:

$$\frac{T_f}{T_{fo}} = \left(\frac{\sigma_n}{\sigma_{no}} \right)^{b_{Tn}} \quad (3-5)$$

where

σ_{no}	= reference level for normal stress	[M/LT ²]
T_{fo}	= fracture transmissivity at $\sigma_n = \sigma_{no}$	[L ² /T]
b_{Tn}	= empirical constant	[-]

Experiments show a range of approximately $-3 \leq b_{Tn} \leq -0.2$ (Carlsson and Olsson, 1986). Figure 3-7 shows data compiled by Dershowitz *et al.* (1991c).

There is a tendency for the magnitude of tangent value of b_{Tn} to decrease with increasing σ_n . Witherspoon *et al.* (1979) suggested that this happens because, for rough fractures, the contact area between opposing fracture surfaces increases with σ_n , increasing the fracture stiffness.

The Barton-Bandis joint model (Bandis *et al.*, 1983 and subsequent papers) gives an empirical description of this behavior. The hydraulic aperture is related to mechanical aperture by:

$$\epsilon_m [\mu\text{m}] = \sqrt{\epsilon_h [\mu\text{m}] \cdot \text{JRC}_o^{2.5}} \quad (3-6)$$

where

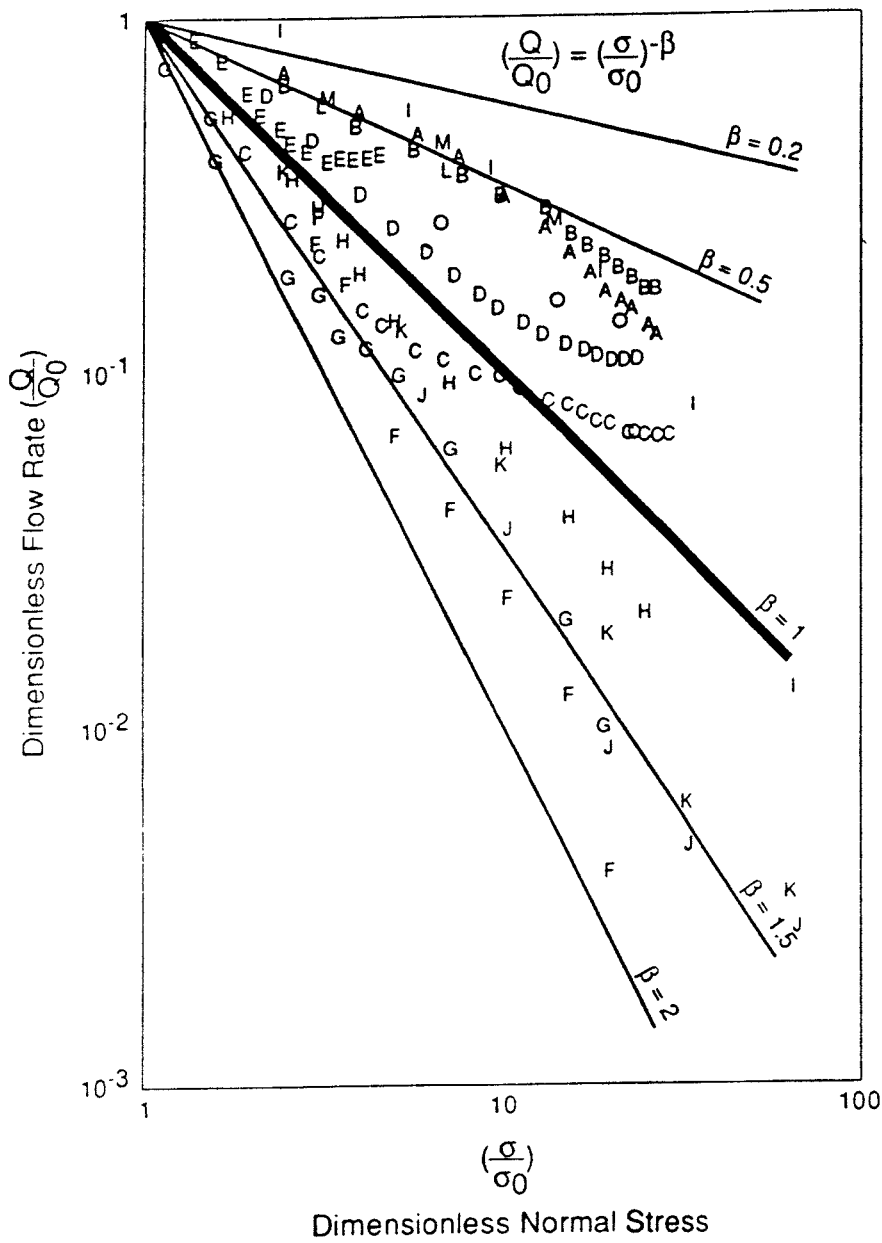
JRC_o	= joint roughness coefficient	[-]
----------------	-------------------------------	-----

As discussed further in §3.4.1, the above relationship is not very satisfactory for describing fractures of transmissivities which are of concern in near-field models. The most widely accepted use of the Barton-Bandis model is for describing joint deformation in purely mechanical models of jointed rock. A hyperbolic model for the change in ϵ_m is expressed in terms of joint normal stiffness κ_n as:

$$\kappa_n = \kappa_{no} \left(1 - \frac{\sigma_n}{\delta_m \kappa_{no} + \sigma_n} \right)^{-2} \quad (3-7)$$

where

κ_{no}	= tangent value of κ_n at start of loading cycle	[M/TL ³]
δ_m	= maximum joint closure, <i>i.e.</i> maximum $\epsilon_{no} - \epsilon_m$	[L]
ϵ_{no}	= initial mechanical aperture	[L]



Raven and Gale (1985)

A Test 1

B Test 2

C Test 3

D Test 5

E Pratt et al. (1977)

Gale et al. (1987)

F Test STR2

G Test STR3

H Test STR7

Pyrak - Nolte et al. (1987)

I Test E35

J Test E30

K Test E32

Sundram et al. (1987)

L 1st loading

M 2nd loading

O 3rd loading

(Dershowitz et al., 1991b)

FIGURE **3-7**
**COMPILATION OF DATA FOR
 EFFECTS OF NORMAL STRESS
 ON FRACTURE TRANSMISSIVITY**

SKB-91/DFNST

Integrating $1/\kappa_n$ along the loading path gives ϵ_m as a function of σ_n :

$$\epsilon_m - \epsilon_{m0} = \delta_m \left[\frac{\sigma_n}{\delta_m \kappa_{m0} + \sigma_n} \right] \quad (3-8)$$

Bandis *et al.* (1983) suggested empirical relations relating κ_{m0} and δ_m to ϵ_{m0} , JRC_o , and JCS_o (the joint compressive strength), with parameters depending on the stress history of the joint. κ_n for mismatched joints can differ from κ_n for interlocked joints by a ratio of 0.4 to 0.15 (Bandis *et al.*, 1983).

Apart from the Barton-Bandis model, there have been many attempts to develop theoretical models of joint normal stiffness, based on fundamental rock properties and statistical models of surface roughness (e.g. Tsang and Witherspoon, 1983; Brown and Scholz, 1986). Difficulties arise from the need to consider deformation of the rock adjacent to the fracture and coupling among asperities, as well as deformation of the asperities (Hopkins *et al.*, 1990). Numerical modelling of this behavior for an isolated crack is possible (Zimmerman *et al.*, 1990) but the approach is computationally intensive for even a single fracture. The problems become more complicated when interacting fractures are considered.

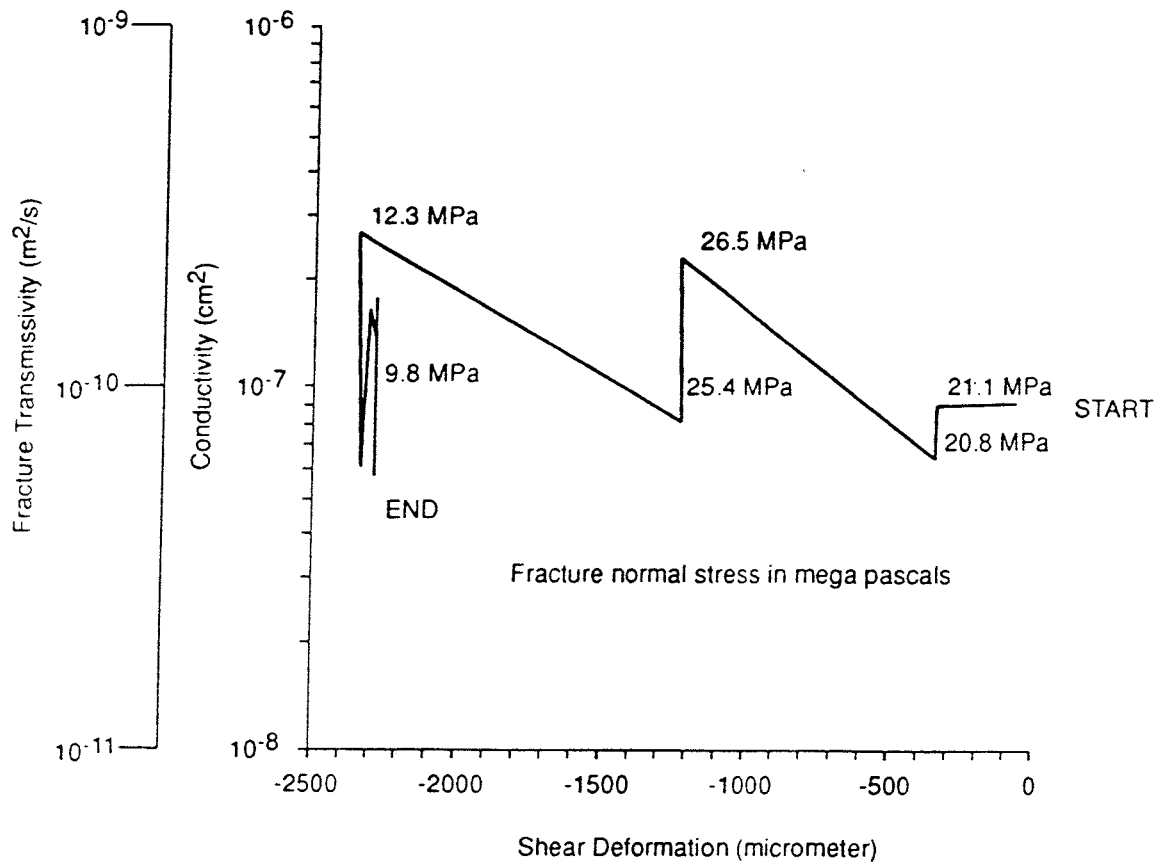
For the present study, a very simple, approximate model is needed for the relationship between σ_n and T_f . The Barton-Bandis model appears to be the most widely accepted of the joint stiffness models. This model, however, requires data concerning distributions of ϵ_{m0} , JCS_o , and JRC_o , "joint matedness," and possibly infilling. JRC_o and JCS_o distributions are available from the Stripa site (Makurat *et al.*, 1990a). These may be reasonable for the Finnsjön site, but there is little information about the other required parameters. Furthermore the relation of the model parameters to fracture hydraulic properties is not clear, as mentioned above and discussed further in the following sections.

A simpler alternative is suggested by the T_f vs. σ_n relationship for individual experiments (Figure 3-7). Dershowitz *et al.* (1991c) modelled stress effects in the Stripa SCV Drift experiment, by treating the log-slope b_{T_n} as a constant ($b_{T_n} = -1.0$) for $\sigma_n \leq 10$ MPa, for all fractures. For higher stresses the fractures were assumed to be infinitely stiff. The predicted effects of drift excavation on inflow were fairly close to observations.

Extension of this approach to the Finnsjön site is described in §5.6. The approach of Dershowitz *et al.*, (1991c) was chosen for the present study because of its simplicity, which means that the necessary parameters can be estimated from field data.

3.2.2 Shear stress and transmissivity

The effect of shear stress on T_f has also been the subject of laboratory experiments, but the results are even more complex than for σ_n . Apparently the change in T_f is controlled by the shear displacement. Figure 3-8 shows results of shear-loading tests on fractures in 200 mm Stripa granite cores by Makurat *et al.* (1990b). For an initially mated fracture, small displacements produce increased T_f due to dilation of the fracture, but more extensive shear



Shear loading effect on joint conductivity in joint sample 1,
0.2m core (aperture = 8×10^{-6} to 18×10^{-6} m)

(Makurat et al., 1990)

FIGURE **3-8**
**EFFECTS OF SHEAR DISPLACEMENT
ON FRACTURE TRANSMISSIVITY**

SKB-91/DFNST

deformation may also reduce T_f due to changes in mating of the fracture surfaces, failure of asperities, and/or gouge formation. Thus, depending on a number of complex processes during shear deformation, T_f may increase or decrease. Results of the Stripa Phase 3 project indicate that, in the highly disturbed zone adjacent to a tunnel, shear deformation may have a greater effect than normal stress on fracture transmissivity. However, due to the complexity of the effects mentioned above, shear stress/deformation effects cannot be modelled realistically until much additional research on these effects has been performed.

3.2.3 Normal stress and storativity

Effects of stress on fracture storativity have received little mention in the literature. Defining the storativity for a fixed area A of a fracture:

$$S = \frac{1}{A} \frac{\partial}{\partial p} (\rho_f g A \epsilon_v) = \frac{\partial \rho_f}{\partial p} g \epsilon_v + \rho_f g \frac{\partial \epsilon_v}{\partial p} \quad (3-9)$$

If infilling is neglected so that $\epsilon_m = \epsilon_v$ and the increase in mechanical aperture with respect to pressure is taken as $1/\kappa_n$, the storativity is (Doe and Osnes, 1985):

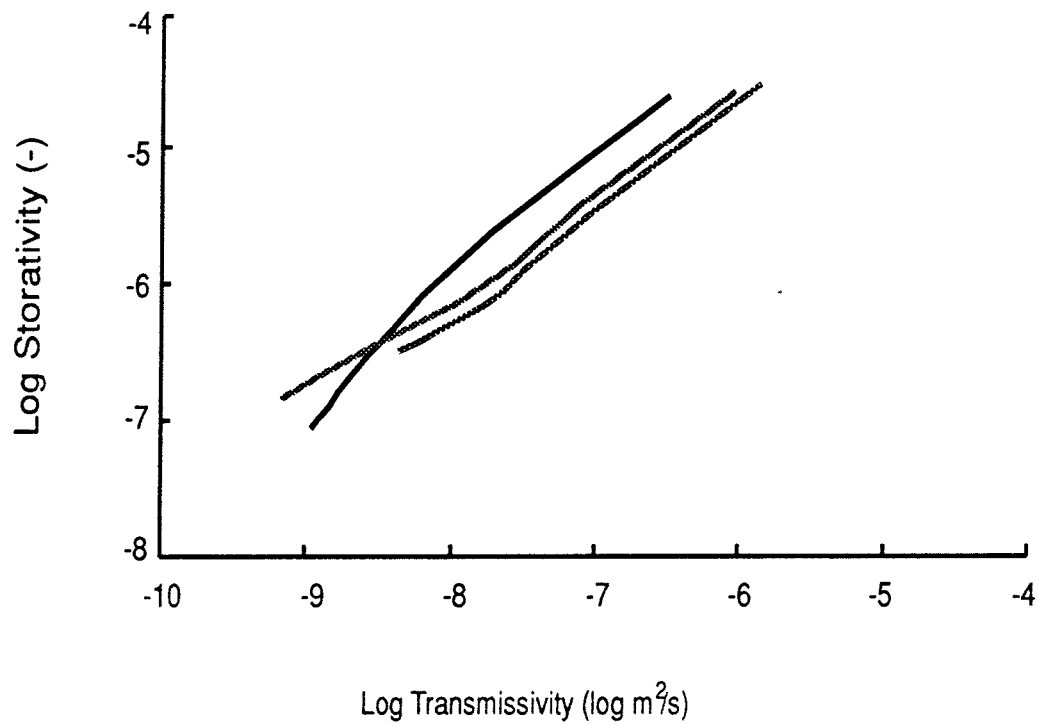
$$S = \rho_f g \left[\epsilon_m C_f + \frac{1}{\kappa_n} \right] \quad (3-10)$$

where:

$$C_f = \text{fluid compressibility} \quad [LT^2/M]$$

This expression (as noted by Doe and Osnes) contains two terms, describing fluid compressibility and fracture deformability, respectively. Substituting Eqs. 3-7 and 3-8 will give S as a function of (effective) σ_n , C_f , and the fracture properties ϵ_{m0} , δ_m and κ_{n0} . The last two properties depend on the stress history of the particular fracture, which makes this approach impractical for DFN modelling. However, by using the expression of Bandis *et al.* relating ϵ_m and ϵ_n (Eq. 3-6) and the Barton-Bandis model for fracture normal deformation, it is possible to plot T_f vs. S for some reasonable fracture properties, to give a rough idea as to what sort of relationship can be expected. Figure 3-9 shows examples based on parameters for three joints tested in the Stripa project, which can be compared with an empirical model derived directly from transient packer test interpretations in §5.7.

When infilling is taken into account, Equation 3-10 must include terms for pore compressibility within the infilling, and effects of infilling stiffness as a component of κ_n . For realistic models of a partially filled or coated fracture with multiple asperities, it may not be physically meaningful to discuss these terms separately. Since transmissive fractures commonly are mineralized, Equation 3-10 and Figure 3-9 should be viewed only as initial steps toward developing an empirical model for S vs. T_f .



- 1 Based on mechanical properties of a 1 m in-situ fracture.
- 2 Based on mechanical properties of a fracture in 200 mm core (1).
- - - - - 3 Based on mechanical properties of a fracture in 200 mm core (2).

Fracture		1	2	3	
Joint stiffness coefficient	JCS	160	125	150	MPa
Joint roughness coefficient	JCR	3.8	1.9	3.8	
Initial aperture	E_o	0.114	0.084	0.127	mm
Joint compressive strength	σ_c	200	200	200	MPa
Initial joint stiffness	κ_{ni}	24	24	40	MPa/mm
Maximum closure	v_{max}	0.103	0.075	0.114	mm

FIGURE **3-9**
STORATIVITY VS. TRANSMISSIVITY
FOR BANDIS-BARTON MODEL

SKB/SKB91 DFNST

(Fracture property data from Makurat et al., 1990)

3.3 Fracture infilling

Most natural fractures in granitic rock have some type of surface coating or infilling, produced by alteration, precipitation, and/or mechanical processes. Apart from their effects on the hydrological and hydromechanical properties of fractures, these coatings or infillings may influence matrix diffusion (Skagius and Neretnieks, 1985) and sorption of radionuclides.

Regarding the goal of predicting radionuclide transport parameters in a discrete fracture network with infillings, three basic issues may be stated:

- What correlations exist between fracture infilling type and transmissivity?
- For a fracture with a given infilling type and transmissivity, what ranges of fracture specific wetted surface s_{wf} and void aperture ϵ_v may be expected?
- For a given infilling type, should s_{wf} be weighted to account for sorption or diffusion characteristics, relative to other infilling types?

§3.3.1 - 3.3.4 give a review of the applicable data on the subject, and suggest methods for considering the effects of infilling in estimating flow porosity and flow wetted surface for transport models.

3.3.1 Types of infilling in Fennoscandian granitic rock

The effects of fracture infilling on transport properties may depend on both the mineralogical composition and the structure of the infilling. Descriptions of infilling mineralogy and appearance are often recorded during core logging and outcrop mapping, but there are few cases where these data have been analyzed systematically.

The most detailed studies of fracture infillings for Swedish granite have been performed for the Gideå (Tullborg and Larson, 1983), Klipperås (Tullborg, 1986; Landström and Tullborg, 1990) and Äspö (Tullborg, 1989) study sites.

Tullborg and Larson listed the following as the most common infilling minerals at Gideå:

- Calcite
- Chlorite
- Pyrite
- Laumontite
- Stilbite (a zeolite mineral)
- Smectite
- Quartz
- Epidote

Essentially the same suite of infillings was seen at the Klipperås site by Olkiewicz and Stejskal (1986). Detailed studies at Klipperås (Tullborg, 1986), and at Äspö (Tullborg, 1989) also noted:

- Hematite and Fe-oxyhydroxide
- Muscovite and clay minerals

- Brecciated infillings with slight calcitic cementation

Tullborg's studies at Klipperås and Äspö indicated some rough correlations between infilling types and fracture geometry (orientation and spacing). Infilling studies from these sites are relevant to the present study, since the core from Finnsjön exhibit the same group of infillings (Ahlbom and Tirén, 1991).

Infilling *structure* within fracture planes (and at intersections between fractures) may be just as important as the mineralogy, since the structure determines the surface area accessible to radionuclides. This has not been the subject of much systematic study. Some of the required information can be obtained from core logs which contain codes indicating:

- *Fresh* fractures
- *Sealed* fractures
- *Coated* fractures

Fractures with no observable infilling or coating are normally classified as fresh, and are considered to have been created during core recovery. The distinction between sealed and coated fractures is somewhat fuzzy. "Coated" fractures may have been sealed *in situ*, but broken during core recovery. A fracture that is "sealed" in one place may be open and "coated" a few centimeters away.

A fourth category is seen in core log comments but is not recorded systematically:

- Fractures containing *fractured*, *crushed* or *brecciated* infilling (often including fragments of the wall rock)

Examination of detailed core logs (§5.8.1) for borehole KFI 11 at Finnsjön shows that the highest-conductivity sections contain fractures with brecciated infilling.

3.3.2 Infilling type and transmissivity

Quantitative studies of fracture infilling and its relation to transmissivity are rare. The studies by Tullborg and Larson (1983) and by Tullborg (1986) were concerned primarily with a geochemical interpretation of the historical and recent groundwater chemistry at the site. Although the latter study discusses infilling occurrence related to fracture zone proximity, and fracture sealing by clay minerals, calcite and chlorite, the information directly applicable to DFN models is limited. For this purpose, the best available information comes from semi-quantitative observations of inflow to tunnels, and multivariate regression analysis of borehole data.

3.3.2.1 Observations in tunnels

Based on observations of inflows in tunnels, Palmqvist (1990) gives observations on the hydrologic significance of these infillings which can be summarized as follows:

- **Calcite** is often released from fractures in conjunction with water leakage. The distribution within a single fracture is often uneven. 12% of laumontite or calcite-filled fractures at the SFR are aquiferous. Calcitic fractures often exhibit strong channelling. Lundström and Rybäck (1989, as cited by Palmqvist 1990) hypothesized that channels form in precipitation regimes where the flow of water is sufficient to prevent recrystallization only within a few channels. Further observations of this process are given by Hakami *et al.*, (1991).
- **Chlorite** often functions as a sealant in relatively smooth fractures. However, 20% of chlorite-filled fractures at the SFR are aquiferous.
- **Iron-oxide hydrates** are often found in aquiferous fractures and zones. These are interpreted as an indication of water-bearing fractures.
- **Clay** is used as a general term for fine-grained fillings. The actual clay (<2 μm size fraction) content is typically less than 20%, and often less than 10%. The remainder consists of silt and coarser size fractions. Capacity for sealing fractures varies, depending on the presence of swelling clay (smectites). 60% of clay-bearing fractures at the SFR show water inflow.
- **Epidote, quartz, and feldspar** are most often found in impermeable (sealed) fractures.
- **Crushed or brecciated zones** often show well-distributed leakage in granite, but some shear zones may be completely dry.

Of the aquiferous fractures at the SFR, 25% have some type of infilling material. Palmqvist's observations indicate that transmissivity is unevenly distributed with respect to infilling type.

Some caution is needed in applying these observations, because the circumstances of fracture flow adjacent to a tunnel are quite different from the situation within the undisturbed rock mass. For instance:

- The stress field near a tunnel is highly disturbed, and fractures with weaker infilling types may be preferentially opened or closed by the shifting of rock blocks.
- The high-gradient flow adjacent to a tunnel may produce outwashing of infillings which would not be disturbed by *in situ* gradients.
- Groundwater flow in the more conductive rock may have been perturbed by grouting programs and/or drainage to another section of the tunnel.

These observations are also limited to high- T_f fractures, since seepage from tight fractures may not be visible.^[11] This is not a problem if the high- T_f fractures are responsible for most of the flow porosity and specific wetted surface, as is likely to be the case. However, the other problems listed above are potentially serious enough, that these observations cannot be incorporated directly into the present study.

¹¹ Watanabe (1991a,b) has developed an evaporation measurement system which is capable of identifying low-to-intermediate transmissivity fractures. However, this type of data was not yet available for use in the present project.

3.3.2.2 Analyses of borehole data

Packer test data, in combination with core data on fracture fillings, are another source of information regarding correlations between transmissivities and infilling types. The advantages of borehole data relative to observations in tunnels are that:

- Quantitative (*vs.* qualitative) data may be obtained by packer testing.
- Fractures of lower T_f may be studied by isolation with packers.
- Groundwater and stress conditions are presumably less extensively disturbed around a borehole than around a tunnel.

However, there are also problems with the use of borehole data:

- Usually more than one fracture is seen in the core from a single packer interval.
- A borehole is unlikely to intersect a conductive portion of a strongly channelized fracture. Hence the likelihood of high T_f may be underestimated for infilling types which tend to be channelized.
- Strong sampling bias may lead to errors if, for instance, infilling type is correlated to fracture orientation.

Tullborg and Larson (1983) examined hydraulic conductivity and fracture frequency data at Gideå, and noted that (in dolerite) there is simultaneous high fracture frequency and low conductivity, indicating that the fractures have been sealed by formation of smectite.

Multivariate analyses of correlations among fracture infillings, packer-test conductivities, and various other single-borehole logging data have been performed by Andersson and Lindqvist (1988) for the Klipperås study site, and by Carlsten *et al.* (1989) for sites at Finnsjön, Klipperås, Saltsjö tunnel, Stripa, and Ävrö.

Interpretation of the results of these studies is difficult because the analyses lumped together multiple rock types. Trends in more conductive rock types may obscure the actual behavior of fractured granitic rock. However, some general conclusions in agreement with the observations of Palmqvist (1990) may be noted.

The results of Andersson and Lindqvist show that:

- Calcite is positively correlated to conductivity at depth (in the calcite precipitation regime), but negatively correlated near surface (less than 200-300 m, in the calcite dissolution regime).
- Chlorite is the dominant mineral in nonconductive sections.
- The iron mineral laumontite occurs in highly-conductive intervals.

In the case of Carlsten *et al.* (1989), a primary concern was possible correlations between radar data and various properties of conductive zones. Their analysis included the infilling minerals calcite, Fe-oxide, hematite, pyrite, epidote, and chlorite. The results of Carlsten *et al.* imply that:

- At Finnsjön, hydraulic conductivity has a positive correlation with calcite.
- At Stripa, hydraulic conductivity may be correlated with epidote.

More definite statements could perhaps be made if the above studies were extended to specifically investigate transmissivity and its relation to infilling.

3.3.3 Infilling type and transport properties

For the purpose of discussion, flow through a fracture with infilling can be classified into three types according to infilling structure (Figure 3-10):

Porous-media flow through infilling which seals the fracture
 Variable-aperture flow between coated surfaces of a fracture.
 Flow through brecciated infilling "rubble"

The relationship among T , ϵ_v and s_{wf} for a given fracture will depend upon which type of structure is present. §3.3.3.1-3 discuss flow and transport for each type.

3.3.3.1 Sealed fractures

In a sealed fracture flow can only occur by seepage through the infilling. In this case the relationship among T , ϵ_v and s_{wf} is analogous to the relationship among permeability, porosity and specific surface for a very thin, well-consolidated formation. The relationship of these properties can vary greatly even within a single rock type (*e.g.* Monicard, 1980). The infilling properties, on the scale of a single fracture, are undoubtedly dependent upon the crystallization texture, which can be quite variable.

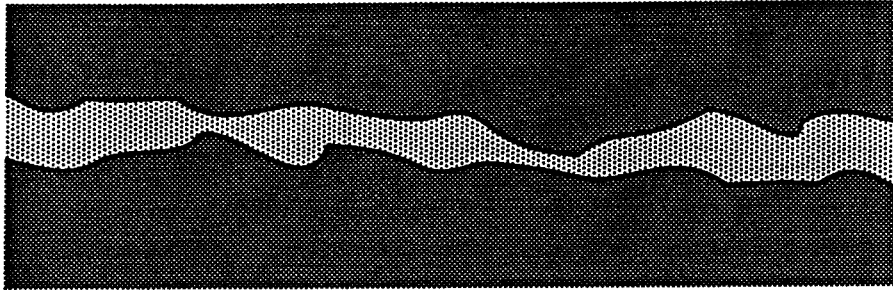
Fortunately the case of sealed fractures is unlikely to be relevant in fractured granite. Table 3-1 gives values of K and ϕ for two representative infilling minerals. In some cases, as noted in the table, data are taken from rocks having composed mainly of the infilling minerals.

Table 3-1. Properties of representative infilling minerals			
Infilling	Hydraulic Conductivity (m/s)	Porosity (%)	Thickness of 10 ⁸ fracture (mm)
Calcite (1)	7x10 ⁻⁹	12	1000
Calcite (2)	-	3	
Quartz (3)	< 10 ⁻¹⁰	0.15	100,000

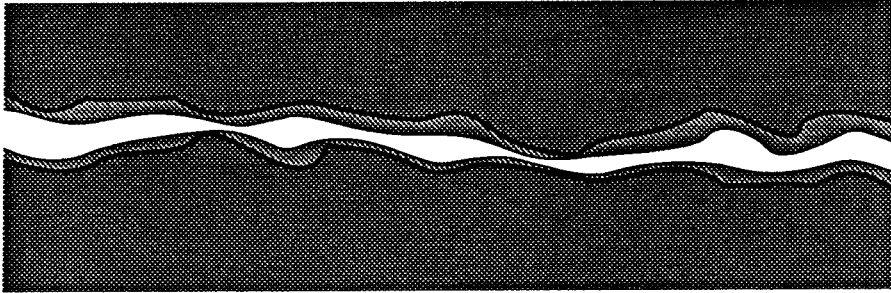
(1) Krech *et al.*, 1974. Based on properties of Salem limestone, a calcitic, fossiliferous limestone.

(2) Skagius and Neretnieks, 1985.

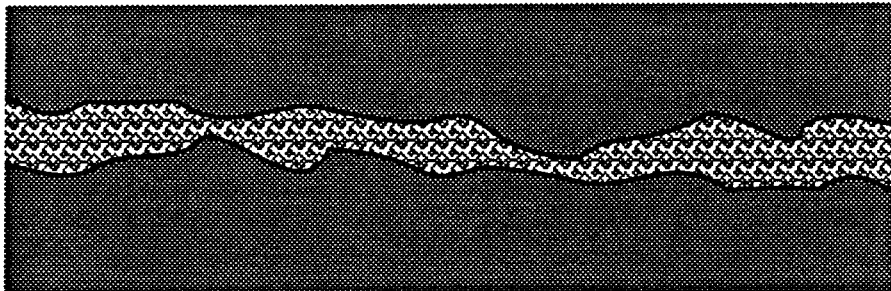
(3) Krech *et al.*, 1974. Based on properties of Sioux quartzite, a fine-grained quartzite with a silica cement.



a) Sealed fracture



b) Coated fracture



c) Breccia-filled fracture

FIGURE 3-10
TYPES OF INFILLING STRUCTURE
SKB-91/DFNST

These fractures will be negligible unless the product of infilling thickness times K is comparable to T_f of fractures carrying the main flow. The table gives the thicknesses (apertures) needed for a sealed fracture to have a transmissivity of at least 10^{-8} m²/s. Obviously seepage through sealed fractures will not be significant in fracture networks dominated by fractures with $T_f \geq 10^{-8}$ m²/s. Therefore it is assumed, in the present study, that significantly conductive portions of fractures are not sealed.

3.3.3.2 Coated fractures

The most common class of significantly transmissive fractures is likely to be the coated fractures. In terms of flow and transport properties, coated fractures can be expected to behave as pairs of rough surfaces in partial contact.

The actual value of ϵ_v for a coated fracture will include both the void volume between the coating surfaces, and the pore volume within the coating. The importance of the coating porosity can be observed by calculating the ratio of coating ϵ_v to total ϵ_v for some reasonable fracture properties. For a fracture with a 1 mm calcitic coating ($\phi \approx 3\%$, from Table 3-1) on each surface, with $T_f = 1 \times 10^{-7}$ m²/s ($\epsilon_h \approx 50$ μ m), a reasonable $\epsilon_m \approx 90$ μ m, based on Eq. 3-6. The coating ϵ_v is $2 \times 1 \text{ mm} \times 3\% = 60 \mu\text{m}$, which is 40% of the total ϵ_v for the fracture. The relative importance of coating porosity will increase as T_f decreases and/or coating thickness increases.

For the case of s_{wf} estimation, apart from the possible dependence of s_{wf} on coating thickness and pore structure, there is also question as to whether sorption properties vary with infilling mineralogy and radionuclide type. If so, then s_{wf} estimates may only be valid for specific radionuclides, and these estimates may need to be weighted in proportion to the sorption capacities for particular infillings.

Eriksen and Locklund (1989) found no experimentally significant differences in sorption coefficients among three radionuclide species sorbing on crushed rock. Their data for two different fracture coatings (one with higher chlorite content) and fresh granite showed possible differences in sorption between granite and infillings, but no apparent difference between the two types of infillings.

Skagius and Neretnieks (1985) noted that, in diffusivity measurements using uranine, there was indication of sorption for fracture coating material although uranine is considered to be non-sorbing for granite. Landström and Tullborg (1990) noted that fracture fillings, relative to the granite, have higher proportions of minerals that participate more actively in sorption processes (e.g. hematite/Fe-oxhydroxide, carbonates, clay minerals, and chlorite).

Despite these indications, no quantitative statements may be made about variation among infilling types. Therefore in the present study all coatings are assumed to have identical sorption characteristics, and different infillings will not be weighted in estimation of wetted surface.

3.3.3.3 Fractured, crushed or brecciated infilling

This class of fractures has not received much study. However, examination of the detailed core logs for one borehole at Finnsjön (§5.8) showed that the most hydrologically significant fractures were in this category. For these fractures the relationship of T_f , ϵ_v and s_{wf} will depend strongly on the size distribution of the particles in the gouge or breccia, and whether or not the particles are cemented. Relative to a coated fracture of the same T_f , a breccia-filled fracture can be expected to have much higher s_{wf} and perhaps higher ϵ_v .

Tullborg (1986) described brecciated infillings at the Klipperås site, but was not concerned with size distributions or measurement properties related to T_f , ϵ_v and s_{wf} . Some of the brecciated infillings were slightly cemented, and some had been sealed by Fe-oxyhydroxides.

Skagius and Neretnieks (1985) measured porosities and diffusivities of a few samples of breccia with mineral coatings from the Finnsjön site and the Stripa mine. Porosities of the pieces ranged from < 1% to 7%. No description was given of the particle-size distributions for the samples. The measurements were performed on single pieces from the breccias, so the porosities may not reflect the bulk properties of the breccia material.

The most detailed studies of fault breccias and gouge have been studies of the frictional properties of the gouge material. Particle-size distributions in natural gouge are typically lognormal or power-law (see summary of results by Marone and Scholz, 1989). For granular materials, permeability and porosity decrease and specific surface increases if the particle sizes are distributed rather than uniform, so based on the above, fractures filled with breccia or gouge can be expected to have high s_{wf} relative to porosity and T_f .

Experiments with synthetic gouge materials indicate that the porosity of gouge materials can vary considerably with shear displacement and normal loading (Morrow and Byerlee, 1989; Marone and Scholz, 1989), due to comminution and changes in packing. Both on a laboratory scale (Marone and Scholz) and larger scales (Hull, 1988) breccias may be stratified, with layers of relatively fine particles aligning in shear deformation bands. Marone and Scholz measured a decrease in ϕ from 34% to 18% by applying 100 MPa hydrostatic pressure to a sand (mean grain diameter 0.4-0.8 mm), and further reduction to 10-11% by shearing. This gives some idea of the porosity range that can be expected for granular infillings. For coarse breccias, the value of ϕ_c is probably in the high end of this range.

The reduction of grain size, porosity, and permeability by shearing could in part explain the observation of Palmqvist (1990) that crushed or brecciated zones typically show much leakage but some shear zones are completely dry.

3.4 Effective Transport Porosity and Wetted Surface

3.4.1 Porosity

For a coated fracture, the physical value of ϵ_v for a given area A is simply the average ϵ_m plus the ϵ_v due to the fracture coating:

$$\epsilon_v = \bar{\epsilon}_m + \bar{\epsilon}_c \phi_c \quad (3-11)$$

where

$$\begin{aligned} \phi_c &= \text{coating porosity} && [-] \\ \epsilon_c &= \text{coating thickness (total for both sides of fracture)} && [L] \end{aligned}$$

Gelhar (1987) considered only the effect of ϵ_m , in which case this reduces to $\epsilon_v = \epsilon_m$ and showed that this is the appropriate ϵ_v for transport predictions, for a stochastic model for solute transport. For lognormally distributed ϵ_m , Gelhar's model predicts^[12] that, neglecting sorption and diffusion, the effective ϵ_v for advective transport is related to ϵ_h by:

$$\frac{\epsilon_v}{\epsilon_h} = e^{\sigma_{\ln \epsilon_m}^2 / 2} \quad (3-12)$$

where

$$\sigma_{\ln \epsilon_m} = \text{standard deviation of the natural log of } \epsilon_m.$$

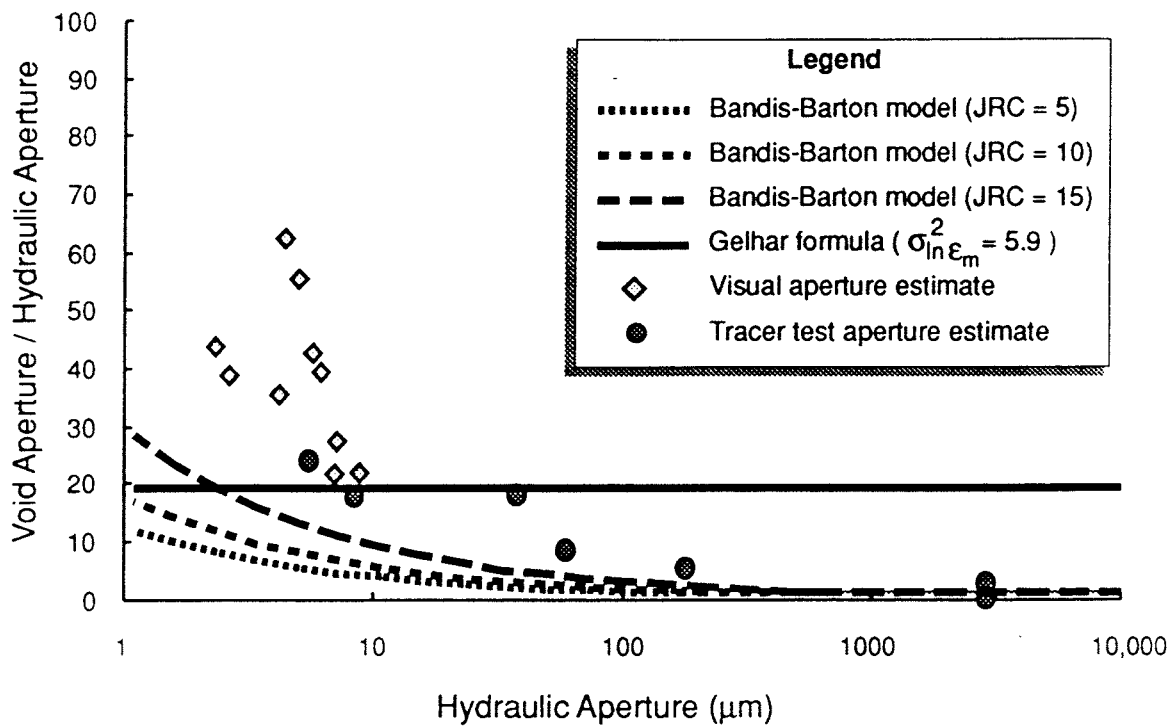
Unfortunately fracture aperture variation is not yet well understood (§3.1), and in particular there is not enough data to estimate $\sigma_{\ln \epsilon_m}$ for a fracture with a given ϵ_h .

Another possible way to estimate ϵ_v from T_f is to apply the empirical formula of Bandis *et al.* (1983), Eq. 3-6, to estimate the average ϵ_m . The ϵ_m used in the rock mechanics literature to describe joint closure may not be applicable for estimating ϵ_v , since ϵ_m is measured macroscopically. For instance, Makurat *et al.* (1990a) describe ϵ_m as the aperture which "can be measured with feeler gages or on resin-grouted joints." Other possible problems could arise from scale effects, as coupled stress-flow experiments are usually performed on relatively small samples.

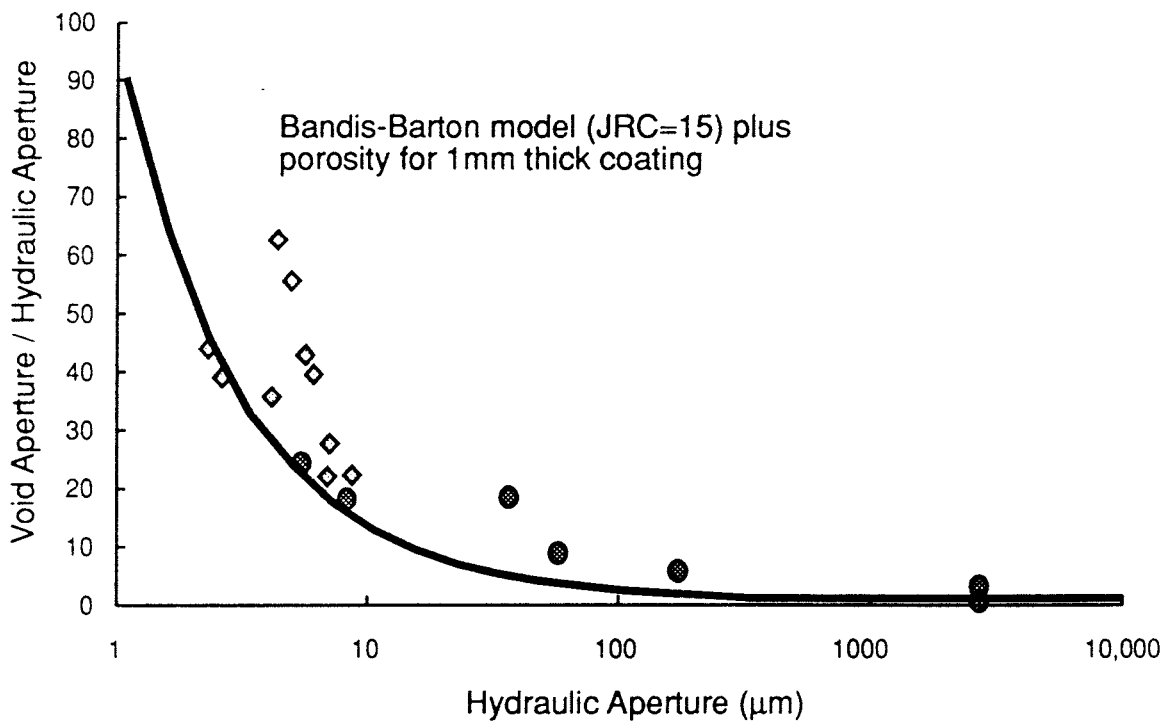
Methods for estimating ϵ_v from ϵ_h can be compared with results from tests in single fractures. Figure 3-11a compares *in-situ* estimates^[13] of ϵ_v with curves for several JRC_o values. The circles

¹² The formula given by Gelhar (1987, p. 18) gives the reciprocal of this, but the above result is clearly what was intended.

¹³ A JRC_o of 7.5 is fairly typical for tension joints in granite. A JRC_o of 20 is theoretically the highest possible JRC_o, without there being "steps" in the fracture. Measurements at 360 m depth in Stripa give values of JRC_o typically in the range from 5 to 9, with a mode around 7.5 (Makurat *et al.*, 1990a).



a) Comparison of data with theories for unfilled fractures



b) Effect of infilling

FIGURE **3-11**
THEORETICAL AND EXPERIMENTAL ESTIMATES
OF HYDRAULIC vs VOID APERTURE RELATIONSHIP
 SKB/SKB91 DFNST

in the plot represent ϵ_v values estimated from tracer tests.^[14] The diamonds represent ϵ_v values estimated from the visual aperture profiles of Abelin *et al.* (1990).^[15]

The horizontal line in Figure 3-11a is based on the formula of Gelhar (1987), assuming a lognormal distribution for ϵ_m , with $\sigma^2_{\ln \epsilon_m}$ independent of ϵ_h . The value $\sigma^2_{\ln \epsilon_m} = 5.9$ used here was the largest of the values derived by Gelhar from tracer test data. A better fit to the data may be obtained by allowing $\sigma^2_{\ln \epsilon_m}$ to vary linearly with ϵ_h , for the data below this line. However, there is no sense in fitting the model to the data above this line, as a log variance of 5.9 is already high for a formula based on perturbation methods.

The discrepancy between Eq. 3-6 and measured ϵ_T or ϵ_v is largest for the data from the Stripa experiments (Abelin *et al.* 1985; Abelin *et al.*, 1990). All of the fractures tested in these experiments were extremely tight ($T_f < 2 \times 10^{-9}$ m²/s), compared with the more transmissive packer intervals at Finnsjön. The data from other experiments show somewhat better agreement with increasing T_f . However, in general the estimates of ϵ_v from Equation 3-6 are too low. Based on this evidence, it is questionable whether Eq. 3-6 can be applied in the context of the present study.

Porosity of fracture coatings (see §3.3.3.2) may account for some of the difference between Equation 3-6 and estimates of ϵ_v from tracer experiments. Figure 3-11b compares the same data with ϵ_v calculated based on Equation 3-6 plus a component due to fracture coating porosity (Equation 3-11). Here the coating on each surface of the fracture is assumed to be $\epsilon_c = 1$ mm thick, with $\phi_c = 3\%$, for all ϵ_h . This is more similar to tracer results. Better agreement could be obtained with higher ϕ_c or ϵ_c , but more data and analysis are needed to determine which values are appropriate.

The visual ϵ_m of Abelin *et al.* (1990) do not include coating thicknesses, and so coating porosity cannot account for the discrepancy between these and the ϵ_m predicted by Eq. 3-6. Furthermore, the visual ϵ_m are similar to the ϵ_v estimates of Abelin *et al.* (1985) and of Abelin *et al.* (1990). In the latter experiment, estimates of ϵ_v from tracer tests in one of the fractures ranged from 22 to 4000 μm , depending on assumptions about diversion of the tracer into

¹⁴ Values cited include estimates of ϵ_v and ϵ_h by Abelin *et al.* (1985a), Novakowski *et al.* (1985), and Shapiro (1988), from the single-fracture tests described in Section 3-1. For the test in limestone by Shapiro (1988), the value used for ϵ_v is the estimated product $\epsilon_v \phi$. Values of ϵ_v and ϵ_h for tests at Studsvik and at Finnsjön are taken from Gelhar (1987); the original sources for these values, as cited by Gelhar, are: Klockars and Persson (1981, 1982) for the Studsvik test, and Gustafsson and Klockars (1981, 1984) for the Finnsjön test. The test zone at Studsvik included four fractures. The values given are based on the assumption that flow was equally divided among the four fractures (Gelhar, 1987).

¹⁵ Abelin *et al.* (1990) described the distributions of ϵ_m as lognormal and reported statistics for $\log_{10} \epsilon_m$. The estimates of mean ϵ_m shown in the figure, and used in §5.8, are calculated directly from these statistics based on the assumption that the distributions are perfectly lognormal. A simple average of the actual measurements would be preferable, but these estimates are more conveniently obtained from the published data. Comparison by eye with the histograms of Abelin *et al.* indicates these values are roughly correct.

adjacent fractures. Abelin *et al.* concluded that flow apertures (ϵ_v) could not be determined "with any accuracy" from the tracer tests, but that the estimated values lay in the same range as the estimated ϵ_m from profiles.

The results of Abelin *et al.* (1990) seem to imply that the ϵ_v measured in tracer tests can be explained entirely by variations in ϵ_m which contribute pore volume not recognized in the more macroscopic measurements of ϵ_m in joint closure experiments. However, Abelin *et al.* note that visual ϵ_m in their experiment may have been overestimated due to chipping of infillings and/or wall rock during drilling.

In summary, there does not seem to be clear evidence for any particular physical explanation of the discrepancy between measured ϵ_v and ϵ_h . However, when taken together fracture roughness, small-scale ϵ_m variation, and fracture coating porosity can account for the observations, even though their individual contributions to ϵ_v are not clear. An empirical model based on the limited data from single-fracture tests is developed in §5.8.2.

For fractures with **crushed or brecciated infilling**, the relationship between ϵ_h and ϵ_v will depend upon the particle size distribution. Kozeny's equation (Monicard, 1980) expressed in terms of hydraulic conductivity is:

$$K = \frac{\phi}{k_o \tau s_v^2} \cdot \frac{\rho_w g}{\mu_w} \quad (3-13)$$

where

τ	= tortuosity	[-]
k_o	= pore shape factor (geometric constant)	[-]
s_v	= wetted surface per unit pore volume	[L ⁻¹]

gives a theoretical relationship among permeability, specific surface, and porosity. In terms of a fracture of aperture ϵ_m filled with particles,

$$s_v = \frac{s_{vf}}{\phi_c \epsilon_m} \quad (3-14)$$

and Equation 3-15 may be written as:

$$T_f = \frac{\rho_w g}{\mu_w \tau k_o} \cdot \frac{\epsilon_m^3 \phi_c^3}{s_{vf}^2} \quad (3-15)$$

This may be useful for obtaining rough estimates of s_{w_f} or ϵ_v for a given T_f . §5.8 gives examples of application of this formula to a few high- T_f fractures for which ϵ_m can be estimated from core logs. A range of reasonable porosity values should be considered in using this formula.

3.4.2 Wetted Surface

For a coated fracture, s_{w_f} is the combined surface area of the two surfaces of the fracture, per unit area of the fracture plane. For an ideal, parallel-plate fracture with impermeable coating, $s_{w_f} = 2$.

For real fractures, contact between fracture surfaces and local sealing around asperities will reduce s_{w_f} in proportion to the contact area. Since contact area increases with fracture closure under normal stress (§3.2.1), fractures at depth will tend to have a higher fractional contact area. It is reasonable to assume that fractional contact area is negatively correlated with T_f .

Surface roughness will increase s_{w_f} for the open areas of a fracture. Fractal theories of surface roughness (e.g. Brown and Scholz, 1985) predict that s_{w_f} increases indefinitely with decreasing scale of measurement. However, in estimating s_{w_f} for sorption predictions, the appropriate scale of measurement for area is that used in laboratory measurements of sorption properties. Measurements by Eriksen and Locklund (1989) used rock chips 1.2 cm². For typical JRC_o values, the surface area of a fracture measured by tiling with 1.2 cm² squares is virtually identical to the area projected into the fracture plane. Thus surface roughness effects are negligible in comparison with the reduction in area due to contact between surfaces.

The effect of a permeable coating on s_{w_f} could be large, depending on the accessible surface area of voids within the coating material. Eriksen and Locklund (1989) found that sorption in short-term (48 hour) experiments depended mainly on the outer surface area. Eriksen (1988) obtained similar results in a laboratory experiment to measure sorption during flow through a single coated fracture in a core specimen.

These results indicate that the voids within the coatings were not active within the time of the experiment. This might not be true for longer experiments. However, if sorption is viewed as a retarding mechanism, it is "conservative" to assume that voids within the coatings are not accessible to sorption any more than are the voids within the granite (which are modelled in other ways), so that the coating contribution to the effective s_{w_f} is negligible.

Thus for **coated fractures**, a reasonable, conservative estimate of s_{w_f} is simply 2 times the fractional open (non-contact) area of the fracture. Based on the the single-fracture flow experiments (§3.1.1), active channels are restricted to about 10-20% of the fracture plane, but if stagnant "pools" are included the fractional open area may be as high as 65%.

For **breccia-filled fractures**, the uncertainty in s_{w_f} will be high because there is very little knowledge of particle size distributions and hydrologic properties of brecciated infillings. An estimate of the possible range of s_{w_f} for a given fracture can be obtained by applying the Equation 3-15 for a range of ϕ_c . Due to the high uncertainty, this should be compared with more conservative calculations based on the relationships for coated fractures.

4. MODELLING APPROACH

4.1 Objectives

The goals of the present study were to give quantitative predictions, based on a DFN interpretation of the Finnsjön site, regarding the following topics:

- Existence of an equivalent or effective conductivity tensor K_e on the scale of SC model blocks.
- Mean values, anisotropy, and variability of K_e , if the tensor exists.
- Autocovariance of K_e .
- Relationships of K_{Mogjes} estimates to K_e .
- Flux-weighted estimates of porosity ϕ_Q and specific wetted surface S_{wQ} .

The information on K_e could be useful in developing a SC model for the site. The estimates of ϕ_Q and S_{wQ} may be used for comparison with alternative methods of estimation, and possibly as input data for DPST and CN models.

§4.1.1-5 give further discussion and definition of these objectives.

4.1.1 Existence of a conductivity tensor for SC models

When modelling fractured rock with SC models, a fundamental question is whether there exists some reasonable scale at which the rock can be described by an effective conductivity tensor. If the rock cannot be described by an effective tensor on the scale of the blocks used in the SC model, the finite-element or finite-difference equations contradict the physics of the problem, and the results obtained are invalid.

The question of true "equivalent porous medium" (EPM) is a broader issue, and requires consideration of scaling relations and existence of heterogeneous connections. This issue can be resolved only by extensive cross-hole testing. Field experiments on a scale at which an EPM could be expected to exist are rare, even for more conventional heterogeneous porous media (Desbarats and Srivastava, 1991). For the Finnsjön site, the cross-hole testing has been performed mainly within Zone 2 (Andersson *et al.*, 1991), and there is little information concerning an EPM scale for the rock mass.

A DFN model cannot be used to establish the physical validity of a SC model. This can be decided only by direct comparison to field experiments. However, a DFN model can be applied for a more limited purpose:

Objective 1. To decide if the requirement of an effective conductivity tensor is likely to be satisfied for the rock at Finnsjön.

Past applications of DFN models being used to evaluate block-scale conductivity include 2-D modelling (Long *et al.*, 1982; Robinson, 1984; Endo *et al.*, 1984; Khaleel, 1989) and 3-D modelling (Axelsson *et al.*, 1990; Cacas *et al.*, 1990a). The 3-D methods have been extended to characterization of scale effects on effective dispersivity for transport (Dverstorp and Andersson, 1990; Cacas *et al.*, 1990b).

In the SKB 91 study, the SC model HYDRASTAR (Norman, 1991) is used mainly for prediction of steady-state velocities and streamlines for the DPST transport model. Therefore use of the DFN model to evaluate aspects of EPM behavior is restricted to the question of effective conductivity tensors for steady-state flow.

4.1.2 Average conductivity tensor, variability, and anisotropy

If the DFN model predicts that, on a block scale s , an effective conductivity tensor $K_s(x)$ can be estimated for a given x , then a primary objective is:

Objective 2: To provide a set of estimates of $K_s(x)$ which can be characterized in terms of an expected value and covariance, after taking some suitable transformation of $K_s(x)$, for use in the SC model.

Even if the effective conductivity concept is found to be inapplicable, the DFN model can be used to estimate equivalent conductivity values which approximately describe the block-scale response to a uniform gradient across a block, to allow a working SC representation to be developed, even where the concept is not strictly valid. The block-scale anisotropy is of particular interest.

Effective anisotropy is of interest for SC modelling, but is extremely difficult to evaluate by field testing. Therefore an additional objective is:

Objective 3: To estimate the degree of anisotropy that can be expected due to fracture network geometry and stress effects.

4.1.3 Spatial structure of effective or equivalent conductivity

The spatial structure of block-scale conductivity can be expressed in terms of the autocorrelation of $K_b(x)$, which is expected to arise from extensive geological structures in the rock. For derivation of a SC model, the form of the autocorrelation function $C_\chi(h)$ must ordinarily be chosen from a few analytically tractable cases. Possibilities to validate the choice of $C_\chi(h)$ are limited, because K_p data are obtained only for a few, widely-spaced line samples, and most of the sampled lag vectors h are either coparallel, or are of magnitude larger than typical correlation lengths. Thus:

Objective 4: To predict the autocorrelation structure that results from large-scale features in the rock, by producing estimates of $C_\chi(h)$ for a wide variety of magnitudes and orientations of h .

4.1.4 Relation of packer tests to block-scale conductivity

A major problem in constructing a SC model, as discussed in §2.3.1, is the question as to how packer test data K_p relate to the block-scale K_b . The existence of a "scale effect" is widely recognized, and numerous theories have been proposed for extrapolating from the packer-test "scale" to the block scale (see review by Durlofsky, 1991). The problem is much more serious, though, since in a typical packer test in fractured rock, neither the shape nor the volume of the region influenced by the test is known with certainty (Doe and Geier, 1990). In the "worst" case¹⁶, a test may affect only a short path connecting to the borehole above the packer.

Given this situation, the possibility of deriving a valid, theoretical "scaling law" is at best remote. A more feasible alternative, based on the DFN model, is:

Objective 5 To model packer tests within simulated blocks of the Finnsjön granite, to interpret the simulated K_p according to the same method used to evaluating K_p from field tests, and to develop an empirical relationship between the simulated values of $K_p(x_1)$ and $K_b(x_1 + h)$, for a variety of lag vectors h .

If both simulated and actual tests are interpreted by identical methods, the effect of assumptions about flow geometry is greatly reduced. If a significant correlation of K_p to K_b is shown to exist, then the results can be used to develop conditional SC models based on K_p data.

¹⁶ Much worse scenarios, such as undetected equipment failures, are of course possible in the field, but simulation of these is far beyond the scope of the present study.

However, preliminary results of this study, as given in Chapter 7, show that the correlation predicted by the DFN model is extremely poor. This raises strong questions about the usefulness of packer test data for this purpose.

4.1.5 Transport parameters for DPST and CN models

Two critical properties for transport modelling, with either the DPST model or the CN model, are the flow porosity ϕ_w and flow specific wetted surface S_w for the main flow paths. These properties can be estimated from cross-hole tracer tests, but the accuracy of these estimates is limited because the geometries of the regions tested are unknown. A further deficiency for the Finnsjön site is that tracer-test data for the rock outside of Zone 2 are very limited. Therefore the present study includes a final goal:

Objective 6: To estimate ϕ_w and S_w based on the flux distribution obtained in block-scale simulations, and reasonable assumptions about the transport properties of single fractures.

4.2 Major considerations for the DFN model

Site characteristics relevant to DFN modelling were described in §2.1. The following sections summarize key issues that are evident from the site description, and from a preliminary DFN modelling study (Geier and Axelsson, 1991).

4.2.1 Characteristics of the major features

Based on the information in §2.1, the following points are evident:

- Of 14 identified, "major" zones, only two are well-characterized with respect to fracturing character and subsurface location.
- Unidentified "major" zones may exist within the Finnsjön block.
- Numerous "minor" zones exist, with extents less than about 200 m. In a few cases the location, orientation, and/or lateral extent of these zones are known, but in general the geometry is uncertain. Many undetected minor zones most likely exist.

Regarding the most well-characterized feature, Zone 2, the following can be said:

- Zone 2 consists of several subparallel subzones, which give strong lateral connections.
- Within the subzones, cross-hole testing shows possible anisotropy, boundary effects or other irregularity, indicating that the subzones may be discontinuous.
- The lower boundary of Zone 2 is less distinct than the upper boundary.

The geological conceptual model for Zone 2 allows a qualitative explanation of the observed hydrologic variability, but is difficult to cast in quantitative terms. The uncertainty regarding the major features, as a group, makes deterministic modelling of these features less worthwhile, in view of the extra difficulties (§4.3) this would entail.

4.2.2 Characteristics of the fracture population

Based on §2.2.2-4, key aspects of the fracturing at Finnsjön are as follows:

- Three fracture sets have been identified: two subvertical sets and a subhorizontal set that is poorly represented in outcrop data.
- The fracturing in the upper part of the northern (Brändan) block is less intense than that in the southern (Gåvastbo) block. Other differences in fracturing character are apparent between the two blocks.
- Fractures below Zone 2 show some geological similarity to fractures at surface in the Gåvastbo Block.
- No significant change in fracturing frequency is seen at depth in the southern block.

The stress and conductivity measurements in boreholes indicate that:

- The minimum principal stress is vertical and increases linearly with depth.
- K_p decreases with depth near surface. However, the pattern varies from one borehole to another. Below 200 m there is little clear evidence of a trend.

The direction of the minimum stress suggests that subhorizontal fractures will have higher T_f than subvertical fractures. In a well-connected system, this could produce higher directional K in the horizontal plane, as was seen in the cross-hole tests. Preferred mineralization could have effects greater than that of stress but this cannot be considered in the present study due to lack of applicable data. The somewhat ambiguous decrease in K_f with depth may be due to increased stress with depth. Weathering or other geochemical effects (*e.g.* calcite dissolution by surface waters) cannot be excluded, but the magnitude of their effect is difficult to estimate. Stress-transmissivity effects have been the subject of considerable research, and may be sufficient to explain the limited K_f variation with depth seen at Finnsjön.

Some problems related to application of a DFN model are that:

- Fracture size and orientation have been completely characterized only at one location at surface. The fractures at this location are considered to be atypical.
- More extensive scanline mapping provides fracture spacing and strike data, but not size or dip data.
- There are no data concerning fracture size at depth.
- Orientation data at depth are limited to dip data.

The differences between the blocks suggest the possibility of modelling the blocks as separate statistical regions. However, the limitations of the size and orientation data at surface, and the complete lack of these data at depth, mean that realistically only variations in fracturing intensity can be considered.

4.2.3 Preliminary results from the feasibility study

Preliminary DFN modelling of the Finnsjön rock mass was performed by Geier and Axelsson (1991). Aside from the problems of dataset adequacy discussed in §4.2.2, the preliminary analysis indicated the following:

- A large percentage of T_f measurements at or near the equipment measurement limit $T_{threshold}$ results in non-uniqueness in estimating conductive fracture frequency f_c and the distribution of cross-fracture transmissivity T_f .
- This indicates a high intensity of marginally transmissive fractures.

- A generalized-radial flow (GRF) analysis of a small sample of transient packer tests showed a high proportion with $2 \leq D_f \leq 3$. This indicates a fairly well-connected fracture population in intervals with measureable flow. A few tests in the sample showed subradial flow, indicating possible channeling effects in places.
- Both fractures and lineaments appear to fit a power-law size distribution, when analyzed using a weighted sampling approach.

Simulations based on the preliminary dataset demonstrated a validation procedure based on the GRF interpretations, and gave some preliminary estimates of block-scale conductivities. However, the preliminary DFN model was based on assumptions of simplified uniform transmissivity throughout each fracture plane, and a size distribution which is inconsistent with results of more recent analysis (§5.2).

4.3 Conceptual model definition

This section describes alternative conceptual models which were considered, and reasons for choosing the eventual DFN model. The models were assessed in terms of:

- Consistency with geological data.
- Practicality of the DFN/SC model interface.

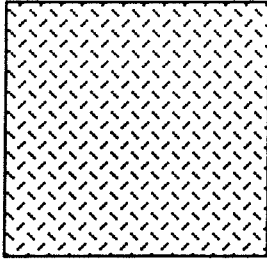
These criteria produce conflicts, so in the end a compromise was necessary. The following sections (§4.3.1-2) describe issues considered in selecting the conceptual model.

4.3.1 Comparison of alternative models

Two approaches were considered (Figure 4-1):

- A **single-domain model** based on a single statistical population of fractures, throughout the modelling region. This does not exclude multimodal distributions, spatial trends, or clustering of fractures, provided that these can be described by regionally valid statistics.

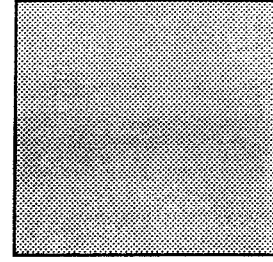
DFN MODEL



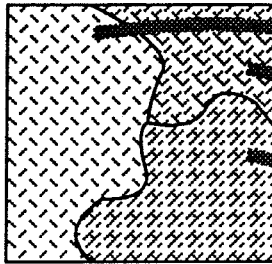
Single, statistically homogeneous fracture population for entire region.

a) Single-domain model

SC MODEL



Single stochastic continuum represents the entire region; possibly with continuously varying properties.



Multiple domains defined within modeling region.

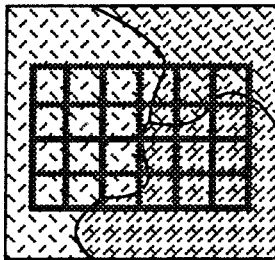


Properties of each domain estimated independently.

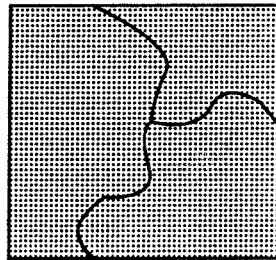


Distinct stochastic continuum for each domain.

b) Multi-domain model (Type I)



Multiple domains defined within the modeling region and modeled simultaneously.

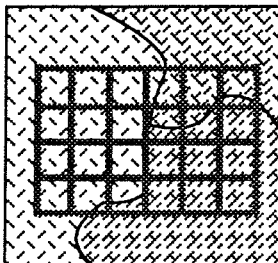


Autocovariance estimated for full region after transforming conductivity estimates to remove spatial trends (discrete and/or continuous).

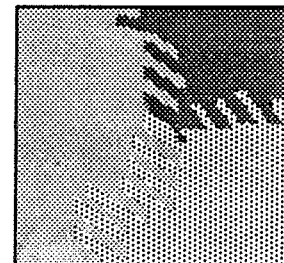


Separate stochastic continuum for each domain, but globally applicable covariance defines transition between domains.

c) Multi-domain model (Type II)



Multiple domains defined within the modeling region and modeled simultaneously.



Simultaneous coregionalization, with coupled stochastic continua for the different subregions.

d) Multi-domain model (Type III)

FIGURE 4-1
SINGLE-DOMAIN AND MULTI-DOMAIN
DFN MODELS
SKB-91/DFNST

- A **multi-domain model** with distinct populations of fractures in different units of the rock, *e.g.* fracture zones and "good rock." Transitions between rock units may be discrete, or some interpolation of properties may be specified.

These two approaches are compared in §4.3.1.1-4.

4.3.1.1 Ability to reproduce heterogeneity

Both single-domain and multi-domain models may include spatial trends in the fracture statistics. A single-domain model can simulate strong heterogeneity (*e.g.* fracture zones or swarms) only if fracture location is assumed to be autocorrelated in some respect. Single-domain DFN models capable of simulating strong heterogeneity include the Parent-Daughter model (Long and Billaux, 1987), various fractal models (Lee, 1988; Geier *et al.*, 1989), and the Nearest Neighbor model (Geier *et al.*, 1989).

In multi-domain models, the heterogeneity is explicit. The various rock units may be modelled independently (*e.g.* Herbert and Splawski, 1990), in which case the transition between rock units is abrupt. Alternatively, all rock units may be simulated simultaneously (*e.g.* the deterministic War Zone model, Dershowitz *et al.*, 1990a), so that transition regions between units occur due to connections between fractures from adjoining regions.

4.3.1.2 "Hard" data requirements

A single-domain model is simpler because only one set of fracture statistics must be derived. Additional statistics are needed to describe spatial structure of fracture properties.

A multi-domain model treats each rock unit separately, and therefore would require somewhat more data analysis, calibration, and simulation effort than a single-domain model. As the number of rock units increases, the model becomes less well-determined because there is less data per rock unit. However, for the limited data set available for the Finnsjön site, a multi-domain model would need to be based largely on so-called "soft" data.

4.3.1.3 "Soft" data utilization

The use of "soft" geological data is often avoided in hydrologic models because uncertainties are difficult to assess. However, given the limitations of the "hard" data as discussed in §2.2, methods for strengthening the models by including "soft" data are desirable.

Use of "soft" data in single-domain models requires conversion to a quantitative, statistical description of heterogeneity. Possible methods for incorporating this type of data, such as fuzzy kriging, had not been implemented in DFN models at the time of this study.

Multi-domain models favor the use of "soft" data in defining rock units. "Soft" data such as geologists' theories of fracture zone genesis may be used as the basis for defining the fracture population in a particular rock unit, if "hard" data are insufficient for statistical definition.

4.3.1.4 Feasibility of DFN/SC interface

A single-domain model greatly simplifies derivation of SC model parameters, because, after removing spatial trends, the expected values of the physical properties are independent of location.

A multi-domain model that treats each rock unit independently (Figure 4-1b) would also simplify derivation of SC model parameters, since effectively the separate units are treated as independent coregionalizations in the SC model. However, this approach gives no information about possible transitions among units, which may be crucial. For instance, if at Finnsjön the highly conductive sections of the "rock mass" are spatially correlated with highly conductive sections of a fracture zone, the main transport paths will be, on average, more conductive and localized. To consider these possibilities, the various rock units must be modelled simultaneously. This leads to problems of complexity for the DFN-SC interface, because the conductivity field is inherently nonstationary.

One possibility is to model the various rock units simultaneously (Figure 4-1c), and to apply a spatially-varying transformation to remove non-stationary effects from the simulated conductivities, prior to estimation of the autocovariance structure. This approach leads to more realistic models, but the problem of estimating an admissible transformation was viewed as formidable, from the SC standpoint.

Alternatively, the various rock units can be treated as simultaneous coregionalizations (Figure 4-1d). The difficulty with this type of model is in the estimation of cross-correlation terms between conductivities for different units. This requires more simulations to estimate the additional terms, and increases the bookkeeping difficulties.

4.3.2 Description of conceptual model

After preliminary data analysis, a single-domain DFN model was selected which treats the rock as a single region, described by a single set of statistics throughout. Large fracture zones, similar to the zones seen at Finnsjön, are included in the model, but their location is taken to be random so that the $K(x)$ field will be stationary (except for a possible vertical trend). The main reasons for choosing a single-domain model were:

- A single-domain model allows much simpler derivation of SC model parameters.
- The dataset for fracture geometry is too limited to justify a division into northern and southern blocks.¹⁷
- Core data for dips (§5.1) did not support any particular multi-domain model.

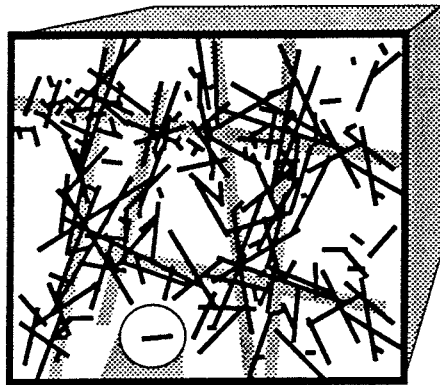
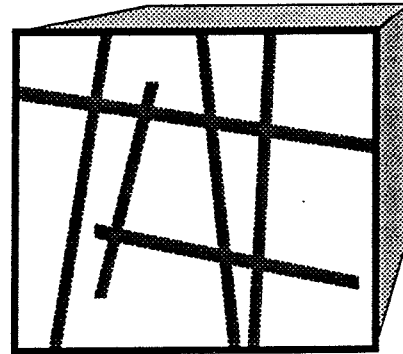
The main disadvantage of this choice is that much of the information concerning specific geological structures cannot be utilized. However, this does not result in so much loss of information as it may seem, because of the substantial uncertainty regarding most of the zones, and the probable existence of many uncharacterized zones, as discussed in §4.2.1.

The following is an overview of the model. The methodology is described in §4.4-6. Detailed properties of the model, and their derivation, are described in Chapter 5.

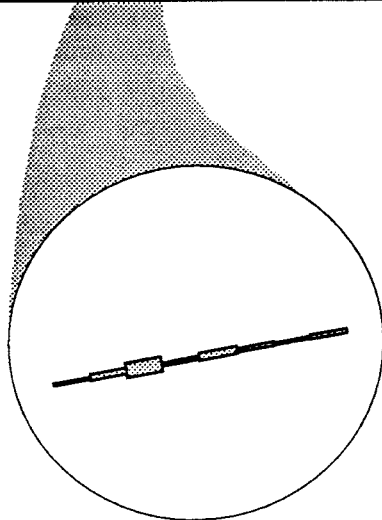
The **geometric model** is defined at scales from 1 m to 1 km. On the largest scale, the model consists of planar zones (Figure 4-2a). The geometry of these zones is statistically similar to the geometry of major and minor zones at Finnsjön (§2.2.1). The model contains a range of zone sizes, from 50 m to 1 km.

¹⁷ The magnitude of the contrast between blocks could be estimated by separate runs of the model with different fracture intensities, but otherwise identical fracture populations. Fracture intensity, based on core fracturing, is the only aspect of fracture geometry which is reasonably well characterized across the site.

FRACTURE ZONES



FRACTURES



DETAILED PROPERTIES

FIGURE 4-2
CONCEPTUAL MODEL FOR FRACTURE SYSTEM
SKB/SKB91 DFNST

The fundamental unit of the model is the single fracture. The location of fractures is correlated to the planes of the zones, giving a higher fracture intensity in the zones (Figure 4-2b). However, fractures may occur anywhere in the rock. The statistical properties of the fractures match observations on outcrops and in core (§2.2.2).

Fractures are divided into "subfractures" (Figure 4-2c), the properties of which vary according to a fractal rule. Detailed geometry on a smaller scale (§3.1) is not represented explicitly.

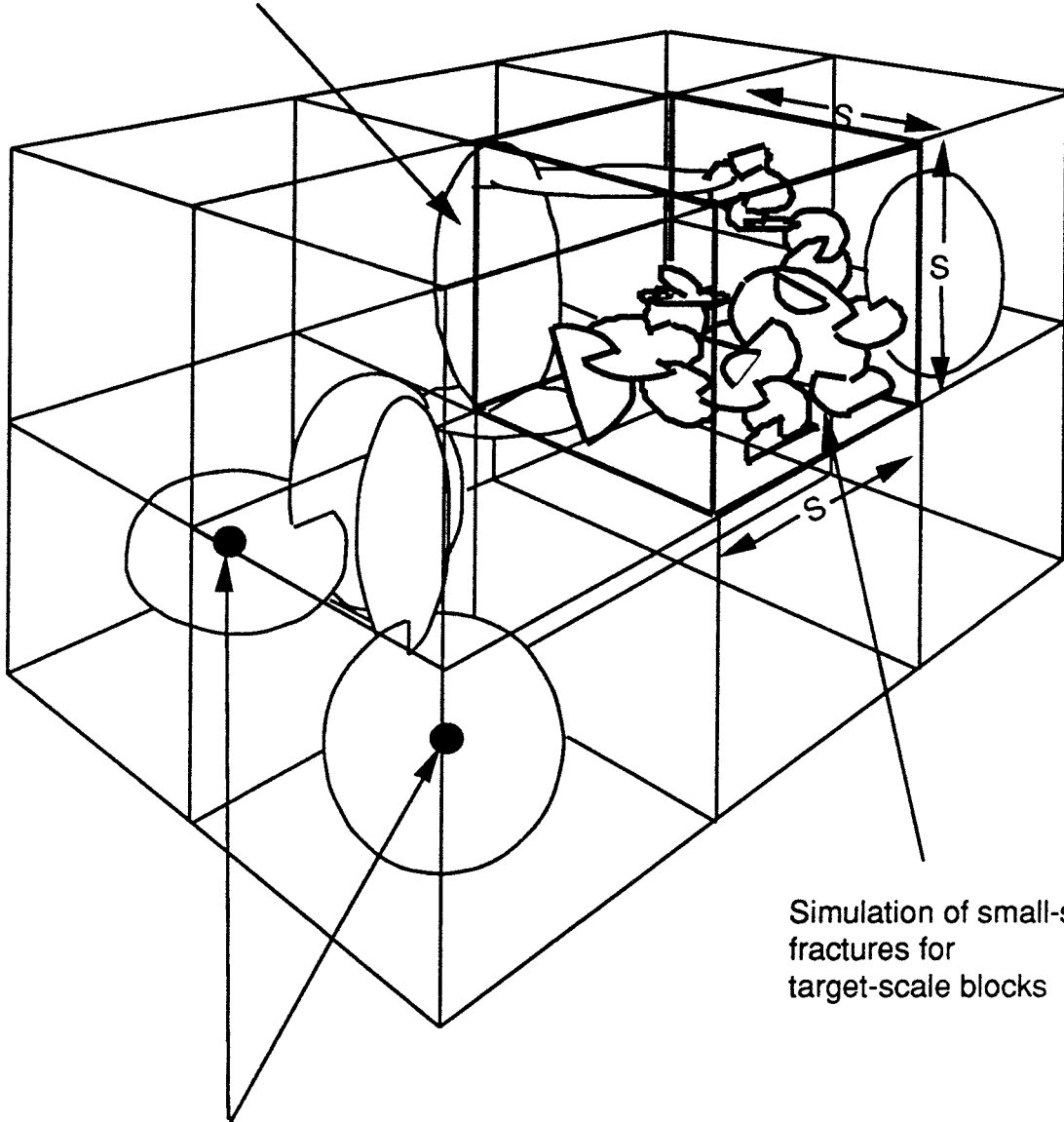
The hydrological behavior of the fracture system is modelled explicitly for scales up to the block size for 3-D SC models. The larger-scale behavior is described in terms of spatial correlation of block-scale properties (Figure 4-3).

Each subfracture is assigned an average cross-fracture transmissivity T_f and storativity S . These depend on the stress field, which is a function of depth. T_f , S , and the geometry of intersection are assumed to completely define the hydrology on the scale of a fracture network.

Two different types of flow are simulated within realizations of this model: transient flow from constant-head packer tests (Figure 4-4a), and steady flow in response to a unit gradient across a block (Figure 4-4b). Transient packer-test responses are compared with actual packer tests, to validate the model. The block-scale conductivities and "steady-state" packer-test conductivity values provide data for a stochastic continuum model conditioned on packer test measurements.

Estimates of ϕ_w and S_w are calculated from the cross-block simulations, based on probabilistic relationships among subfracture transmissivity, flow aperture, and wetted surface. These estimates can be used for DPST and CN models, either as input or for comparison.

Simulation of population of fracture zones and large-scale fractures throughout large-scale region



Simulation of small-scale fractures for target-scale blocks

Spatial correlation among blocks results from zones plus network effects of larger fractures

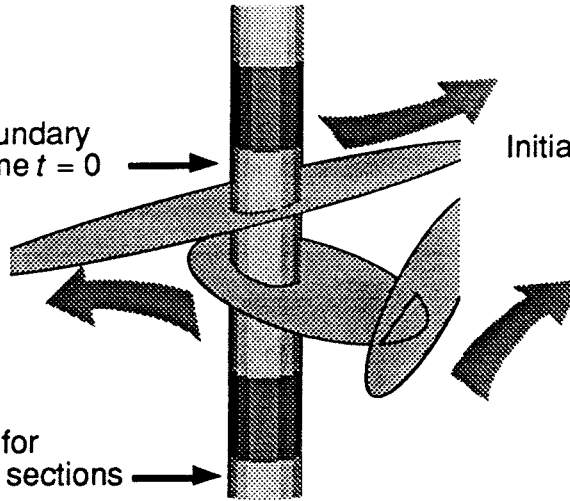
FIGURE 4-3
CONCEPTUAL MODEL FOR SPATIAL
CORRELATION AMONG BLOCKS

SKB/SKB91 DFNST

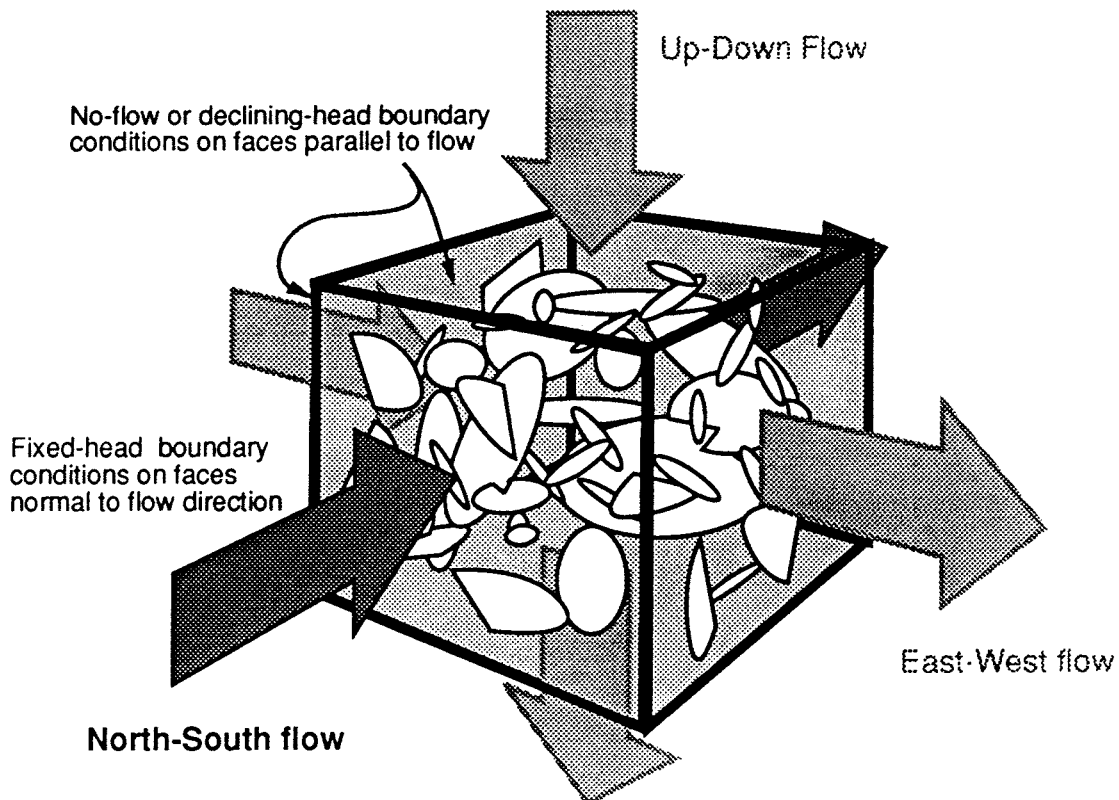
Constant-pressure boundary condition applied at time $t = 0$

Initial condition $p = p_i$

Group-flux $Q_{net} = 0$ for adjacent, packed-off sections



a) Simulation of constant-head packer tests



b) Simulation of cross-block flow (N-S, E-W, or Up-Down)

FIGURE 4-4
SIMULATIONS OF PACKER TEST AND BLOCK-SCALE FLOW
SKB-91/DFNST

4.4 Modelling Methodology

The derivation, validation and application of the DFN model to model flow in the Finnsjön rock mass was based on the FracMan DFN methodology, implemented in the FracMan/MAFIC modelling package (Figure 4-5). The main steps in the process were (Figure 4-6):

- Data analysis
- Monte Carlo simulation
- Calibration and validation
- Analysis of model predictions

The components of the methodology, and the FracMan/MAFIC package in particular, have been described most recently by Dershowitz *et al.* (1991a). The following description focuses on unique aspects of the present application of this methodology.

4.4.1 Derivation of parameters

Input data for the model include outcrop maps and scanline surveys, core data, and steady-state packer test interpretations K_p . Preliminary processing of these data yields distributions of tracelength λ_f , orientation, and packer test transmissivities T_p .

Fracture population statistics are estimated from these distributions with the Fracman module FracSys, which uses forward modelling to correct for various types of sampling biases and to estimate the underlying distributions of fracture size r_c , transmissivity T_f and conductive fracture intensity P_{32c} .

Estimation of the r_c distribution (§5.2) differed from previous analyses, in that λ_f data from a wide range of scales were considered simultaneously.

Estimation of the T_f distribution and P_{32c} used a modification of the OxFILET algorithm described by Dershowitz *et al.* The modification was needed to consider the effects of heterogeneity, and a vertically varying stress field, on the effective T_f values.

Data from outcrop maps, core, and packer tests were also used to estimate statistics for fracture system heterogeneity. These included termination statistics (§5.3.2), major feature intensity (§5.3.3), and statistics for the Nearest Neighbor model. The major feature frequency at depth

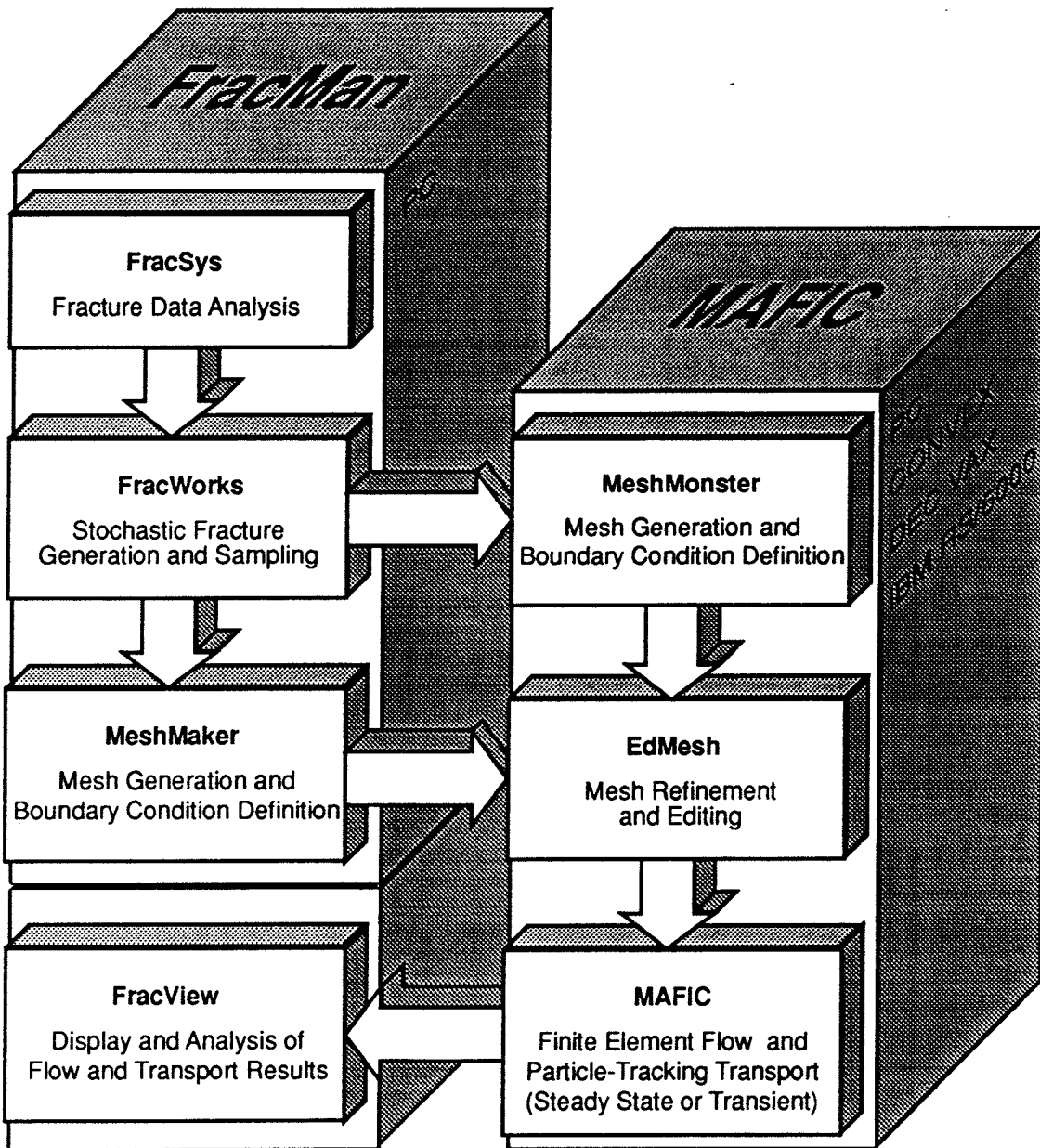


FIGURE 4-5
FRACMAN/MAFIC
DISCRETE FEATURE MODELING PACKAGE
 SKB-91/DFNST

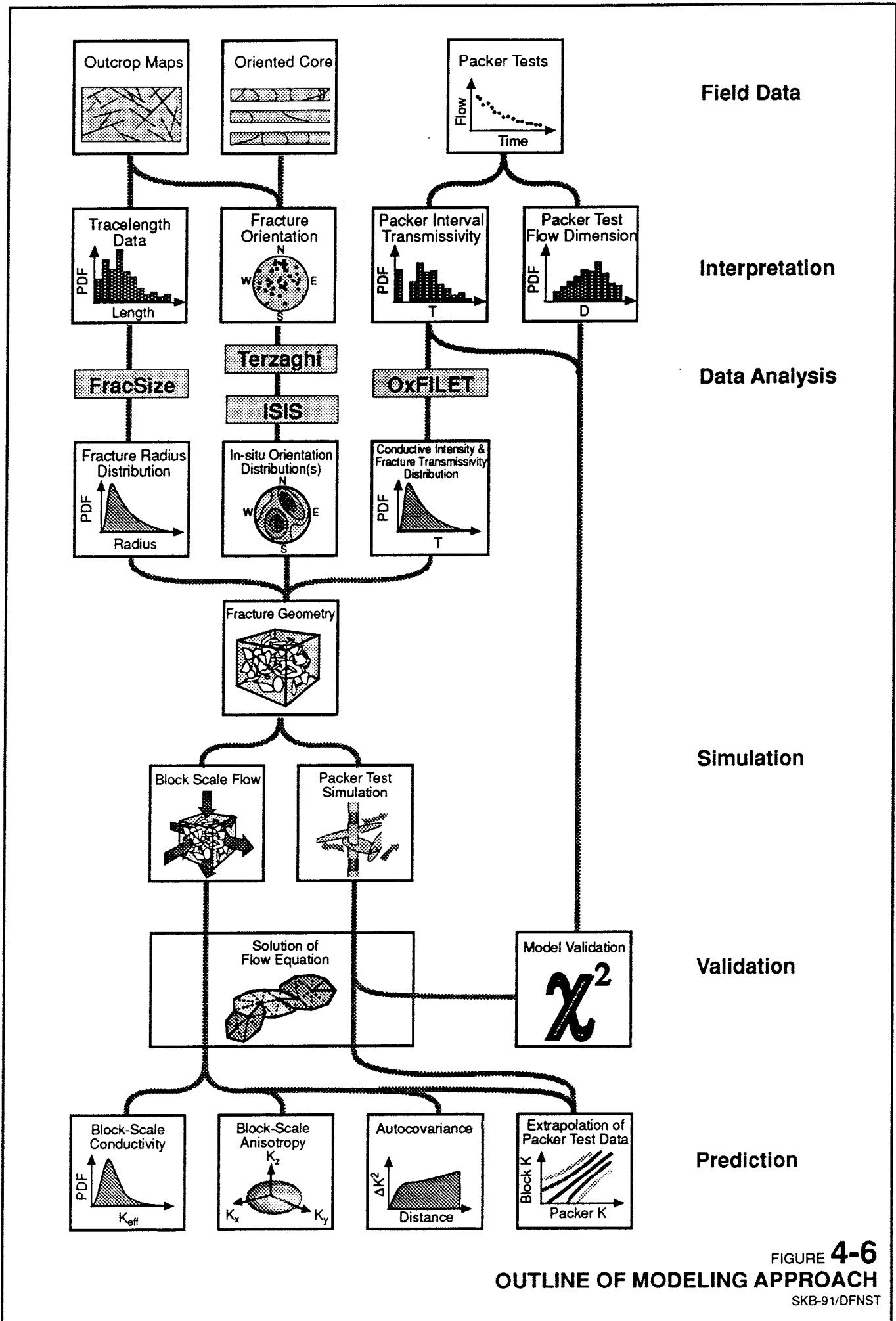


FIGURE 4-6
OUTLINE OF MODELING APPROACH
 SKB-91/DFNST

was estimated from core and packer test data, using a simplified version of the "fracture zone index" suggested by Olsson *et al.* (1989) to identify "fracture zones" in two boreholes. The estimate thus obtained was compared with borehole radar interpretations.

Due to insufficient surface data, the Nearest Neighbor statistics were also estimated from core data, by estimating the rate at which fracture intensity decays with distance from the most fractured sections of the identified "fracture zones." Details are given in §5.4.1.

4.4.2 Simulation

Realizations of the fracture population were produced by Monte Carlo simulation using the FracWorks module of the FracMan package (Dershowitz *et al.*, 1991a). Boundary geometries were defined using the module MeshMaker. Fracture and boundary geometries were combined by the Convex-based program MeshMonster, for each realization of the fracture population, to produce a triangular finite element mesh. Discretization of fractures into subfractures was performed as the preliminary stage of mesh generation.

The finite element mesh editor EdMesh (Geier, 1991) is used to apply specific boundary conditions and possibly to modify element properties (*e.g.* to apply stress-transmissivity relationships) prior to running each flow simulation. Assembly and solution of the transient or steady-state finite element equations is performed by MAFIC (Miller, 1990).

4.4.3 Validation approach

Derivation of a DFN model is based on analysis of geometric and hydrologic data, to give a set of statistics which describes fundamental properties of fractures in the DFN model, such as size and T_f . The various procedures for deriving these statistics are largely independent of each other. The transient, hydrologic behaviour of the DFN model depends upon the combination of the derived distributions of fracture properties. The ways in which these properties interact in the aggregate DFN model are complicated, and not directly constrained by the derivation methods.

Therefore the conceptual model can be validated, at least in part, by comparing the transient hydrologic behaviour predicted by the DFN model with the transient, constant-pressure test data. In the present study, GRF analysis was used to estimate *observed* distributions of T_{GRF} and flow dimension D_F , based on the transient data for three boreholes.

The constant-pressure tests were simulated in the DFN model, and the predicted transient responses were analyzed by identical methods, to produce *simulated* distributions of T_{GRF} and D_f . Statistical comparison of simulated and observed distributions provides a check on the validity of the model. In particular, the comparison of predicted and observed D_f is a fairly strong test of the fracture network characteristics.

This project was the first full application of this validation procedure for a 3-D DFN model. In practice complications arose, due to non-uniqueness in the estimation of the T_f distribution, which arose from limitations of the K_p dataset, as discussed in §5.6. The result was that the procedure was used partly as a "discrimination" procedure, to choose among several candidate models, as discussed in §6.3. However, the interpreted D_f were not used in the discrimination process, and therefore provide a dataset for partial validation of the model.

4.4.4 Prediction

The partly-validated DFN model was used to predict characteristics of the $K_s(x)$ field, plus ϕ_w and S_w , by steady-state flow simulations in several directions, in blocks of appropriate scale. Relationships between $K_{Moyes}(x)$ and the $K_s(x)$ field were estimated by simulating packer tests within the blocks and calculating statistics relating the simulated K_{Moyes} to the estimated $K_s(x)$ for a range of scales s .

A methodology developed for this purpose is described in §4.5. Due to scheduling conflicts, the algorithms and software necessary for incorporating these statistics into the SC model could not be fully developed. Therefore calculations were performed only for a preliminary DFN model, and not the final model. However, a partial implementation of the methodology using the final model produced some interesting results, as reported in §8.

The estimates of ϕ_w and S_w were obtained by postprocessing the block-scale flow simulations. Details of these calculations are given in §4.6.

4.5 Interface to the stochastic continuum model

The following sections describe a methodology for deriving a stochastic continuum model from a DFN description of a fractured rock mass. A major portion of this methodology was developed by S. Norman, in cooperation with the authors of the present report, in preparing the work plan (Norman and Geier, 1991) for the DFN/SC interface. Some changes have been made herein, to reflect late modifications in the DFN conceptual model. Although in the end only the DFN aspects of the interface were implemented, the methodology is given here as a

description of work done and for future reference. The methodology has some significant advantages, mainly that it gives the possibility to estimate more complex SC models, based on structural information, than can be estimated from packer test data alone. The method also gives the possibility to test the common assumption that packer tests are a direct measure of SC properties on a scale related to the interval length.

4.5.1 Basic definitions and assumptions

The SC model consists of a continuum defined in terms of a spatially variable conductivity tensor $K(x)$ which is related to an averaging volume V so that:

$$\langle u \rangle(x) = -K(x) \nabla \langle h \rangle(x) \quad (4-1)$$

where:

$$\langle h \rangle(x) = \frac{1}{|V(x) \cap \Omega_f|} \int_{V(x) \cap \Omega_f} h(\xi) dV \quad (4-2)$$

is an averaged head and:

$$U(x) = \langle u \rangle(x) = \frac{1}{|V(x)|} \int_{V(x) \cap \Omega_f} u(\xi) dV \quad (4-3)$$

is an average flow velocity, with:

- $V(x)$ = averaging volume centered at x
- ξ = location within the region of integration
- Ω_f = the 3-D region (not necessarily contiguous) consisting of the union of the hydraulic volumes of all fractures.
- $\Omega_f \cap V(x)$ = region of integration within both Ω_f and $V(x)$
- $|\Omega_f \cap V(x)|$ = volume of the region $\Omega_f \cap V(x)$
- dV = infinitesimal element of $\Omega_f \cap V(x)$

In the implementation of the SC model, the rock is modelled as a collection of blocks corresponding to averaging volumes. Each block has anisotropic conductivity characterized by K . In its most general form K has 9 components K_{ij} , 6 of which are independent: K_{11} , K_{12} , K_{13} , K_{22} , K_{23} , and K_{33} , and 3 determined by symmetry: $K_{21} = K_{12}$, $K_{32} = K_{23}$, and $K_{31} = K_{13}$.

Measurements of conductivity from packer tests yield local estimates $K_p(x)$. These are assumed to be probabilistically related to the $K(x)$. The relationship is assumed to be defined as follows. Let:

$$K_1(x), K_2(x), \dots, K_M(x) \quad (4-4)$$

denote the M components of K for a block of scale s centered at x .^[18] $M = 6$ for the full tensor, 3 if only the principal components are considered, or 1 if isotropy is assumed. Let:

$$K_{M+1}(x), K_{M+2}(x), \dots, K_{M+N}(x) \quad (4-5)$$

denote the results of N K_p measurements from packer intervals centered at x , of different lengths and/or inclination. The case $N = 1$ is of primary concern.

Together these constitute a coregionalization denoted by the $(M+N) \times 1$ vector K :

$$K(x) = [K_{M+1}(x), K_{M+2}(x), \dots, K_{M+N}(x)]^T \quad (4-6)$$

where the superscript T indicates transpose.

Estimation of the covariance matrix function requires that:

Assumption 1: A transformation can be found whereby the random vector $K(x)$ can be converted to a vector $Y(x)$ such that the values of the components $Y_i(x)$ of $Y(x)$ for all points in the domain are normally distributed.

Possible transformations are discussed in Appendix 1. The following assumption is adopted to simplify the analysis to the case $N = 1$:

Assumption 2: The results of 2 m and 3 m packer tests can be treated as realizations of a single process, independent of the variation in length and of the borehole inclination.

¹⁸ An alternative representation is to let K_1 be the octahedral conductivity $K_o = (K_{11} + K_{22} + K_{33})$ and let $\{K_2(x), \dots, K_M(x)\}$ represent $M-1$ independent anisotropy ratios $\{K_{11}/K_o, K_{22}/K_o, \dots\}$. Treatment of the alternative representations in the following analysis is for the most part identical. The above notation is understood to refer to the particular representation chosen.

If most packer tests of length $b_w < 3$ m are dominated by a single fracture, this assumption is reasonable. The methodology could be extended to divide the packer test data into different classes according to length and inclination, but this would increase the complexity of the analysis.

To verify the method of conditional simulation employed in HYDRASTAR, the following assumption is needed:

Assumption 3: The vector $Y(x)$ is locally stationary in the sense that $E[Y(x)]$ is approximately constant over distances comparable to the correlation length of $Y(x)$.

To allow simulation conditioned on the K_{Moyes} values, one of the following must be introduced:

Assumption 4a: The ratios $E[Y_j(x)]/E[Y_{M+1}(x)]$, $j = 1, 2, \dots, M$, calculated from the DFN model are independent of x .

Assumption 4b: The spatial trends in $E[Y_{M+1}(x)]$ predicted by the DFN model do not differ significantly from the local expectations for the transformed $K_{Moyes}(x)$ values, if the effects of zone location are taken into account.

Assumption 4b is equivalent to supposing that a simulation of the DFN model, with the major features fixed in their interpreted locations, would give the same expectation as observations. This assumption is preferable, but would require additional, semi-deterministic or conditional DFN simulations to verify. Assumption 4a would be simpler to test, based only on unconditional simulations.

4.5.2 Generation of independent realizations of the DFN model

With the chosen DFN conceptual model, spatial correlation in conductivity on a scale larger than the block scale results mainly from the continuity of major features between blocks. Up to the scale of the largest fractures ("minor features"), 50 m, correlation can also result from the continuity of single fractures between blocks. These features must be generated consistently between blocks if spatial correlation is to be estimated properly.

The preferred way to do this is to simulate the entire fracture population for the site simultaneously, and to choose blocks from within the large-scale simulation. However, for the

DFN model derived in §5, the number of conductive fractures in a 1 km cube is approximately 1.5×10^8 . Simulation of the entire population on the site scale would not be feasible.

Instead, an alternative, nested simulation scheme was developed. The populations of major features and fractures are divided into a number of classes, according to size. Only the largest features are simulated on the largest scale. The region is then subdivided in multi-domain fashion (Figure 4-7). A few subregions are chosen for simulation of the next largest size class, and so on down to the scale at which the complete fracture population (with $r_c \geq 1$ m) can be simulated. Blocks for simulation are chosen from within these smallest-scale generation regions. Specifics of the method (including issues relating to the use of finite generation regions) are described in Appendix 2.

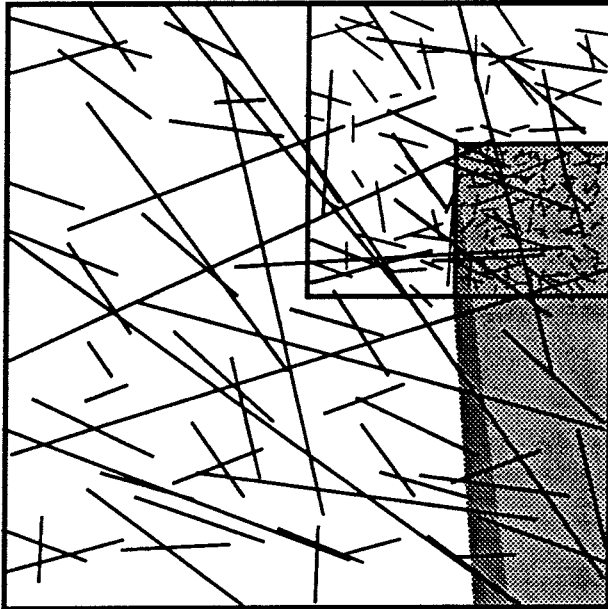
4.5.3 Estimation of the conductivity tensor

Previous applications of DFN models to evaluate EPM behavior have used a "permeameter" approach. In this approach, a head gradient $\nabla_x h$ is applied to a block of rock. The equivalent directional conductivity K_x is calculated from the net flux through the block in the direction of $\nabla_x h$. K_x is evaluated by applying $\nabla_x h$ in several directions, and estimating a best-fit tensor. Boundary conditions on the faces of the block parallel to the flow direction may be either declining-head (Long and Witherspoon, 1985) or no-flow (Axelsson *et al.*, 1990). The approach has two main problems:

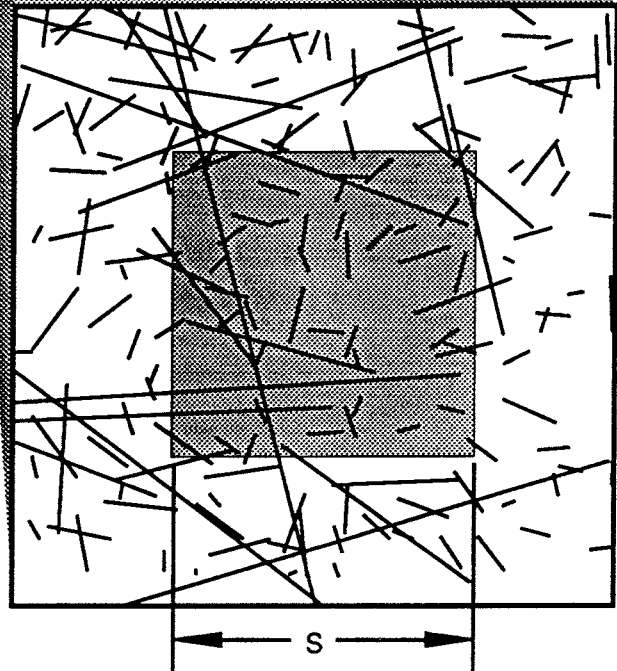
- Calculations of net flux through the blocks may depend strongly on choice of boundary conditions (*cf.* Long and Witherspoon, 1985; Axelsson *et al.*, 1990).
- Multiple block orientations are needed to measure a sufficient number of distinct K_x , to estimate \mathbf{K} , and decide if **minimal** criteria for EPM behavior are met. This means that multiple finite element meshes must be generated for each region simulated. For 3-D modelling, mesh generation is often more computationally intensive than subsequent flow calculations.

For the present study, an alternative to the permeameter approach was developed based on a suggestion by S. Norman (personal communication, 1991). The orientation of the simulated block is held constant. Numerous, distinct sets of boundary conditions are applied. The existence of an effective \mathbf{K} , is evaluated by calculating average head gradients

Largest fractures and/or fracture zones modelled on maximum generation region scale.



Full fracture population modelled only within smallest generation region scale.



Mesh Generation on Target Scale from Within Simulation Region

FIGURE 4-7
NESTED SIMULATION SCHEME FOR
PRODUCING SPATIAL CORRELATION
SKB-91/DFNST

$\nabla\langle h \rangle(x)$ and average flow velocities $\langle u(x) \rangle$ within *averaging volumes* smaller than the simulation region. Formulae for efficient calculation of $\nabla\langle h \rangle(x)$ and $\langle u(x) \rangle$ from the DFN model are given in Appendix 3. Equivalent conductivity is estimated by fitting K_e to the model given by Eq. 4-1, as described in Appendix 4. If a block has a true, "effective" K_e , then Eq. 4-1 must be satisfied for *every* possible set of externally applied boundary conditions. However, for practical reasons only a limited number of sets of boundary conditions can be simulated for each block.

Advantages of the averaging-volume approach are:

- Off-diagonal components of K_e are obtained without reorienting the simulation mesh.
- Multiple estimates of K_e for several scales s , may be produced with a single simulation.
- The use of volume-averaged quantities reduces bias due to boundary effects.

In the preliminary stages of the present study, both averaging-volume and permeameter approaches were used, to allow comparison between the methods.

4.5.4 Packer test simulations

A method for simulation of constant-head packer tests in boreholes was developed in the feasibility study (Geier and Axelsson, 1991). 2 m packer tests are simulated in both vertical and inclined boreholes. The packer tests are analyzed both by Moyes' formula and by GRF analysis. The GRF analyses are used to validate the model by comparison with GRF analyses of field tests. The K_{Moyes} values are appropriate for derivation of the SC model, as the main part of the database for conditional simulation consists of K_{Moyes} estimates.

Five packer tests are simulated within each 40-50 m block. Specific boundary conditions for the simulated packer tests are discussed in §6.1.

4.5.5 Covariance matrix function estimation

Each block simulation produces one estimate each of the K_i , $i = 1, 2, \dots, M$. Estimates of K_{M+1} are obtained at each packer test location within a block. These form the basic dataset for estimation of the covariance matrix function.

As a first step, the transformation $K(\mathbf{x}) \rightarrow Y(\mathbf{x})$ must be estimated. For the trial simulations there was no vertical trend in the model, so the transformation is simplified. Approximately Gaussian behavior was obtained by a logarithmic transformation.

Preliminary analysis indicated that, for the components K_i , $i = 1, 2, \dots, M$ (corresponding to the components of the tensor \mathbf{K}), a component-by-component transformation would be invalid because the tensor nature of these components would be violated. Instead a tensor log transformation was used which maps a tensor onto a tensor, for the first M components of $K(\mathbf{x})$. This is defined in Appendix 5. For the component K_{M+1} corresponding to the K_{Moyes} estimates, a scalar logarithmic transformation is suitable, although the problem is complicated by the intervals below the measurement threshold, as is the case with the field data.

For further statistical inference the transformed vectors $Y(\mathbf{x})$ must follow a multinormal distribution. This is assessed by calculation of the multivariate skewness and kurtosis as defined by Mardia *et al.* (1979) and by χ^2 and Kolmogorov-Smirnov tests on the components of $Y(\mathbf{x})$. To simplify this analysis, the transformation $K(\mathbf{x}) \rightarrow Y(\mathbf{x})$ includes a Mahalanobis transformation (see Mardia *et al.*), giving $E[Y(\mathbf{x})] = \mathbf{0}$ and resolving $Y(\mathbf{x})$ to principal components with standardized variance. Details are given in Appendix 5.

The covariance matrix function (CMF) is estimated from the transformed data pairs $\{Y(\mathbf{x}_1), Y(\mathbf{x}_2)\}$ over the range of lag separations $\mathbf{h} = \mathbf{x}_2 - \mathbf{x}_1$. There is some restriction on the admissible pairs $\{\mathbf{x}_1, \mathbf{x}_2\}$ due to the nested simulation scheme used to generate the fracture population (§4.5.2). Data pairs $\{Y(\mathbf{x}_1), Y(\mathbf{x}_2)\}$ are inadmissible if the separation distance $|\mathbf{h}|$ is less than the scale on which significant correlation can be produced by the fractures smaller than the minimum size generated in the smallest block containing both \mathbf{x}_1 and \mathbf{x}_2 . As a heuristic rule, if r_{ij} is the minimum fracture size for the smallest block containing both \mathbf{x}_1 and \mathbf{x}_2 , then:

$$\|\mathbf{h}\| > c_h r_{ij}, \quad c_h > 2 \quad (4-7)$$

If $c_h < 2$ a fracture smaller than r_{ij} could connect between the measurement points, so clearly there would be a chance of correlation. The best value of $c_h > 2$ may be determined by sensitivity analysis. However, to save time it is reasonable to say that if the admissibility criterion is set at $c_h \geq 5$, correlation produced by fractures smaller than r_{ij} will be negligible.

A nonparametric estimate of the covariance function $C_f(\mathbf{h})$ is obtained from the differences between admissible pairs $\{Y(\mathbf{x}_1), Y(\mathbf{x}_2)\}$ as follows:

The *lagspace* is defined as a vector space containing all lags h between admissible pairs. The lagspace is divided into discrete *lag classes*, or "bins," denoted L_n . Bins are defined in spherical coordinates, with logarithmic radial spacing, to provide for greater resolution for small magnitudes of h .

Admissible data pairs are identified from the DFN output, and are sorted into the appropriate lag classes. The elements of the covariance matrix are estimated as:

$$\Gamma_{kl}(L_n) = \frac{1}{N_{L_n}} \sum_i \sum_{h_j \in L_n} Y_k(x_i + h_j) Y_l(x_i) \quad (4-8)$$

where the summations are taken over all admissible pairs and where N_{L_n} is the number of admissible data pairs in class L_n .

The set of estimators $\Gamma_{kl}(L_n)$ over all L_n gives a nonparametric estimate of the covariance matrix function $C_{kl}(h)$.

4.6 Interface to the stream tube model

The DFN model for the estimation of SC model parameters was extended to furnish estimates of flow porosity ϕ_w and specific wetted surface S_w and S_b (wetted surface per unit volume flowing water, and per unit bulk volume, respectively). This section gives equations for estimating these parameters from DFN model geometry and single-fracture properties for which working models are estimated in §5.8. The estimates of ϕ_w and S_w can be used as alternative estimates of parameters for the DPST and CN models. The other main source of estimates of these values are tracer tests, which are subject to a wide variety of interpretations due to uncertain flow geometry. The S_b estimates were produced by intermediate calculations, and are presented for the sake of interest.

Two types of estimates were produced for ϕ_w , S_w and S_b :

- Flux-weighted averages
- Histograms giving the sums for specific ranges of element flux.

The flux-weighted averages are directly related to the quantities used in the FARF31 stream tube model (Norman and Kjellbert, 1991). The histograms are produced to give more detailed information. Among other things these may be useful for comparison to correlations of S_w and ϕ to channel flowrates used in the CN model. The following set of flux ranges was chosen:

$$\begin{aligned}
 L_1: & \quad \{ Q > 10^4 \text{ m}^3/\text{s} \} \\
 L_2: & \quad \{ 10^5 < Q \leq 10^4 \text{ m}^3/\text{s} \} \\
 L_3: & \quad \{ 10^6 < Q \leq 10^5 \text{ m}^3/\text{s} \} \\
 L_4: & \quad \{ 10^7 < Q \leq 10^6 \text{ m}^3/\text{s} \} \\
 L_5: & \quad \{ 10^8 < Q \leq 10^7 \text{ m}^3/\text{s} \}
 \end{aligned}$$

Both flux-weighted and histogram estimates were calculated by making slight modifications (Appendix 3) to the volume-averaging program that was developed for the SC interface. Limited Monte-Carlo simulation within the program was used to account for the large uncertainty in the relations of ϵ_v and s_w to ϵ_p .

4.6.1 Porosity

The flux-weighted porosity was estimated as:

$$\phi_Q = \frac{1}{V} \cdot \frac{\sum_{i=1}^N A_i \epsilon_{vi} Q_i}{Q_{net}} \quad (4-9)$$

where:

ϵ_{vi}	= the void aperture of the <i>i</i> th element, related probabilistically to the element ϵ_i .	
Q_i	= the magnitude of flowrate through the <i>i</i> th triangular element	[L ³ /T]
A_i	= the area of the <i>i</i> th element.	[L ²]
Q_{net}	= the net flow passing through the averaging volume.	[L ³ /T]
V	= the volume of the averaging region.	[L ³]

The porosity histogram estimates were calculated for each flux bin L_k as:

$$\phi_k = \frac{1}{V} \sum_{L_k} A_i \epsilon_{vi} \quad (4-10)$$

The probabilistic relationship of ϵ_v to ϵ_h is estimated in §5.8.2.

4.6.2 Wetted surface

Flux-weighted estimates of the quantities S_b and S_s were calculated for each averaging volume as:

$$S_{bQ} = \frac{1}{V} \cdot \frac{\sum_{i=1}^N A_i S_{vi} Q_i}{Q_{net}} \quad (4-11)$$

$$S_{wQ} = \frac{S_{bQ}}{\phi_Q} \quad (4-12)$$

where:

s_{wi} = the fracture specific wetted surface s_{wf} of the i th element,
related probabilistically to the element ϵ_h . [L⁻¹]

The specific surface histogram estimates were calculated for each flux interval L_k as:

$$S_{sk} = \frac{1}{V} \sum_{L_k} A_i s_{wi} \quad (4-13)$$

$$S_{wsk} = \frac{S_{sk}}{\phi_k} \quad (4-14)$$

An estimate of the probabilistic relationship of s_{wf} to ϵ_h is obtained in §5.8.3.

5 DATA ANALYSIS FOR THE FRACTURE NETWORK MODEL

5.1 Statistical homogeneity

A major question is, "Are surface data representative of the rock at depth?" Since the only subsurface fracture data from Finnsjön is taken from unoriented core, the three main types of evidence regarding variation in the fracture population with depth are:

- Fracture frequency
- Dip angles α , from the vertical holes
- Fracture infillings

Fracture infilling data are qualitative, and require a multivariate interpretation approach which would be beyond the scope of the present study. Therefore dip angle data and fracture frequency are the most suitable for analysis of heterogeneity with depth.

5.1.1 Dip angle data

Since there are no *complete* orientation data from subsurface, a question is whether the orientations from at surface can be applied at depth. To test possible changes in the fracture orientation distribution with depth, dip angle distributions $f(\alpha)$ for parts of 2 vertical boreholes (KFI 06 and KFI 11) were used to characterize the variability of the fracture orientation with depth.

Because dip angles are only one component of the bivariate orientation population, there is no possibility to prove that the orientation population within any given rock unit is homogeneous. However, there *is* a possibility to disprove such a hypothesis. This follows from the fact that each component of a bivariate variable defines a specific univariate distribution. To accept the validity of a specific bivariate distribution, a *minimum* requirement (necessary condition) is that the individual components both follow the expected univariate distributions. Likewise if a bivariate distribution is homogeneous, the univariate distributions of both components must be homogeneous. Thus to show that a bivariate distribution is heterogeneous, it is sufficient to show that one component is heterogeneous.

The data were divided into rock below, above, and within Zone 2. These classes were further subdivided at increments of 50 m depth. Comparisons of $f(\alpha)$ for different regions were made by calculating Kolmogorov-Smirnov (KS) and χ^2 statistics.

These comparisons (Appendix 6) revealed no obvious pattern in the data. Denoting the dip distributions above, within, and below Zone 2 as $f_+(\alpha)$, $f_2(\alpha)$, and $f_-(\alpha)$, respectively, the following hypotheses were rejected at the 5% significance level, based on both KS and χ^2 tests:

$$f_+(\alpha) = f_2(\alpha)$$

$$f_+(\alpha) = f_-(\alpha)$$

$$f_2(\alpha) = f_-(\alpha)$$

Little similarity was also found between sections within any single subregion. An exception, but a weak one, is the rock below Zone 2. The $f_-(\alpha)$ for the first 12 m below Zone 2 (338-350 m) is found to be the same as for the bottom 50 m, at the 5% level, for borehole KFI 11. Since these data are all from less than 65 m below Zone 2, the possibility cannot be excluded that the rock below Zone 2 is also locally heterogeneous, on a scale similar to the heterogeneity seen above and within Zone 2. Very few adjacent 50 m intervals show similarity. Thus:

- The fractures within and above Zone 2 are statistically heterogeneous in terms of dip angle, when each subregion is considered as a unit.
- The fractures below Zone 2 *may* be statistically homogeneous, but evidence is weak.
- The fracture dip distribution is heterogeneous, for any line sample 100 m long.

For the reasons stated above, the conclusions of heterogeneity for dip angle can be extended to the full orientation, although a conclusion of homogeneity would not necessarily have been extensible. A possible explanation is that fractures are organized in preferred orientations within and around fracture zones. This is expected from widely held concepts of fracture zone structure. Based on radar data (§2.2.1), the average spacing of major or minor zones is 20-25 m.

In conclusion, the dip data do not support the use of orientation data from surface, for modelling the rock at depth with a single, homogeneous orientation distribution. However, the dip data also do not indicate any systematic change in orientation with depth. The heterogeneity within subregions indicates that there is no reason to distinguish among the subregions in terms of fracture orientation. The orientation data from surface could possibly be extended to depth based on more complex models relating fracture orientation to major feature orientation, but the necessary data and modelling tools to implement such a model

were lacking at the outset of this study. Appropriate modelling tools are currently under development.

An assumption that a single, homogeneous orientation distribution applies at all depths is apparently not justified. However, numerical experiments (*e.g.* Long 1984; Dershowitz 1985), have shown that so long as a range of orientations is present, the precise orientation distribution is less important for network connectivity and effective conductivity than properties such as conductive fracture intensity P_{32c} , transmissivity distribution, and locational correlation. Fortunately the latter quantities are more easily estimated from the available borehole data from Finnsjön, as described in §5.3-6.

5.1.2 Fracture frequency data

As mentioned in §2.2.2, Ahlbom and Tirén (1991) observed that in the southern block the fracture frequency is about 3 m^{-1} , showing no decrease with depth. The northern block above Zone 2 has a lower fracture frequency (1.5 m^{-1}) both in boreholes and fracture surveys, but below Zone 2 the fracture frequency is similar to that in the southern block. The average coated fracture frequency in Zone 2 is 5.2 m^{-1} , but if the two high-transmissivity zones at the upper and lower boundaries are excluded, the coated fracture frequency is nearly the same as below Zone 2. Thus, except for upper part of the northern block, which has relatively low fracture frequency, the "rock mass" within the Finnsjön block has a rather uniform coated fracture frequency of 3 m^{-1} .

Estimates of conductive fracture frequency f_c by Andersson and Lindqvist (1988) predict that f_c is higher for the rock mass above Zone 2 (roughly 1 m^{-1}) than below (roughly 0.6 m^{-1}). Geier and Axelsson (1991) gave a comparable "effective" f_c estimate (0.7 m^{-1}) for the rock below Zone 2. For Zone 2, excluding the most conductive horizons, the f_c estimates by Andersson and Lindqvist (1988) are close to the values for below Zone 2.

Inspection of core logs from KFI 05, 06, and 09 (Ahlbom *et al.*, 1986) and KFI 11 shows that the variation in coated and "sealed" fracture frequencies within subregions above and below Zone 2 is comparable to the difference between subregions. The relatively highly fractured sections (spaced 20-50 m apart, and corresponding to minor zones) are of comparable magnitude above and below Zone 2; the main differences appear to be in the less fractured rock between minor zones. This suggests that the local-scale heterogeneity is of greater significance than the difference in "average" fracturing between subregions.

The above observations suggest that a reasonable model of the fractured rock at Finnsjön may be constructed by treating the rock as a single unit in the vertical direction, with strong local heterogeneity corresponding to the fracture zones on various scales. A fractal model is one possibility, but this was not considered due to a lack of adequate modelling tools at the outset of this study. (The appropriate tools have since then been implemented in FracMan).

Lateral heterogeneity is evident in the upper 200 m of the Finnsjön block, but due to the shortage of subsurface geometric data there is no point in modelling lateral variations in the size and orientation distributions.

A refinement of the model could be to analyze the spatial variation in:

- Frequency of fracture zones (minor and major),
- Conductive fracture intensity P_{32} (based on packer test data).

This approach, by emphasizing the stronger aspects of the dataset, would be more justified than discriminating between subregions based on details of the core data. However, this analysis would most likely lead to a multi-domain DFN model. The simpler, single-domain model was chosen for the present study, due to its substantial advantages in terms of the DFN/SC model interface (§4.3.1).

5.2 Size distribution for major and minor features

The fracture size analysis for the feasibility study (Geier and Axelsson, 1991) considered both cell maps and local-scale lineament maps, but considered each scale separately. This analysis was extended in the present study to consider all four scales (regional, semiregional, and local lineament maps, and detailed fracture maps) simultaneously, using a modified version of the FracSize data analysis module (Appendix 7). This analysis assumes that the fractures are equidimensional (circular) and that size is independent of orientation.

The version of FracSize used included probabilistic censoring. This accounts for the tendency to overlook smaller features on each mapping scale, so that features close to the minimum size mapped are undersampled. This tendency is well-known to field geologists, but there has been little or no systematic study of the resulting sampling bias. In the present study the sampling probability was assumed to be zero for tracelengths $\lambda < \lambda_{min}$ (the smallest recorded trace), and to increase linearly in the range λ_{min} to $c_\lambda \lambda_{min}$, the tracelength above which perfect sampling was assumed to occur. Due to the lack of relevant data for imperfect censoring effects, c_λ was treated as a scale-independent value to be estimated in the fitting process.

The data were analyzed in terms of a power-law distribution:

$$f_r(r_e) = \frac{b_r - 1}{r_{min}} \left(\frac{r_{min}}{r_e} \right)^{b_r}, \quad r_e \geq r_{min} \quad (5-1)$$

where r_{min} is an arbitrary lower limit (to avoid singularity in the distribution) set smaller than the smallest semi-tracelength measured, and b_r is the power-law exponent. This form was used in the feasibility study, because it is implied by the observed power-law distribution for tracelength.

Figure 5-1 shows the K-S statistic KS_r (comparing simulated and observed λ) as a function of b_r and c_λ . Estimated confidence intervals are given by curves of constant KS_r . KS_r is fairly insensitive to variation of c_λ in the range 2 to 6, for values of b_r close to 3.1, so this is a good estimate of b_r , even if the form of the censoring probability differs from the model in Eq. 5-1.

The estimate of $b_r \approx 3.1$ differs significantly from the earlier estimate of 1.89, which was produced using only two mapping scales and an effective $c_\lambda = 1$ (perfect sampling above the censoring limit). The new value encompasses more mapping scales and gives a better fit to the data, partly due to the more reasonable, probabilistic censoring assumption.

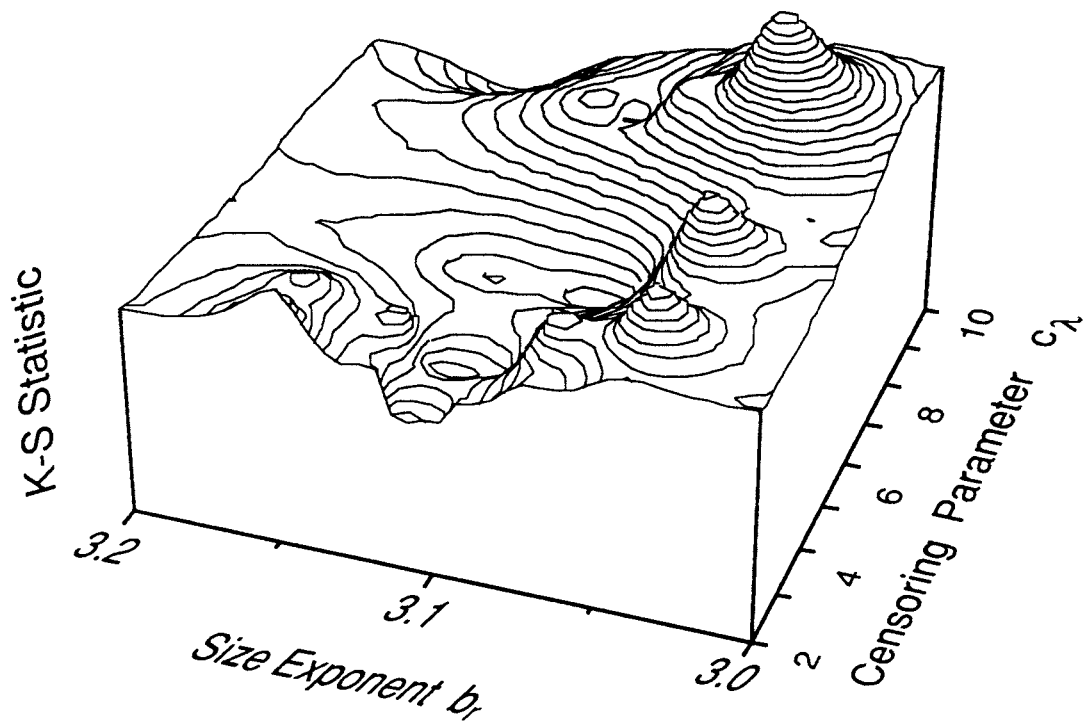


FIGURE **5-1**
**ESTIMATION OF OPTIMUM FIT FOR
 SIZE DISTRIBUTION PARAMETERS**

SKB/SKB91 DFNST

5.3 Geometry of major features

The geometric properties which must be characterized to model the major features include:

- Location
- Orientation
- Size
- Intensity
- Termination

Location of the major features is assumed to be random but conditioned by termination statistics. Major feature transmissivity need not be characterized, because the transmissivity of these features results from clustering of the fractures. A single size distribution is assumed to hold for features on all scales. The size distribution for the large-scale features is the part of this distribution above 50 m. The following sections describe derivation of the remaining properties of the major features.

5.3.1 Orientation distribution

The orientation distribution for major features was based on the following assumptions:

Assumption 1: The orientation distribution for all features down to the scale $r_c = 25\text{m}$ is assumed to be represented at least approximately by the orientation distribution for the major zones that have been identified at the site by Andersson *et al.* (1991).

Assumption 2: The volume of the Finnsjön block is assumed to have been fully investigated with regard to fracture zones on the scale of the identified zones. Thus the issue of directional sampling bias is explicitly neglected.

Assumption 3: The identified fracture zones are interpreted as consisting of approximately "subzones," each of which is approximately subparallel to the parent zone.

Assumption 4: The relative number of subzones within an identified zone is assumed to be in proportion to the interpreted thickness of the zone.

These assumptions are simplistic, but more complicated assumptions are not justified, because there are little or no directional data for features/fractures in the size range $10\text{ m} \leq r_c \leq 200\text{ m}$.

For the subvertical sets, strikes could be taken from lineament maps, but dips are mostly uncertain. This approach would also give no information about the subhorizontal set.

Compilation of a bootstrap dataset based on the above assumptions was extremely simple. For each fracture zone, the normal vector was calculated from the data of Andersson *et al.* (1991). The normal vector directions were weighted in proportion to the interpreted zone thicknesses w_i . Table 5-1 gives the dataset used for simulations. Note that this dataset was used to generate the orientations of the major features themselves, not of the fractures clustered around the major features.

Table 5-1. Normal vector directions and weights for fracture zone bootstrap dataset.					
Zone	Orientation ^[19]		Normal Vector		Weight
	Strike	Dip	Trend	Plunge	
1	N30E	75SE	300	15	0.041
2	N28W	16SW	62	74	0.206
3	N15W	80SW	75	10	0.103
4	N50W	65SW	40	25	0.021
5	N50W	60SW	40	30	0.010
6	N55-65W	60SW	30	30	0.010
7	N55W	60SW	35	30	0.010
8	N50W	90	220	0	0.010
9	N10W	15SW	80	75	0.103
10	NW	85SW	45	5	0.010
11	N5W	35W	85	55	0.175
12	N	90	85°	0	0.052
13	N30E	75SE	300	15	0.041
14	NW	90	45	0	0.206

* Orientation estimated from lineament map.

¹⁹ Data from zone definitions of Andersson *et al.* (1991)

5.3.2 Termination measures

Termination statistics for both major features and fractures were calculated from lineament maps and cell maps. Statistics for both lineaments and fractures are discussed here.

Termination statistics are expressed in the following forms:

$$t_p = \frac{t_{fi}}{I_i} \cdot 100\% \quad (5-2)$$

$$t_{\%} = \frac{t_{fi}}{t_{fi} + t_{ri}} \cdot 100\%$$

where:

- t_p = termination probability
- $t_{\%}$ = termination percentage
- t_{ri} = number of fracture terminations in intact rock per unit area
- t_{fi} = number of fracture terminations at fractures per unit area
- I_i = number of fracture intersections per unit area mapped

Table 5-2 gives termination probabilities and termination percentages for the three mapping scales considered. Termination probability is used in the Enhanced Baecher (EB) Model and, optionally, in the Nearest-Neighbor (NN) Model. Termination percentage is used in the Baecher Revised Terminations (BART) Model.

Table 5-2. Termination statistics for Finnsjön site.		
Mapping Scale	Termination Probability	Termination Percentage
Cell maps	42.5	36.8
Local lineament maps	50.4	88.4
Semiregional lineament maps	27.5	73.1

The termination statistics are apparently scale dependent. This indicates that the fracture system is not self-similar with respect to a change in scale. However, for the detailed-scale cell maps the fractures are considered to be atypical, and for the lineament maps there may be bias in that terminating lineaments are more likely to be classed as local-scale lineaments, so there is reason to doubt the accuracy of these statistics.

Although there is considerable variation in the estimates of termination statistics on different scales, clearly a large number of features terminate at intersections with other features, so some termination would be desirable in the final model. The observed values of t_p are less variable than the values of t_x . Therefore it is preferable to use a model based on t_p , such as the EB or NN model.

5.3.3 Intensity

Lineament maps provide one type of data for estimating the major feature intensity, P_{32z} . However, the maps do not include any lineaments of length less than about 200 m, and it is unlikely that lineaments of approximately this length or less will be noticed, due to the limited resolution. This is a problem, since the power-law distribution with $b, \approx 3.1$ implies that a large fraction of P_{32z} will come from the smaller zones.

Therefore P_{32z} was estimated from borehole data rather than lineament maps. The major-feature frequency, f_m is the number of major or minor fracture zones crossing a borehole, per unit length of hole. Since most of the boreholes are approximately vertical, this is primarily a measure of the intensity of subhorizontal major features.

Major features were inferred from single-hole data using a simplification of the "fracture zone index" concept, developed within the Stripa Project (Olsson *et al.*, 1989). The fracture zone index is a weighted sum of various types of single-hole data, including geophysical, hydrological, and fracture frequency data, where the weights are determined by multivariate regression.

Olsson *et al.* (1989) found that two properties were strongly, positively correlated with most of the geophysical indicators:

- Normalized log hydraulic conductivity
- Normalized log fracture frequency

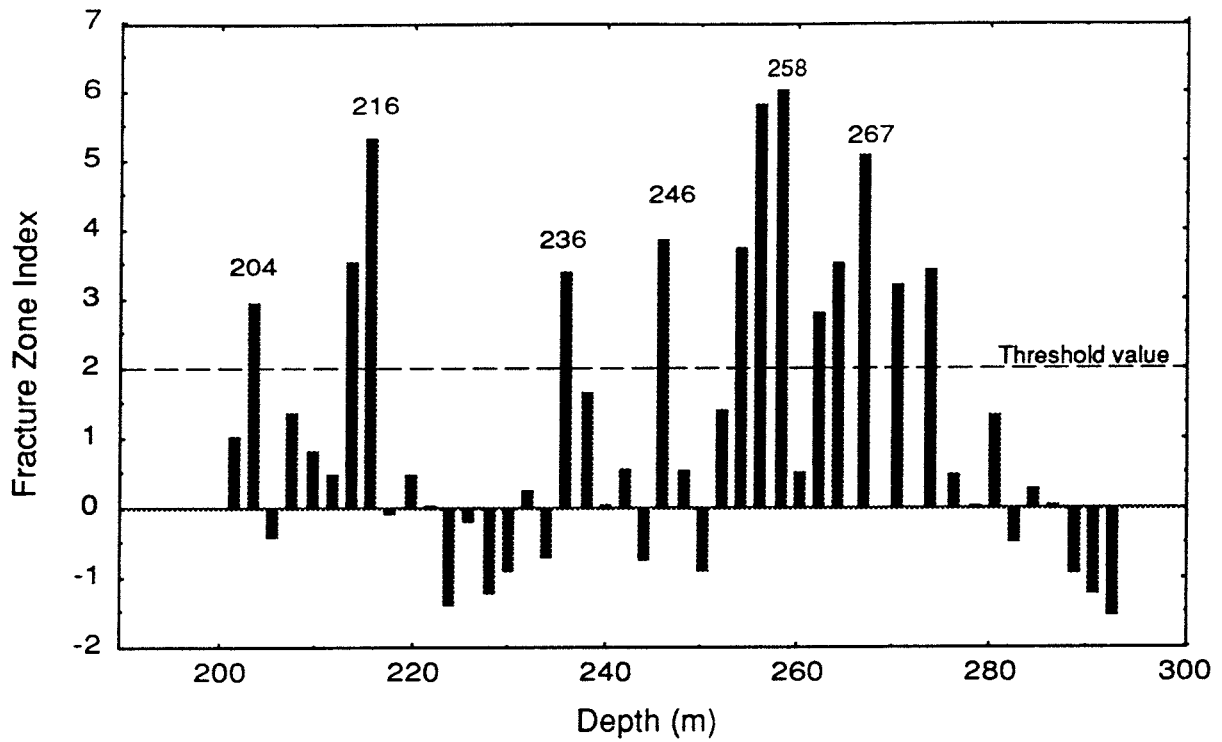
An index which included both of these was an excellent indicator of fracture zones, as corroborated by extensive cross-hole testing.

The scope of the present analysis did not allow inclusion of geophysical logging data. Instead, a weighted sum was taken of the two above-mentioned quantities. The weights for these estimated by Olsson *et al.* were both close to 1. Therefore the simplified fracture zone index was calculated simply as the sum of the two. Intervals for which this sum exceeded 2 were classed as "fracture zones."

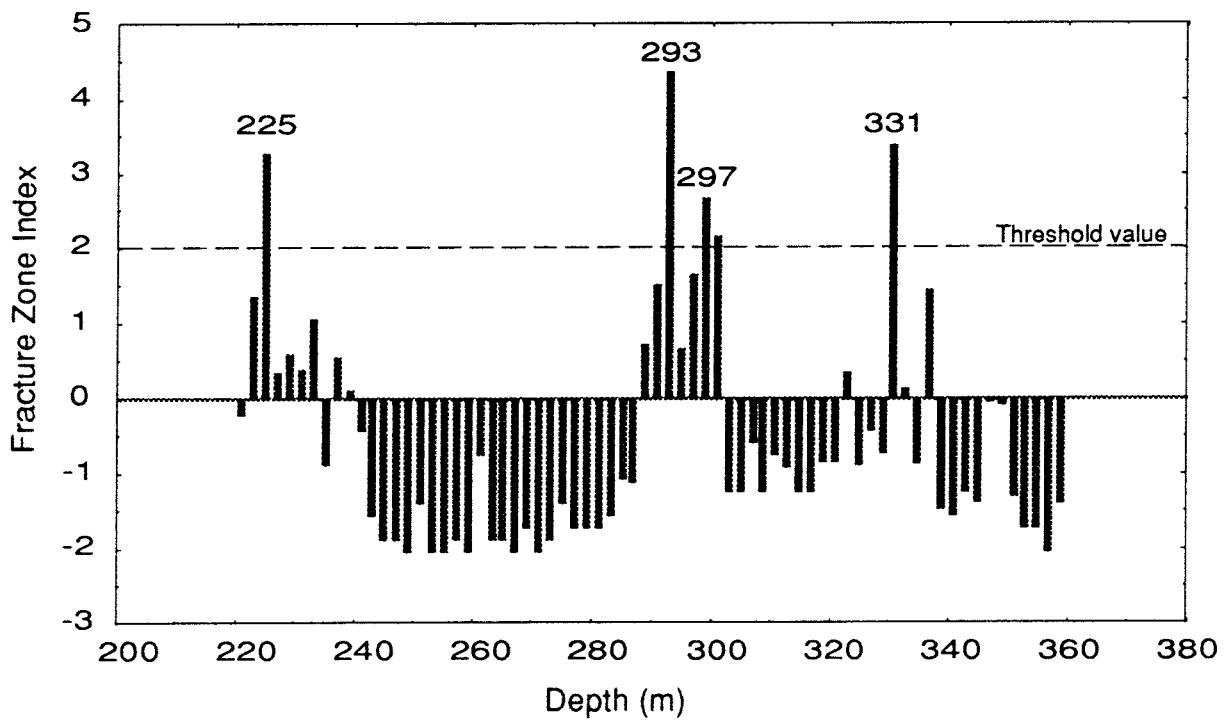
Two boreholes were analysed, KFI 06 and KFI 11. These were the holes for which core data was already on hand. Only the intervals within and below Zone 2 were considered. Intervals for which the index exceeded 2 were identified. Figure 5-2 shows plots of this index for the two holes, indicating the positions of the inferred zones.

In a total of 229 m of hole, 10 zones were identified, giving an estimate of the frequency as $f_m \approx 10/(229 \text{ m}) = 0.044 \text{ m}^{-1}$. This was viewed as a very rough estimate, as only a fraction of the available data were analysed, and due to the limitations of the method. However, this frequency compares well to the interpreted frequencies of minor borehole radar reflections (§2.2.1) across the site, the average of which is 0.049 m^{-1} (Table 2-2).

The geometric factor $C_p = P_{32}/f_z$ for a vertical borehole was estimated by FracMan simulation of the borehole sampling process as 1.23. For an observed zone frequency of 0.040 per m, this gives an estimated zone intensity of $0.049 \text{ m}^2/\text{m}^3$. The variation of radar reflection frequencies (0.024 to 0.077 m^{-1}) in Table 2.2 is an indication of the degree variability of the zone intensity within the site.



a) Borehole KFI 06



b) Borehole KFI 11

Fracture Zone Index = Standardized Joint Frequency + Standardized Log Conductivity

FIGURE 5-2
IDENTIFICATION OF FRACTURE ZONES
BASED ON "FRACTURE ZONE INDEX"

SKB/SKB91 DFNST

5.4 Geometry of minor features (fractures)

Although distinct fracture sets have been identified at surface at the site, the DFN model did not make use of this because of:

- Questionable applicability of these data at depth (§5.1.1).
- Bias of vertical holes means that there is no information on the T distribution of subvertical joint sets.

The use of bootstrap methods to generate fracture orientations allows simulation of irregular, multimodal orientation distributions, including possible multiple sets. For analysis of fracture size and location, all fractures were treated as a single population.

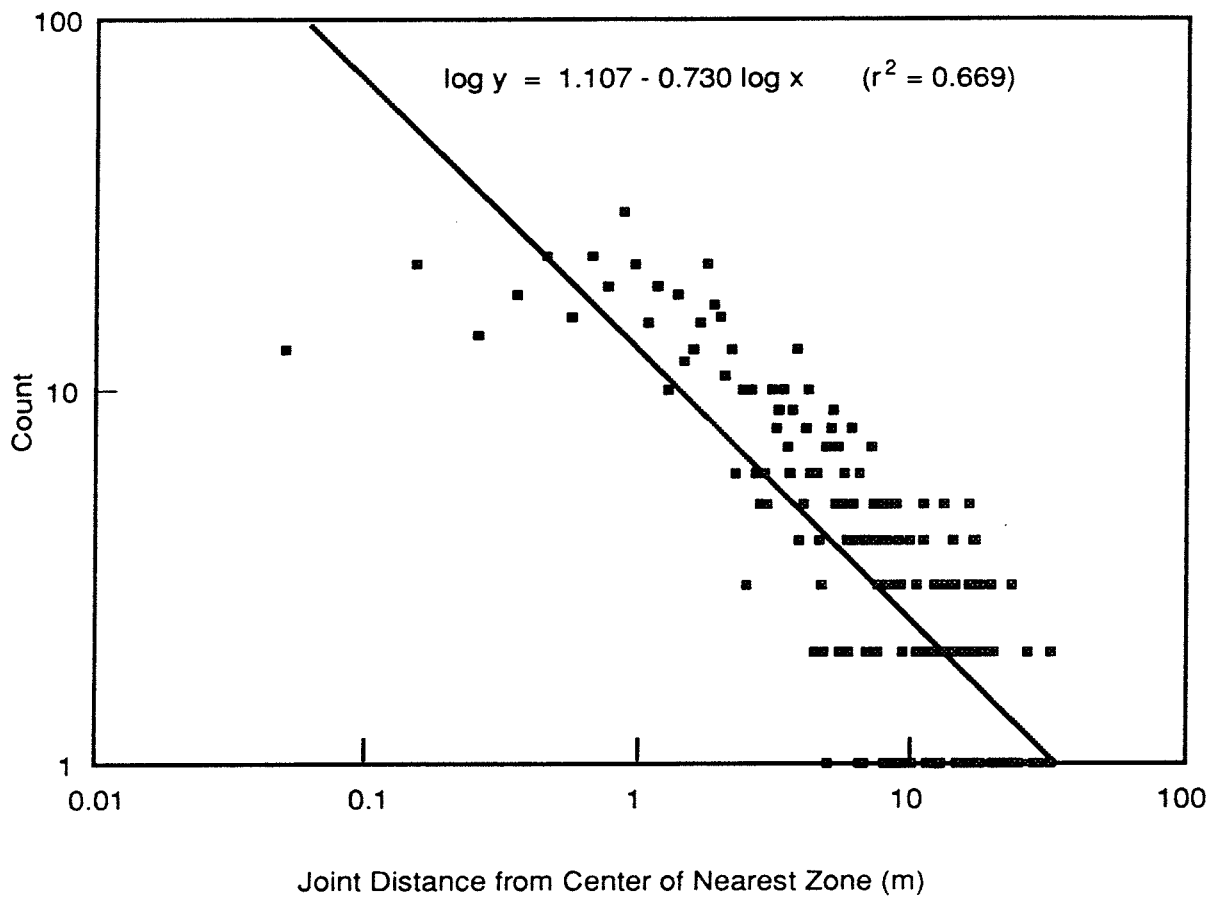
5.4.1 Location

Nearest-Neighbor (NN) statistics were estimated from core data. An estimate of the NN exponent b_{NN} is given by the slope of a log-log plot of fracture frequency *vs.* distance from the nearest "major" fracture.

Zones were identified from the data for KFI 06 and KFI 11 as described in §5.3.3. The center of the zone's intersection with the borehole was taken as the point with the highest fracture frequency, as seen in the core. Figure 5-3 shows a log-log plot of fracture count *vs.* distance from the center of the nearest zone. For the modelling of the Finnsjön site, it was assumed, due to an algebraic error, that b_{NN} was one minus the slope of this line, giving $b_{NN} = 1.73$. As shown in Appendix 8, a better estimate of b_{NN} is in this case 0.73.

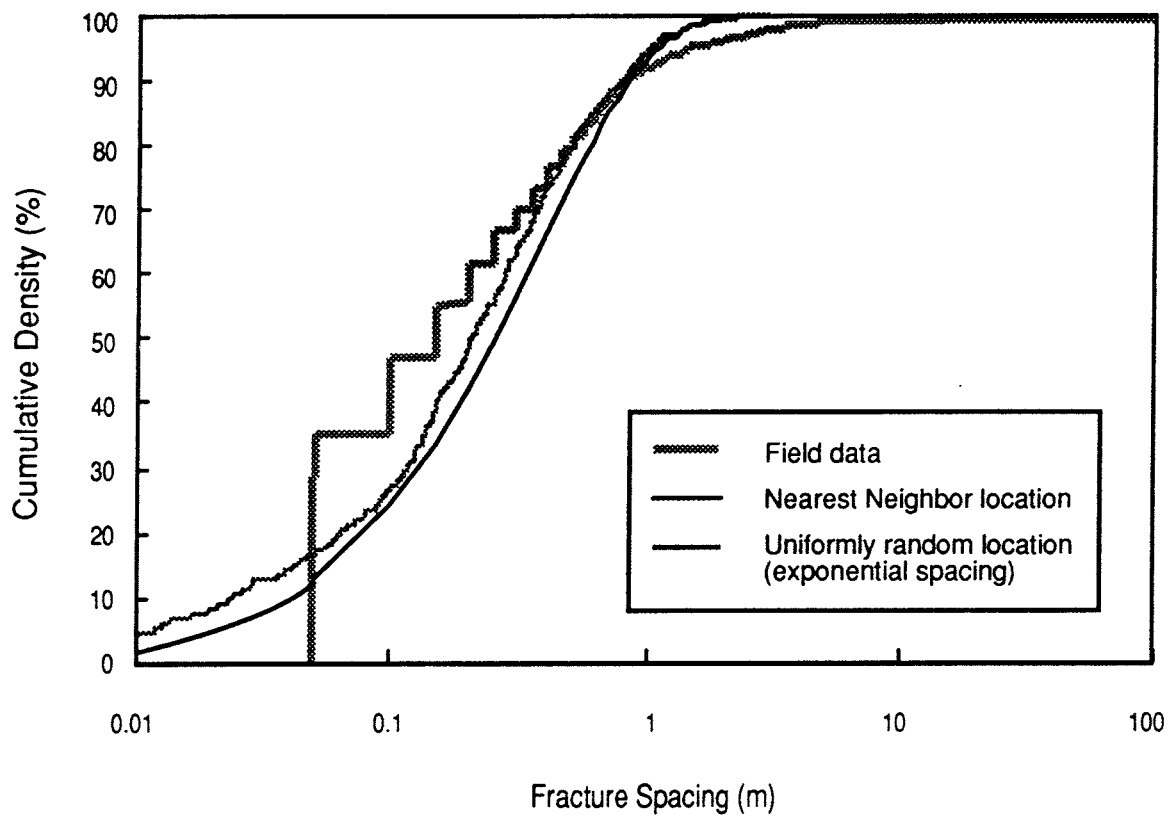
The NN model with $b_{NN} = 1.73$ was compared with an alternative model with uniformly random fracture locations, by comparing the observed distribution of fracture spacing with the distributions predicted by each model. For the model with uniformly random locations, the CDF of fracture spacing can be calculated analytically. The fracture spacing distribution for the NN model was estimated by FracMan simulated borehole sampling, using $b_{NN} = 1.73$, and a 200 m vertical borehole.

Figure 5-4 compares the two models with the spacing of coated fractures in boreholes KFI 06 and KFI 11. The NN model gives the better fit to the sample at the lower end of the CDF function. Both models predict a lower frequency of large values of spacing (> 2 m) than is seen in the sample. The steps in the sample CDF correspond to the core logging precision of 5 cm.



Analysis based on data from boreholes KFI 06 and KFI 11.

FIGURE **5-3**
ESTIMATION OF NEAREST NEIGHBOR STATISTIC
 SKB/SKB91 DFNST



Based on data for coated fractures in boreholes KFI 06 and KFI 11.

FIGURE **5-4**
ANALYSIS OF FRACTURE SPACING DISTRIBUTION

SKB/SKB91 DFNST

Using a bin spacing such that the PDF for the random model was equally divided into 10% intervals, the following χ^2 statistics were calculated:

NN model:	$\chi^2 = 9.85$ (6 degrees of freedom)
Random model:	$\chi^2 = 45.0$ (8 degrees of freedom)

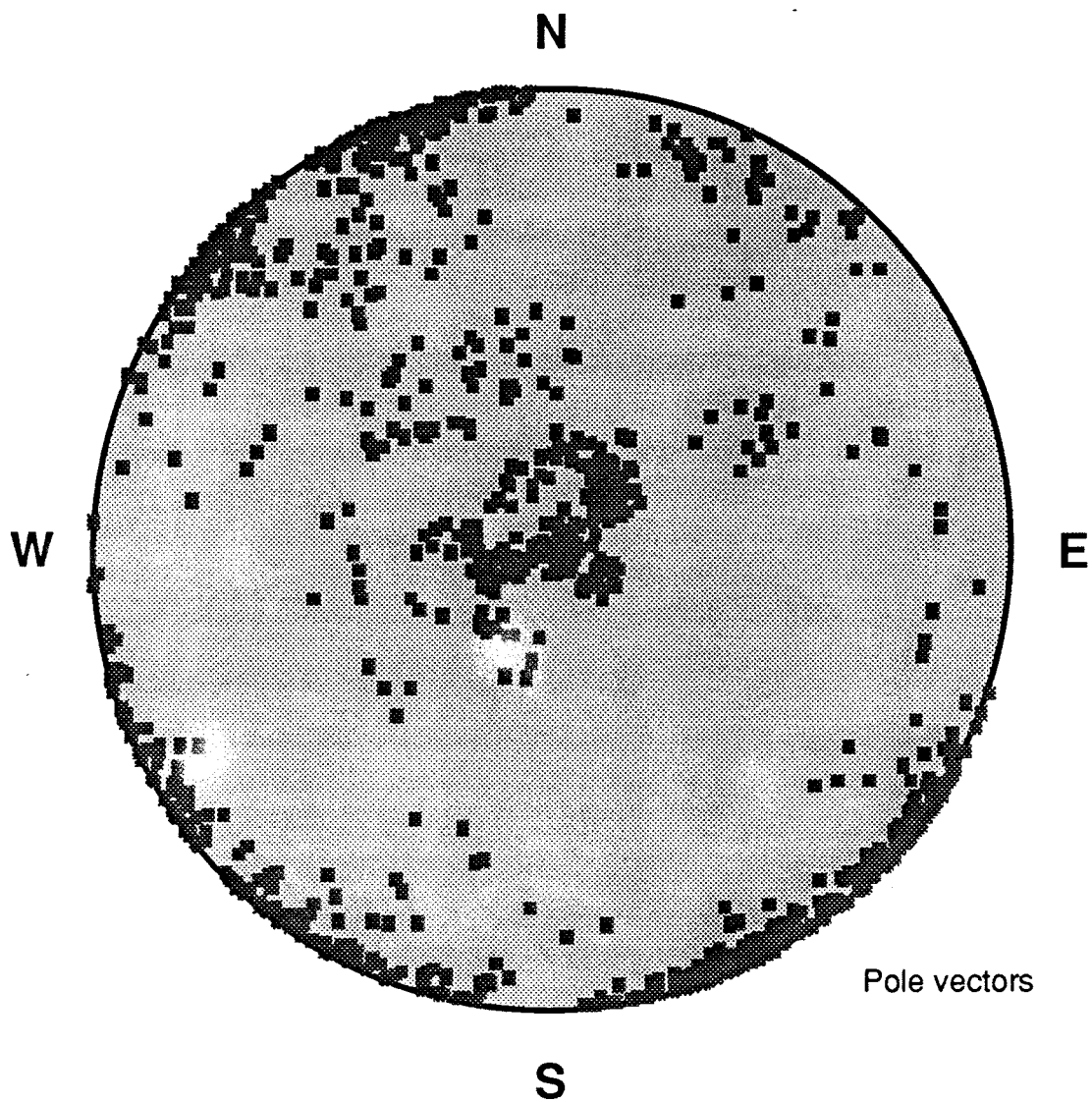
Based on the χ^2 statistic, the NN model was accepted at the 10% confidence level. The random model was rejected at the 1% level.

However, subsequent analysis (see Appendix 8) shows that fracture spacing is an insensitive indicator of fracture location, whereas fracture *frequency* distribution provides a much more discriminating measure of non-uniform location models. Simulated sampling of Nearest-Neighbor models, for a range of values of b_{NN} , indicates that a value closer to $b_{NN} = 0.73$ does indeed give a better model of the fracture population at Finnsjön, than the value $b_{NN} = 1.73$ which was used in the present study. Unfortunately this reanalysis could not be incorporated within the scope of the present study. The probable effect is that, in the model used, the distinction between "good rock" and fracture zones is somewhat stronger than in the actual rock. However, the reanalysis shows that the model which was used gives a markedly superior description of the site, relative to a uniform model for fracture location.

5.4.2 Orientation

The bootstrap orientation dataset compiled previously by Geier and Axelsson (1991) was retained for the present stage of the analysis, despite the weaknesses discussed above. The possibility of improving this dataset was considered, but due to the lack of any consistency in dip angles with depth (§5.1.1) this was not considered to be worthwhile. The uncertainty regarding the orientation distribution is therefore very high. The sensitivity of the results can be tested by comparison with a uniform distribution of orientation.

Figure 5-5 shows the dataset used for bootstrap simulation. Correlations of size to orientation could increase the significance of the orientation distribution. However, in the well-connected fracture system at Finnsjön, the effect of such a correlation is expected to be low relative to the effects of locational autocorrelation.



Pole vectors

FIGURE **5-5**
DATASET FOR FRACTURE ORIENTATION
SKB/SKB91 DFNST

5.4.3 Termination

Termination statistics for the fracture population were estimated from the cell maps near KFI 11, as described in §5.3.2.

5.5 Single fracture aperture variation

5.5.1 Fractal dimension for surface roughness

The aperture variation for single fractures was assumed to follow the fractal model of Wang *et al.* (1989) discussed in § 3.1.3. Mechanical aperture variograms from the Stripa Channeling experiment were digitized and matched to type curves based on the solution of Wang *et al.*, to estimate the fractal dimension for aperture (Appendix 9).

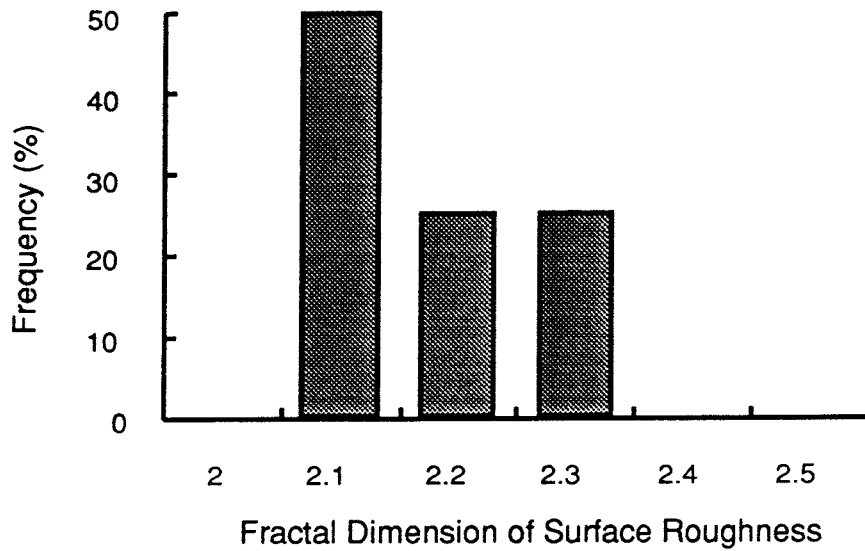
Figure 5-6 shows a typical variogram type-curve match and the distribution of best-fit fractal dimensions. The results of this analysis were uncertain due the limited resolution (5 cm sampling interval) of the fracture aperture measurements, relative to the apparent correlation length for aperture. For a few of the fracture profiles, values of D , anywhere from 2.1 and 2.5 give nearly equally good fits. Since a unique fractal dimension could not be estimated with certainty for any of the variograms, a *triangular distribution* for D , was assumed. This distribution is commonly used when little is known about a random variable (Benjamin and Cornell, 1970). The values of the parameters chosen were:

$$D_{mlv} \text{ (most likely value)} \approx 2.15$$

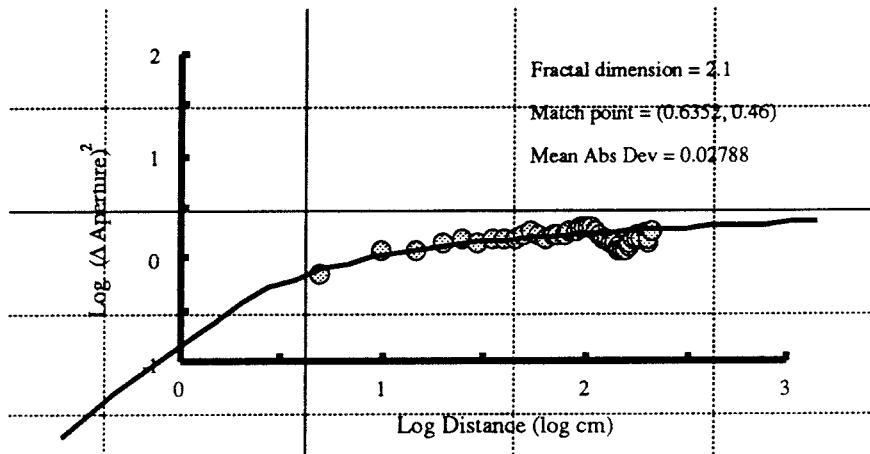
$$D_{min} \text{ (minimum value)} = 2.0$$

$$D_{max} \text{ (maximum value)} = 2.5$$

The values of D_{min} and D_{max} given are the theoretical limits for a fracture surface without overhangs (Brown, 1987). The value of D_{mlv} was roughly the median of the estimates obtained by curve fitting (Figure 5-6a)



a) Distribution of estimated fractal dimension for fracture surface roughness (based on 12 aperture profiles from the Stripa Channeling Experiment, Abelin et. al, 1990)



b) Example of variogram type-curve match

FIGURE 5-6
 FRACTURE APERTURE VARIABILITY
 SKB/SKB91 DFNST

5.5.2 Variance of physical aperture

The fractal model for aperture variation also requires a standard deviation for fracture roughness, at some reference scale. Abelin *et al.* (1990) give log mean and log standard deviation ratio of arithmetic standard deviation to arithmetic mean, for aperture (averaged over 5 cm, the reference scale), as given in Table 5-3. The average $\sigma_e/\mu_e = 1.2$. The corresponding normalized standard deviation for surface height, used in Brown's (1987) model, is:

$$\frac{\sigma_h}{\mu_h} = \frac{1.2}{\sqrt{2}} \quad (5-3)$$

This is assumed to represent the variation in roughness height over a scale of about 5 cm. The fractal model gives larger variance for larger scales, and smaller variance for smaller scales.

5.6 Steady-state packer test data interpretation

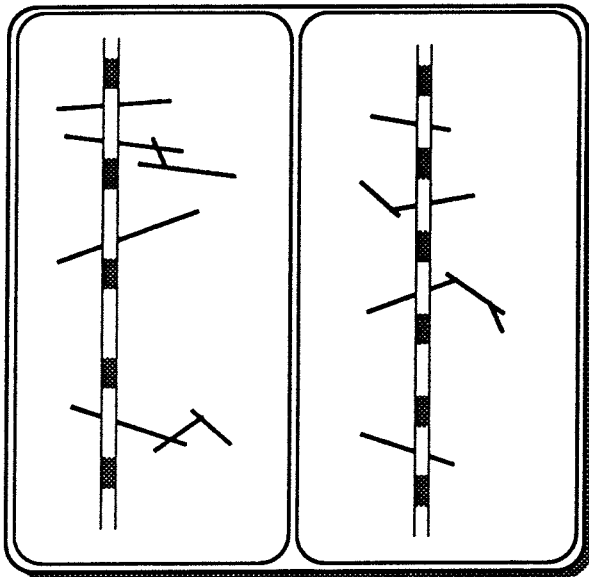
The steady-state packer test data from the site were analyzed to estimate the distribution of T_f . The analysis was done using OxFILZ, an extension of the OxFILET algorithm (Dershowitz *et al.*, 1991a) which allows simulation of:

- Nonuniform models for fracture location,
- Effects of a stress gradient with depth,
- Irregular sampling programs (*e.g.* changes in $T_{\text{threshold}}$ or b_w between boreholes).
- Simultaneous effects of single-fracture roughness and network effects.

The OxFILZ algorithm is illustrated in Figure 5-7; Appendix 10 gives a complete description.

Table 5-3. Aperture variation in a single fracture.				
Mean Log ϵ_m (mm ² /cm)	Standard Deviation Log ϵ_m (mm ² /cm)	Mean of ϵ_m μ_ϵ (mm ² /cm)	Standard Deviation of ϵ_m σ_ϵ (mm ² /cm)	$\sigma_\epsilon/\mu_\epsilon$
-0.224	0.458	1.041	1.101	1.058
0.091	0.508	2.444	2.938	1.202
-0.212	0.675	2.054	4.168	2.030
0.655	0.477	8.259	9.157	1.109
0.034	0.418	1.719	1.656	0.964
0.438	0.446	4.645	4.774	1.028
0.059	0.459	2.002	2.123	1.060
0.014	0.384	1.527	1.369	0.897
0.197	0.570	3.724	5.345	1.435
0.520	0.492	6.291	7.248	1.152
-0.167	0.402	1.045	0.973	0.931
0.122	0.533	2.812	3.622	1.288
Mean of $\sigma_\epsilon/\mu_\epsilon$				1.179
Standard deviation of $\sigma_\epsilon/\mu_\epsilon$				0.295

Single-Hole Packer Tests from One or More Fixed-Interval-Length Testing Programs



Database for interval locations

Model for transmissivity of each interval:

Number of fractures intersecting interval is random number N from location model.

Network length $N_L = 1 + n_L$; n_L from Poisson distribution.

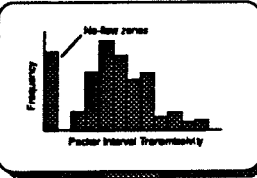
Transmissivity T_i due to the i th fracture intersecting the interval:

$$T_i^{-1} = [T_b(T_{f0})]^{-1} + \sum_{j=1}^{n_L} T_{fj}^{-1}$$

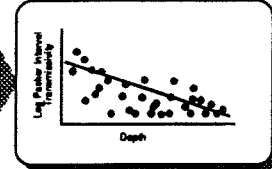
where T_b (T_{fj}) is the at-borehole vs. cross-fracture transmissivity relationship, and T_{fj} is a value from the cross-fracture distribution, corrected for stress effects.

$$\text{Interval transmissivity } T_p = \sum_{i=1}^N T_i$$

Distribution of Packer Interval Transmissivity



Trend in Packer Interval Transmissivity with Depth



Guess parameter set: $\{f_c, \mu_{\log T_f}, \sigma_{\log T_f}, b_{T_N}\}$

Iterative Search

Comparison of simulated and observed packer tests in terms of K-S statistic for T_p and trend of $\log T_p$ with depth.

OK

Final parameter set: $\{f_c, \mu_{\log T_f}, \sigma_{\log T_f}, b_{T_N}\}$

FIGURE 5-7
OxFILZ PACKER TEST INTERPRETATION ALGORITHM
SKB-91/DFNST

5.6.1 At-borehole vs. cross-fracture transmissivity

The OxFILZ analysis requires as input the relationship between at-borehole transmissivity T_b and cross-fracture transmissivity T_f . This relationship was estimated based on 100 single-fracture simulations, using the fractal model for surface roughness, as derived above. Boundary conditions for these simulations were as illustrated in Figure 5-8. Details are given in Appendix 11. Figure 5-9 shows a plot of the T_b vs. T_f . The following parameters were estimated to describe this relationship:

$$\mu_{\log T_f/T_b} = E[\log T_f - \log T_b] = 0.16 \quad (5-4)$$

$$\sigma_{\log T_f/T_b} = \sqrt{\text{Var}[\log T_f - \log T_b]} = 0.52 \quad (5-5)$$

The prediction that T_b is typically higher than T_f is somewhat surprising. However, the value of $\mu_{\log T_f/T_b}$ is small and the main effect of aperture variation, for this model, is to increase the apparent variance of T_f . For the simulations the proportionality T_f/T_b was assumed to be lognormally distributed, using the above parameters.

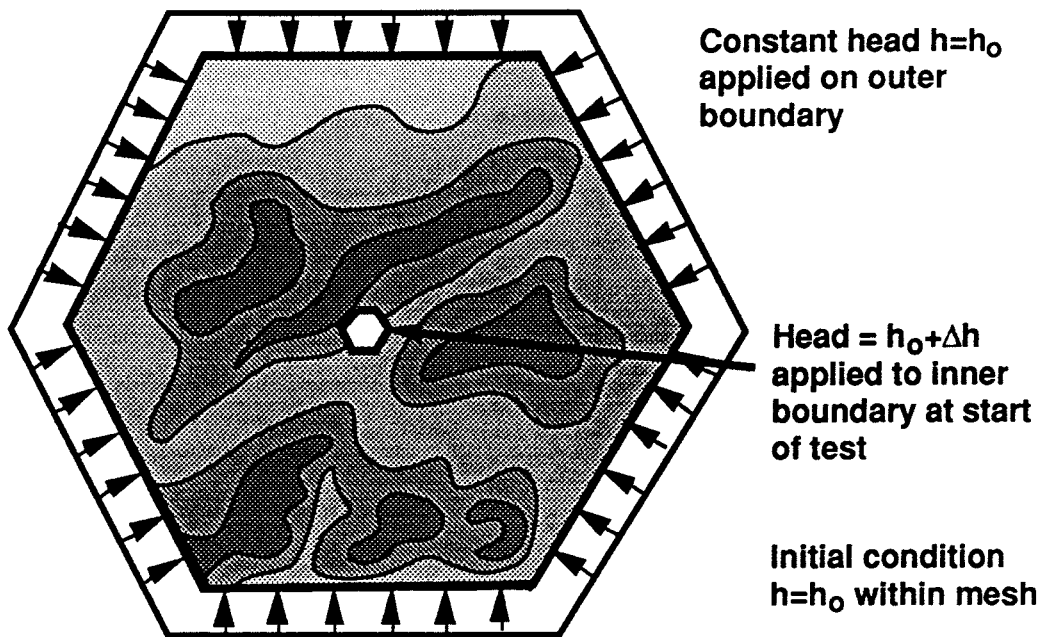
5.6.2 Simultaneous estimation of fracture transmissivity distribution, conductive fracture frequency, and depth-transmissivity dependence

The OxFILZ code was applied to estimate the combination of the following parameters:

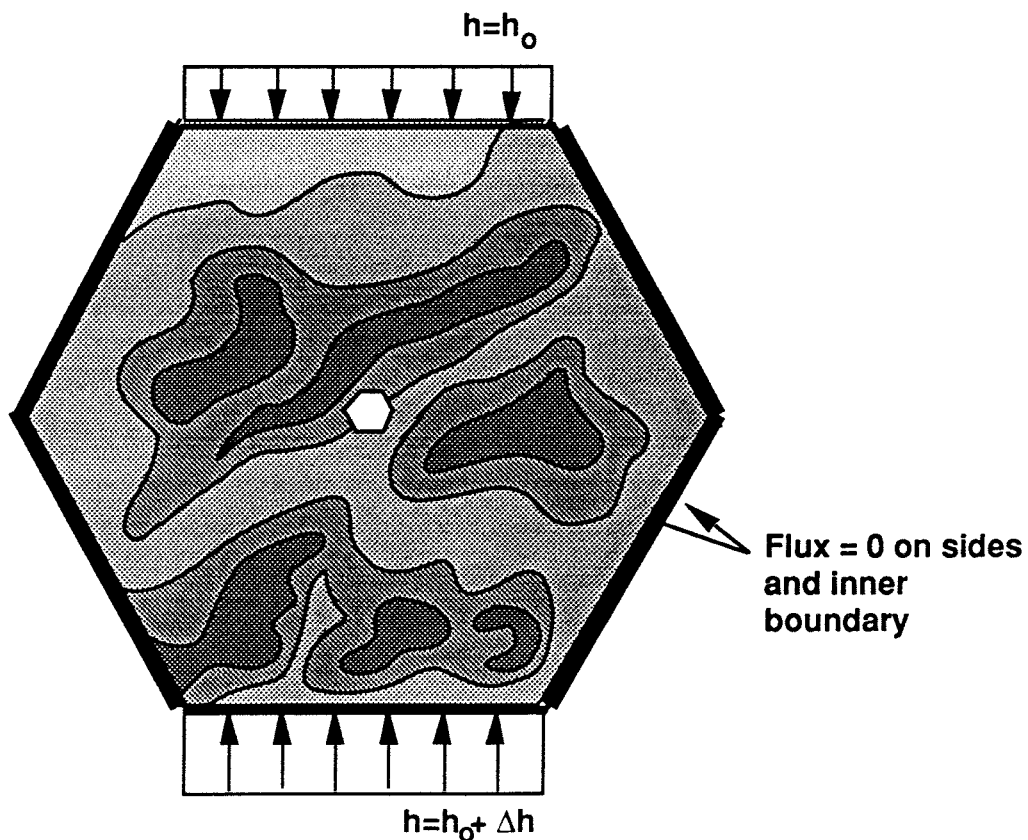
$\mu_{\log T_f}$	=	Mean of $\log T_f$
$\sigma_{\log T_f}$	=	Standard deviation of $\log T_f$
f_c	=	Conductive fracture frequency
b_{Tn}	=	Normal stress vs. transmissivity parameter (§3.2.1)

which gave an optimum fit to the steady-state transmissivity measurements in terms of a weighted combination of:

- Kolmogorov-Smirnov statistic for comparison of the simulated and observed distributions of interval transmissivity T_p , and
- Ratio of simulated and observed gradients of $(\log T_p)$ with depth.



a) At-borehole measurement of transmissivity



b) Cross-Fracture Measurement of transmissivity

FIGURE 5-8
BOUNDARY CONDITIONS FOR ESTIMATION OF
AT-BOREHOLE VS. CROSS-FRACTURE TRANSMISSIVITY

SKB/SKB91 DFNST

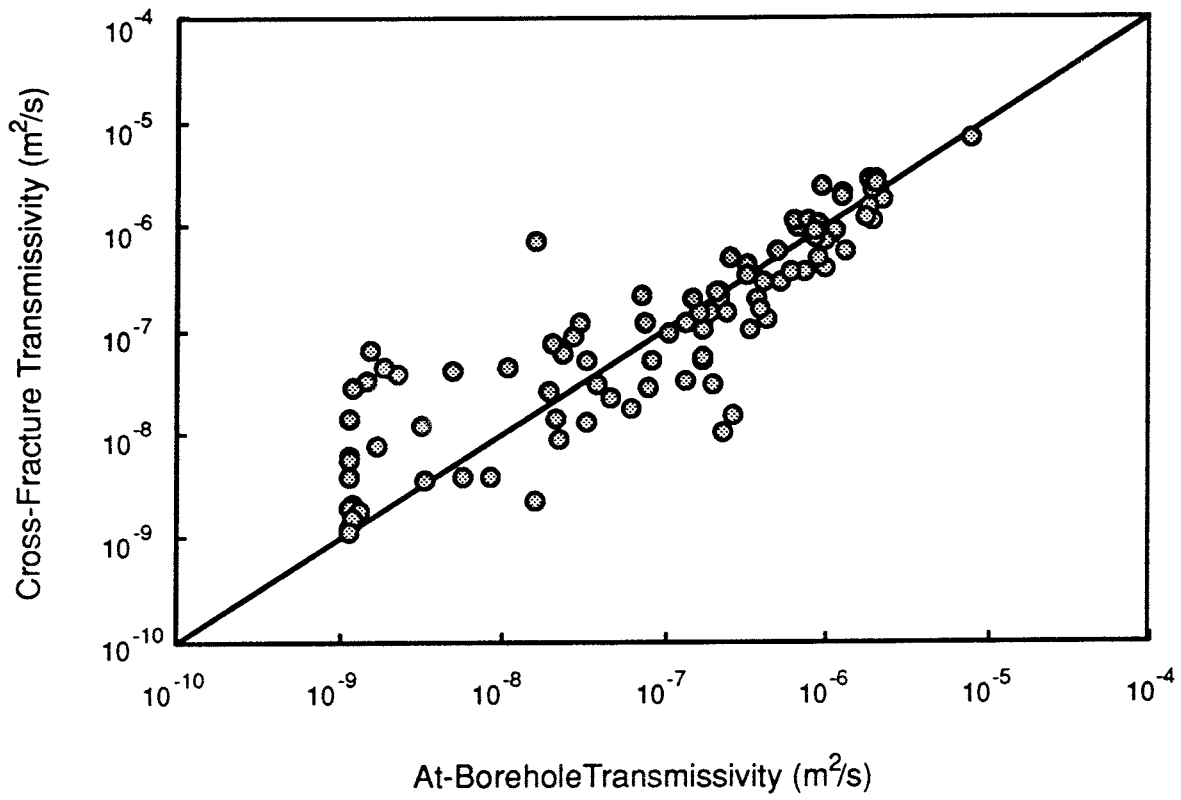


FIGURE **5-9**
ESTIMATED AT-BOREHOLE
vs CROSS-FRACTURE TRANSMISSIVITY
SKB/SKB91 DFNST

The OxFILZ program uses a forward-modelling approach to search for the optimum within the parameter space defined by all possible values of:

$$\{\mu_{\log T_p}, \sigma_{\log T_p}, f_{cr}, b_{TN}\}$$

Input data for the simulations are described in Appendix 12. All 2 m and 3 m section data from the site were used in the analysis. A Nearest-Neighbor model was used for fracture location, with $b_{NN} = 1.73$, as estimated in §5.4.1.

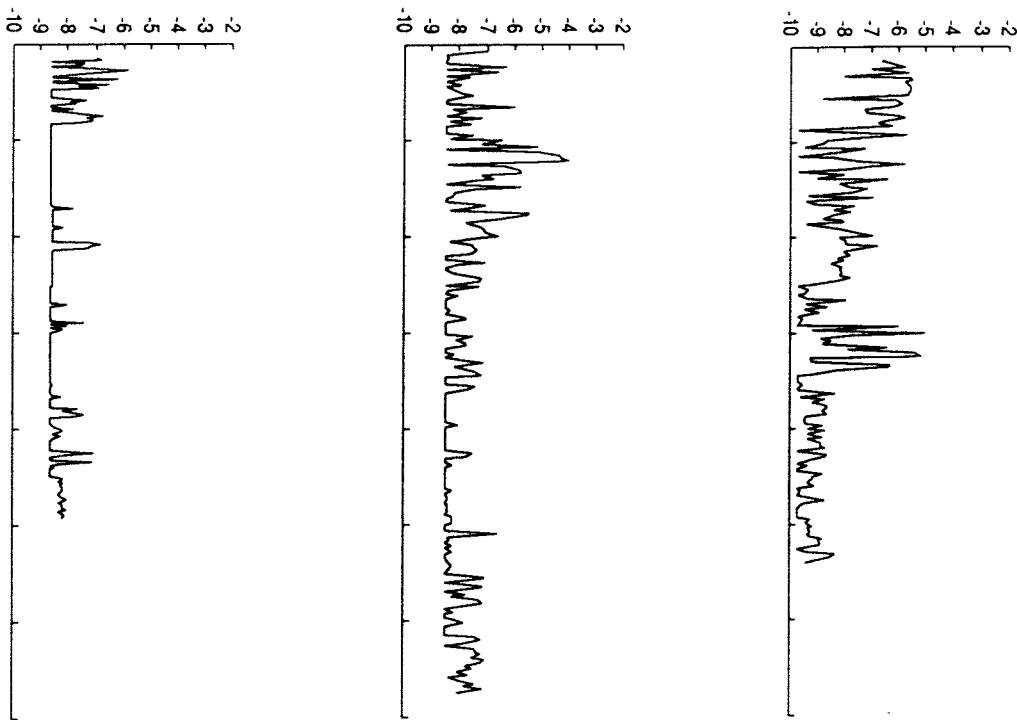
For each set of values $\{\mu_{\log T_p}, \sigma_{\log T_p}, f_{cr}, b_{TN}\}$ tested, the complete set of borehole tests were simulated multiple times to produce stable estimates of the goodness-of-fit statistics. Figure 5-10 shows examples of transmissivity profiles from a single simulation, which can be compared with the field data.

Note that the simulations are not conditional, so there is no reason to expect high- T zones to coincide in both the simulated and the actual profiles. However, some similarity can be expected in terms of trends and correlation patterns, if the T_p distribution and Nearest Neighbor model are reasonably accurate. The simulated T_p profiles show more definite correlation structures than would be expected for a uniformly-random fracture location model, with high- T zones of widths comparable to the high- T zones seen in the field data.^[20] Some qualitative differences are also apparent. For instance, the simulated profiles show a larger number of sharp, high- T peaks than do the field data.

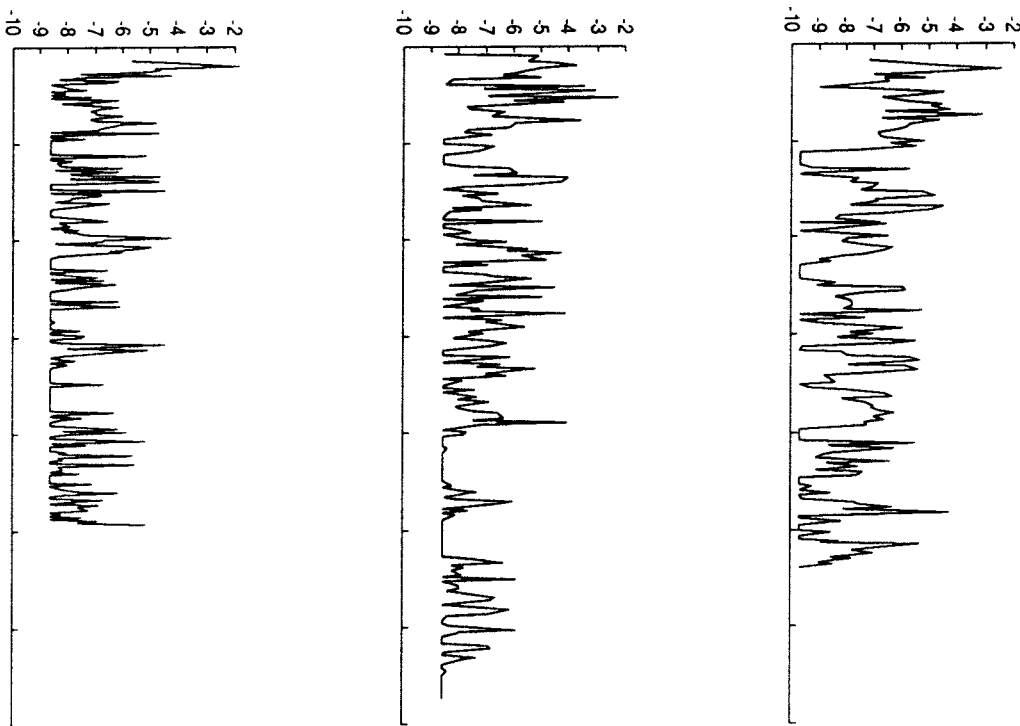
It must be kept in mind that the simulated profiles are based on a simplified, *parallel-conductor* model of network flow. Depending on the fracture system geometry, the corresponding profiles simulated with the complete DFN model may show quite different characteristics.

Figure 5-11 compares the cumulative density functions for the simulated and field T_p data, for the set of parameters that was used in the final DFN model. The stepped appearance of the curves for $T_p < 10^{-8}$ m²/s reflects the variation in measurement limits $T_{p, threshold}$ among boreholes. The fit is least good for the lowest T_p values, which presumably represent a less important part of the fracture system. The "slope statistic" shown in the figure is a measure of the similarity of the simulated and observed gradients in $\log T_p$ with depth.

²⁰ These similarities could be quantified by comparing variograms for the real and simulated data, but this was not done in the present study.



a) Original Data



b) Simulated Profiles

FIGURE 5-10
 EXAMPLES OF CONDUCTIVITY PROFILES
 FROM A SINGLE OXFILZ SIMULATION
 SKB/SKB91 DFNST

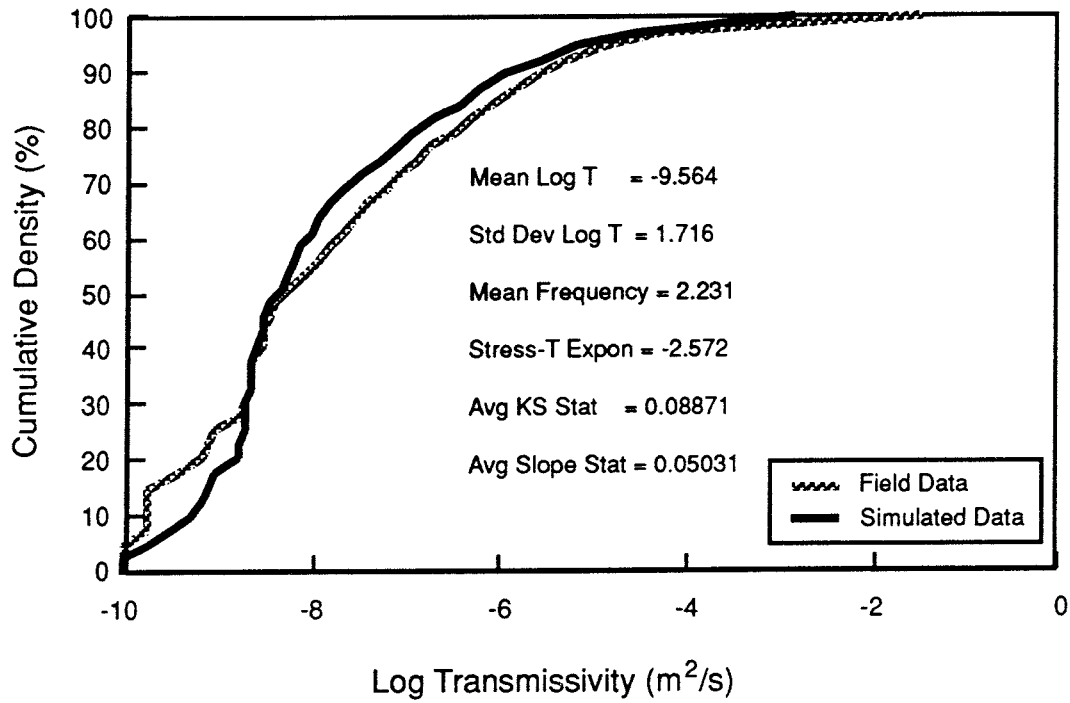


FIGURE 5-11
 OXFILZ DERIVATION OF FRACTURE
 TRANSMISSIVITY DISTRIBUTION
 SKB/SKB91 DFNST

The estimated $\mu_{\log T_p}$ is below $\log T_{\text{threshold}}$ for most of the boreholes. The interpretation of the T_f distribution as lognormal should not be trusted below the higher values of $T_{\text{threshold}}$. The present analysis has shown only that the data can be described by the upper tail of a lognormal distribution.

The apparent fact that the mode of the T_f distribution is below $T_{\text{threshold}}$ leads to non-uniqueness in the parameter estimates, as discussed below. The set of parameters shown in Figure 5-11 was chosen from several possible sets, after preliminary calibration runs as described in §6.2.

The estimated magnitude of the stress-transmissivity exponent ($b_{T_n} = -2.572$) is large compared with estimates from laboratory testing, but within the range seen in *in-situ* testing (see §3.2.2). Effects such as near-surface weathering, and contrasts between the rock above and below Zone 2 may be reflected in this value.

5.6.3 Network effects and non-uniqueness in the estimation of transmissivity parameters

The OxFILET/OxFILZ algorithm is based on very simple models for flow in the fractures that are active during a packer test. In the simplest case (which was considered first), each fracture is considered to act as an independent, effectively infinite conduit. However, if fracture extent (or channel length) is comparable to the scale of influence of the test, then the assumption of effectively infinite conduits may not apply.

A full treatment of network effects is not tractable for the OxFILET/OxFILZ approach, since this would require solving a finite-element flow equation for each simulated interval, for each set of parameters considered. A simpler approach, previously used by Dershowitz *et al.* (1991b), is to assume that the effective conductance of a fracture or channel is the effective conductance of a *series* of conduits. The number of conduits N_L in series is assumed to be random:

$$N_L = 1 + n_L \quad (5-6)$$

where n_L is Poisson-distributed:

$$f(n; \lambda_L) = \frac{\lambda_L^n e^{-\lambda_L}}{n!} \quad (5-7)$$

The mean network length is thus $\bar{N}_L = 1 + \lambda_L$.

Figure 5-12 shows the effect of \bar{N}_L on the estimation of parameters for the T_f distribution. The Kolmogorov-Smirnov statistic as a function of $\mu_{\log T_f}$ and $\sigma_{\log T_f}$ for mean network lengths of 1, 1.5, and 2 (The other parameters, f_c and b_{T_f} , are not represented in the plot). The "valleys" in the figures show regions of near-optimal fit. These plots show two interesting effects:

Firstly, for the case $\bar{N}_L = 1$, the "optimum" fit is non-unique. Two distinct local minima are seen. Both of these lie in a narrow "valley" which runs roughly from $(\mu_{\log T_f}, \sigma_{\log T_f}) = (-13, 2.5)$ to $(-8, 0)$. This non-uniqueness is not of practical significance, because different pairs $(\mu_{\log T_f}, \sigma_{\log T_f})$ within this valley generally have nearly identical shapes for the upper tail, which is the only part of the distribution actually modeled.

Secondly, as \bar{N}_L increases, the location of the valley shifts toward lower $\mu_{\log T_f}$ and higher $\sigma_{\log T_f}$ and the valley widens (The widening effect is exaggerated in the plot for \bar{N}_L , because no data were produced for one corner of the plot). This means that non-uniqueness increases as \bar{N}_L increases. This could be expected, because increased \bar{N}_L length corresponds to a reduction in the resolution of the packer tests for measuring single fracture properties.

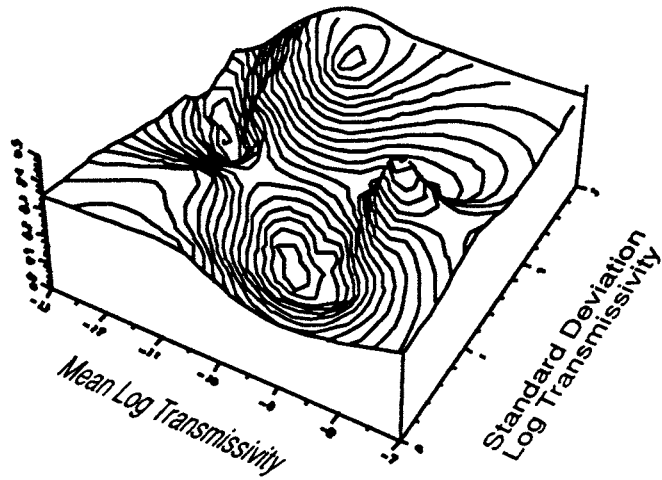
The most serious problem of non-uniqueness comes from the uncertainty regarding effective \bar{N}_L . A criterion is needed to choose among the several parameter combinations which give equally good fits, based on the statistical measure used (*i.e.*, the weighted sum of Kolmogorov-Smirnov statistic and the regression slope ratio). For the present study, the following heuristic rule was adopted:

"If two different parameter sets give approximately the same goodness-of-fit, as measured by the Kolmogorov-Smirnov statistic and regression slope ratio, then choose the parameter set which gives the better match for the high end of the transmissivity distribution."

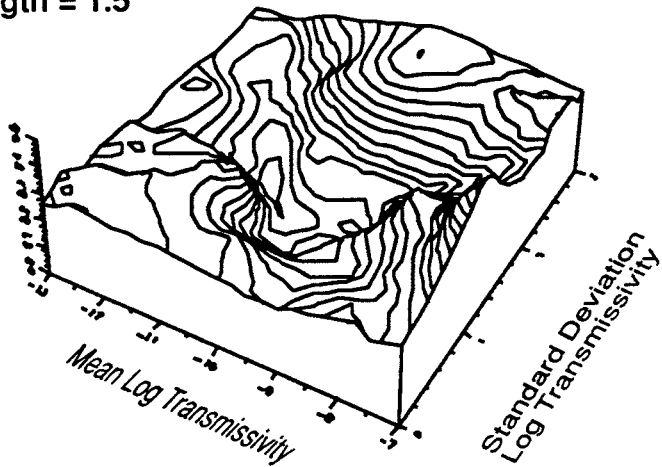
This rule is based on the idea that the most conductive fractures/channels are the most significant, and that the T data close to $T_{threshold}$ are more questionable (or "fuzzy").

The "best-fit" set of parameters given in §5.6.2 was chosen from among the several sets which gave nearly the same goodness of fit, by inspection of CDF plots similar to Figure 5-11. This was done after some preliminary, unsuccessful attempts at model validation, using parameter sets corresponding to the local minima in Figure 5-12a, for the case $\bar{N}_L = 1$. The set of parameters used for the final DFN model was based on the case $\bar{N}_L = 2$.

a) Network Length = 1



b) Mean Network Length = 1.5



c) Mean Network Length = 2

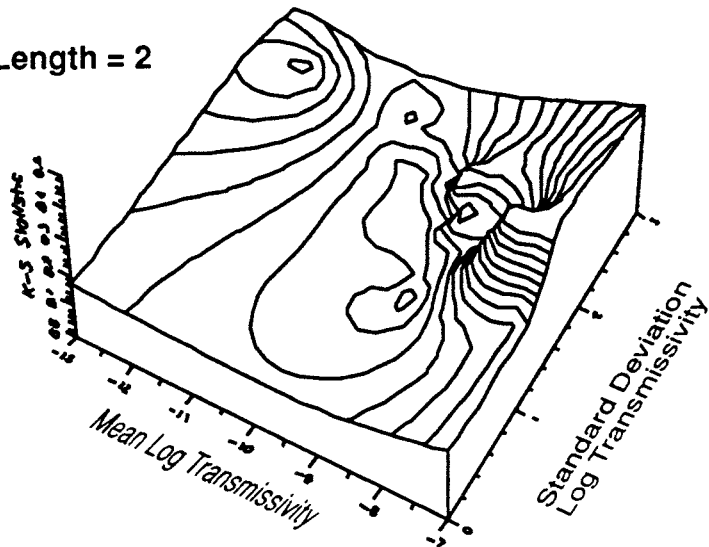


FIGURE 5-12
EFFECT OF NETWORK LENGTH ON ESTIMATION
OF FRACTURE TRANSMISSIVITY DISTRIBUTION
SKB/SKB91 DFNST

It would be preferable to apply a quantitative statistical test which gives greater weight to the high- T intervals, but this was not possible in the present study. The two most commonly used tests, K-S and χ^2 tests, both have the property that all values of the sample are treated equally.

5.6.4 Conductive fracture intensity

FracMan simulation requires that the conductive fracture intensity be specified in terms of P_{32c} , defined as the total conductive fracture area per unit volume. P_{32c} is related to f_c by a factor:

$$C_p = \frac{P_{32c}}{f_c} \quad (5-8)$$

C_p is specific to the fracture orientation distribution $f(\phi, \theta)$ and the borehole orientations and lengths. FracMan simulation of vertical borehole sampling gave an estimated value $C_p = 1.92$. This is close to the theoretical value of 2 for a uniformly random orientation distribution (Dershowitz, 1985).

P_{32c} applies to the entire, inferred lognormal T_f distribution $f(T_f)$. The bulk of $f(T_f)$ is below $T_{threshold}$ (see §5.6.2). Thus there is evidence only for the upper tail of $f(T_f)$, i.e. T_f roughly greater than $10^{-9.5}$ to $10^{-8.5}$ m²/s. Simulation of fractures with $T_f < T_{threshold}$ would be neither practical nor justified.

Hence a **truncated lognormal distribution** was used, with $T_{min} = 10^{-9.5}$ m²/s. The effective intensity P'_{32c} for the truncated $f(T_f)$ was calculated from:

$$P'_{32c} = \left[\frac{1}{2} - \operatorname{erf} \left(\frac{\log T_{min} - \mu_{\log T}}{\sqrt{2} \sigma_{\log T}} \right) \right] P_{32c} \quad (5-9)$$

5.7 Transient packer test reinterpretation

Constant-pressure packer test data from three boreholes (KFI 11, BFI 01 and BFI 02) at Finnsjön were analyzed according to the theory of generalized radial flow (GRF) (Barker, 1988). GRF analysis methods for constant pressure tests (Doe and Geier, 1990) were used to estimate distributions of transmissivity T_{GRF} and flow dimension D_F . These data can be used to validate and/or calibrate the DFN model.

Data from the tests were obtained from the GEOTAB database in the form of raw datalogger records. These were transformed to time, flux and pressure histories using a special-purpose program. The data conversion process is described in Appendix 13. The tests were interpreted by automated type-curve matching, using the GGAB program MatchPt. This program is described in Appendix 13.

Many of the tests were difficult to match uniquely, due to the short duration (15 minutes) and noise in the flowmeter readings, particularly for the lower- T_p tests. Of a total of 214 tests analyzed, 192 (90%) yielded at least very rough estimates of D_F and T_{GRF} , which were of adequate quality for the purposes of this study, *i.e.*, for statistical comparison with simulated test results. The remaining 10% were completely unusable.

Many of the "acceptable" datasets showed one or both of the following deficiencies:

- Very noisy flowrate data, indicating that the flowmeter was close to the lower end of its range.
- Large pressure fluctuations in early time, so that the tests were not truly "constant-head."

The values of T_{GRF} and D_F from individual test interpretations should not be used except in a statistical sense, without further analysis to determine the importance of these deficiencies. If specific values are to be used, a more complete analysis is required to:

- Screen datasets based on the flowmeters characteristics, by reference to calibration records for individual flowmeters.
- Apply variable-rate analysis (*cf.* Doe and Geier, 1990) for the tests with unacceptably large pressure fluctuations in early time.

There is a possibility that the omission of these steps, in the automated type-curve matching, may produce statistical bias in the distributions of T_{GRF} and D_F , but the scope of the present study did not allow a more thorough analysis to reduce this possibility.

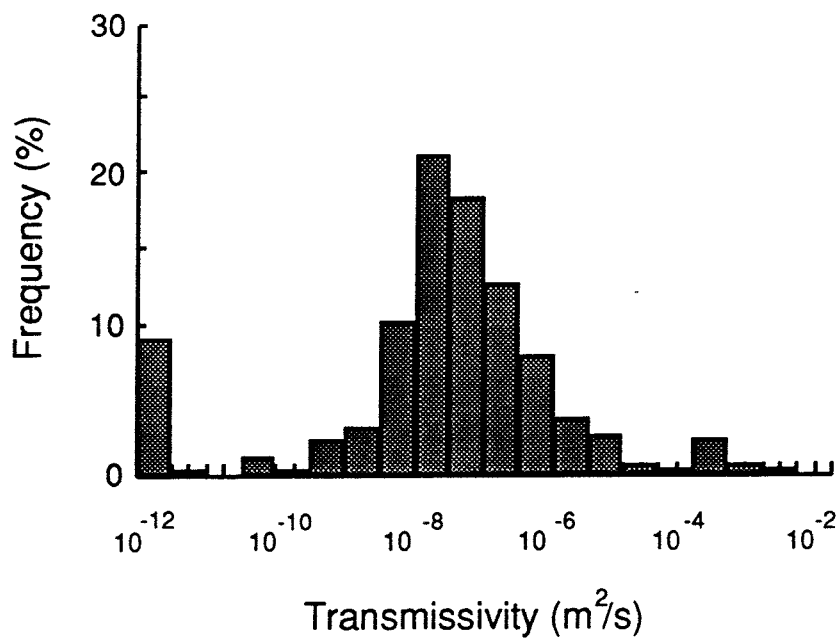
5.7.1 Transmissivity and dimensionality

Figure 5-13 shows histograms and a statistical summary for the T_{GRF} and D_F estimates. The distribution of $\log T_{GRF}$ is roughly normal, but significantly left-skewed on the log scale, with a positive kurtosis. The distribution of D_F is strongly right-skewed, with a majority of the tests exhibiting radial to spherical flow. This indicates a generally well-connected fracture system, but the presence of low- D_F tests indicates regions where flow is restricted to channel-like conduits. These distributions show the same basic patterns as the distributions obtained in the feasibility study (Geier and Axelsson, 1991) for a small subset of these data.

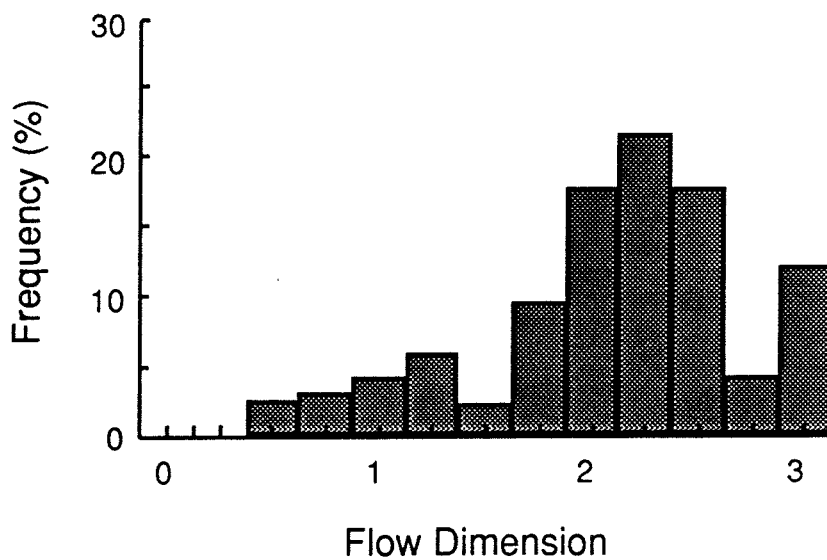
A possible correlation between highly-transmissive zones and flow dimension is of particular importance for assessing the applicability of the different models proposed for the site. Figure 5-14 compares D_F with estimates of (a) conductivity K_{GRF} and (b) transmissivity T_{GRF} . The plot of D_F vs. K_{GRF} shows a clear "outlier" group with high K_{GRF} and sublinear D_F . However, there is also a distinct group of high- K_{GRF} intervals which show approximately spherical flow. In this plot, data from within the "major" fracture zones are lumped together with data from the "rock mass." Possibly the high- K_{GRF} , high- D_F intervals correspond to intensely fractured sections, while the high- K_{GRF} , low- D_F intervals correspond to major, isolated conduits in the "good rock." This possibility was not investigated further in the present study.

The conductivity estimates from GRF analysis can be misleading for low- D_F tests, due to assumptions about conduit cross-sectional area at the borehole (see discussion by Doe, 1990, or Geier and Axelsson, 1991). The generalized transmissivity defined by Doe (1990), referred to herein as T_{GRF} , gives an estimate which is much less sensitive to these assumptions. T_{GRF} gives a more realistic measure of the capacity of the rock adjacent to the interval to absorb or yield fluid during pumping. However, this measure probably underemphasizes the subradial conduits that are present. The plot of D_F vs. T_{GRF} in Figure 5-14b shows evidence of two separate groups of high- T_{GRF} intervals, one linear to sublinear, and the other radial to spherical. However, the distinction is less pronounced than in Figure 5-14a. The intervals of highest T_{GRF} are mainly radial to spherical, but there is a cluster of low-dimension intervals with $T_{GRF} > 10^{-8}$ m²/s.

The large number of high- D_F tests indicates that a large portion of the rock behaves as a porous medium or well-connected fracture network, at least on the scale of a few meters. However, the population of low- D_F intervals of high transmissivity indicates that many of the hydrologically significant sections of the boreholes behave more like a channel network or sparsely connected fracture network.

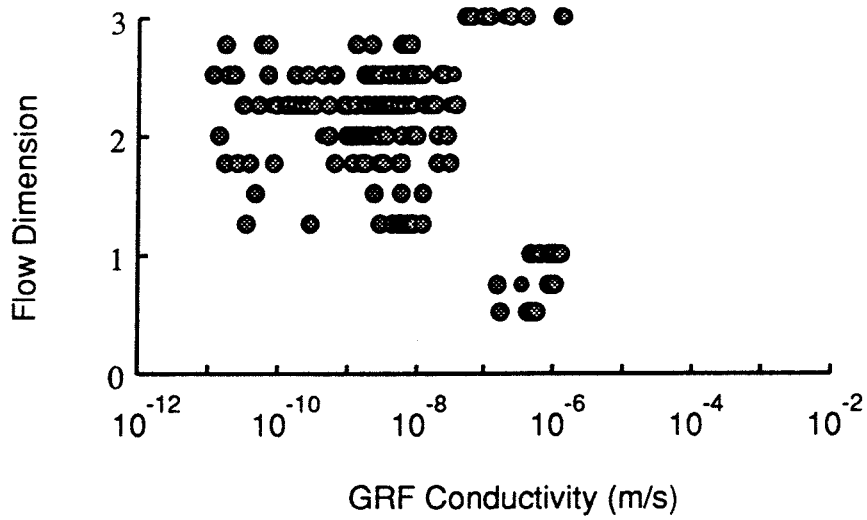


a) Interpreted GRF Transmissivity

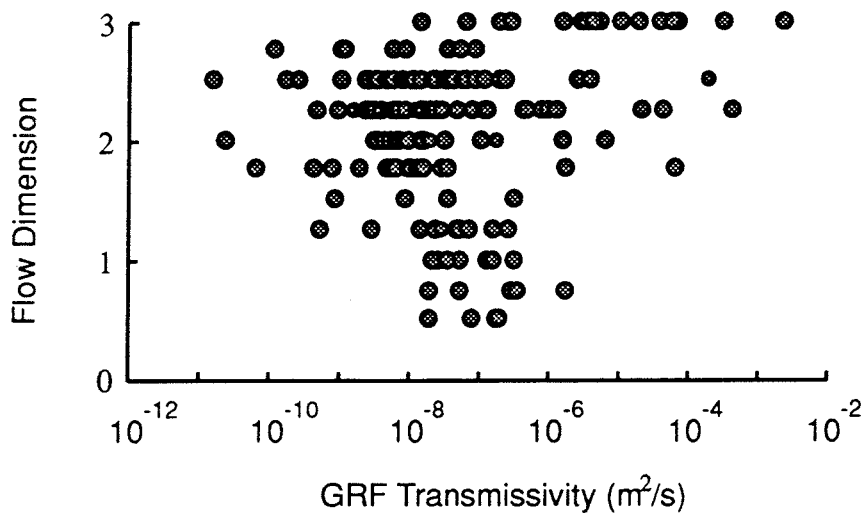


b) Interpreted flow dimension

FIGURE 5-13
DISTRIBUTIONS OF TRANSMISSIVITY AND FLOW DIMENSION
FROM GRF ANALYSIS OF PACKER TESTS
 SKB/SKB91 DFNST



a) Dimension vs. GRF Conductivity



a) Dimension vs. GRF Transmissivity

FIGURE **5-14**
**FLOW DIMENSION VS. GRF CONDUCTIVITY
 AND TRANSMISSIVITY**
 SKB-91/DFNST

5.7.2 Storativity vs. transmissivity

GRF analysis of constant head tests yields estimates of storativity S_{GRF} . Although the reliability of the S_{GRF} estimates is considered to be low (Doe and Geier, 1990), these provide the only information available for estimating possible correlations between fracture transmissivity and storativity.

Figure 5-15 shows a logarithmic plot of S_{GRF} vs. T_{GRF} . Only data from tests with $1.5 \leq D_F \leq 2.5$ (representing approximately radial flow) are included in this plot, because the T_{GRF} and S_{GRF} estimates for this range are less dependent on assumptions about conduit cross-sectional area (Doe and Geier, 1990) and because a nearly radial test is more likely to represent flow in a single fracture plane. Comparison of this plot with the predicted relation of S_f to T_f based on the Bandis-Barton model (Figure 3-10) shows a rather surprising similarity.

A rough loglinear correlation can be seen in Figure 5-15. Regression analysis of these data gives:

$$\log_{10} S_{GRF} = (-0.39 \pm 0.98) + (0.74 \pm 0.07) \log_{10} T_{GRF} \quad r^2 = 0.46 \quad (5-10)$$

where T_{GRF} is in m^2/s . The scatter in the data includes both interpretation uncertainty (which may be more than one order of magnitude for individual tests) and actual deviations from the loglinear model. In applying this relation to the DFN model, it was assumed that (1) the loglinear model estimated for T_{GRF} vs. S_{GRF} represents the relationship of local fracture transmissivity to storativity exactly (without scaling effects, *etc.*), and (2) all of the deviation from the model is due to interpretation uncertainty. Thus it was assumed that, within each fracture plane:

$$S = 10^{-0.39} T^{0.74} = 0.40 T^{0.74} \quad (5-11)$$

The second assumption is probably not correct, but was adopted due to the lack of data to support a particular stochastic model for the error terms.

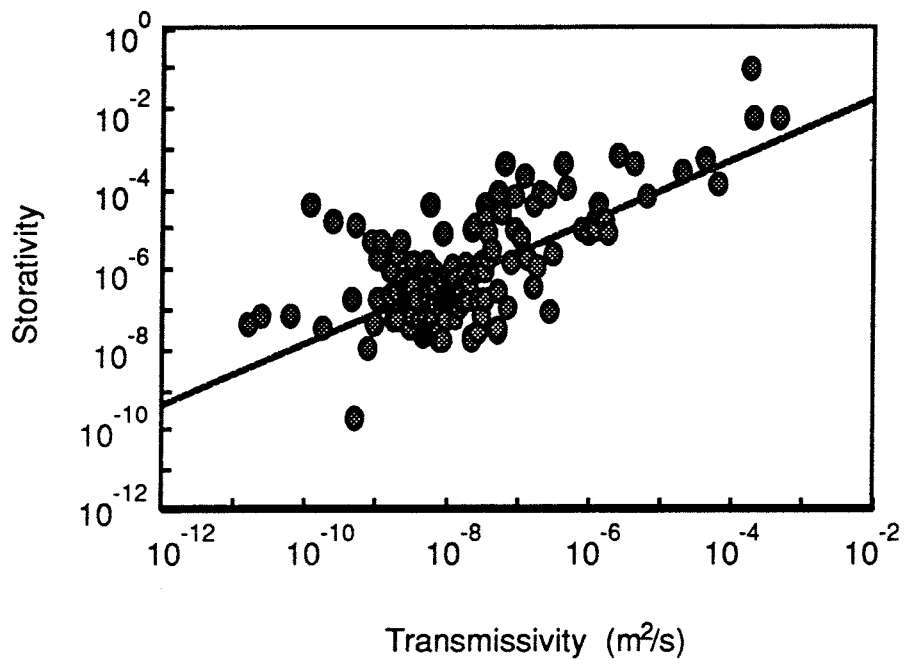


FIGURE 5-15
ESTIMATION OF
STORATIVITY VS. TRANSMISSIVITY RELATION
SKB-91/DFNST

5.8 Detailed fracture properties

5.8.1 Fracture infilling

Fractures at the Finnsjön site were considered in terms of three categories:

- Sealed fractures
- Coated fractures
- Breccia-filled fractures or crush zones

The sealed fractures are unlikely to have $T_f > 10^9$ m²/s (§3.3.3.1). Therefore sealed fractures were not considered for further analysis. Coated fractures are assumed to constitute the main portion of the significantly transmissive fractures at the site.

Breccia-filled fractures and crushed zones are not indicated by standard codes in the core logging, but are indicated as comments in the core logs. This system makes analysis of these features rather time-consuming. For the present study, the detailed core log for just one borehole, KFI 11, was examined by finding all records with comments. These were compared with the packer test interpretations from the same borehole. Table 5-4 gives comments and numbers of coated fractures per interval for the 10 most transmissive intervals in KFI 11. This includes all sections in KFI 11 for which $K_p > 1 \times 10^{-7}$ m/s. The three most transmissive zones all contain brecciated or crushed zones.

Table 5-4 Comparison of most conductive intervals in KFI 11 with core log comments

Depth (m)	Packer Test Conductivity K_{Moyes} (m/s)	Log K_{Moyes} (log m/s)	Comments
223.94	1.90×10^{-4}	-3.72	"gravel"
329.92	6.00×10^{-6}	-5.22	breccia, 20mm Ca
335.92	1.60×10^{-6}	-5.80	8 coated, "partly mech. crushed"
221.94	5.60×10^{-7}	-6.25	6 coated
227.94	3.40×10^{-7}	-6.47	4 coated
287.92	2.90×10^{-7}	-6.54	5 coated
289.92	2.80×10^{-7}	-6.55	14 coated
291.92	2.30×10^{-7}	-6.63	30 coated
213.94	1.60×10^{-7}	-6.80	5 coated
235.94	1.40×10^{-7}	-6.85	5 coated

5.8.2 Porosity

As discussed in §3.4, there are a number of possible physical explanations for the high ϵ_v values seen in tracer tests, relative to the measured ϵ_h values for single fractures. The evidence is not conclusive, but a rough dependence of ϵ_v on ϵ_h is seen in the data from various single-fracture tests. An empirical model for the relationship of ϵ_v to ϵ_h is therefore appropriate. The data in Figure 3-11 display a clear pattern, except for two points from Abelin *et al.* (1985). A linear regression performed on $\log \epsilon_h$ vs. ϵ_v/ϵ_h gives the curve shown in Figure 5-16a. The fitted model may be expressed as:

$$\epsilon_v[\mu\text{m}] = 10^{2.01 \pm 0.28} \epsilon_h[\mu\text{m}]^{0.44 \pm 0.07} \quad (5-12)$$

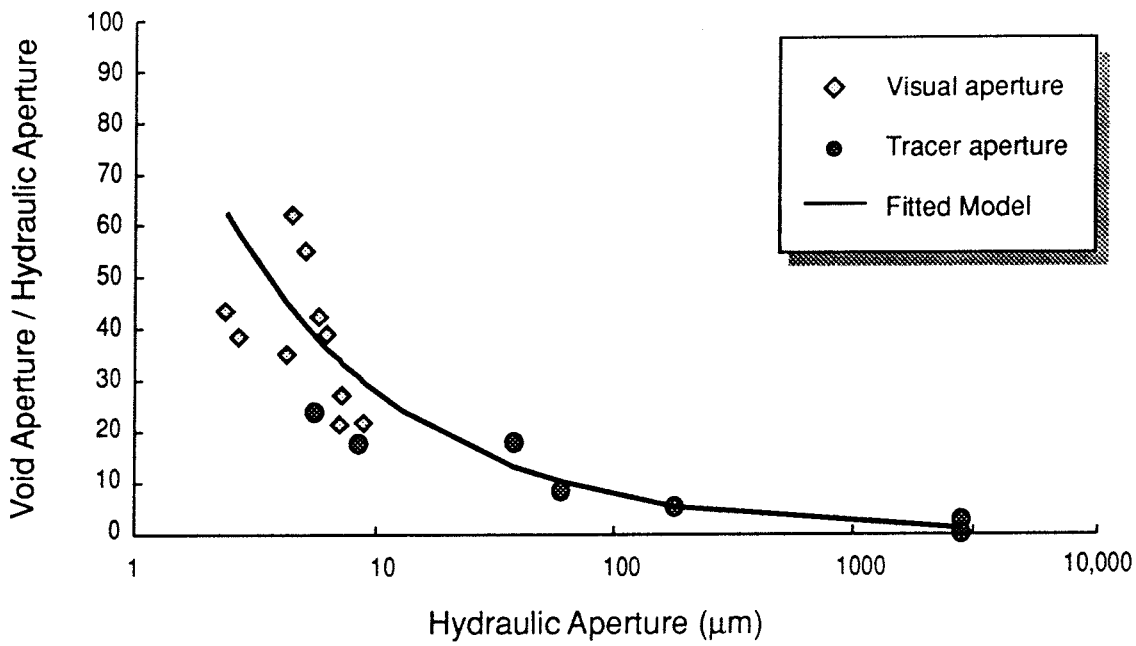
with a regression coefficient $r^2 = 0.78$. Figure 5-16b shows the same curve plotted as ϵ_v vs. ϵ_h . The poorest fit is for lower ϵ_h (and thus T_f), which is much less critical; fractures of this order of T_f were assumed to be negligible in the final DFN model. It is however stressed that the basis of this model is extremely limited, and it is not certain that the data for ϵ_v and ϵ_T are directly comparable. This model should therefore be seen only as a working model.

For breccia-filled fractures the relationship of porosity to transmissivity is expected to be extremely variable, but certainly ϵ_v for a breccia-filled fracture will be greater than a coated fracture with the same ϵ_h . If the above empirical model is used to estimate ϵ_v for breccia-filled fracture as well as coated fractures, the flow porosity will be underestimated. The above empirical model is used as the base case in the present study. The predictions will be conservative if higher porosity along more conductive paths acts to retard radionuclide migration.

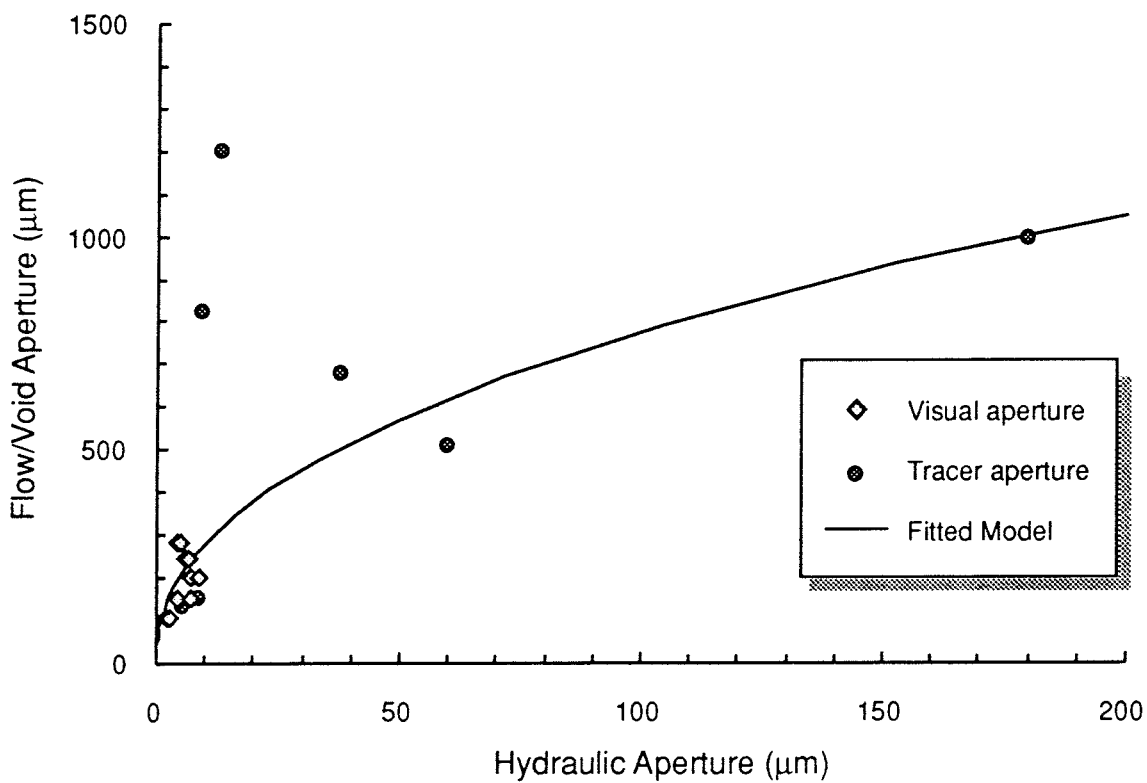
The higher porosity in breccia-filled fractures may strongly increase the flux-weighted porosity, since these seem to be the most transmissive features. The importance of this issue for future studies was investigated by a sensitivity study, assuming that for fractures with $T_f > 2 \times 10^{-6}$ m²/s, the crushed material in the fracture has $K = 10^{-3}$ m/s and $\phi = 0.15$, which are typical values for sandy aquifers (Bear, 1972).

5.8.3 Wetted surface

For coated fractures the available evidence (§3.3.1) suggests that anywhere from 10% to 60% of a fracture plane may be open. In the present study, the fracture specific wetted surface s_{wf} is assumed to be normally distributed and independent of ϵ_h , with $s_w = 0.4 \pm 0.2$, with the restriction $s_{wf} > 0.02$.



a) Semi-log comparison of model with all data.



b) Comparison of model with data for lower transmissivities.

FIGURE 5-16
**EMPIRICAL RELATIONSHIP FOR VOID APERTURE
 AS A FUNCTION OF HYDRAULIC APERTURE**
 SKB/SKB91 DFNST

The specific wetted surface of a breccia-filled fracture will generally be much greater than for a coated fracture with the same ϵ_p . This could strongly increase retardation in the most transmissive conduits. In the base case for the present study, it is assumed that all fractures act as coated fractures. In the sensitivity study, the value of s_w for fractures with $T_f > 2 \times 10^{-6}$ is estimated by using the above values of infilling ϕ and K in Kozeny's equation (Eq 3-14), with $\tau k_o = 4$.

6 MODEL VALIDATION

The DFN model as derived in Chapter 5 was partially *validated* by simulation of transient packer tests, and comparison of interpreted flow dimension and transmissivity distributions from the simulations with those obtained from field data (§5.7.1).

6.1 Conceptual Model Dataset

Figure 6-1 gives a complete statistical description of the conceptual model fracture geometry, as derived in Chapter 5. The dominant characteristics of this model are:

- Concentration of fractures in fracture zones of varying scale, due to the Nearest Neighbor model for fracture location.
- Varying, directional dependence of fracture transmissivity with depth, due to the dependence on a vertically changing stress field.

In this model, the fracturing is sufficiently intense for the fracture population to be well-connected, but sparse enough that strong heterogeneity can be expected on a scale of 0.1 to 50 m due to single fractures with structured transmissivity. Strong heterogeneity on larger scales could result from the major features. The fracture size distribution differs significantly from the model used in the feasibility study (Geier and Axelsson), with a much larger proportion of smaller fractures. This means that typical flow paths will tend to be composed of a larger number of fractures than for the model used in the feasibility study.

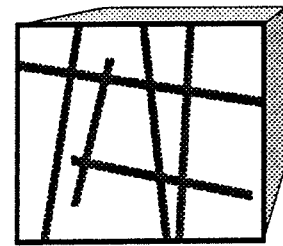
Figure 6-2 shows a 40 m cube from a single realization of the model. The block contains portions of several zones. An intensely fractured zone is clearly visible in the upper, SW corner of the block.

6.2 Packer Test Simulations

The boundary conditions for the packer test simulations are depicted in Figure 6-3. The fracture population was simulated within a 50 m cube, and a finite element mesh was generated from a 40 m cube centered within this region. Packer intervals were simulated as a set of fixed, cylindrical boundaries colinear on a vertical axis through the center of the cube, as depicted. Five 2 m sections, separated by 1 m intervals, were located in the center of the cube. Two 12 m sections simulated the borehole above and below the 2 m sections.

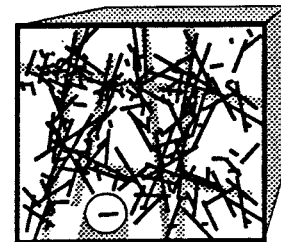
a) Fracture Zones

Location	Uniformly random	Conditioned by termination model
Size	Power Law	$r_g \geq 25 \text{ m}, b_r = 3.1$
Orientation	Bootstrap	Based on major zones
Termination	Revised Baecher	80.5%
Intensity	Constant	$P_{32z} = 0.049 \text{ m}^2/\text{m}^3$
Size of generation region:		500m x 500m x 500m



b) Fractures

Location	Nearest-Neighbor	$b_{NN} = 1.73$
Size	Power Law	$r_g \leq 25 \text{ m}, b_r = 3.1$
Orientation	Bootstrap	Based cell maps & core
Termination	Enhanced Baecher	42%
Intensity	Constant	$P_{32c} = 1.59 \text{ m}^2/\text{m}^3$
Transmissivity	Truncated Lognormal Adjusted for σ_n	$\log T_f \sim N(-9.6, 1.7)$ $\{-9 \leq \log T_f \leq -3\}$
Size of generation region:		50m x 50m x 50m



c) Detailed properties

Local transmissivity from fractal surface roughness model

Fractal dimension of surface Triangular distribution $MLV = 2.15; 2 \leq D_s \leq 2.5$

Storativity Log correlation to local transmissivity $S = 0.4 T^{-0.74}$

Void aperture
 Base case $\epsilon_v = 10^{2.01 \pm 0.28} \epsilon_v^{0.44 \pm 0.07}$
 Breccia case $\epsilon_v = T / (150 \text{ m/s}), T \geq 2 \times 10^{-6} \text{ m/s}$

Specific surface
 Base case $s_w \sim N(0.4, 0.2), s_w > 0.02$
 Breccia case

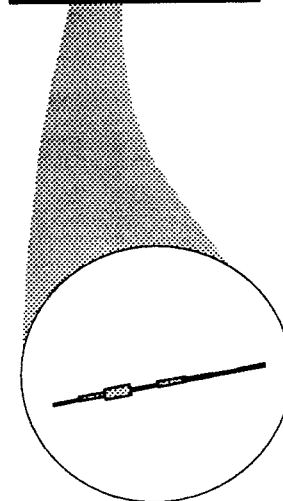
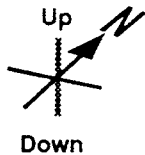
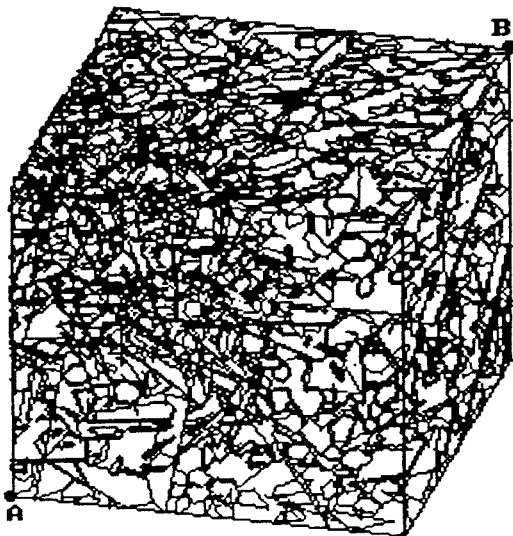
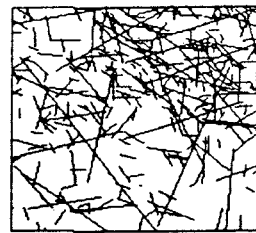


FIGURE 6-1
**STATISTICAL DESCRIPTION OF
 THE DFN CONCEPTUAL MODEL**
 SKB/SKB91 DFNST

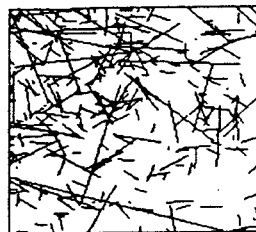


a) Three-dimensional view of block (50m x 50m x 50m)



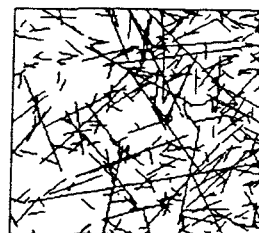
N S

b) Vertical, N-S section through center of block



E W

c) Vertical, E-W section through center of block



E W

d) Horizontal section through center of block

FIGURE 6-2
SINGLE REALIZATION OF THE DFN MODEL
SKB-91/DFNST

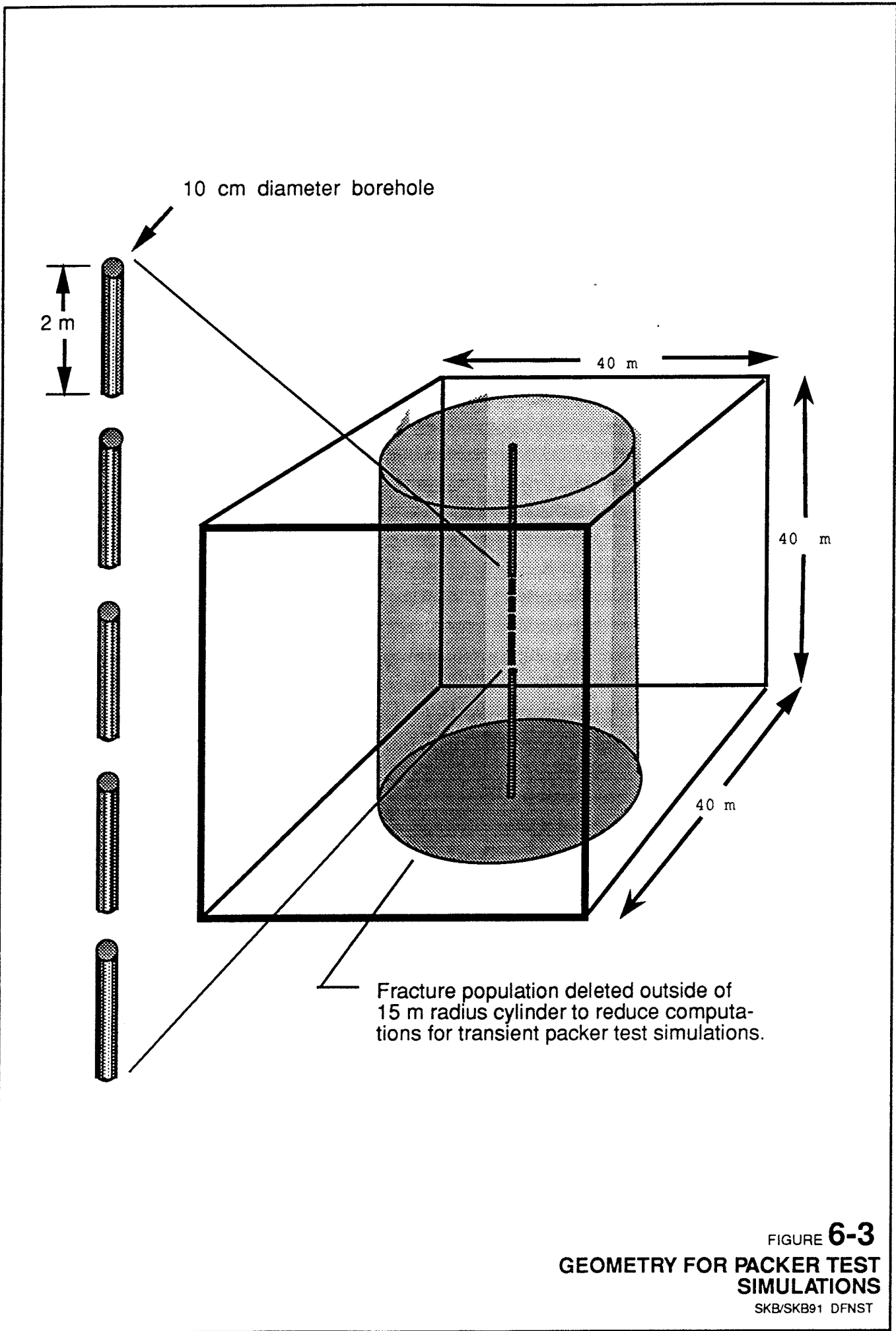


FIGURE 6-3
GEOMETRY FOR PACKER TEST
SIMULATIONS
SKB/SKB91 DFNST

Packer tests were simulated in each of the 2 m sections, successively, by imposing a fixed head of 20 m at $t = 0$ in the test section. The non-test sections were assigned a group-flux boundary condition (see Miller, 1990) so that the net flux into each non-test section was $Q_{net} = 0$. This boundary condition allows the borehole sections to act as connectors between distinct fracture networks. The group-flux boundary condition $Q_{net} = 0$ corresponds to "packing off" borehole sections adjacent to the test sections.

The transient response (head and flowrate) in both test and non-test sections was modelled up to $t = 1000$ s. For all tests, the initial condition was $h = 0$ m throughout the mesh.

Since the packer test analysis results in §5.7.2 were produced from a nonsystematic sampling program, there may be bias due to a nonuniform distribution of test interval depths in the database. In simulating the packer testing program, it is desirable to reproduce this bias as nearly as possible. The best way to do this would be to simulate tests for each of the actual test depths, or for some random sample of those depths. With the current version of EdMesh this was not possible, but an attempt was made to minimize the bias by simulating at a number of fixed depths, chosen roughly in proportion to the packer testing density (as a function of depth) at Finnsjön. For each test section in each block, the simulation was repeated for three different depths, by scaling the fracture element transmissivities according to the stress-transmissivity relation and the stress-depth dependence.

Several reductions in the fracture population were necessary to reduce the size of the finite-element equations to a tractable size (less than about 50,000 nodes):

- Fractures with $10^{-9.5} \leq T_f \leq 10^{-8}$ m²/s were simulated only within a cylindrical region of 15 m radius around the boreholes. This is unlikely to affect packer test simulations significantly, since in general a conductive pathway connected to a borehole will intersect several higher- T_f fractures within a 15 m distance.
- Subfractures with $T_f < 10^{-8.5}$ m²/s after applying the stress-depth dependence were deleted from the meshes. This increases the effective "measurement threshold" $T_{threshold}$ for the simulations, which increases the number of apparently "nonconductive" intervals and leads to some difficulties in interpreting the results.
- For the near-surface (50 m depth) simulations, the above reductions were not sufficient, and so all subfractures were deleted from the region more than 15 m from the simulated borehole. This is equivalent to imposing a no-flow boundary

condition at a 15 m radius from the borehole. It is possible that this influenced results for a few of the tests, but spot checks showed that the head changes at this radius rarely exceeded 0.05% of the applied head, so it is unlikely that any of the tests were affected significantly. Analysis of the transient response data (see below) showed a few indications of closed-boundary or leaky-boundary effects, but in general the interpreted distance to these boundaries was just a few meters, suggesting that the observed effects were due to flowpath constrictions within the modelled population, rather than effects of model boundaries.

The most significant of these reductions was the removal of the lower- T_f fractures since this reduces the number of fractures that connect directly to a packer test interval. Particularly for the low- T_f intervals, the first 1 or 2 fractures connecting to the interval will dominate the response. Possibilities for addressing this problem are discussed in §9. A reduction in the simulation threshold would have been preferable but was not possible due to computational constraints.

6.3 Results of Validation Exercise

The transient test responses were interpreted using MatchPt. The interpretation procedure was identical to that for the field tests (§5.7). Of course, the simulated data were of considerably higher quality due to the ideal "test conditions." That is, the applied heads were constant and flowrates were recorded to within a relative error of 10^{-6} or better. Appendix 14 gives a few examples of the type-curve matches to the simulated, transient tests. In these plots, one can see distinct changes in slope which reflect changes in conductance and/or boundary effects along the flow paths. This type of behavior is quite diagnostic of discrete fracture flow, and has been observed in tests using state-of-the-art equipment (Doe and Geier, 1990; Black *et al.*, 1991), although the best instruments, as of yet, do not give quite such good resolution as the simulated tests.

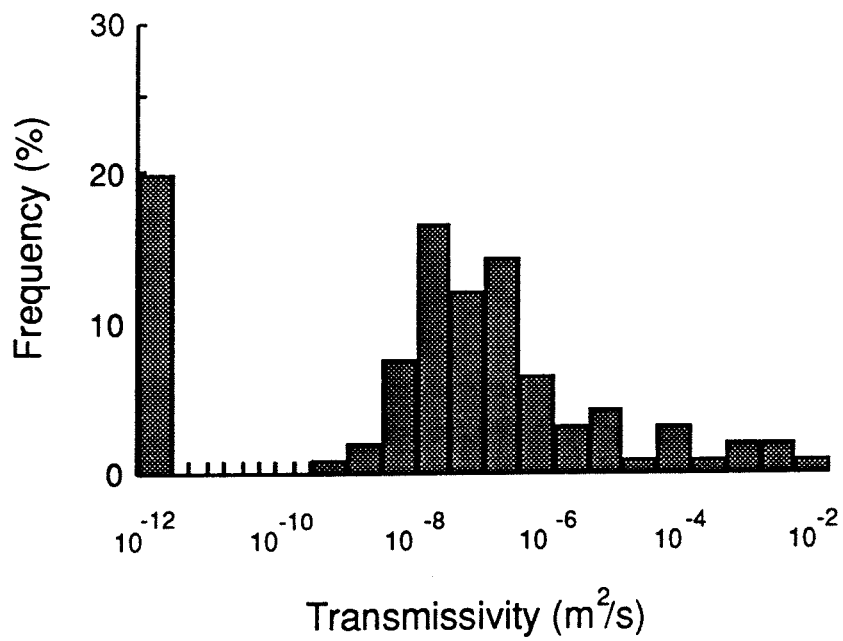
Figure 6-4 gives distributions of interpreted T_{GRF} and D_f for the simulated packer tests using the model defined in Figure 6-1. Some similarity is seen for $T_{GRF} > 10^{-8}$ m²/s. Below this value, the differences are noticeable, but may be largely due to the effects of the simulation threshold for T_f . For the simulated tests, 22% of the intervals are nonconductive. Direct comparison of this with the nonconductive percentage in the field tests is not possible, due to uncertainty as to the effective "measurement limit" in both cases. Table 6-1 gives a statistical comparison of the field and simulated data. For this comparison it was assumed that:

- All nonusable test records (§5.7.1) correspond to intervals with $T_{GRF} < T_{threshold}$. This assumption is reasonable because extremely noisy data are indicative of an under-ranged flow meter.
- No distinction should be made among tests with $T_{GRF} < 10^{-8.5}$ m²/s, due to ambiguity regarding the simulation and measurement thresholds.

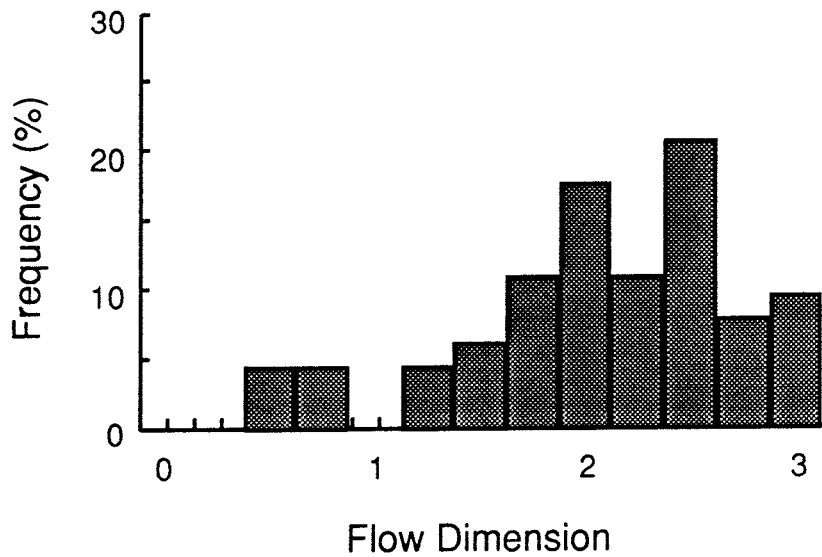
Table 6-1 also gives a comparison of the distributions for D_f . The confidence level for the hypothesis that the two T_{GRF} distributions are identical is low. A better fit could undoubtedly be obtained by calibration of the T_f distribution but further refinement was not possible within the scope of this study. The match to the dimensionality distribution is better, but still rough. (Some of the roughness may result from the fact that the bin spacing is close to the resolution of the GRF analysis). This indicates that the variation of connectivity in the model is similar to that in the rock, but there is probably room for refinements such as division into subregions.

Table 6-1. Statistical comparison of simulated and field test interpretations				
Variable	Bins Used For Comparison	χ^2	Number of Degrees of Freedom	Confidence Level for Accepting Hypothesis that Distributions are Identical
Log GRF Transmissivity (log m ² /s)	{-8.5, 8, ..., -5.5, -2.5}	6.26	7	51.0%
Flow Dimension	{0.5, 1, ..., 3}	2.54	5	77.1%

This validation exercise represents a second attempt, after a preliminary model based on a different transmissivity distribution (but statistically identical fracture geometry) was found to be inadequate. The preliminary model was developed prior to recognition of the non-uniqueness in the OxFILZ derivation, as described in §5.6.3.



a) Interpreted GRF Transmissivity



b) Interpreted flow dimension

FIGURE **6-4**
**DISTRIBUTIONS OF FLOW DIMENSION
 AND TRANSMISSIVITY FOR THE DFN MODEL**
 SKB/SKB91 DFNST

The final model was subsequently chosen from among several sets of equally-likely parameters, based on the criterion given in §5.6.3. **Calibration** of this model was not used, if the term "calibration" is understood in the usual sense of adjustment of parameters to produce a better fit between simulated and observed behavior. However, a comparison between simulated and observed estimates of K_{Moyes} estimates was used in the process of developing this criterion. Since the K_{Moyes} are correlated to T_{GRF} estimates, to some extent the T_{GRF} data were incorporated in the process of selecting the best set of parameters from among several candidate sets.

Therefore the T_{GRF} data do not constitute an independent data set for validation. However, the D_F data do provide such a set. Flow dimension is a measure of flowpath conductance variation, and thus is a particularly good test of a DFN model. To the extent that constant-head packer tests of 15 minute duration give a measure of local fracture network properties, the DFN model defined in Figure 6-1 appears to be a reasonably valid model for transient flow behavior at the Finnsjön site, although there is room for refinement as suggested above.

7. ESTIMATION OF PARAMETERS FOR THE STOCHASTIC CONTINUUM MODEL

The DFN aspects of the DFN/SC interface were developed to the point of producing nonparametric estimates of the covariance matrix function (CMF). Software development is still needed, from the SC standpoint, to fit a parametric CMF, based on these estimates.

Within the present study, a demonstration dataset was produced (Appendix 15) by simultaneous simulation of packer tests and block-scale flow. This dataset can be used in developing and testing the required software for estimating a parametric CMF. The DFN model used to develop the dataset is based on a more sparse fracture population than was inferred from the present study for the Finnsjön site, but may be representative of less highly fractured sites such as might be considered for an actual repository.

For the final model, the scope of the simulations was reduced to concentrate on estimation of parameters for the DPST model (flow porosity and wetted surface). Block-scale flow simulations were therefore performed only for three independent sets of boundary conditions (permeameter simulations parallel to the geological coordinate axes). Therefore estimates of the full block-scale conductivity tensor \mathbf{K} , were not obtained, and existence of an effective tensor could not be evaluated.

However, the permeameter simulations, together with the packer test simulations carried out during model validation, provide information which is relevant to the SC modeling regarding:

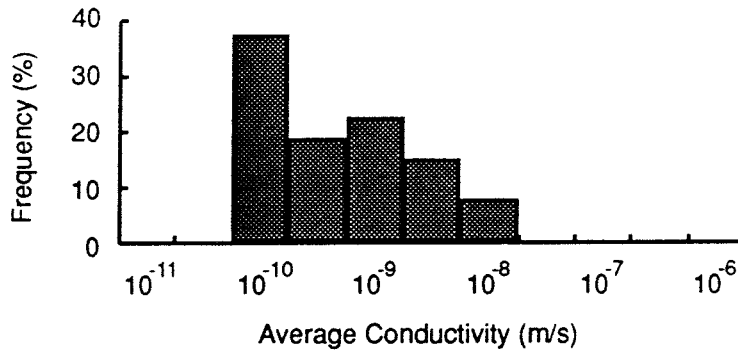
- Block-scale conductivity and anisotropy.
- Trends in block-scale conductivity and anisotropy with depth.
- Correlation of packer-test conductivity and block-scale equivalent conductivity.

The output data from the simulations could also be analyzed to give information regarding:

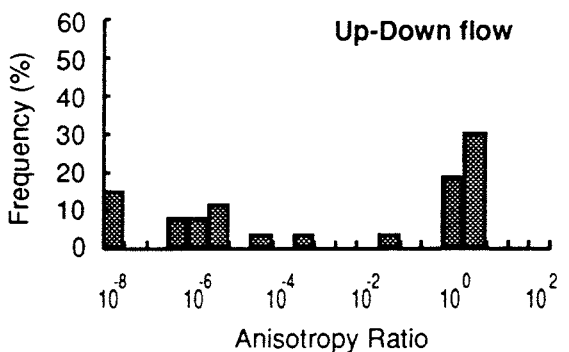
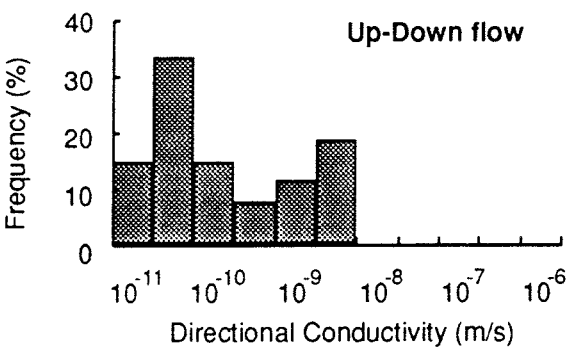
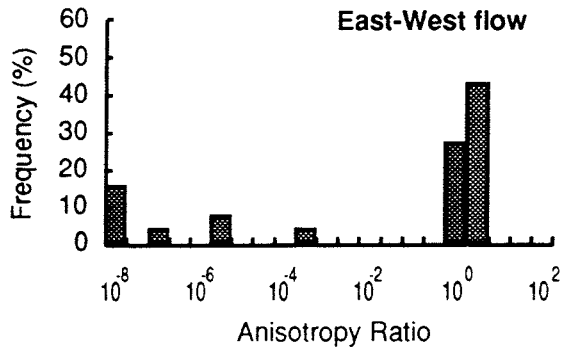
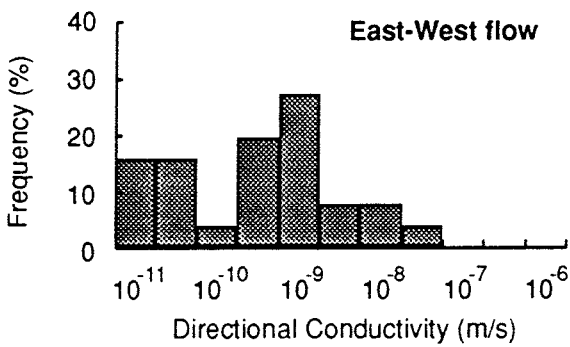
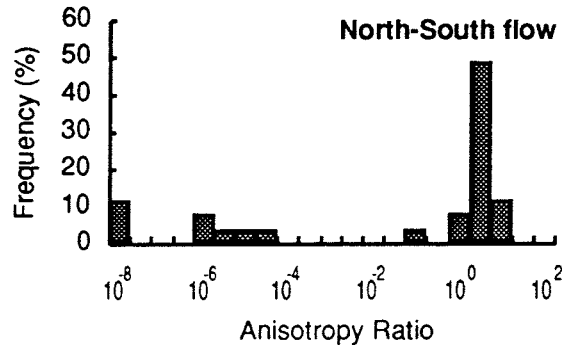
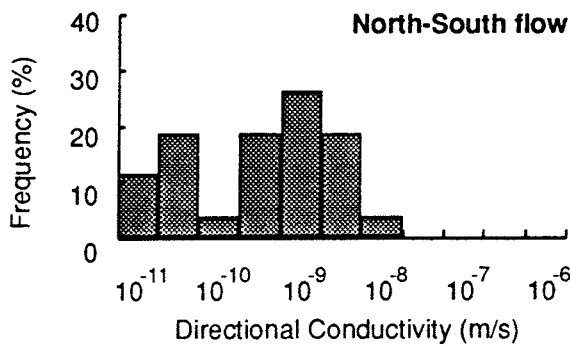
- Autocorrelation of conductivity on a scale < 40 m.

but this has not been done due to a lack of time.

The estimates of directional $K_{s=40m}$ obtained from the permeameter simulations are summarized in Figure 7-1. These plots give data from simulations at the 500m depth (for which the most extensive simulations were performed). At this depth, in any particular



a) Arithmetic Mean of Directional Conductivities



b) Directional Conductivities

c) Ratios of directional conductivities to mean of directional conductivities for each block.

FIGURE 7-1
**EQUIVALENT CONDUCTIVITY FOR 40m BLOCKS
 AT 500 m DEPTH**
 SKB/SKB91 DFNST

direction 10-15% of the blocks were effectively nonconductive, but no blocks were effectively non-conductive in all three directions. Figure 7-1a shows a histogram of the arithmetic mean of $K_{z=40m}$ measurements in the three directions. The plot indicates either a bimodal or a left-skewed distribution on the logarithmic scale.

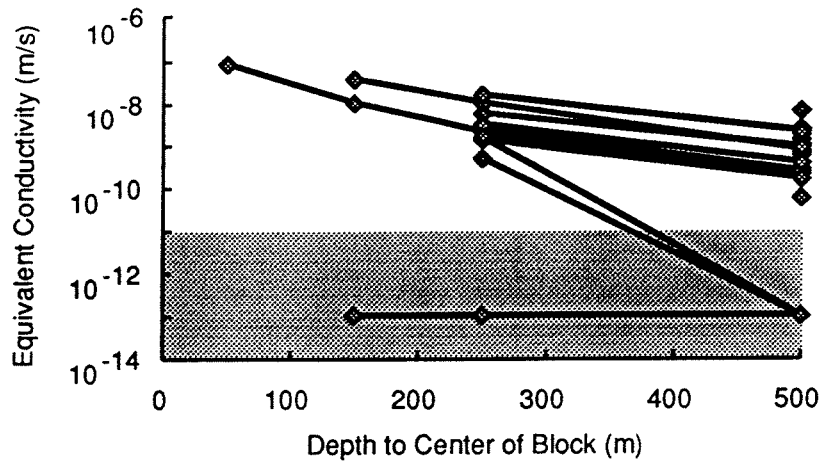
Plots of the directional conductivities (Figure 7-1b) show more distinctly bimodal behavior. The number of blocks simulated (26 or 27, depending on flow direction) is small, but the bimodality seen is quite pronounced. This bimodality can be expected from the two-stage DFN model. The populations of blocks containing fracture zones (major or minor) which are aligned in the flow direction will have distinctly higher conductivities than blocks without such favorably oriented zones. Since the average zone frequency is about 1 per 20 m, nearly all 40 m blocks will contain a favorably oriented zone for at least one of the flow directions, but often not for all three flow directions. Histograms of the anisotropy ratios (Figure 7-1c) show that, in general, directional conductivities are either within one order of magnitude of the arithmetic mean, or they are many orders of magnitude lower. A possible interpretation of these observations is thus that, for directions in which there is no favorably oriented zone (*i.e.*, in the "rock mass"), the cross-block flow paths are very sparse and are controlled by the least conductive fractures in the pathway. This interpretation suggests that the DFN model does not behave as an equivalent porous medium on this scale, but unfortunately this could not be tested explicitly within the scope of the project.

The difference in conductivity distributions between the horizontal and vertical flow directions, at the 500 m depth, probably results mainly from the horizontal preference for fracture zones, as determined by the bootstrap data set. At shallower depths the stress field is more anisotropic, and a lower σ_v could result in even stronger anisotropy. The difference between E-W and N-S directional conductivity is probably not significant for the number of realizations.

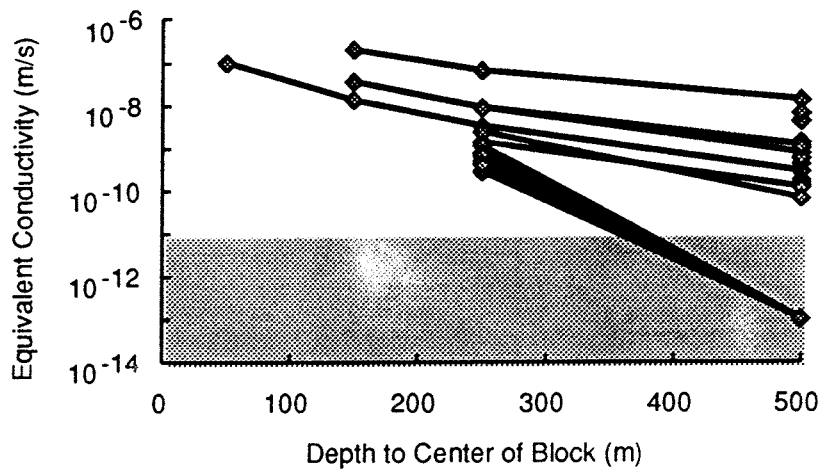
The dependence of directional conductivity on depth for individual blocks is illustrated by Figure 7-2. Since emphasis was placed on simulations at the 500 m depth, only a few blocks were simulated for 3 or 4 depths. The lines between points show the change in K_i for individual realizations, as a function of depth. The shaded regions of the plots represent blocks below the simulation threshold for K_i . The behavior is quite uniform for each flow direction, except where the blocks drop below the simulation threshold. A detailed analysis is not warranted due to the small number of simulations.

A major question for SC modeling is, "How much information do one or several packer tests give about block-scale conductivities in fractured rock?" Figure 7-3 shows the arithmetic mean of K_{Moyes} estimates from 5 packer tests in a block, versus the "average" K_i defined as (a) the

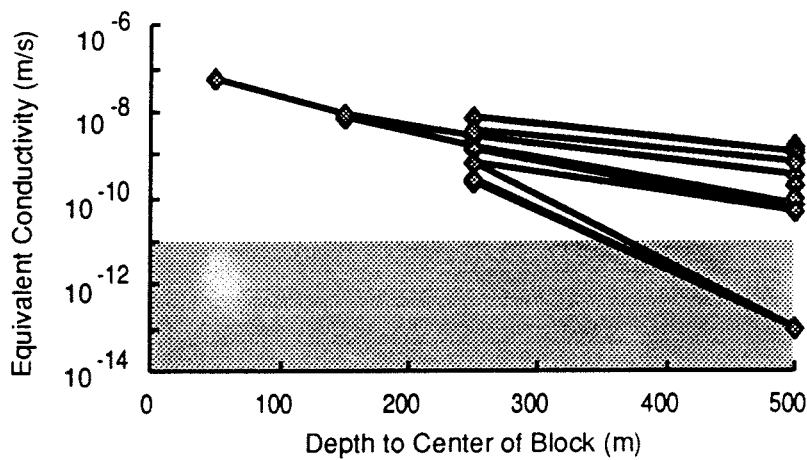
arithmetic mean of all three directional conductivities, and (b) the arithmetic mean of the two horizontal conductivities. In both plots the correlation is extremely weak. Other possible ways of plotting these data (*e.g.* comparison of geometric means, and plots of single K_{Moyes} vs. K_v values) show similarly poor correlation.



a) North-South flow

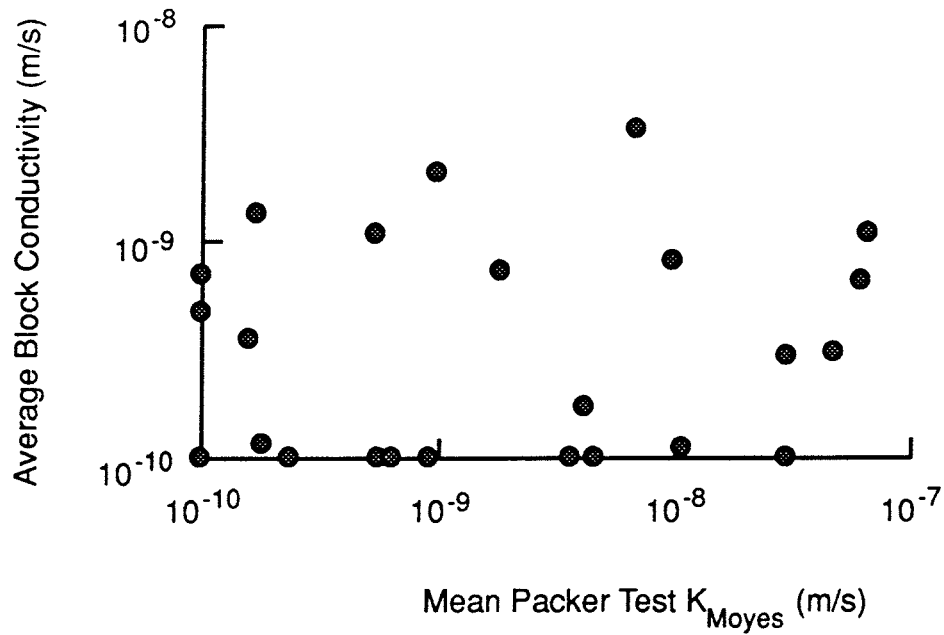


b) East-West flow

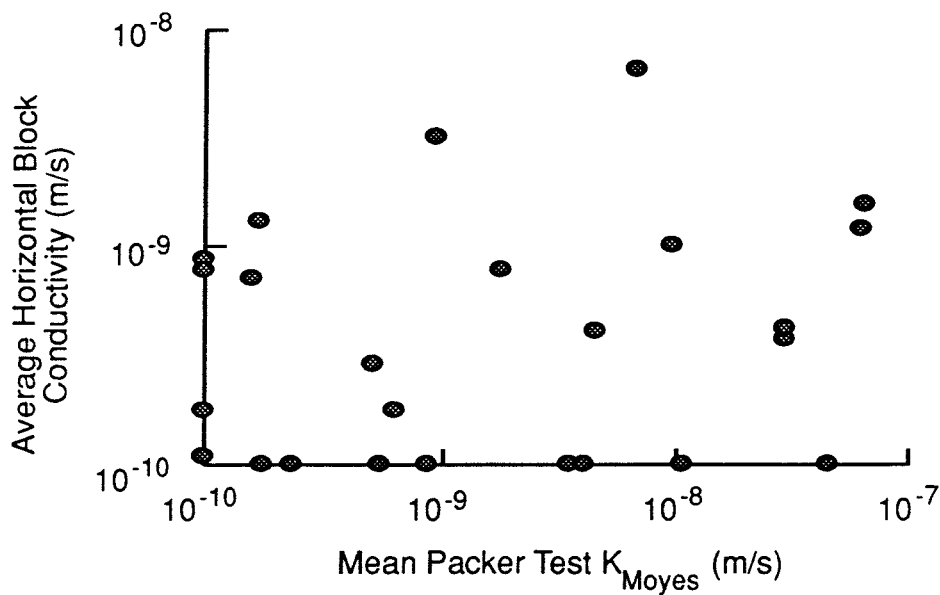


c) Up-Down flow

FIGURE 7-2
TRENDS IN BLOCK-SCALE CONDUCTIVITY WITH DEPTH
SKB-91/DFNST



a) Comparison of average block-scale conductivity (mean of all 3 directional measurements) with arithmetic mean of 5 packer test measurements near the center of the block.



b) Comparison of average horizontal block-scale conductivity (mean of N-S and E-W directional measurements), with the arithmetic mean of 5 packer test measurements near the center of the block.

FIGURE 7-3
CORRELATION OF BLOCK-SCALE CONDUCTIVITY
TO MULTIPLE PACKER TEST MEASUREMENTS

SKB91 DFNST

8. ESTIMATION OF TRANSPORT PARAMETERS

Transport parameters (flow porosity ϕ_w , rock-mass specific wetted surface S_w , and flow specific wetted surface S_w) were estimated by postprocessing the results of cross-block flow simulations, for 40 m blocks at 500 m depth. Two types of estimates were produced:

- The distribution of flux-weighted averages from multiple simulations, plotted as frequency *vs.* porosity/wetted surface.
- Estimates of effective porosity/wetted surface for different element flux ranges, plotted as average values for all simulations, *vs.* flux magnitude.

The first type of estimate is considered to be appropriate for the DPST model. The second type provides insight into the distribution of porosity and wetted surface among flow paths of varying magnitude, within the DFN model. These values may be of interest for comparison with values used in the CN model. Formulae for calculating these quantities from the flow simulations are given in §4.6. It is stressed here that these estimates are based on simplistic empirical models fitted to a very small dataset of field estimates, and that the empirical models used are not very satisfactory, but simply an example of what can be done with existing data.

Two sets of estimates were produced, one for the "base case," and one for the case where all fractures with $T > 10^{-6.7}$ are assumed to be breccia-filled, with a conductivity-porosity-wetted surface relationship of a typical sandy aquifer (properties as given in §5.8 of the report). The main reason for including this case was to investigate the effects on specific wetted surface, since for a breccia-filled fracture, s_w (the wetted surface per unit area of the fracture plane) may be orders of magnitude higher than for a coated fracture.

Estimates were produced for averaging volumes on scales ranging from 20 m to 40 m. This report presents results only for 35 m averaging volumes centered in the blocks. The estimates are presented for flow in response to unit gradients in the x , y , and z directions, corresponding to North-South, East-West, and Up-Down gradients, respectively. The block-scale conductivities in the x and y directions are generally higher than in the z direction, by about an order of magnitude (see §7).

The plots do not include estimates for blocks with directional conductivities below $10^{-10.5}$ m/s (approximately the resolution of the model) on the 40 m scale. Also, for a few blocks no solution was produced, in most cases due to memory limits, and occasionally due to "pathological" fracture intersections which resulted in poorly conditioned meshes. Although it

would be possible to produce results in the latter cases by manual modification of the meshes, this was not done, to avoid bookkeeping difficulties. Table 8-1 summarizes the simulation results.

Table 8-1. Summary of 40 m block simulations.				
Flow Direction	Total number of simulations	Successful simulations	Conductivity below threshold	"Conductive" blocks
X	30	27	3	24
Y	30	26	4	22
Z	30	27	4	23

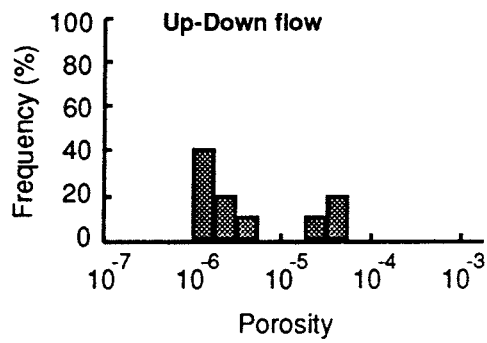
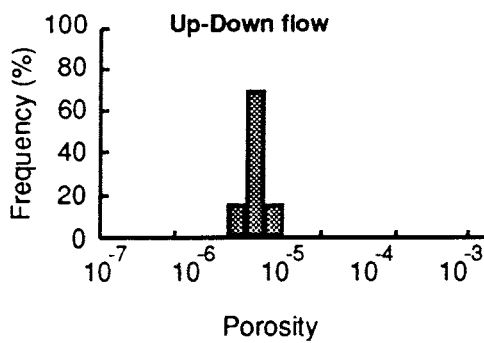
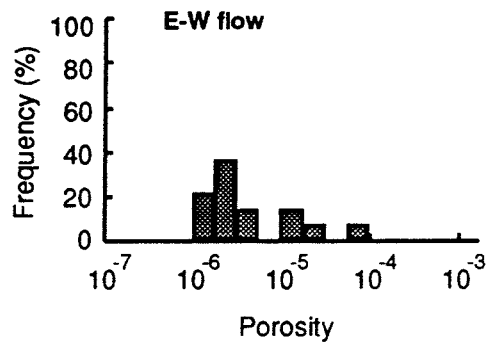
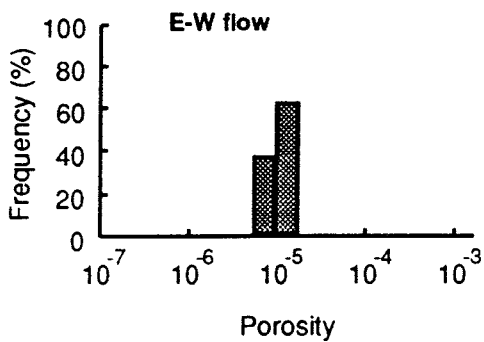
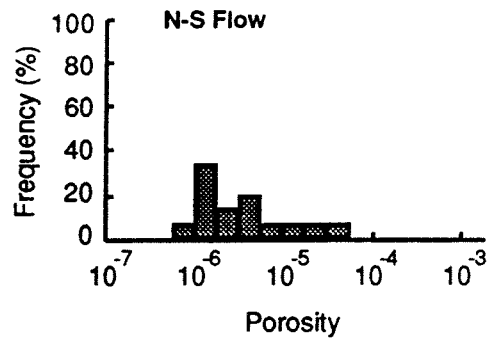
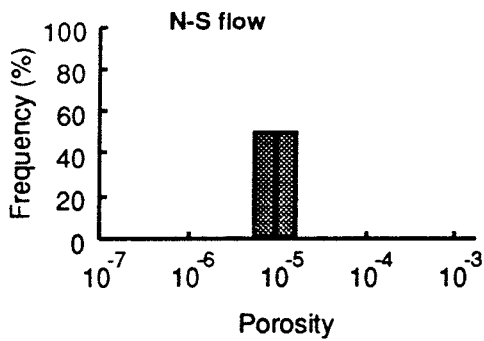
8.1 Flow Porosity

Flux-weighted estimates of flow porosity, ϕ_Q (Figure 8-1) for the base case are tightly clustered around 6×10^{-6} . The mean estimate is fairly independently of flow direction.

The low variance in ϕ_Q indicates that, for the DFN model used, a 35 m volume contains a sufficient number of pathways for the effects of fracture population heterogeneity to be "averaged out," in terms of the porosity of the major flow paths. A larger variance for ϕ_Q might be expected for this scale if the fracture transport properties are strongly correlated along the major flowpaths.

The ϕ_Q values for the breccia case are *lower* than for the base case. This is somewhat surprising at first glance, but follows from the relationships used for flow aperture ϵ_v vs. hydraulic aperture ϵ_h . The empirical model for the base case allows for a high ratio ϵ_v/ϵ_h , which results from highly variable fracture aperture in natural fractures, arising from any number of causes (The cases used to estimate this relation might even include breccia-filled fractures).

The rule used for the breccia case assumes a uniform mechanical aperture filled with "sand." For the most conductive fractures (roughly $T > 10^{-6} \text{ m}^2/\text{s}$), this gives a higher ϕ_Q to the "breccia-filled" fractures, but for the fractures in the range $10^{-6.7} T < 10^{-6} \text{ m}^2/\text{s}$ (which are much more frequent), the rule for "breccia-filled" fractures gives a *lower* porosity than the empirical model for the base case. Since the fractures in the range $10^{-6.7} T < 10^{-6} \text{ m}^2/\text{s}$ dominate the ϕ_Q estimates, the result is that the porosities for the breccia case are generally lower than for the base case.



a) Base Case

b) Breccia Case

Flow Direction	N	Mean	Standard Deviation	Minimum	Maximum
X	18	6.11E-6	1.17E-6	4.88E-6	8.20E-6
Y	16	4.95E-6	4.73E-6	4.66E-6	4.07E-5
Z	13	5.18E-6	5.58E-6	4.91E-6	2.60E-5

Flow Direction	N	Mean	Standard Deviation	Minimum	Maximum
X	15	4.56E-6	6.71E-6	5.50E-7	2.29E-5
Y	14	5.66E-6	1.05E-5	9.12E-7	4.07E-5
Z	10	6.73E-6	9.59E-6	6.30E-7	2.60E-5

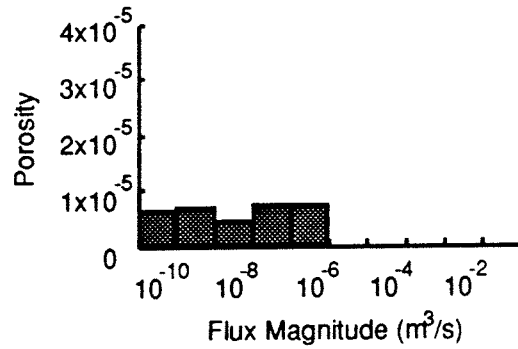
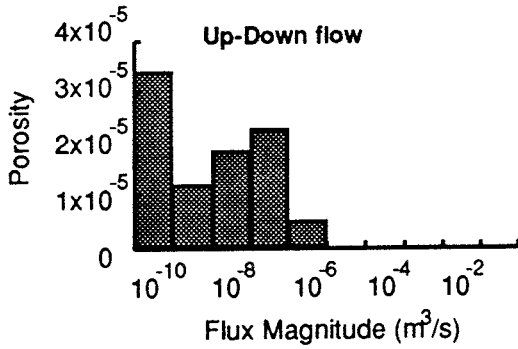
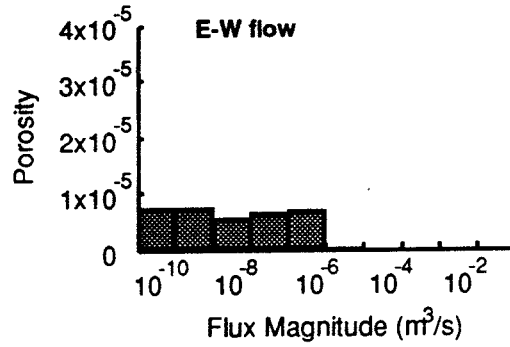
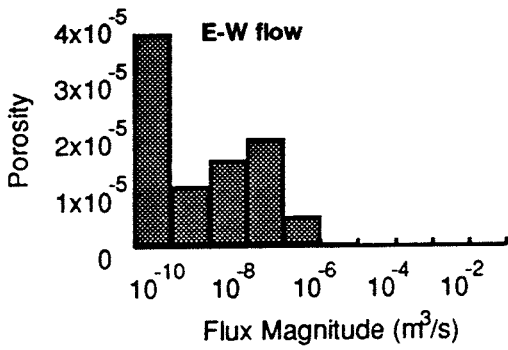
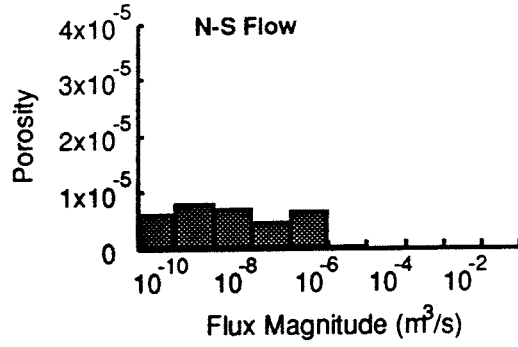
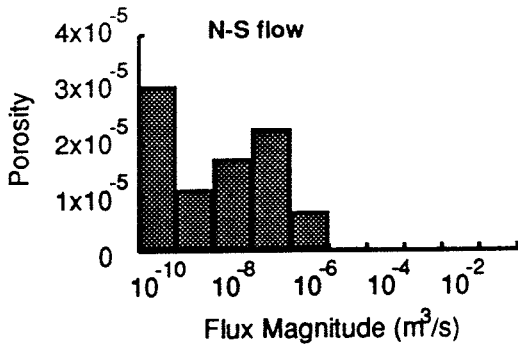
FIGURE **8-1**
FLUX-WEIGHTED ESTIMATES OF FLOW POROSITY
 SKB/SKB91 DFNST

The estimates of ϕ_Q for the the breccia case should therefore be disregarded, except insofar as the *magnitude* of the difference between the two cases suggests how sensitive this calculation is to the assumptions used. The wetted surface estimates for the breccia case are of more interest, as discussed below.

Plots of porosity fraction as a function of *vs.* flux magnitude (Figure 8-2) give a more detailed picture of the distribution of porosity among flow paths. The fractions for flux magnitudes $> 10^6$ m³/s are approximately equal to the flux-weighted estimates. The appearance of the histograms suggests that porosity may be modelled as a function of flux magnitude, somewhat more right-skewed than:

$$f(Q) = C_1 e^{-C_2 (\log Q)^2} \quad (5-13)$$

The histogram bars for 10^{-10} m³/s include values for all fracture elements with $Q < 10^{-10}$ m³/s, so these do not necessarily indicate a bimodal function.



a) Base Case

b) Breccia Case

FIGURE 8-2
 POROSITY AS A FUNCTION OF FLUX MAGNITUDE
 SKB/SKB91 DFNST

8.2 Specific wetted surface

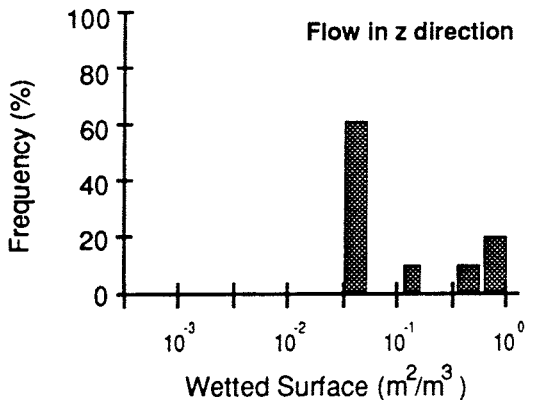
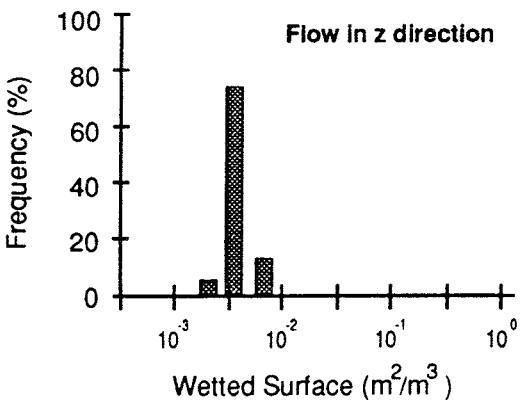
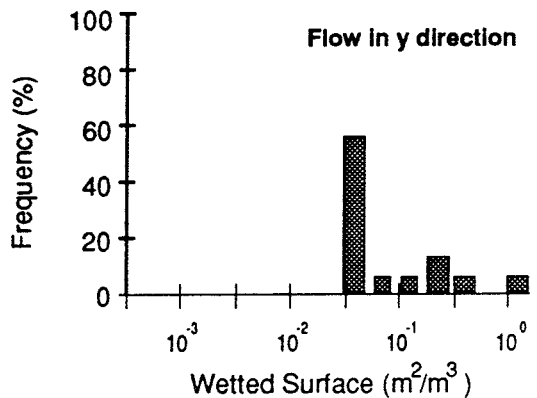
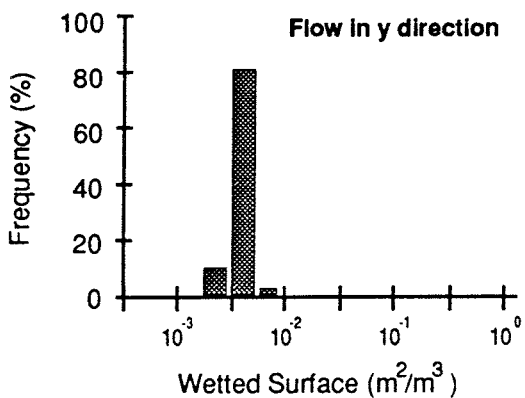
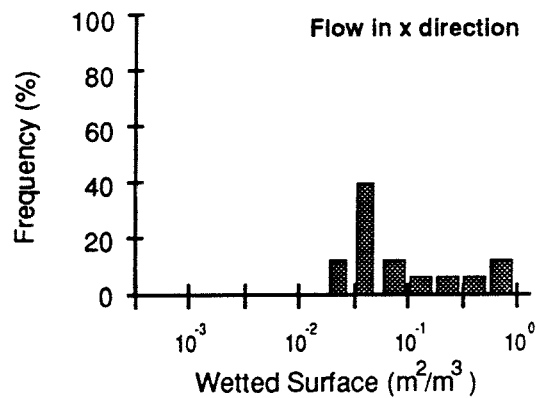
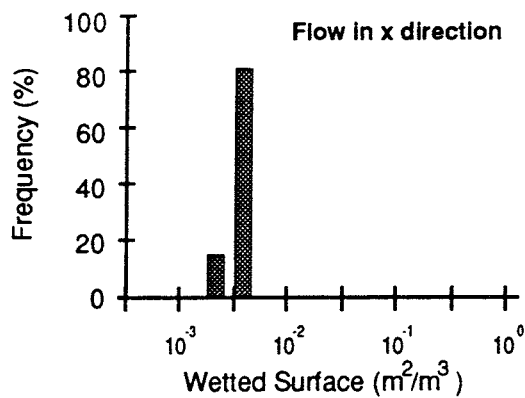
Specific wetted surface estimates are given both in terms of S_w , the wetted surface area per unit volume of rock, and S_{wQ} , the wetted surface per unit volume of flowing (mobile) water. The latter quantity, S_{wQ} , is used in the DPST model. The quantity S_b is obtained as an intermediate result, and is of interest for the CN formulation of the transport process, and possibly for matrix diffusion calculations, for cases in which the range of matrix diffusion is larger than the dimensions of the flow conduits (*cf.* Neretnieks, 1990) so that S_b may have a limiting effect.

Figures 8-3 and 8-4 give distributions of flux-weighted estimates of S_w , and distributions of S_b , as a function of flux magnitude, respectively. The flux-weighted estimates of S_b are clustered tightly around around $2 \times 10^{-3} \text{ m}^2/\text{m}^3$. These estimates are fairly independent of flow direction.

The mean flux-weighted estimates of S_b for the breccia case are two orders of magnitude higher than for the base case, and the variance is greatly increased. The increase in the mean S_b follows directly from the expected tendency for high- T_f fractures to be included in the most important flow paths, and the much higher s_w values for these fractures if they are breccia-filled. The increased variance results from the rarity of these high- T_f fractures.

The high wetted surface for the less frequent, more conductive fractures results in a nearly uniform distribution of wetted surface with respect to flux magnitude, for the particular case modelled.

Figures 8-5 and 8-6 give the corresponding estimates for flow specific wetted surface, S_{wQ} . These were calculated from the S_b estimates for each block, by dividing by the estimated flow porosity ϕ_Q . Due to the small variance for ϕ_Q , little difference is seen in the figures except for a change of scale. An exception to this is the set of histograms showing S_{wQ} fractions as a function of flux magnitude, where a nearly uniform distribution is seen on the log scale (as opposed to a right-skewed distribution). This results from a rough, negative sample correlation between S_{wQ} and ϕ_Q , as shown in Figure 8-7, which is not statistically significant. This appearance of the plots could thus be an artifact of the small number of simulations.



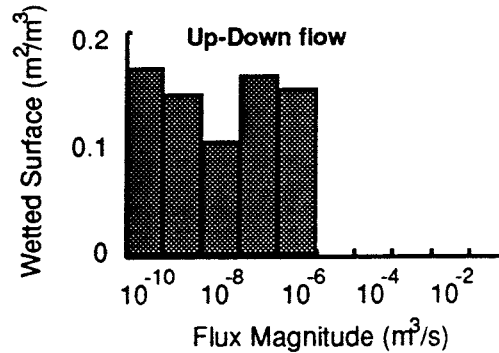
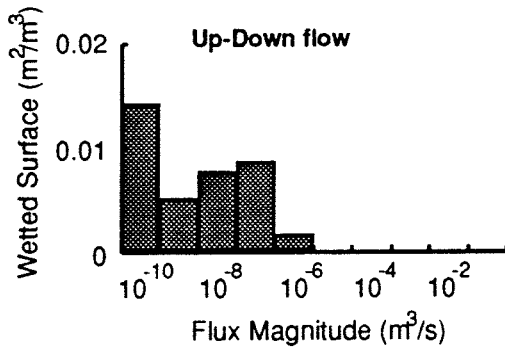
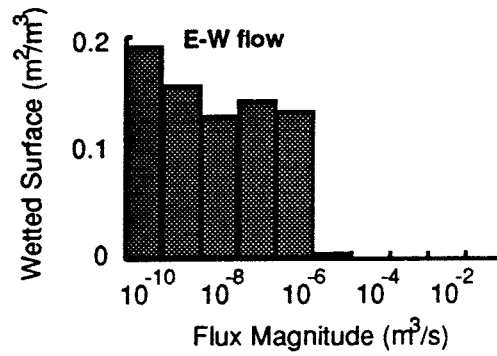
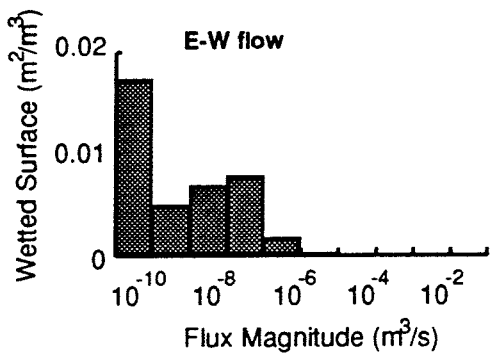
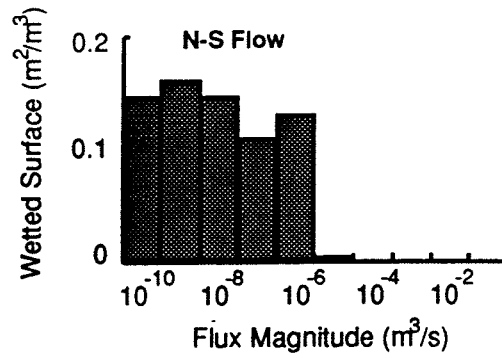
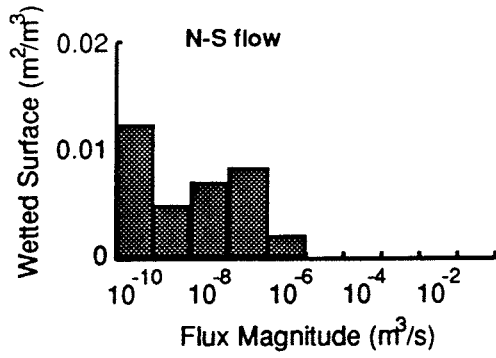
a) Base Case

b) Breccia Case

Flow Direction	N	Mean	Standard Deviation	Minimum	Maximum
X	18	2.14E-03	3.60E-04	1.44E-03	2.90E-03
Y	16	2.25E-03	4.93E-04	1.38E-03	3.26E-03
Z	13	2.51E-03	6.09E-04	1.42E-03	3.77E-03

Flow Direction	N	Mean	Standard Deviation	Minimum	Maximum
X	15	0.092	0.129	0.015	0.442
Y	14	0.113	0.201	0.022	0.783
Z	10	0.134	0.184	0.020	0.502

FIGURE 8-3
FLUX-WEIGHTED ESTIMATES OF ROCK-MASS
SPECIFIC WETTED SURFACE
 SKB/SKB91 DFNST

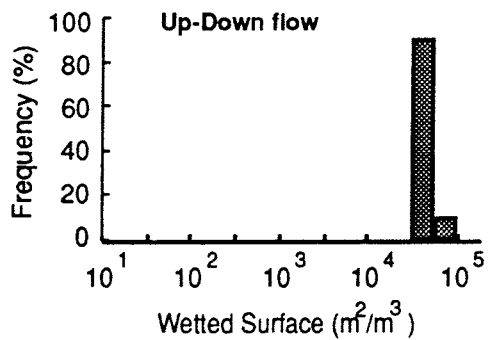
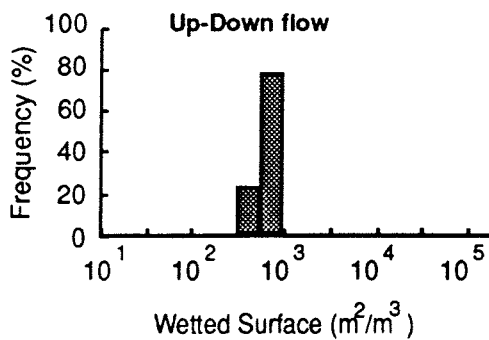
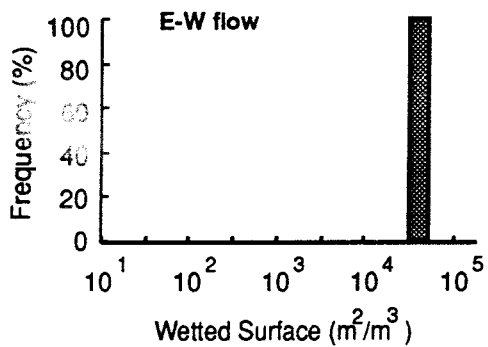
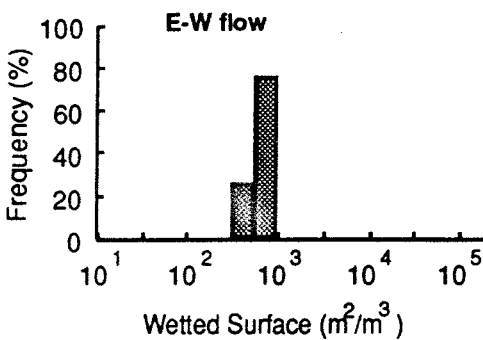
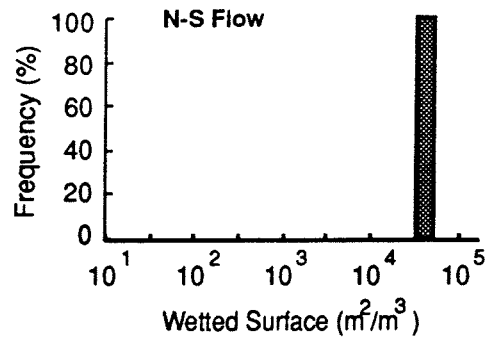
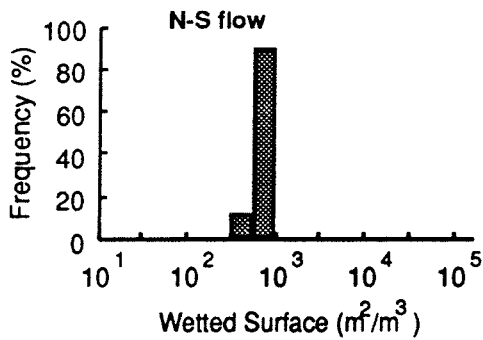


a) Base Case

b) Breccia Case

FIGURE 8-4
**ROCK-MASS SPECIFIC WETTED SURFACE
 AS A FUNCTION OF FLUX MAGNITUDE**

SKB/SKB91 DFNST



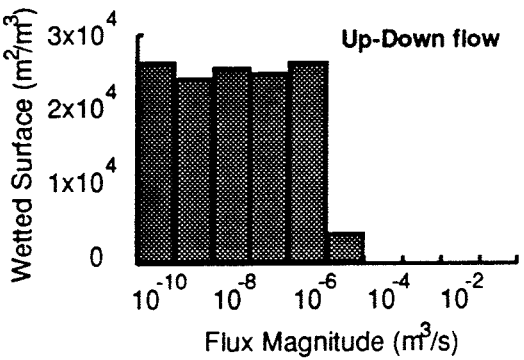
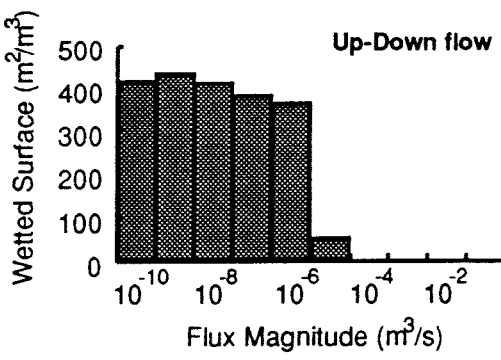
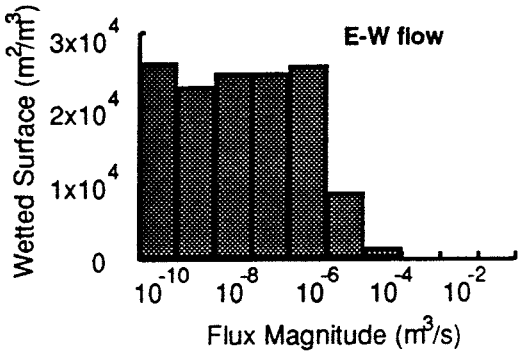
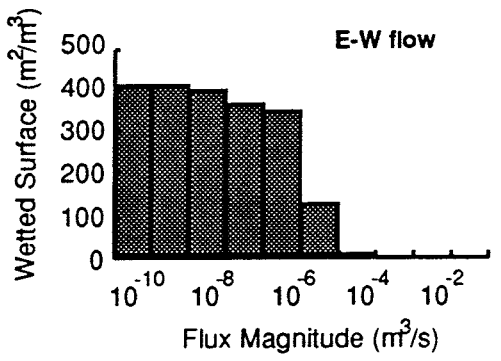
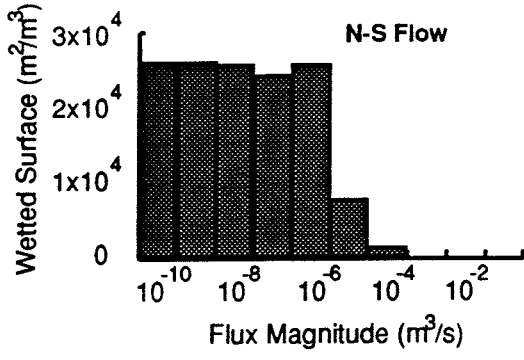
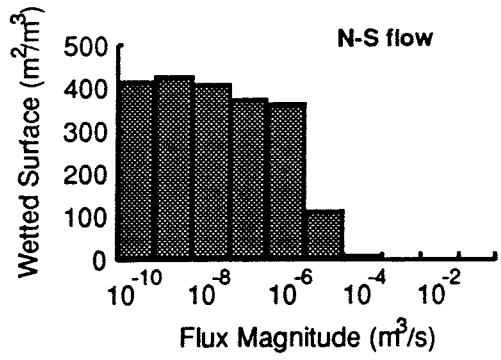
a) Base Case

b) Breccia Case

Flow Direction	N	Mean	Standard Deviation	Minimum	Maximum
X	18	354	42	267	425
Y	16	347	59	236	468
Z	13	351	53	256	437

Flow Direction	N	Mean	Standard Deviation	Minimum	Maximum
X	15	22,710	3140	19,320	28,930
Y	14	22,470	2960	19,270	28,380
Z	10	23,830	5150	19,290	33,780

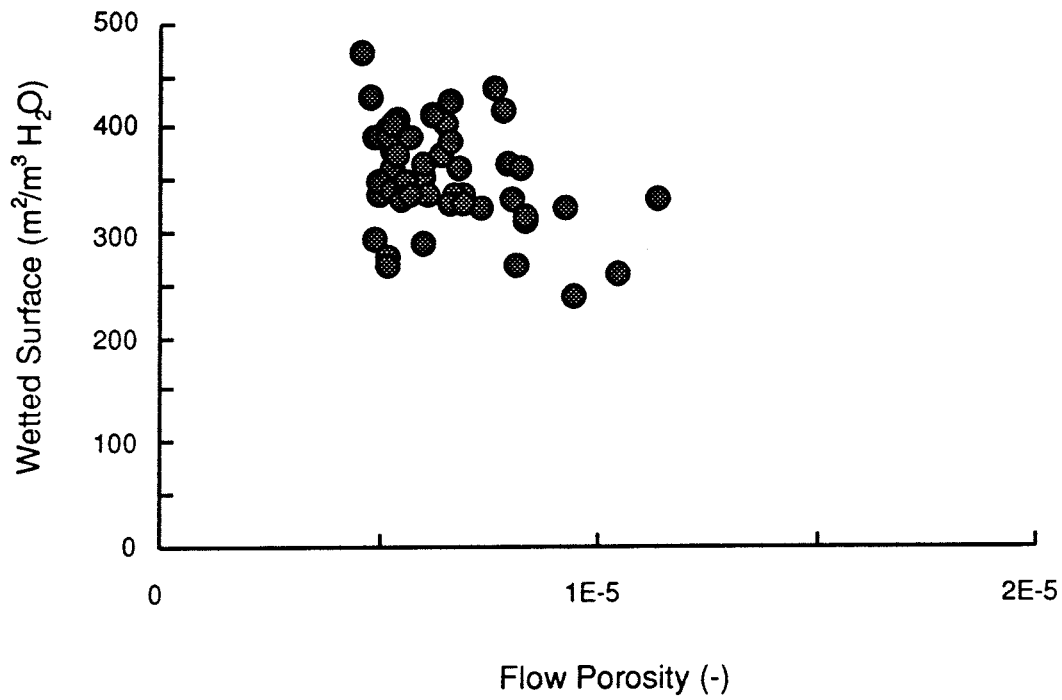
FIGURE **8-5**
FLUX-WEIGHTED ESTIMATES
OF FLOW SPECIFIC WETTED SURFACE
 SKB/SKB91: DFNST



a) Base Case

b) Breccia Case

FIGURE 8-6
**FLOW SPECIFIC WETTED SURFACE
 AS A FUNCTION OF FLUX MAGNITUDE**
 SKB/SKB91 DFNST



Regression Model: $S_{wQ} = A + B \phi_Q$

A	429
Standard Error of a' Estimate	47
R Squared	0.137
No. of Observations	47
Degrees of Freedom	45

B Estimate	-1.196E7
Standard Error of B	4.478E6

FIGURE 8-7
**CORRELATION OF FLOW SPECIFIC WETTED SURFACE
 TO FLOW POROSITY**
 SKB/SKB91 DFNST

9. DISCUSSION OF RESULTS

This report considers a wide range topics, including:

- Characterization of the fracture system geometry at Finnsjön
- Interpretation of flow dimension for transient packer tests
- Review of the information available regarding the detailed hydrologic properties of single fractures
- Tests of the sufficiency of the database for highly-conductive features
- Development of a methodology for a discrete-fracture-network/stochastic-continuum interface
- Estimation of block-scale flow properties
- Estimation of correlations between packer test results and block-scale properties
- Estimation of transport properties based on extrapolation from block-scale flow simulations.

Discussion of specific issues related to the above topics is given in the corresponding sections of the report. The following sections discuss some issues of general importance for interpreting the results.

9.1 Limitations of the DFN model

The DFN model used for these simulations was necessarily simplified due to:

- Lack of geometric data at depth.
- Constraints of the SC interface.

The DFN model was developed to the level of detail appropriate, in consideration of these constraints. The modelling approach did not incorporate a large amount of "soft" geological data regarding heterogeneity in the fracture population. In an actual repository safety assessment, "soft" data should be used to identify heterogeneous regions in the rock. This will lead to multi-domain DFN models. Further development of the DFN/SC interface will be needed to handle this case.

The most serious waste of information was for Zone 2, which is the most well-characterized rock unit. The unconditional, single-domain model used is not constrained to produce a large-scale structure in the same location, and with the same observed, small-scale structures as seen in boreholes through Zone 2.

However, the model can produce large-scale, subhorizontal zones with an internal structure similar to Zone 2 (multiple subzones with predominantly horizontal connection but with irregular properties and interconnection), since the model includes some locational autocorrelation of the major features, and contains a tendency for horizontal fractures to be more conductive due to a lower vertical stress.

Some of the limitations of the dataset, such as the lack of fracture orientation and size data at depth, would be less problematic in a risk assessment for an actual repository, particularly for a final risk assessment when detailed subsurface data should be available. Even for a preliminary site investigation, it is now feasible to obtain full fracture orientation data from boreholes, using recently developed logging tools. Thus some of the dataset limitations encountered in the present study would simply not exist if the characterization program were repeated today, using state-of-the-art methods, with an emphasis on procuring data specifically for a DFN model.

9.2 Computational limitations

The relatively high degree of fracturing in the Finnsjön block makes modeling of the full conductive fracture population expensive in terms of computer time, particularly for the stress-relieved, near-surface region. The necessity of truncating the transmissivity distribution above the field measurement threshold, in the near-surface packer test simulations, led to some complications in interpreting the validation results. For the block-scale simulations this restriction is less significant, due to the much lesser importance of the low- T_f fractures in cross-block flow.

9.3 Estimates of transport parameters

The estimates of transport parameters are based on extrapolation from flow simulations, based on some simple relationships between hydraulic aperture, void aperture, and fracture specific wetted surface. The limitations of this approach should be borne in mind, particularly:

- The limited database for single-fracture detailed hydrologic properties.
- The extremely limited database for fracture infilling properties.
- The complete lack of data for detailed properties on the scale of a few fractures, including possible correlation of channeling between fractures.
- The assumption that flow paths result only from random combinations of fracture geometry, due to this lack of data.

Calibration of the model to tracer tests could reduce these limitations, but this was not possible within the current project scope. Nevertheless, the current model predictions are of interest, simply because the methods for estimating transport properties from tracer tests are not very reliable, particularly for the "average rock."

The estimates of flow porosity and specific wetted surface obtained in §7 can be compared with values estimated by interpretation of tracer tests in granite. The estimate $\phi_Q \approx 6 \times 10^{-6}$ is lower by 2-3 orders of magnitude than the estimates given by Andersson *et al.* (1991), based on intervals within highly-conductive sections in Zone 2. The estimates given here are a factor of 4 to 25 lower than the interpreted results of the 3-D Tracer Migration Experiment at Stripa (Neretnieks *et al.*, 1989).

The flow specific wetted surface estimates for the base case ($S_{wQ} \approx 350 \text{ m}^{-1}$) are larger by two orders of magnitude than the estimates obtained from the Stripa experiment. The estimates obtained here are extremely high by comparison, but there are great differences in flow geometry and rock conductivity. The average conductivity for the Stripa experiment was estimated as 2×10^{-11} to 4×10^{-11} m/s, which is about 2 orders of magnitude than the estimates obtained here for the Finnsjön rock.

The S_{wQ} estimates depend on the estimates of ϕ_Q . Therefore assumption of a larger value of ϕ_Q would give a proportional decreases in the S_{wQ} estimates. The S_i values are independent of the porosity estimates, and thus may be used to obtain S_{wQ} estimates based on alternative values for ϕ_Q . An assumed flow porosity of 10^{-4} would give S_{wQ} estimates on the order of $25 \text{ m}^2/\text{m}^3$.

10. CONCLUSIONS

10.1 Site Characteristics

A review of the data for the Finnsjön site indicates the following main points regarding fracture zones at the site:

- The site contains a multitude of "minor" fracture zones. Evidence for this is seen in lineament maps and borehole radar interpretations.
- Most of the zones have not been characterized in any detail.
- The most well-characterized zone (Zone 2) shows signs of lateral heterogeneity.
- For 10 of the 14 "major" zones, heterogeneity cannot be evaluated because only one borehole (at most) intersects the zone.

Regarding the population of individual fractures at the site:

- Fracture frequency in core indicates that the northern block above Zone 2 is less fractured than the rest of the Finnsjön block.
- Core data also indicate local heterogeneity in the fracture population on a scale less than 100 m.

However, geometric data from subsurface are not adequate for a detailed fracture model with multiple subregions. The local heterogeneity seen in core may correspond to organization of fractures in minor zones.

A large number of packer test measurements is perhaps the strongest part of the dataset, for development of a DFN model. However, a large number of fractures near the packer-test measurement threshold leads to non-uniqueness in DFN model parameters.

GRF analysis of transient tests shows a distinct set of low flow dimension, high-T test intervals, indicating local behavior similar to a channel network or sparse fracture network. Thus **some significantly transmissive sections show markedly non-continuum behaviour**. However, many high-transmissivity intervals show high flow dimension, indicating much of the rock behaves locally (*i.e.*, on the scale of a packer test) as a well-connected fracture network.

10.2 Discrete Fracture Network Model

The evidence of a **multitude of minor fracture zones** on a range of scales implies a multi-level structure for the fracture system. This was represented by a two-stage DFN model consisting of zones and locationally correlated fractures. The distributions of single-fracture properties (*e.g.* orientation) are considered to be of lesser importance than this spatial structure. The main features of the model were:

- A single fracture population throughout the rock mass. This is assumed due to the lack of geometric data at depth.
- Presence of fracture zones on a wide range of scales, including zones which could not be characterized deterministically within the scope of the SKB 91 program.
- Spatial structure (heterogeneity) due to clustering of fractures in major and minor zones.

Simulated packer tests show that this fracture model adequately reproduces the observed transient test response, for short-duration tests in 2 m sections. Most importantly, the model adequately reproduces the distribution of flow dimension, which indicates that the **variability of connectivity** within the model approximates that of the real fracture system.

This model was used to predict block-scale flow properties and effective transport parameters.

10.3 Effective block-scale conductivity

The model predicts moderate block anisotropy on the scale $s = 40$ m, with horizontal conductivity typically higher than vertical conductivity, by typically less than an order of magnitude. A trend in conductivity with depth is indicated, with a decrease in K_f of 2 orders of magnitude, from 50 m to 500 m depth.

The results of even multiple 2 m tests are predicted to be poorly correlated to 40 m block-scale conductivity. For constant-head packer tests which are comparable to the tests which comprise a large part of the Finnsjön data set (in terms of scale and duration), even a set of 5 packer tests, all near the center of a block, gives very little information about the block conductivity on a 40 m scale. This means "conditional" SC models based on such data may not

be "well-conditioned." This prediction is consistent with sampling probabilities for a conductivity field with a multi-scale structure.

10.4 Effective transport parameters

Estimates of transport parameters (flow porosity and specific wetted surface) were calculated from the block-scale flow simulations, based on the geometry of the fracture network, the calculated flow fields, and simple models for the relationships between fracture transmissivity, void aperture, and wetted surface. These models are based on a very small database for single-fracture properties. Flow porosity is estimated using an empirical relationship between transmissivity and transport aperture, based on single-fracture experiments. Specific surface is estimated using *plausible* relationships for coated or breccia-filled fractures. The model for flow porosity thus has a somewhat stronger basis than the model for specific surface.

The flow porosity estimates (about 6×10^{-6}) are roughly an order of magnitude less than values estimated from tracer tests at the Stripa site. The estimates of flow specific wetted surface, S_w , are two orders of magnitude or more higher than estimates from Stripa. However, the estimates of both flow porosity and S_w are comparable to independent estimates which were considered to be reasonable for the more highly fractured rock at Finnsjön (Anders Ström, personal communication, February, 1992). A variational study indicates that estimates of S_w are strongly dependent on fracture infilling structure, for which the database is extremely weak.

10.5 Methodology

This project used a DFN model in an effort to bridge the gap between site characterization methods and site-scale flow and transport models. A major result has been the development and demonstration of a DFN methodology to interpret packer tests in terms of fracture network properties, and:

- Predict relationships between packer test results and block-scale properties.
- Predict autocorrelation of conductivity for a rock mass containing fracture zones on a wide range of scales.

Current stochastic continuum approaches require assumptions on these points. The methodology developed in the present study may eventually may prove useful for testing the adequacy of these assumptions, for future sites, particularly sites where more geometric data are available for development of a DFN model.

This project also demonstrates the use of transient packer test data to validate a DFN model in terms of hydraulic behavior. In particular, flow dimension provides a measure of how well the local-scale connectivity of the model matches that of the rock mass.

The present study highlights the need for more information regarding:

- The effects of stress on flow through a fractured rock mass.
- The nature of channelling in fracture networks.
- The effects of fracture infilling on transport properties.

The shortage of data on single-fracture properties (infilling types, structure, and channeling) and data regarding channeling on the scale of a few fractures, is a major barrier to obtaining more reliable estimates of transport properties.

10.6 Recommendations for further study

Further **field investigations** are needed to focus on detailed properties on the scale of a few connected fractures. For investigation of channeling effects both within and between fractures, there is a clear need for more *in situ* testing on a relevant scale. However, **multivariate analysis of core and conductivity data** could provide some insight into single-fracture properties. A more systematic treatment of important features such as crush zones in core is recommended to support this type of analysis.

Back-analysis of existing, small-scale tracer test data by calibration of the DFN model is recommended to minimize uncertainty in DFN predictions of transport parameters, given the existing database.

11. ACKNOWLEDGEMENTS

The modelling work described in this report was funded by SKB. The project managers, Nils Kjellbert and Anders Ström, deserve thanks for their help in defining the project goals, suggestions regarding the estimation of transport parameters, and generally their patience throughout. Anders Ström and Sverker Nilsson of SKB both provided timely user-support for part of the work done on the SKB Convex. Discussions with Sven Tirén and Jan-Erik Andersson of Geosigma AB contributed to the development of the conceptual model, and also served to highlight the size of the gap which still exists between discrete fracture models and geological reality. Sven Norman, formerly of STARPROG AB, provided most of the ideas for the DFN/SC interface. Lastly, credit is owed to Bill Dershowitz, Tom Doe, Ian Miller, and the rest of the fracture-flow group in the Seattle office of Golder Associates, for their work in developing the overall methodology.

12. REFERENCES

Abelin, H., L. Birgersson, J. Gidlund, L. Moreno, I. Neretnieks, H. Widén, and T. Ågren, 1987. "3-D migration experiment - Report 3, Part I. Performed experiments, results and evaluations," Stripa Project Technical Report 87-21, SKB, Stockholm.

Abelin, H., L. Birgersson, H. Widén, T. Ågren, L. Moreno, and I. Neretnieks, 1990. "Channeling Experiment," Stripa Project Technical Report 90-13, SKB, Stockholm.

Abelin, H, I. Neretnieks, S. Tunbrant, and L. Moreno, 1985. "Final report of the migration in a single fracture - Experimental results and evaluation," Stripa Project Technical Report 85-03, SKB, Stockholm.

Ahlbom, K., P. Andersson, L. Ekman, E. Gustafsson, J. Smellie, and E-L Tullborg, 1986. "Preliminary investigations of fracture zones in the Brändan area, Finnsjön study site," SKB Technical Report 86-05, SKB, Stockholm.

Ahlbom, K., P. Andersson, L. Ekman, and S. Tirén, 1987. "Characterization of fracture zones in the Brändan area, Finnsjön study site, Central Sweden," SKB Technical Report 88-09, SKB, Stockholm.

Ahlbom, K. and S. Tirén, 1991. "Overview of geologic and geohydrologic conditions at the Finnsjön site and its surroundings," SKB Technical Report 91-08.

Andersson, J-E, L. Ekman, E. Gustafsson, R. Nordqvist, and S. Tirén, 1989a. "Hydraulic interference tests and tracer tests within the Brändan area, Finnsjön study site -- The Fracture Zone Project -- Phase 3," SKB Technical Report 89-12, SKB, Stockholm.

Andersson, J-E, R. Nordqvist, G. Nyberg, J. Smellie, and S. Tirén, 1991. "Hydrogeological conditions in the Finnsjön area -- compilation of data and conceptual model," SKB Technical Report 91-xx, SKB, Stockholm.

Andersson, J-E, L. Ekman, R. Nordqvist, and A. Winberg, 1989b. "Hydraulic testing and modelling of a low-angle fracture zone at Finnsjön, Sweden," in SKB Technical Report 89-19, SKB, Stockholm.

Andersson, J-E. and L. Lindqvist, 1988. "Prediction of hydraulic conductivity and conductive fracture frequency by multivariate analysis of data from the Klipperås study site," SKB Technical Report 89-11, SKB, Stockholm.

Andersson, P., and S. Carlsten, 1987. "Radar measurements performed in Borehole BFi 2 within the Brändan area, Finnsjön study site," SGAB IRAP 87 399, Swedish Geological Co., Uppsala.

Axelsson, C-L., E-K. Jonsson, J.E. Geier, and W.S. Dershowitz, 1990. "Äspö Hard Rock Laboratory Discrete Fracture Modelling", SKB HRL Progress Report 25-89-21, SKB, Stockholm.

Bandis, S., A.C. Lumisden, and N.R. Barton, 1981. "Experimental studies of scale effects on the shear behaviour of rock joints," *Int. J. Rock Mechanics, Mining Science and Geomechanics Abstracts* Vol. 18, pp. 1-21.

Bandis, S., A.C. Lumisden, and N.R. Barton, 1983. "Fundamentals of rock joint deformation," *Int. J. Rock Mechanics, Mining Science and Geomechanics Abstracts* Vol. 20, pp. 249-268.

Barker, J.A., 1988. "A Generalized Radial-Flow Model for Pumping Tests in Fractured Rock," *Water Resources Research*, Vol. 24, pp. 1796-1804.

Bear, J., 1972. *Dynamics of Fluid Flow in Porous Media*, Dover Publications, New York, New York.

Bjarnesson, B. and O. Stephansson, 1988. "Hydraulic fracturing stress measurements in the borehole Fi 06, Finnsjön site," SKB Working Report R&D 88-54, SKB, Stockholm.

Brown, S.R., 1987. "Fluid flow through rock joints: The effect of surface roughness," *Journal of Geophysical Research*, Vol. 92, 1337-1347.

Brown, S.R. and C.H. Scholz, 1985. "Broad bandwidth study of the topography of natural rock surfaces," *Journal of Geophysical Research*, Vol. 90, pp. 12,575-12,582.

Brown, S.R. and C.H. Scholz, 1986. "Closure of rock joints," *Journal of Geophysical Research*, Vol. 91, pp. 4939-4948.

Brown, S.R., R.L. Kranz, and B.P. Bonner, 1986. "Correlation between the surfaces of natural rock joints," *Geophysical Research Letters*, Vol. 13, pp. 1430-1434.

Bourke, P.T., 1987. "Channeling of flow through fractures in rock," *Proceedings of the GEOVAL - 87 International Symposium*, Stockholm, April 7-9.

Cacas, M.C., E. Ledoux, G. de Marsily, B. Tillie, A. Barbreau, E. Durand, B. Feuga, and P. Peaudecerf, 1990a. "Modelling fracture flow with a stochastic discrete fracture model -- Calibration and validation: 1. The flow model," *Water Resources Research*, Vol. 26, pp. 479-490.

Cacas, M.C., E. Ledoux, G. de Marsily, A. Barbreau, P. Calmels, B. Gaillard, and R. Margritta, 1990b. "Modelling fracture flow with a stochastic discrete fracture model -- Calibration and validation: 2. The transport model," *Water Resources Research*, Vol. 26, pp. 491-500.

Carlsten, S., L. Lindqvist, and O. Olsson, 1989. "Comparison between radar data and geophysical, geological, and hydrological borehole parameters by multivariate analysis of data." SKB Technical Report 89-15.

Carlsson, L. and G. Gidlund, 1983. "Evaluation of the hydrogeological conditions at Finnsjön," SKBF KBS Technical Report 83-56, SKB, Stockholm.

Carlsson, A. and T. Olsson, 1986. "Large scale in-situ tests on stress and water flow relationships in fractured rock," R,D&D report, Vattenfall, Vällingby.

Dershowitz, W.S., 1984. "Rock joint systems," PhD thesis, Department of Civil Engineering, Massachusetts Institute of Technology.

Dershowitz, W.S. and H. Herda, 1992. "Interpretation of fracture spacing and intensity," *Proceedings of the 33rd US Symposium on Rock Mechanics*, Santa Fe, New Mexico, June 3-5.

Dershowitz, W.S. and W.J. Roberds, 1990. "Methodology for evaluation of exploration strategies," Golder Associates report 883-1577 prepared for NAGRA, Baden, Switzerland.

Dershowitz, W.S., G. Lee, and J.E. Geier, 1991a. "FracMan Version β 2.3 Interactive Discrete Feature Data Analysis, Geometric Modelling, and Exploration Simulation User Documentation," Report 913-1358, Golder Associates Inc., Redmond, Washington.

Dershowitz, W.S., P. Wallmann, J.E. Geier, and G. Lee, 1991b. "Preliminary Discrete Fracture Network Modelling of Tracer Migration Experiments at the SCV Site," Stripa Project Technical Report 91-xx, SKB, Stockholm.

Dershowitz, W.S., P. Wallmann, and S. Kindred, 1991c. "Preliminary Discrete Fracture Modelling for the Stripa Site Characterization and Validation Drift Inflow Predictions," Stripa Project Technical Report 91-xx, SKB, Stockholm.

Desbarats, A.J. and R.M. Srivastava, 1991. "Geostatistical characterization of groundwater flow parameters in a simulated aquifer," *Water Resources Research*, Vol. 27, pp. 687-698.

Doe, T.W., 1990. "Analysis of large-scale cross-hole response at the Stripa SCV site," GAI Internal Report, Golder Associates Inc., Redmond, Washington.

Doe, T.W. and J.E. Geier, 1990. "Interpretation of Fracture System Geometry Using Well Test Data," Stripa Project Technical Report 91-03, SKB, Stockholm.

Doe, T.W. and J.D. Osnes, 1985. "Interpretation of fracture geometry from well tests," *Proceedings of the International Symposium on Rock Joints*, Björkliden, September, 1985.

Doe, T.W., M. Uchida, J.S. Kindred and W.S. Dershowitz, 1990. "Simulation of dual-porosity flow in discrete fracture networks," Paper No. CIM/SPE 90-120 presented at International Technical Meeting of the Petroleum Society of CIM and the Society of Petroleum Engineers, Calgary, Alberta, June 10-13.

Durlafsky, L.J., 1991, "Numerical calculation of equivalent grid block permeability tensors for heterogeneous porous media," *Water Resources Research*, Vol. 27, pp. 699-708.

Dverstorp B. and J. Andersson, 1990. "Estimation of effective transport parameters for predictive use in fractured rock," paper submitted to *Water Resources Research*, September, 1990.

Efron, B., 1982. *The Jackknife, the Bootstrap, and Other Resampling Plans*, monograph published by the Society for Industrial and Applied Mathematics, Philadelphia, Pennsylvania.

Elsworth, D. and T.W. Doe, 1986. "Application of non-linear flow laws in determining rock fissure geometry from single-borehole pumping tests," *International Journal of Rock Mechanics, Mineral Science, and Geomechanics Abstracts*, Vol. 23, pp. 245-254.

Endo, H.K., J.C.S. Long, C.R. Wilson, and P.A. Witherspoon, 1984. "A model for investigating mechanical transport in fracture networks," *Water Resources Research*, Vol. 20, pp. 1390-1400.

Eriksen, T.E., 1988. "Radionuclide transport in a single fissure -- A laboratory flow system for transport under reducing conditions," SKB Technical Report 88-28, SKB, Stockholm.

Eriksen, T.E. and B. Locklund, 1989. "Radionuclide sorption on granitic drill core material," SKB Technical Report 87-22.

Fournier, A., D. Fussell, and L. Carpenter, 1982. "Computer rendering of stochastic models," *Communications of the Association for Computing Machinery*, Vol. 25, pp. 371-384.

Gale, J.E., 1987. "Comparison of coupled fracture deformation and fluid flow models with direct measurements of fracture pore structure and stress-flow properties," *Proceedings of 28th U.S. Rock mechanics Symposium*, Tucson, Arizona, June 29-July 1, 1987.

Gale, J.E. and K.G. Raven, 1980. "Effects of sample size on the stress-permeability relationship for natural fractures," Report LBL-11865/SAC-48/UC-70, Swedish-American Cooperative Program on Radioactive Waste Storage in Mined Caverns in Crystalline Rock, SKB, Stockholm.

Geier, J.E., 1991. "EdMesh: Mesh Editor for the MAFIC discrete-fracture flow and transport model," GGAB internal report, Golder Geosystem AB, Uppsala.

Geier, J.E. and C-L Axelsson, 1991. "Discrete fracture modelling of the Finnsjön rock mass — Phase 1: feasibility study," SKB Technical Report 91-13.

Geier, J.E., Dershowitz, W.S., and G. Sharp, 1990. "Prediction of inflow into the D-holes at the Stripa mine," Stripa Project Technical Report 90-06, SKB, Stockholm.

Geier, J.E., K. Lee, and W.S. Dershowitz, 1989. "Field validation of conceptual models for fracture geometry," paper submitted to *Rock Mechanics and Rock Engineering*.

Gelhar, L.W., 1987. "Applications of stochastic models to solute transport in fractured rocks," SKB Technical Report 87-05, SKB, Stockholm.

Gentier, S., 1986. "Morphologie et comportement hydromechanique d'une fracture naturelle dans une granite sous contrainte normale," PhD. dissertation, L'Universite d'Orleans.

Gentier, S., D. Billaux, and L. van Vliet, 1989. "Laboratory testing of the voids of a fracture," *Rock Mechanics and Rock Engineering*, Vol. 22, pp. 149-157.

Gustafsson, E., and K-E Klockars, 1981. "Studies on groundwater transport in fractured crystalline rock under controlled conditions using nonradioactive tracers," KBS Teknisk Rapport 81-07.

Gustafson, G., 1990. "Identification and nomenclature of fracture zones," *Proceedings of the 3rd NEA/SKB Symposium on In Situ Experiments Associated with the Disposal of Radioactive Waste*, Stockholm, 3-4 October 1989, pp. 218-222. OECD, Paris.

Hakami, E., 1989. "Water flow in Single Rock Joints," Stripa Project Technical Report 89-08.

Hakami, E., A. Ekstav, and U. Qvarfort, "Sealing of rock joints by induced calcite precipitation. A case study from Bergforsen hydro power plant," SKB Technical Report 91-10.

Haldeman, W.R., Y. Chuang, T.C. Rasmussen, and D.D. Evans, 1991. "Laboratory analysis of fluid flow and solute transport through a fracture embedded in porous tuff," *Water Resources Research*, Vol. 27, pp. 53-65.

Hässler, L. "Grouting of rock -- Simulation and classification," Ph.D. dissertation, Dept. of Soil and Rock Mechanics, Royal Institute of Technology, Stockholm.

Heath, M.J., 1984. "Solute migration experiments in fractured granite, South West England," *Design and Instrumentation of In Situ Experiments in Underground Laboratories for Radioactive Waste Disposal; Proceedings of a Joint CEC-NEA Workshop*, Brussels, May 15-17.

Herbert, A., and B. Splawski, 1990. "Prediction of inflow into the D-holes at the Stripa mine," Stripa Project Technical Report 90-14, SKB, Stockholm.

Hopkins, D.L., N.G.W. Cook, and L.R. Myer, 1990. "Normal joint stiffness as a function of spatial geometry and surface roughness," *Rock Joints: Proceedings of the International Symposium on Rock Joints*, Loen, Norway, June 4-6, pp. 203-210.

Hull, J., 1988. "Thickness-displacement relationships for deformation zones," *Journal of Structural Geology*, Vol. 10, pp. 431-435.

Hyett, A.J. and J.A. Hudson, 1990. "A photoelastic investigation of the stress state close to rock joints," *Rock Joints: Proceedings of the International Symposium on Rock Joints*, Loen, Norway, June 4-6.

Iwai, K., 1976. "Fundamental studies of fluid flow through a single fracture," Ph.D. dissertation, University of California, Berkeley.

Jaeger, J.C. and N.G.W. Cook, 1979. *Fundamentals of Rock Mechanics*, 3rd edition, Chapman & Hall, London.

Karasaki, 1986. "Well test analysis in fractured rock," PhD Thesis, Dept. of Materials Science and Mineral Engineering, University of California, Berkeley.

Karasaki, K., J.C.S. Long and G.S. Bodvarsson, 1985. "A new fracture and matrix mesh generator," in *Annual Report 1985 Earth Sciences Division*, Lawrence Berkeley Laboratory, Berkeley, California.

Khaleel, R., 1989. "Scale dependence of continuum models for fractured basalts," *Water Resources Research*, Vol. 25, pp. 1847-1855.

Klockars, K-E and O. Persson, 1982. "The hydraulic properties of fracture zones and tracer tests with non-reactive elements in Studsvik," SKBF-KBS Technical Report 82-10, SKB, Stockholm.

Krech, W.W., F.A. Henderson, and K.E. Hjelmstad, 1974. "A standard rock suite for rapid excavation research," BuMines RI 7865, United States Bureau of Mines, Washington, D.C.

Kutilake, P.H.S.W, D.N. Wathugala, M. Poulton, and O. Stephansson, 1990. "Analysis of structural homogeneity of rock masses," *Engineering Geology*, Vol. 29, pp. 195-211.

Landström, O. and E-L Tullborg, 1990. "The influence of fracture mineral/groundwater interaction on the mobility of U, Th, REE, and other trace elements," SKB Technical Report 90-37, SKB, Stockholm.

Lee, K., 1988. "Report on development and validation of conceptual models for major fracture zones," GAI report 873-1313.011, Golder Associates Inc., Redmond, Washington.

Long, J.C.S, 1983. "Investigation of equivalent porous medium permeability in networks of discontinuous fractures," PhD dissertation, College of Engineering, University of California, Berkeley.

Long, J.C.S. and D. Billaux, 1986. "The use of geostatistics to incorporate spatial variability in the modeling of flow through fracture networks," LBL Report 21439, Lawrence Berkeley Laboratory, Berkeley, California.

Long, J.C.S. and D. Billaux, 1987. "From field data to fracture network modeling -- an example incorporating spatial structure," *Water Resources Research*, Vol. 23, pp. 1201-1216.

Long J.C.S, J.S. Remer, C.R. Wilson, and P.A. Witherspoon, 1982. "Porous media equivalents for networks of discontinuous fractures," *Water Resources Research*, Vol. 18, pp. 645-658.

Long and Witherspoon, 1985. "The relationship of the degree of interconnection and permeability in a fracture network," *Journal of Geophysical Research*, Vol. 90, pp. 3087-3098.

Lovius, L., S. Norman, and N. Kjellbert, 1990. "Uncertainties in repository performance from spatial variability of hydraulic conductivities — statistical estimation and stochastic simulation using PROPER," SKB Technical Report 90-03, SKB, Stockholm.

Mardia, K.V., J.T.Kent, and J.M.Bibby, 1979. *Multivariate Analysis*, Academic Press.

Makurat, A., N. Barton, L. Tunbridge and G. Vik, 1990a. "The measurement of joint properties at different scales in the Stripa project," *Rock Joints: Proceedings of the International Symposium on Rock Joints*, Loen, Norway, June 4-6, pp. 541-548.

Makurat, A., N. Barton, G. Vik and L. Tunbridge, 1990b. "Site characterization and validation — Coupled stress-flow testing of mineralized joints of 200 mm and 1400 mm length in the laboratory and in situ, Stage 3," Stripa Project Technical Report 90-07.

Mantuoglu, A. and J.L. Wilson, 1982. "The turning bands method for simulation of random fields using line generation by a spectral method," *Water Resources Research*, Vol. 18, pp. 1379-1394.

Marone, C. and C.H. Scholz, 1989. "Particle-size distribution and microstructures within simulated fault gouge," *Journal of Structural Geology*, Vol. 11, pp. 799-814.

Matheron, G., 1971. *The theory of regionalized variables and its applications*, Monograph No. 5, Les Cahiers du Centre de Morphologie Mathématique de Fontainebleau, France.

Miller, I., 1990. "MAFIC β 1.2 Matrix/Fracture Interaction Code with Solute Transport — User Documentation," Golder Associates Inc. report prepared for Battelle Memorial Institute, Office of Waste Technology Development, Willowbrook, Illinois.

Monicard, R.P., 1980. *Properties of Reservoir Rocks: Core Analysis*, translated by D. Berley. Gulf Publishing Co., Houston, Texas. 165 pp.

Moreno, L., Y. Tsang, C.F. Tsang, and I. Neretnieks, 1988. "Flow and transport in a single fracture. A two-dimensional statistical model," SKB Technical Report 88-03.

Moreno, L., and I. Neretnieks, 1991. "Fluid and solute transport in a network of channels," SKB Technical Report 91-44, SKB, Stockholm.

Moreno, L., S. Arve, and I. Neretnieks. "SKB WP-Cave Project -- Radionuclide release from the near-field in a WP-Cave repository to the biosphere," SKB Technical Report 89-05.

Morrow, C.A. and J.D. Byerlee, 1989. "Experimental studies of compaction and dilatancy during frictional sliding on faults containing gouge," *Journal of Structural Geology*, Vol. 11, pp. 815-825.

Moyes, D.G., 1967. "Diamond drilling for foundation exploration," *Civil Engineering Transactions*, pp. 95-100.

Neretnieks, I., 1990. "Solute transport in fractured rock -- Applications to radionuclide waste repositories," SKB Technical Report 90-38, SKB, Stockholm.

Neretnieks, I., H. Abelin, L. Birgersson, L. Moreno, H. Widén, and T. Ågren, 1989. "A large scale flow and tracer experiment in granite," paper in *In Situ Experiments Associated with the Disposal of Radioactive Waste*, Proceedings of the 3rd NEA/SKB Symposium on the International Stripa Project, October 3-4, Stockholm.

Neretnieks, I., T. Eriksen and P. Tähtinen, 1982. "Tracer movement in a single fracture in granitic rock: Some experimental results and their interpretation," *Water Resources Research*, Vol. 18, pp. 849-858.

Neuman, S.P., 1990. "Universal scaling of hydraulic conductivities and dispersivities in geologic media," *Water Resources Research*, Vol. 26, pp. 1749-1758.

Neuzil, C.E. and J.V. Tracy, 1981. "Flow through fractures," *Water Resources Research*, Vol. 17, pp. 191-199.

Nicholas, J.R., 1988. "Overview of a Hydrogeological Study of Fractured Dolomite in Northeastern Illinois," *Symposium Proceedings of International Conference on Fluid Flow in Fractured Rocks*, Georgia State University, Atlanta, Georgia, May 15-18, pp. 1-11.

Niva, B., "Detailed investigations of fracture zones in the Brändan area, Finnsjön study site. Borehole radar measurements in the borehole BFi 1," SKB Working Report 87-28.

Norman, S., 1991. "Verification of HYDRAST Working Report — A code for stochastic continuum simulation of groundwater flow," SKB Technical Report 91-27, SKB, Stockholm.

Norman, S. and J. Geier, "Interface Between Discrete-Fracture Network and Stochastic Continuum Models for the SKB 91 Safety Assessment Study," draft work plan submitted to SKB.

Norman, S. and N. Kjellbert, 1990. "FARF31 — A far field radionuclide migration code for use with the PROPER package," SKB Technical Report 90-01.

Novakowski, K.S., G.V.Evans, D.A.Lever, and K.G. Raven, 1985. "A field example of measuring hydrodynamic dispersion in a single fracture," *Water Resources Research*, Vol. 21, pp. 1165-1174.

Olsson, O., J.H. Black, J. Gale, and D. Holmes, 1989. "Site characterization and validation Stage 2 -- Preliminary predictions," Stripa Project Technical Report 89-03, SKB, Stockholm.

Palmqvist, K., 1990. "Groundwater in crystalline bedrock," SKB Technical Report 90-41, SKB, Stockholm.

Palmqvist, K. and Lindström, 1991. "Channel widths," SKB Technical Report 91-14, SKB, Stockholm.

Papp, T., 1990. "Work Description for SKB-91," SKB Progress Report Working Report 90-27. SKB, Stockholm.

Piggott, A.R. and D. Elsworth, 1990. "Laboratory studies of transport within a single rock fracture," *Rock Joints: Proceedings of the International Symposium on Rock Joints*, Loen, Norway, June 4-6.

Pyrak-Nolte, L.J., L.R. Myer and N.G.W. Cook, 1985. "Determination of fracture void geometry and contact area as a function of applied load," in *Earth Sciences Division Annual Report 1985*, report LBL-20450, Lawrence Berkeley Laboratory, Berkeley, California, pp. 16-17.

Pyrak-Nolte, L.J., N.G.W. Cook, and D.D. Nolte, 1988. "Fluid percolation through single fractures," *Geophysical Research Letters*, Vol. 15, pp. 1247-1250.

Raven, K.G., K.S. Novakowski, K.S., and P.A. Lapcevic, 1986. "Interpretation of field tracer tests in a single fracture using a transient solute storage model," *Water Resources Research*, Vol. 24, pp. 2019-2032.

Robinson, P.C., 1984. "Connectivity, flow and transport in network models of fractured media," Ph.D. dissertation, St. Catherine's College, Oxford University, Oxford, England, UK.

Shapiro, A.M., 1988. "Interpretation of Tracer Tests Conducted in an Areally Extensive Fracture in Northeastern Illinois," *Symposium Proceedings of International Conference on Fluid Flow in Fractured Rocks*, Georgia State University, Atlanta, Georgia, May 15-18, pp. 12-22.

Sharp, J.C., 1970. "Fluid flow through fissured media," Ph.D dissertation, University of London, Imperial College of Science and Technology, London, U.K.

Skagius, K. and I. Neretnieks, "Porosities and diffusivities of some non-sorbing species in crystalline rocks," SKB Technical Report 85-03.

Stille, H., A. Burgess, and U.E. Lindblom, 1977. "Groundwater movements around a repository. Geological and geotechnical conditions," KBS Teknisk Rapport 54:01, S Kärnbränslesäkerhet, Stockholm.

Stratford, R.G., A.W. Herbert, and C.P. Jackson, 1990. "A parameter study of the influence of aperture variation on fracture flow and the consequences in a fracture network," *Rock Joints: Proceedings of the International Symposium on Rock Joints*, Loen, Norway, June 4-6, pp. 413-422.

Tirén, S., 1989. "Geological setting and deformation history of a low angle fracture zone at Finnsjön, Sweden," in SKB Technical Report 89-19.

Tirén, S., 1990. "Detailed fracture mapping -- cell mapping and scanline mapping at borehole KFI 11, Brändan area, Finnsjön, central Sweden," SGAB IRAP 90251, SGAB, Uppsala.

Tsang, Y.W., 1984. "The effects of tortuosity on fluid flow through a single fracture," *Water Resources Research*, Vol. 20, pp. 1209-1215.

Tsang, Y.W. and F.V. Hale, 1988. "A study of the application of mercury porosimetry method to a single fracture," *Symposium Proceedings of International Conference on Fluid Flow in Fractured Rocks*, Georgia State University, Atlanta, Georgia, May 15-18, pp. 267-283.

Tsang, Y.W. and C.F. Tsang, 1987. "Channel model of flow through fractured media," *Water Resources Research*, Vol. 23, pp. 467-479.

Tsang, Y.W. and P.A. Witherspoon, 1981. "Hydromechanical behavior of a deformable rock fracture subject to normal stress," *Journal of Geophysical Research*, Vol. 86, pp. 9287-9298.

Tsang, Y.W. and P.A. Witherspoon, 1983. "The dependence of fracture mechanical and fluid flow properties on fracture roughness and sample size," *Journal of Geophysical Research*, Vol. 88, pp. 2359-2366.

Tullborg, E-L. and S.Å. Larson, 1983. "Fissure fillings from Gideå, central Sweden," SKBF KBS Technical Report 83-74.

Tullborg, E-L., 1986. "Fissure fillings from the Klipperås study site," SKB Technical Report 86-10.

Tullborg, E-L, 1989. "Fracture fillings in the drillcores KAS05-KAS08 from Äspö, southeastern Sweden," SKB HRL Progress Report 25-89-21, SKB, Stockholm.

Wang, J.S.Y, T.N. Narasimhan, and C.H. Scholz, 1988. "Aperture correlation of a fractal fracture," *Journal of Geophysical Research*, Vol. 93, pp. 2216-2224.

Wang, J.S.Y. and T.N. Narasimhan, 1988. "Fractal and statistical characterization of rough fracture," *Symposium Proceedings of International Conference on Fluid Flow in Fractured Rocks*, Georgia State University, Atlanta, Georgia, May 15-18, pp. 220-228.

Watanabe, K., 1991. "Evaporation measurements in the validation drift -- Part 1, Stripa Project Technical Report 91-06, SKB, Stockholm.

Watanabe, K., and M. Osada, 1991. "Evaporation measurements in the validation drift -- Part 2, Stripa Project Technical Report 91-27, SKB, Stockholm.

Winberg, A., T. Chan, P. Griffiths, and B. Nakka, 1989. "Post-excavation analysis of a revised hydraulic model of the Room 209 fracture, URL, Manitoba, Canada -- A part of the joint AECL/SKB characterization of the 240 m level at the URL, Manitoba, Canada," SKB Technical Report 89-27.

Winberg, A., K.C. Shan, W. X. Huan, and V. Cvetkovic, 1990. "SKB 91 stochastic continuum modelling of mass arrival at Finnsjön — parametric and non-parametric approaches. Results of a preliminary study," SKB Working Report 90-40, SKB, Stockholm.

Witherspoon, P.A., 1979. "Observations of a potential size effect in experimental determination of the hydraulic properties of fractures," *Water Resources Research*, Vol. 15, pp. 1142-1146.

Witherspoon, P.A., J.S.Y. Wang, K. Iwai, and J.E. Gale, 1979. "Validity of cubic law for fluid flow in a deformable rock fracture," Report LBL-9557/SAC-23/UC-70, Swedish-American Cooperative Program on Radioactive Waste Storage in Mined Caverns in Crystalline Rock, SKB, Stockholm.

Zimmerman, R.W., D.W. Chen, J.C.S. Long, and N.G.W. Cook, 1990. "Hydromechanical coupling between stress, stiffness, and hydraulic permeability of rock joints and fractures," *Rock Joints: Proceedings of the International Symposium on Rock Joints*, Loen, Norway, June 4-6, pp. 571-577.

13. NOTATION

13.1 Symbols for variables and constants

A	= area	[L ²]
A_c	= conduit cross-sectional area	[L ²]
b_r	= fracture size distribution parameter	[L ⁻¹]
b_{NN}	= Nearest Neighbor fracture location model parameter	[L ⁻¹]
b_{Tn}	= empirical parameter of loglinear relation of normal stress to fracture transmissivity	
b_w	= packer interval length	[L]
c_h	= admissibility factor for lag data pairs	[-]
c_λ	= tracelength censoring factor	[-]
c	= generic constant	
$C_{k,l}(h)$	= covariance matrix function of the lag h	
$C_Y(h)$	= covariance function of the lag h	
C_f	= fluid compressibility	[LT ² /M]
C_p	= geometric factor P_{32z}/f_c	[-]
D_F	= flow dimension for a packer test	[-]
D_p	= fractal dimension of a surface profile	
D_s	= fractal dimension of a surface	
f_c	= conductive fracture frequency	[L ⁻¹]
f_z	= fracture zone (major feature) frequency	[L ⁻¹]
g	= gravitational acceleration	[L/T ²]
h	= total hydraulic head	[L]
h	= lag (separation) vector	
I_i	= number of fracture intersections per unit area mapped	
JCS _o	= joint strength/stiffness coefficient	[]
JRC _o	= joint roughness coefficient	
K	= vector of conductivity scalar values or tensor components, with components K_i	[L/T]
\mathbf{K}	= hydraulic conductivity tensor with components K_{ij}	[L/T]
\mathbf{K}_s	= effective hydraulic conductivity tensor for the scale s	[L/T]
K_c	= conduit hydraulic conductivity	[L/T]
K_{Moyes}	= hydraulic conductivity estimated from Moyes' formula	[L/T]
K_{GRF}	= hydraulic conductivity estimated by GRF analysis	[L/T]
K_p	= hydraulic conductivity estimated from a packer test	[L/T]
K_z	= hydraulic conductivity of a fracture zone	[L/T]
K_s	= effective conductivity (scalar) for the scale s	[L/T]
L_i	= the i th lag class or flux bin	
N_L	= network length (number of fractures)	[-]
p	= pressure	[M/LT ²]
p_i	= initial pressure prior to a packer test	[M/LT ²]
p_w	= wellbore pressure during a packer test	[M/LT ²]
P_{32z}	= conductive fracture intensity	[L ⁻¹]
P_{32z}'	= conductive fracture intensity for truncated fracture population	[L ⁻¹]
P_{32z}	= fracture zone intensity	[L ⁻¹]
q	= flux density vector with components q_i	
Q	= flowrate (fluid flux)	[L ³ /T]
Q_f	= final flowrate measured at the end of a packer test	[L ³ /T]

Q_{net}	= net flowrate through a rock block	[L ³ /T]
r	= radial distance	[L]
r_e	= effective radius of a polygonal fracture	[L]
r_{min}	= minimum radius for a truncated power-law distribution	[L]
r_w	= wellbore radius	[L]
$R_{p/z}$	= geometric factor P_{3z}/f_c	[-]
s	= averaging scale	[L]
s_f	= fracture spacing	[L]
$S_{w/f}$	= total surface area accessible to fluid within a fracture, per unit area of the fracture plane	[-]
S	= storativity	[-]
S_v	= specific wetted surface per unit pore volume	[-]
S_b	= specific wetted surface per unit bulk volume (rock mass)	[-]
S_w	= specific wetted surface per unit volume of flowing water (connected pore volume)	[-]
S_{wk}	= estimate of the S_w fraction for the k th flux bin L_k	
S_{wQ}	= flux-weighted estimate of S_w (connected pore volume)	[-]
S_p	= storativity estimated from a packer test	[-]
S_{GRF}	= storativity estimated from a packer test by GRF analysis	[-]
t_p	= termination probability	
$t_{\%}$	= termination percentage	
t_{ri}	= number of fracture terminations in intact rock per unit area	
t_{fi}	= number of fracture terminations at fractures per unit area	
T	= transmissivity	[L ² /T]
T_f	= cross-fracture transmissivity	[L ² /T]
T_{f0}	= cross-fracture transmissivity at the reference stress level σ_{no}	[L ² /T]
T_{GRF}	= transmissivity estimated from a packer test by GRF analysis	[L ² /T]
$T_{threshold}$	= minimum transmissivity that can be measured for a given testing procedure	[L ² /T]
T_p	= transmissivity estimated from a packer test	[L ² /T]
T_z	= fracture zone transmissivity	[L ² /T]
u	= local fluid velocity, with components u_i	[L/T]
U	= average fluid velocity, with components U_i [L/T]	
V_B	= bulk volume	[L ³]
V_v	= void volume	[L ³]
V_w	= water volume	[L ³]
x	= coordinate vector with components x_i	[L]
Y	= transformed vector K , with components Y_i	
z	= elevation	[L]
Z	= depth	[L]
$\Gamma_{k,i}(L_n)$	= estimate of the covariance matrix function for the lag class L_n	
δ_m	= maximum joint closure	[L]
ϵ_h	= hydraulic aperture	[L]
ϵ_m	= mechanical aperture	[L]
ϵ_{m0}	= initial mechanical aperture	[L]
ϵ_v	= void aperture	[L]
ϵ_T	= estimate of aperture from a tracer test	[L]
κ_n	= joint normal stiffness	
κ_{n0}	= initial joint normal stiffness	
λ_L	= mean network length - 1	

λ_f	= fracture trace or lineament length	[L]
λ_m	= mean fracture spacing	[L ⁻¹]
λ_{min}	= minimum trace length measured	[L]
λ	= direction vector	
μ_f	= fluid viscosity	
μ_w	= water viscosity	
ξ	= local coordinate vector with components ξ_i	[L]
ρ_f	= fluid density	[M/L ³]
ρ_w	= water density	[M/L ³]
σ_h	= minimum horizontal stress	[M/LT ²]
σ_H	= maximum horizontal stress	[M/LT ²]
σ_n	= fracture normal stress	[M/LT ²]
σ_{no}	= reference value of fracture normal stress	[M/LT ²]
σ_v	= vertical stress	[M/LT ²]
ϕ	= total porosity	[-]
ϕ_c	= fracture coating or infilling porosity	[-]
ϕ_w	= flow porosity	[-]
ϕ_Q	= flux-weighted estimate of flow porosity	[-]
ϕ_k	= estimate of the porosity fraction for the k th flux bin L_k	
Ω_f	= region consisting of the union of the hydraulic volumes of all fractures within a specified averaging volume	

13.2 Other Mathematical Notation

∇	= gradient operator
$f()$	= generic function
$E[x]$	= expected value of a random variable x
$F[\alpha, \beta, \gamma; \zeta]$	= hypergeometric function
μ_x	= mean value of a random variable x
σ_x	= standard deviation of a random variable x
$P[A B]$	= conditional probability of A given B
$Var[x]$	= variance of a random variable x
χ^2	= Chi-squared (refers to statistical test)
$\Gamma(\alpha, z)$	= $\int_z^\infty e^{-t} t^{\alpha-1} dt$ = incomplete gamma function of the second type
$\gamma()$	= variogram

APPENDICES

TABLE OF CONTENTS

A1	Significance of the single-conduit-per-interval assumption for estimating the distribution of conduit conductances. A1.1 Analysis of single-conduit assumption A1.2 Conclusions regarding the single-conduit assumption and dataset sufficiency
A2	Nested simulation scheme for a DFN/SC interface
A3	Formulae for calculating volume-averaged head gradients and velocities
A4	Estimation of a 3-D conductivity tensor from multiple simulations A4.1 Tests of validity for a conductivity tensor
A5	Estimation of covariance matrix function
A6	Comparison of dip data among sections of boreholes KFI 06 and KFI 11
A7	FracSize analysis algorithm
A8	Estimation of Nearest-Neighbor statistic from borehole data
A9	Fracture roughness profile analysis
A10	OxFILZ analysis algorithm
A11	Derivation of at-borehole <i>vs.</i> cross-fracture transmissivity relationship
A12	Details of OxFILZ analysis
A13	Method for transient packer test interpretation
A14	Generalized-radial-flow analysis of simulated packer tests
A15	Partial demonstration of the DFN/SC interface
A16	Data from simulations to estimate transport properties

APPENDIX 1 EFFECTS OF MULTIPLE CONDUITS PER PACKER INTERVAL ON ESTIMATION OF PARAMETERS FOR CHANNEL NETWORK MODELS

This appendix describes analysis performed by GGAB in accordance with Subtask 2.1 of the "Work Plan for Discrete-Fracture Network Modelling and Packer Test Data Analysis in Support of Channel-Network and Stream-Tube Modelling for the SKB 91 Safety Assessment Study."

The objective of this subtask was to estimate the sensitivity of the channel-network (CN) model parameters to the one-conduit-per-interval assumption that has been proposed to allow estimation of the parameters directly from packer-test data.

The analysis for the CN model is simplified if an assumption can be made that each packer interval contains either 0 or 1 conductive channel (above some threshold transmissivity). If the assumption can be justified, then CN model parameters can be derived directly from packer-test data, by use of a nonparametric approach.

To investigate this possibility, the following analysis was performed:

- Using the derived single-fracture T distribution and conductive fracture frequency f_c from Phase 1 DFN model, Monte Carlo simulations were produced of the compound Poisson process defined by:

$$T_{interval} = \begin{cases} 0, & n = 0 \\ \sum_{i=1}^n T_i, & n \geq 1 \end{cases} \quad (A1-1)$$

where n is the number of conduits (fractures or channels) intersecting an interval (distributed as a Poisson process with mean value f_c) and T_i are the (lognormally distributed) transmissivities of the individual features. Preliminary simulations were performed using the Lotus 1-2-3 add-on @Risk, but because this allowed only limited analysis of the simulated data, a short C code was used in the main analysis.

- For a range of percentages p , the threshold transmissivity $T_t(p)$ was defined as the transmissivity such that packer intervals with $T > T_t(p)$ account for $p\%$ of the total transmissivity. The distribution of interval transmissivities specified by the above compound Poisson process, such that $T_{interval} > T_t(p)$, was compared with the assumed single-feature distribution. This provided a direct comparison between an assumed, underlying distribution of single-conduit transmissivities, and the distribution which would be inferred if it were assumed that each packer interval is contains at most one conduit.
- This analysis was repeated using an f_c comparable to the estimates of conductive fracture frequency for within Zone 2 (from Andersson *et al.*, 1989), to predict sensitivity of analysis to this assumption within Zone 2.

A1.3

- In the course of the above analyses, it was noted that the derivation of CN model parameters is quite sensitive to the quantity of data. To avoid confounding this effect with the effects of the one-conduit-per-interval assumption, the above analyses were performed using a very large simulated dataset, equivalent to 50 km of packer test results.
- To investigate the effects of the limited dataset on CN model parameter derivation, 25 synthetic datasets, each equivalent to 1.5 km of packer test data, were produced by Monte Carlo simulation using the above model. For each of these datasets, values of $T_c(p)$ were estimated according to the procedures that would be used in the actual derivation of CN model parameters. These values were compared with the "true" threshold transmissivity levels, which were calculated analytically from the parameters of the underlying distribution of single-conduit transmissivity. This analysis gives an indication of how large the errors in estimating these threshold levels can be, for a dataset of size comparable to the size of the available dataset for Finnsjön.
- Based on the 25 synthetic datasets, an analysis was produced of the possibilities for errors, due to the smallness of the dataset, in characterizing the probability density function (PDF) for the more conductive conduits. This estimated PDF would presumably be used to randomly specify conductances for individual conduits in the CN model.

The details of this analysis are given below.

A1.1 Analysis of single-conduit assumption

The types of errors that can occur in the analysis of data for the channel network model include the following components:

- Assumption of only one channel per packer interval.
- Estimation of threshold conductivity based on limited field data.
- Estimation of channel frequency above threshold transmissivity, based on limited field data.

The analysis of the first effect can easily be confused with the latter effects, if a comparison is made on the basis of a limited number of simulated sampling intervals. To avoid this, in the present analysis these effects were considered separately.

The significance of the one-conduit-per-interval assumption was evaluated based on a very large simulated dataset, equivalent to 50 km of borehole testing. This is much larger than the available dataset, which, for the rock mass below Zone 2, includes less than 1.5 km worth of packer-test results.

Figure A1-1 compares two separate, 50 km simulations of the compound Poisson process (Equation A1-1) with the assumed, single-conduit transmissivity distribution.

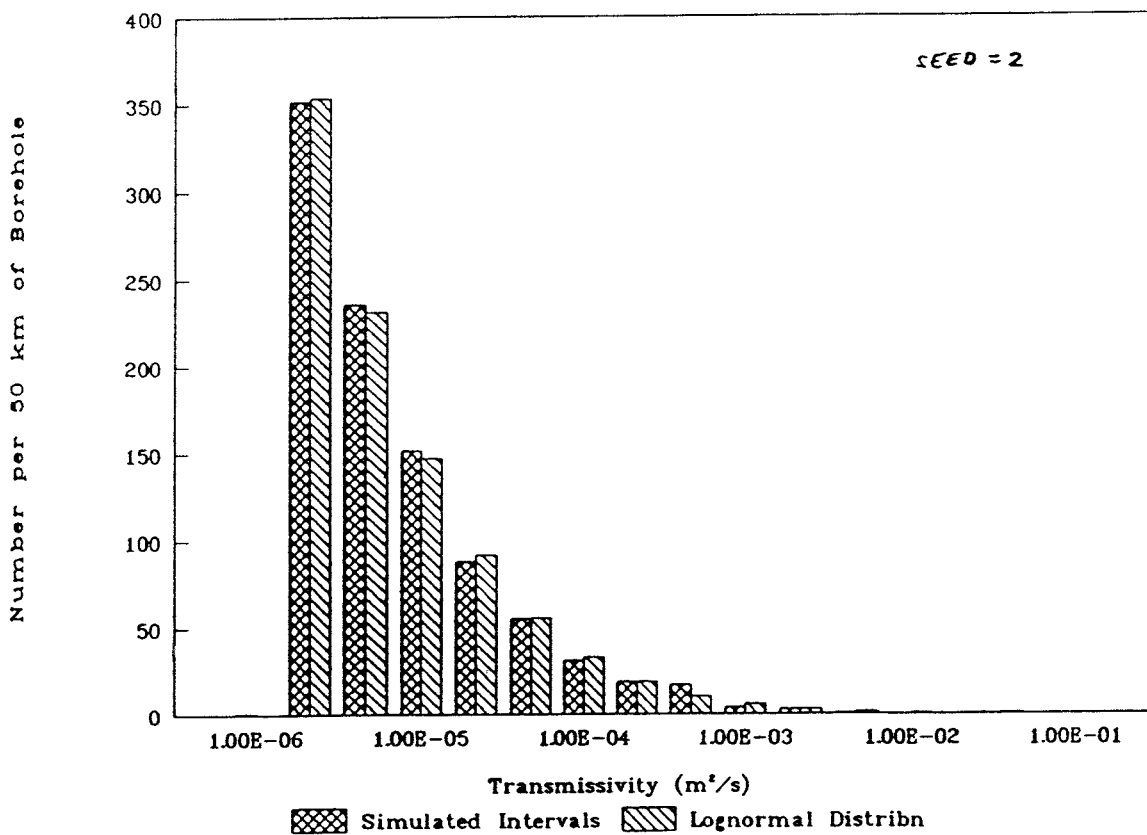
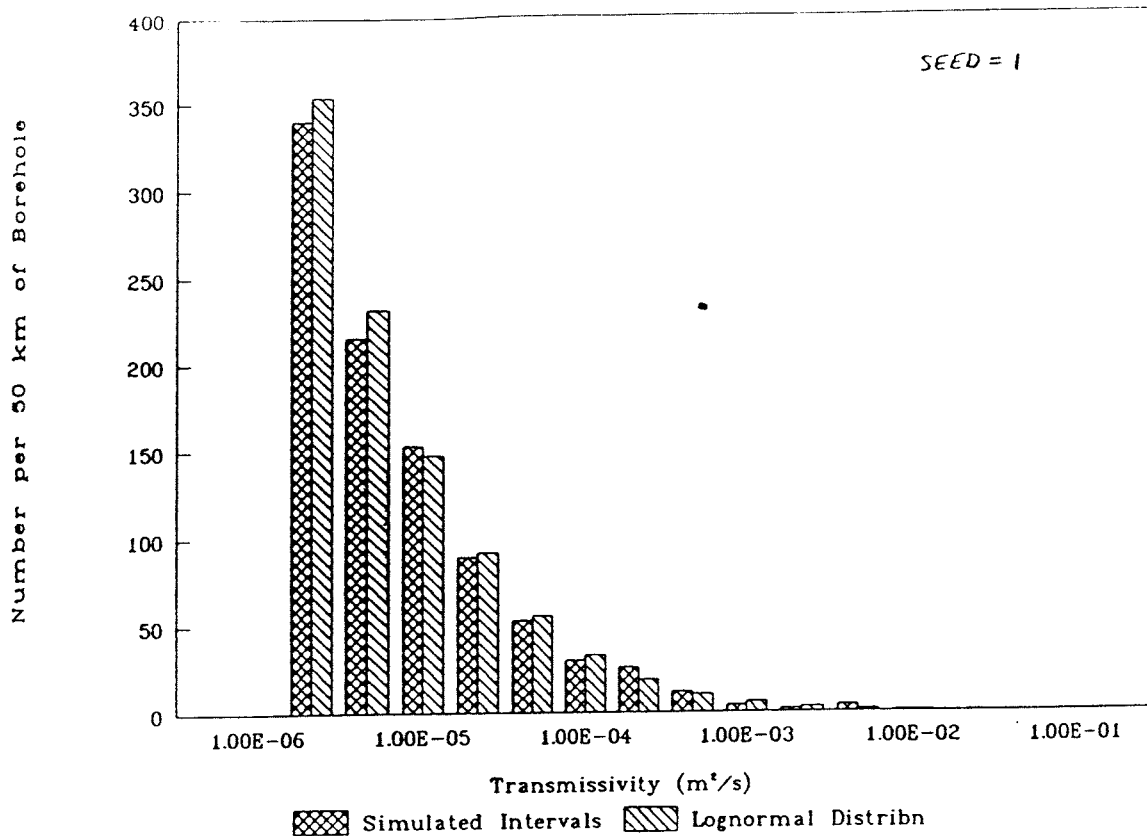


FIGURE **A1-1**

**COMPARISON OF SIMULATED INTERVAL TRANSMISSIVITY
VS. SINGLE-CONDUIT TRANSMISSIVITY DISTRIBUTION**

SKB/SKB91 DFNST

A1.5

The parameters of the assumed, single-conduit lognormal distribution were:

Mean of log transmissivity	$\mu_{\log T} = -11.3 \log \text{ m}^2/\text{s}$
Standard deviation of log transmissivity	$\sigma_{\log T} = 2.1 \log \text{ m}^2/\text{s}$

The compound Poisson process was characterized by the above distribution parameters and:

Conductive fracture frequency	$f_c = 3.29 \text{ m}^{-1}$
-------------------------------	-----------------------------

As is apparent from the figure, the differences between the the two models are small for both simulations. The χ^2 statistic, which gives a measure of the discrepancy between the simulated and the underlying distribution, was insignificant at the 1% level in both cases.

The conclusion may be drawn that, for a very large dataset such as this, the single-conduit assumption will have no significant effect on the derivation of the PDF for the more conductive ($T_i \geq 10^{-6} \text{ m}^2/\text{s}$) conduits.

The results obtained are basically the same when the same analysis is performed for a higher conduit frequency, as might be seen within Zone 2. Figure A1-2 shows a comparison of two 50 km simulations with the underlying distribution, for a conductive fracture frequency $f_c = 6.6 \text{ m}^{-1}$. The χ^2 statistic was insignificant at the 1% level in both cases. In this case the discrepancies between the models, though small, are consistent between the two simulations. However, the magnitude of the discrepancies diminishes with increasing transmissivity. The significance of the discrepancies thus diminishes as higher threshold transmissivities are applied. For example, if $T_i = 2.51 \times 10^{-5} \text{ m}^2/\text{s}$ were used ($p = 0.95$), the χ^2 statistics for comparison of the simulated and underlying distributions for $T \geq T_i$ are insignificant at the 0.5% level.

The above analysis is based on simulated datasets much larger than the actual, available dataset for Finnsjön. In preliminary simulations using datasets comparable to the available dataset, it was noticed that the agreement between the simulated and underlying distributions was much worse. Since it was determined that this disagreement was due to sample size, and not the single-conduit assumption, an attempt was made to characterize this effect separately.

First, the sensitivity of the error in estimation of threshold transmissivity due to a finite dataset was evaluated, based on a simulated dataset equivalent to 1.5 km of borehole testing. The threshold transmissivity is defined as the transmissivity such that conduits having transmissivities above this value account for some specified fraction p of the total conductive capacity.

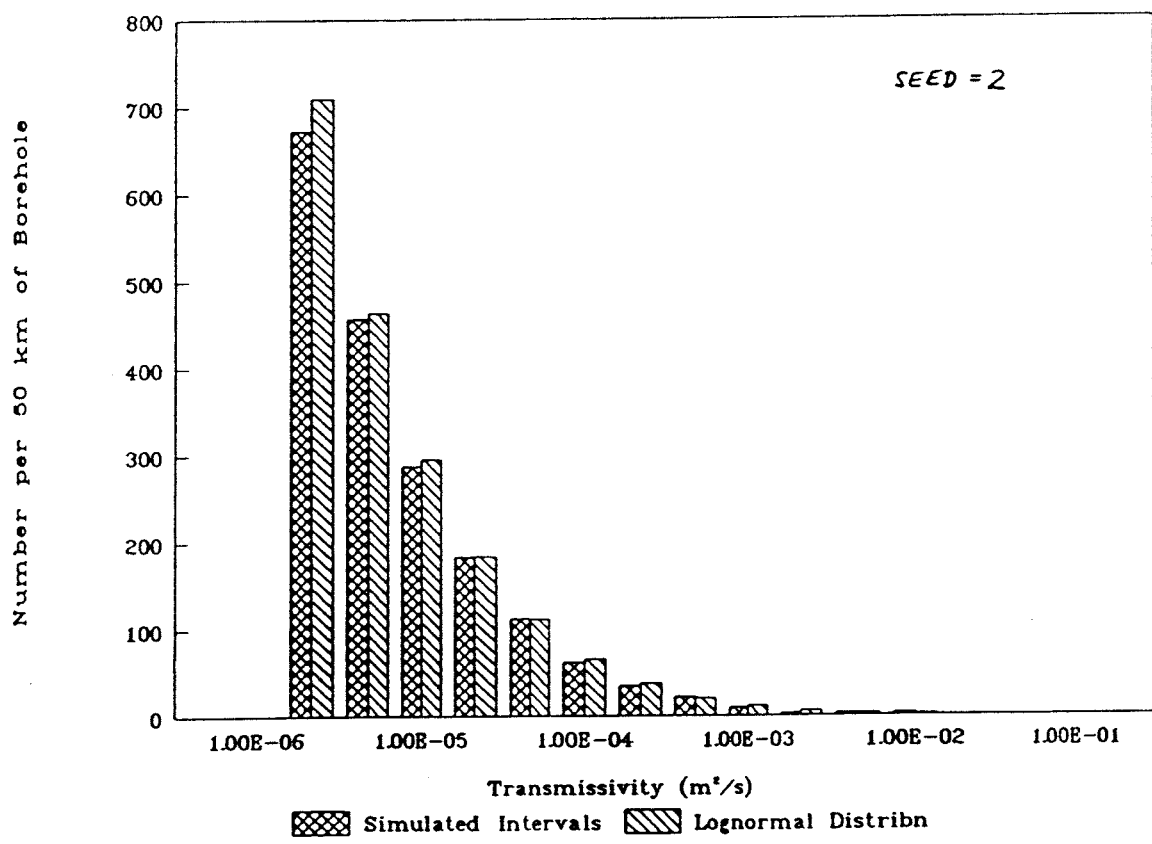
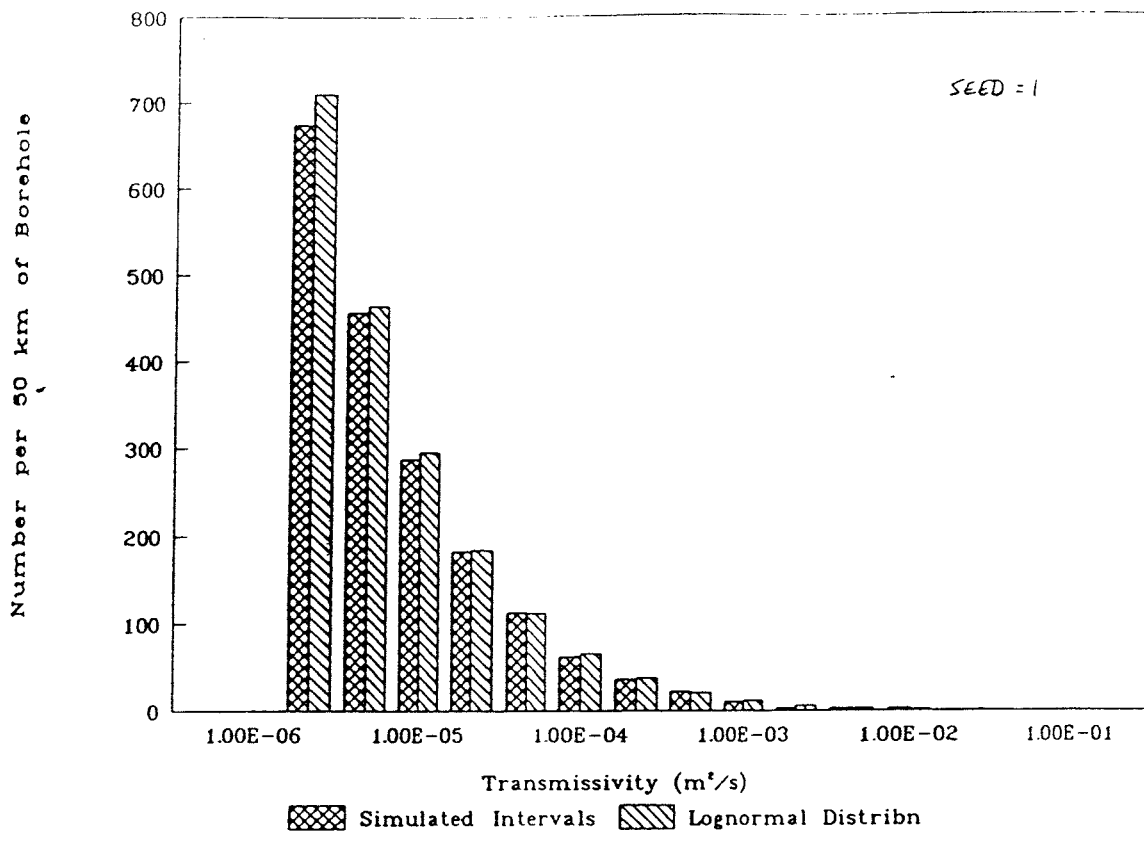


FIGURE **A1-2**
COMPARISON OF SIMULATED INTERVAL TRANSMISSIVITY VS. SINGLE-CONDUIT TRANSMISSIVITY DISTRIBUTION FOR ELEVATED CONDUCTIVE FRACTURE FREQUENCY
 SKB/SKB91 DFNST

In mathematical terms, the threshold transmissivity corresponding to a given fraction p is defined as the value of $T_i(p)$ such that:

$$\frac{\int_{T_i(p)}^{\infty} f_T(t) t dt}{\int_0^{\infty} f_T(t) dt} = p \quad (\text{A1-2})$$

where:

$f_T(t)$ = the probability density function for single-conduit transmissivity.

A threshold transmissivity $\hat{T}_i(p)$ estimated from a finite number of single conduits will differ from the (theoretical) value for an infinite sample.

Assuming a lognormal distribution, the PDF for single-fracture transmissivity can be expressed in terms of the PDF for the logarithm of transmissivity:

$$f_{\ln T}(x) = \frac{1}{\sqrt{2\pi} \sigma} e^{-(x - \mu)^2 / 2\sigma^2} \quad (\text{A1-3})$$

where

$\mu_{\ln T}$ = mean of $\ln T$
 $\sigma_{\ln T}$ = standard deviation of $\ln T$

Then the numerator in Equation A1-2 can be written as:

$$\frac{1}{\sqrt{2\pi} \sigma} \int_{T_i(p)}^{\infty} e^{-(x - \mu)^2 / 2\sigma^2} e^x dx = \frac{1}{2} e^{\mu + \sigma^2 / 2} \operatorname{erfc} \left(\frac{\ln T_i(p) - \mu - \frac{\sigma^2}{2}}{\sqrt{2} \sigma} \right) \quad (\text{A1-4})$$

where $\operatorname{erfc}(x)$ is the complementary error function and the denominator is simply:

$$\frac{1}{\sqrt{2\pi} \sigma} \int_{-\infty}^{\infty} e^{-(x - \mu)^2 / 2\sigma^2} e^x dx = e^{\mu + \sigma^2 / 2} \quad (\text{A1-5})$$

Thus for a lognormal distribution the threshold transmissivity $\hat{T}_i(p)$ can be obtained by solving the equation:

$$p = \frac{1}{2} \operatorname{erfc} \left(\frac{\ln \hat{T}_i(p) - \mu - \frac{\sigma^2}{2}}{\sqrt{2} \sigma} \right) \quad (\text{A1-6})$$

for any given value of p .

Assuming that the true distribution of conduit transmissivities is a lognormal, with:

$$\begin{aligned}\mu &= \mu_{\log T} \ln 10 = -11.3 \ln 10 \\ \sigma &= \sigma_{\log T} \ln 10 = 2.1 \ln 10\end{aligned}\tag{A1-7}$$

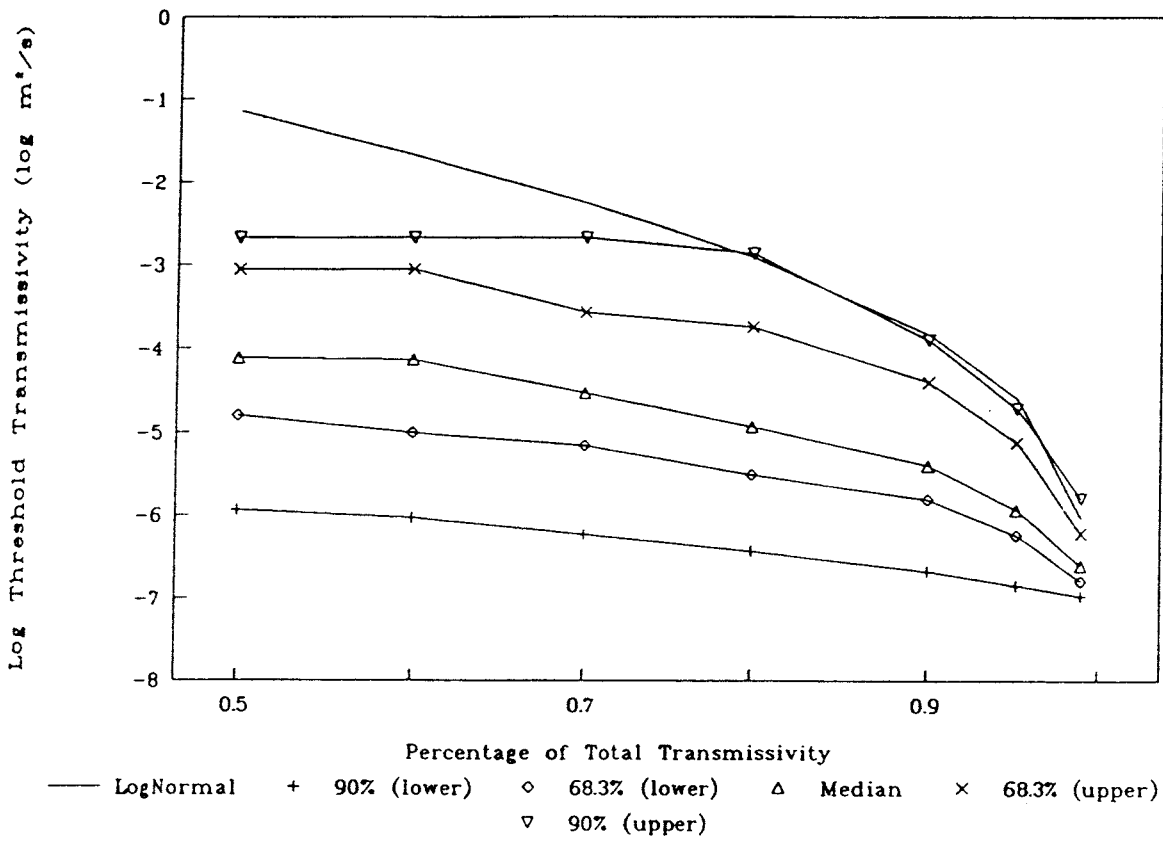
then the threshold transmissivities may be calculated as in Table A1-1. In this table, the number of channels with $T > T(p)$, per kilometer of borehole, is given based on a conductive conduit frequency of 3.29 m^{-1} .

To determine how inaccurate threshold transmissivity estimates are likely to be, 25 1.5 km synthetic datasets were produced by Monte Carlo simulation, using the distribution parameters given above. For each dataset, the threshold transmissivities corresponding to transmissivity fractions $p = 50, 60, 70, 80, 90, 95,$ and 99% were calculated as they would be from field data. Figure A1-3 compares these estimates with the "true" threshold values. The lines in the figure give the median estimates of $T_i(p)$, and 68.3 and 90% confidence intervals for this estimate. The "true" threshold value is above even the 90% confidence interval, for all values of p except $p = 99\%$, which corresponds to the lowest threshold values of around 10^7 m²/s.

Because the conduits which account for most of the flow in this model are so rare, there almost no chance of obtaining a "correct" estimate of $T_i(p)$ for values of $p < 99\%$, for this quantity of data. If the assumed model is even remotely similar to reality, then it must be taken for granted that an estimate of $T_i(p)$ taken in this manner will be significantly less than the actual value.

The main effect of errors in the estimation of threshold transmissivity levels is probably to give a misleading estimate of the fraction of total transmissivity that is actually being modelled. Most likely, the fraction of flow carried by the less conductive conduits will be overestimated. This error is probably secondary in importance to possible errors in the estimation of the PDF for transmissivity of the most conductive conduits. The latter effect was investigated by comparing, for a range of transmissivities, the number of conduits per 1.5 km of simulated data.

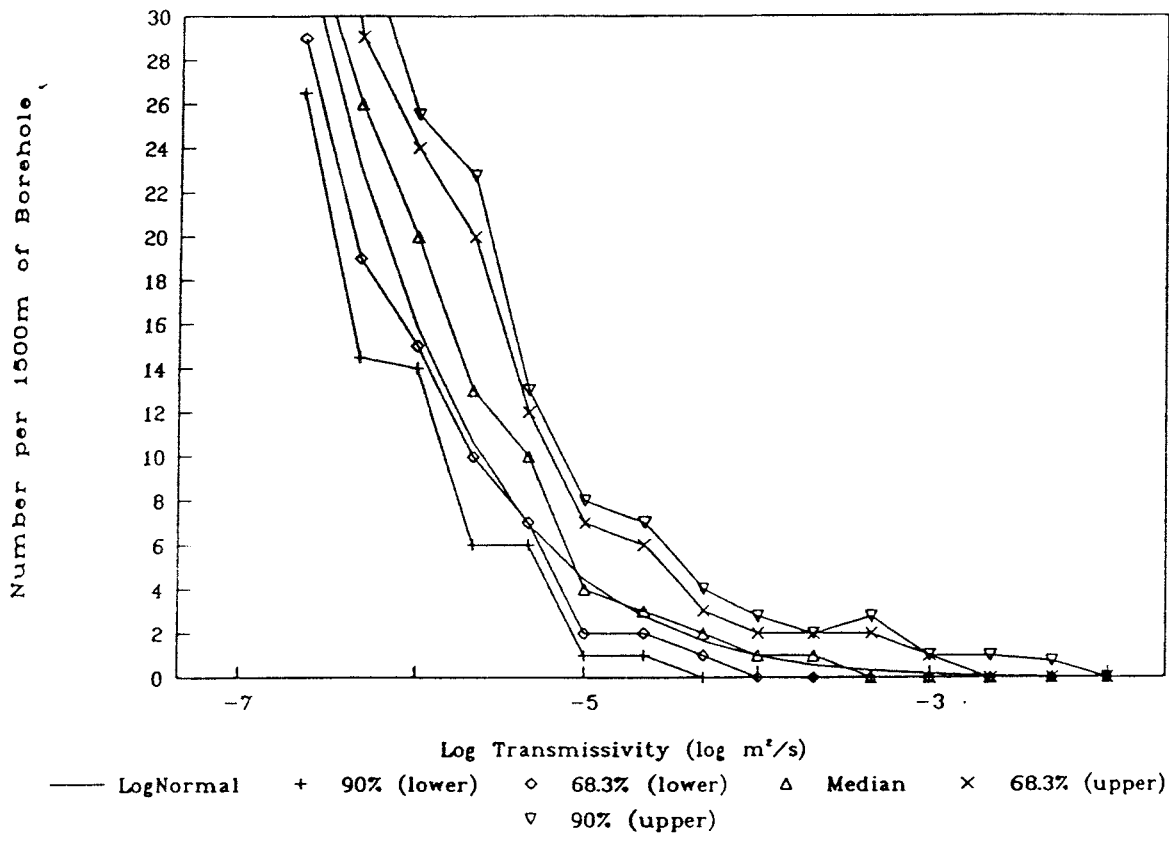
Figure A1-4 compares the median and 68.3 and 90% confidence intervals for estimated conduit frequencies with the frequency per 1.5 km in the underlying distribution. From this it is seen that the median estimate is in close agreement with the underlying distribution for transmissivities up to 10^4 or more, and that even the 90% confidence limits are within 100% up to this point. However, from Table 1 it is seen that conduits of $T_i < 10^4$ are expected to account for only about 10% of the total conductive capacity. Conduits of $T_i > 10^3$ (which are expected, in this model, to account for about 80% of the conductive capacity) are represented in less than half of the 1.5 km datasets. In other words, it is most likely that, in a dataset of this size, no representatives of the conduit population that carries the majority of the flow will be sampled. The practical significance of this type of error is thus far greater than the errors due to the single-conduit assumption or misestimation of the threshold conductivity values.



25 x 1.5 km Monte Carlo simulations

FIGURE **A1-3**
ESTIMATION OF THRESHOLD TRANSMISSIVITY LEVELS
FROM 1.5 km SAMPLE OF PACKER-TEST DATA

SKB/SKB91 DFNST



25 x 1.5 km Monte Carlo Simulations

FIGURE **A1-4**
ESTIMATION OF CONDUIT FREQUENCIES
FROM 1.5 km SAMPLE OF PACKER TEST DATA
 SKB/SKB91 DFNST

A1.2 Conclusions regarding the single-conduit assumption and dataset sufficiency

Based on simulations of an assumed, simple model for the conduit population in the rock, the one-conduit-per-interval assumption appears to introduce no significant error in the estimation of channel-network model parameters.

However, simulations using the same model show that, most likely, the fraction of the conduit population that accounts for most of the conductive capacity will not be represented in a dataset of size comparable to the Finnsjön dataset. This is a serious problem, as it implies that the most important pathways will not have not been characterized.

Possibly this problem may be reduced by the use of parametric rather than nonparametric distributions for conduit transmissivity, since these at least make allowance for the existence of conduits more transmissive than any that have been observed. However, the sensitivity of parametric distribution parameters (*e.g.*, the parameters of the lognormal distribution used above) to the smallness of the data set has not been investigated.

It should be noted that this problem is probably not unique to the estimation of channel-network model parameters, although the sensitivities of other models (discrete-fracture-network, stochastic-continuum, and stream-tube) have not been investigated in the present analysis.

A secondary effect of the small size of the dataset is that, most likely, the fraction of flow carried by the less conductive conduits will be overestimated. The main effect of this is presumably practical in nature: there will be a tendency to include an unnecessarily large number of less-conductive conduits in the channel-network model.

APPENDIX 2 NESTED GENERATION SCHEME FOR A DFN/SC INTERFACE

Spatial correlation in conductivity among blocks of rock within the Finnsjön site is assumed to result from the continuity of large-scale features from one block to the next. For the simplest model implemented in FracMan, the Baecher model, fracture locations are uniformly random, independent of size, and hence spatial correlation can result only from continuity of large fractures from one block to the next. For other FracMan conceptual models, which include some form of spatial correlation among fractures, the smaller fractures can contribute to spatial correlation if they act as part of an extensive fracture swarm or zone.

The SC model requires that covariance functions for block-scale conductivity be defined over a range of scales up to the correlation lengths for the quantities of interest. These correlation lengths are not known *a priori*, but because the maximum feature size is limited only by the size of the Finnsjön block, the possibility of correlation up to this scale must be considered, at least at the outset.

Simulation of the entire fracture population in such a large region is not computationally tractable, due to the very large number of small fractures. Instead, portions of the fracture population must be simulated within smaller regions in such a way that spatial correlation due to the continuity of large-scale features is preserved.

This is achieved by a nested generation process. The fracture population is divided into N classes according to size:

$$\begin{aligned} L_0: & \infty \leq r_e \leq r_0 \\ L_1: & r_0 \leq r_e \leq r_1 \\ & \cdot \\ & \cdot \\ & \cdot \\ L_N: & r_{N-1} \leq r_e \leq r_N \end{aligned}$$

For each size class L_i there is a corresponding generation scales s_i , with $s_{i+1} = 1/2s_i$. Only L_0 is generated for the entire realization, over the largest scale s_0 . Successively smaller classes are generated in blocks of successively smaller scale within the larger-scale populations, until the smallest class L_N has been generated.

The largest ($s_0 \times s_0 \times s_0$) generation region is iteratively divided into subregions by binary division parallel to the three coordinate axes (Figure A2-1). At each level of subdivision this produces eight cubes of the smaller scale. A random subset of these smaller-scale cubes is chosen for repeated subdivision. Fracture populations for flow simulation are taken from within the smallest-scale (s_N) blocks.

For the Baecher model, nested generation can be done very efficiently, because the L_i are mutually independent. Each size class L_i can be generated independently in several blocks of the corresponding scale s_i , and then combined to form cubes of scale s_N containing the full fracture population. Figure A2-2 is a 2-D depiction of this generation scheme.

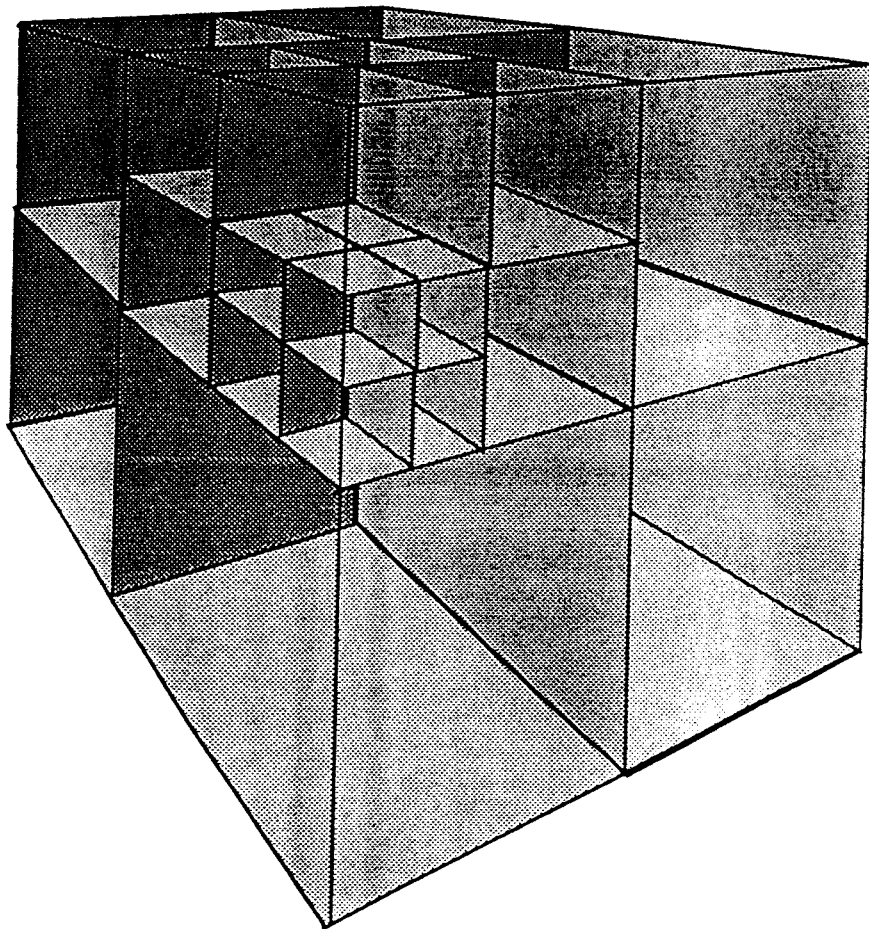
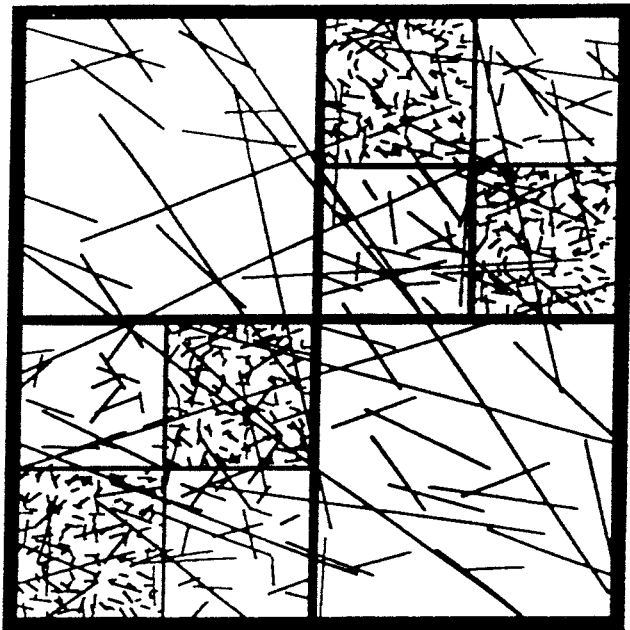
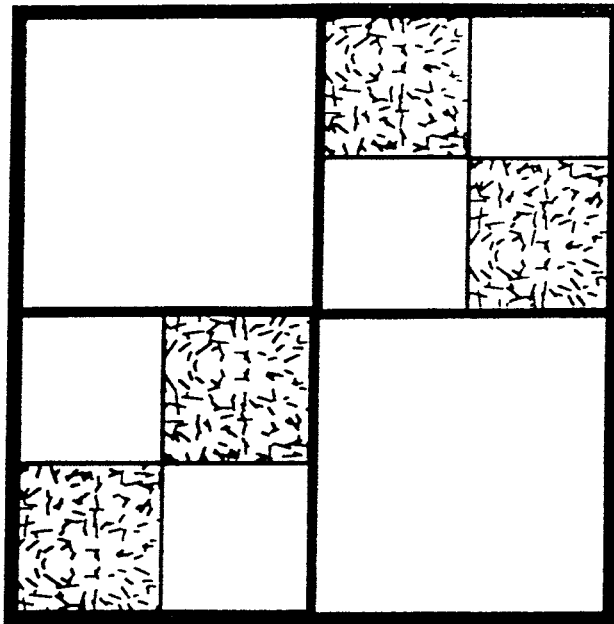


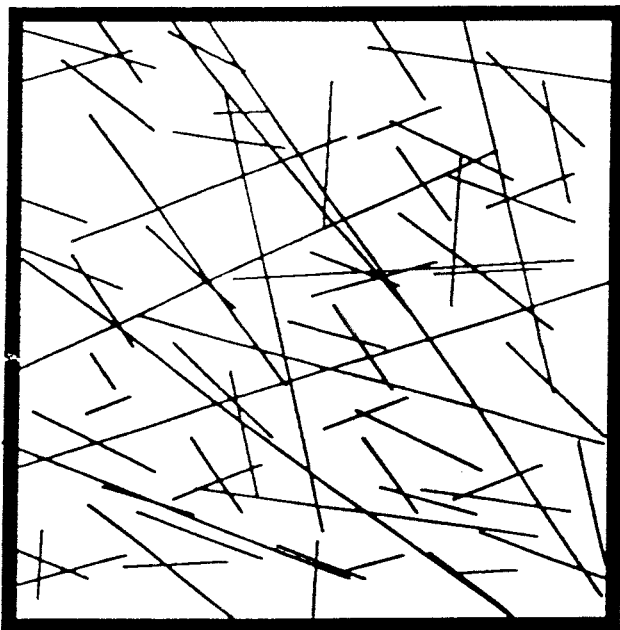
FIGURE **A2-1**
BINARY SUBDIVISION OF GENERATION REGION
SKB/SKB91 DFNST



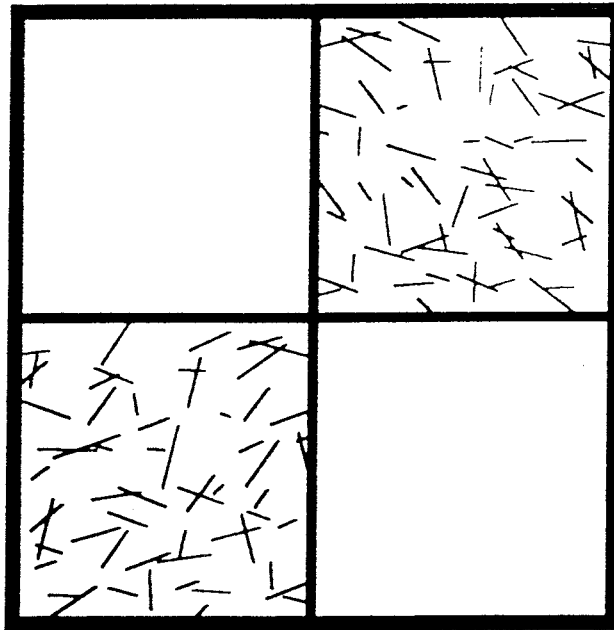
a) Combined model



c) Fracture class 3



b) Fracture class 1



d) Fracture class 2

FIGURE **A2-2**
**NESTED FRACTURE SIMULATION SCHEME
FOR UNCORRELATED LOCATION MODELS**

SKB/SKB91 DFNST

A2.4

For the other conceptual models, nested generation is more difficult, because the fracture locations are autocorrelated. For models in which the smaller fracture locations depend on the location of larger fractures or features (*e.g.* the Nearest Neighbor model), an alternative, nested generation scheme may be employed, as depicted in Figure A2-3. The largest class L_0 is generated for the region of scale s_0 , as for the Baecher model, using a specified seed value I_0 for the random number generator. The generation region is subdivided in binary fashion, and one of the 8 subregions is selected for generation of the next class, L_1 . The random number generator is reinitialized using a second seed value, I_1 , and the class L_1 is generated within that subregion. This process is repeated until the final class, L_N has been generated, within a single cube of scale s_N . The dataset for later simulation includes only those fractures or parts of fractures which lie within this cube; the remainder are discarded.

Additional cubes of scale s_N are simulated in the same way, taking care that the random number seeds I_i are identical for populations generated within the same region of scale s_i , for populations which are intended to represent the same realization of the fracture population. This scheme produces populations of large-scale fractures which are consistent among the simulations for a given realization. The scheme is somewhat less efficient than the simpler scheme for the Baecher model, since identical simulations of the larger classes are produced repeatedly, and many of the generated fractures are discarded, in the end. An alternative would be to save the simulations of the larger classes to disk, and recall them for repeated simulations. However, the latter scheme would complicate the bookkeeping, and may even be slower (depending on the model) because disk access may require more time than the calculations to generate the fractures.

One problem with both of the generation schemes outlined above is the well-known "finite generation region" problem, which results in lower fracture intensity close to the edges of a fracture generation region. To reduce this effect, the binary subdivision scheme outlined above should be modified slightly, as follows. At each stage of the nested generation process, after simulating the class L_i in a cube of size s_i , the subregions for simulating the next class L_{i+1} should be formed by binary subdivision of the cube of size αs_i , centered in the s_i -scale cube, with:

$$\alpha \leq 1 - \frac{r_{i-1}}{s_i}, \quad i > 0 \quad (\text{A2-1})$$

This excludes the zone affected by the fact that the generation region is finite. For the first level of subdivision, it is not possible to eliminate this effect, if the maximum size of the previous class L_0 is infinite as assumed above. For this level, α should be made as small as practical. If there is reason to suppose an upper bound r_1 for the first size class, then the correct value of α may be calculated from Equation A2-1 with $i = 0$.

The choice of r_i values for the different classes is determined mainly by memory limitations and the size of diskettes (1.44 Mbyte) used for data transfer from the PC to the mainframe computer. The number of classes required, and the r_i values, depend on the conceptual model, the fracture size distribution, and the conductive fracture intensity.

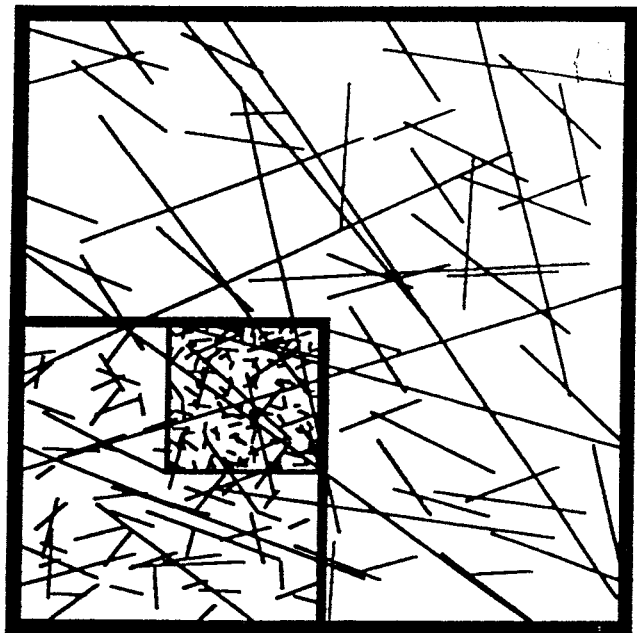
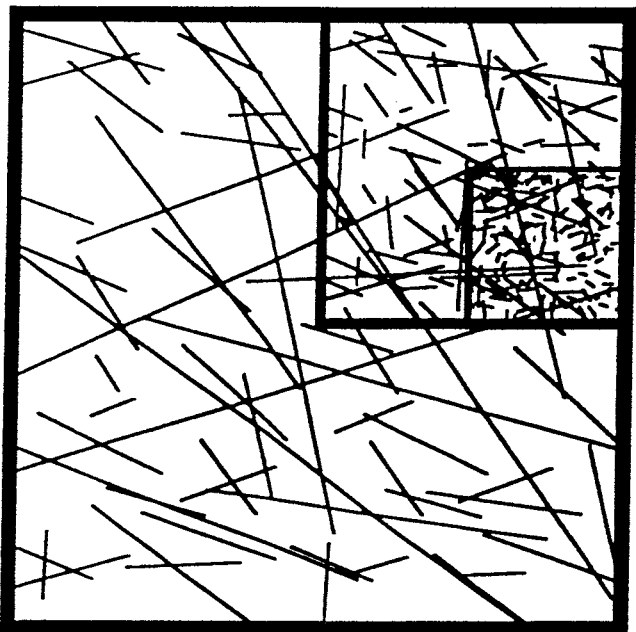
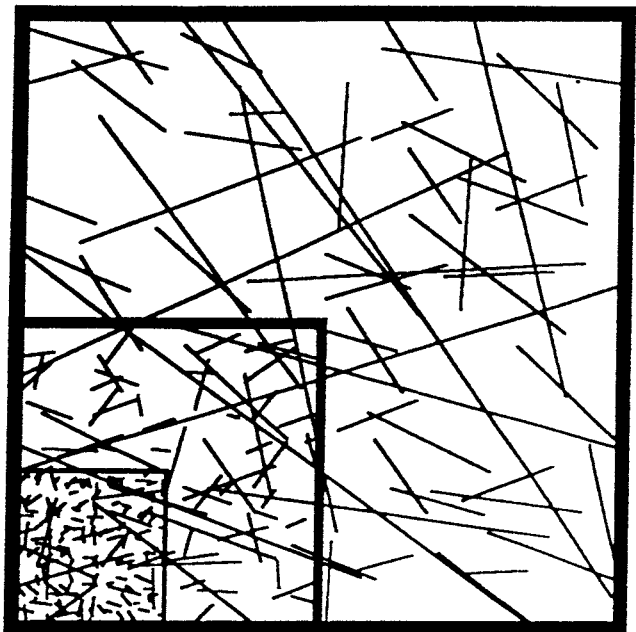
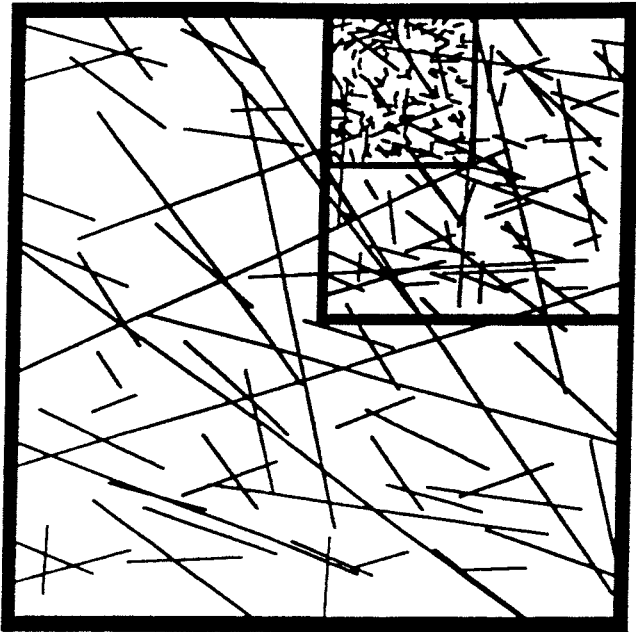


FIGURE **A2-3**
**NESTED FRACTURE GENERATION SCHEME FOR
CORRELATED LOCATION MODELS**

SKB/SKB91 DFNST

APPENDIX 3 FORMULAE FOR CALCULATING VOLUME-AVERAGED HEAD GRADIENTS AND VELOCITIES

The SC model consists of a continuum defined in terms of a spatially varying conductivity tensor $\mathbf{K}(\mathbf{x})$ which is related to a movable averaging volume $V(\mathbf{x})$ such that:

$$\langle \mathbf{u} \rangle = -\mathbf{K}(\mathbf{x}) \nabla \langle h \rangle^f(\mathbf{x}) \quad (\text{A3-1})$$

where

$$\begin{aligned} \langle h \rangle^f(\mathbf{x}) &= \text{volumetric average of head, taken over } V(\mathbf{x}) \cap \Omega_f & [\text{L}] \\ \langle \mathbf{u} \rangle(\mathbf{x}) &= \text{volumetric average of the flow velocity, taken over } V(\mathbf{x}) & [\text{L/T}] \\ \Omega_f &= \text{the union of the volumes of all } \textit{connected} \text{ fractures in a realization} & [\text{L}^3] \end{aligned}$$

The average head $\langle h \rangle^f$ is defined explicitly as:

$$\langle h \rangle^f = \frac{\int_{V(\mathbf{x}) \cap \Omega_f} h(\boldsymbol{\xi}) \epsilon(\boldsymbol{\xi}) dA}{\int_{V(\mathbf{x}) \cap \Omega_f} \epsilon(\boldsymbol{\xi}) dA} \quad (\text{A3-2})$$

where

$$\begin{aligned} h(\boldsymbol{\xi}) &= \text{head at the point } \boldsymbol{\xi} \text{ corresponding to } dA & [\text{L/T}] \\ \epsilon(\boldsymbol{\xi}) &= \text{aperture of a fracture at the point } \boldsymbol{\xi} & [\text{L}] \end{aligned}$$

The average flow velocity is defined similarly as:

$$\langle \mathbf{u} \rangle(\mathbf{x}) = \frac{1}{|V(\mathbf{x})|} \int_{V(\mathbf{x}) \cap \Omega_f} \mathbf{u}(\boldsymbol{\xi}) \epsilon(\boldsymbol{\xi}) dA \quad (\text{A3-3})$$

where

$$\mathbf{u}(\boldsymbol{\xi}) = \text{velocity vector at the point } \boldsymbol{\xi} \quad [\text{L/T}]$$

The aperture $\epsilon(\boldsymbol{\xi})$ used in the above equations is supposed to be a "suitably defined" aperture. The *void aperture* ϵ_v , as defined in §2.1, is most suitable, particularly for calculating the porosity. However, the DFN model is defined in terms of fracture transmissivity, which is related directly to *hydraulic aperture* ϵ_h , but not directly to ϵ_v . As discussed in §3.1 there is high variability in the relationship between ϵ_h and ϵ_v .

In the present study, the definition:

$$\epsilon(\boldsymbol{\xi}) = \epsilon_h(\boldsymbol{\xi}) \quad (\text{A3-4})$$

was adopted, mainly because the relation of ϵ_h to quantities used in the DFN model is unambiguous. The result is that the averaged quantities are simply *weighted averages* which do not necessarily conform to Equation A3-1, on the scale of a single fracture. However, there is little physical reason to expect Equation A3-1 to apply, for small area elements within a fracture, since on a fine scale the flow is likely to be non-Darcy (e.g., flow between two rough fracture surfaces, which must be described as Reynolds or Navier-Stokes flow). A more suitable definition of effective aperture could perhaps be substituted for Equation A3-4, but the formulae which follow would be unaffected.

The *pseudo-porosity* of the averaging volume is defined as:

$$\eta(\mathbf{x}) = \frac{1}{|V(\mathbf{x})|} \int_{v(\mathbf{x}) \cap \Omega_f} \epsilon(\boldsymbol{\xi}) dA \quad (\text{A3-5})$$

Here the notation η is used to prevent confusion with actual porosity. If Equation A3-4 were replaced with the definition $\epsilon = \epsilon_w$, this quantity η would of course be identical to the *flow porosity* ϕ_w , as defined in §2.1.4. However, here η is defined simply for the sake of mathematical convenience, and is not assumed to have any particular physical significance.

The DFN model treats fractures as consisting of triangular elements. Each element i is considered to have a constant aperture ϵ_i . Thus Equations A3-2, A3-3, and A3-5 can be written, respectively, as:

$$\langle h \rangle^f = \frac{\sum_{i=1}^{N_e} \epsilon_i \int_{A_i(\mathbf{x})} h(\boldsymbol{\xi}) dA}{\sum_{i=1}^{N_e} \epsilon_i \int_{A_i(\mathbf{x})} dA} \quad (\text{A3-6})$$

$$\langle u \rangle(\mathbf{x}) = \frac{1}{|V(\mathbf{x})|} \sum_{i=1}^{N_e} \epsilon_i \int_{A_i(\mathbf{x})} u(\boldsymbol{\xi}) dA \quad (\text{A3-7})$$

and:

$$\eta(\mathbf{x}) = \frac{1}{|V(\mathbf{x})|} \sum_{i=1}^{N_e} \epsilon_i \int_{A_i(\mathbf{x})} dA = \frac{1}{|V(\mathbf{x})|} \sum_{i=1}^{N_e} \epsilon_i |A_i(\mathbf{x})| \quad (\text{A3-8})$$

where

$$\begin{aligned} A_i(x) &= \text{the part of the } i\text{th fracture element, if any, lying within } V(x) \\ N_e &= \text{the number of fracture elements} \end{aligned}$$

The gradient of average head, $\nabla\langle h \rangle_f$, could be calculated by a difference approximation, by shifting the averaging volume in three orthogonal directions δx_1 , δx_2 , δx_3 . This requires calculating the summations in the above equations at least four times for each measurement of $\nabla\langle h \rangle_f$. For linear elements the integrals in these equations are trivial, but

A more efficient way of obtaining an estimate of $\nabla\langle h \rangle_f$ is based on a variant of Whitaker's Averaging Theorem. The following is a reproduction of the derivation of formulae for this approach, originally derived by S. Norman (personal communication, 1991) and presented in a draft work plan for part of this project (Norman and Geier, 1991).

The gradient of averaged head $\nabla\langle h \rangle_f$ may be expressed as:

$$\begin{aligned} \nabla\langle h \rangle_f(x) &= \nabla \left[\frac{\langle h \rangle_f(x)}{\eta(x)} \right] \\ &= \frac{\nabla\langle h \rangle_f(x)}{\eta(x)} - \frac{\nabla\eta(x)}{\eta^2(x)} \langle h \rangle_f(x) \end{aligned} \quad (\text{A3-9})$$

where

$$\langle h \rangle_f = \frac{1}{|V(x)|} \int_{V(x) \cap \Omega_f} h(\mathbf{E}) \eta(\mathbf{E}) dA \quad (\text{A3-10})$$

Taking the gradient of both sides of Equation A3-6 gives:

$$\nabla\langle h \rangle_f(x) = \frac{1}{\eta(x)} \nabla\langle h \rangle_f(x) - \frac{\nabla\eta(x)}{\eta^2(x)} \langle h \rangle_f(x) \quad (\text{A3-11})$$

where:

$$\langle h \rangle_f = \frac{1}{|V(x)|} \sum_{i=1}^{N_e} e_i \int_{A_i(x)} h_i(\mathbf{E}) dA \quad (\text{A3-12})$$

The first term in Equation A3-12 can be written in terms of the j th component of the gradient as:

$$\begin{aligned} \frac{\partial \langle h \rangle_f}{\partial x_j} &= \frac{\partial}{\partial x_j} \sum_{i=1}^{N_s} e_i \int_{A_f(x)} h(\mathbf{E}) dA \\ &= \sum_{i=1}^{N_s} \frac{\partial}{\partial x_j} \int_{A_f(x)} h(\mathbf{E}) dA \end{aligned} \quad (\text{A3-13})$$

The derivative of the integral in the second line is:

$$\begin{aligned} \frac{\partial}{\partial x_j} \int_{A_f(x)} h(\mathbf{E}) dA &= \lim_{\delta \rightarrow 0} \frac{1}{\delta} \left[\int_{A_f \cap V(x + \delta e_j)} h(\mathbf{E}) dA - \int_{A_f \cap V(x)} h(\mathbf{E}) dA \right] \\ &= \lim_{\delta \rightarrow 0} \left[\frac{1}{\delta} \int_{A_f \cap \partial V(x)} h(\mathbf{E}) \delta e_j \cdot ds(\mathbf{E}) + o(\delta) \right] \\ &= \int_{A_f \cap \partial V(x)} h(\mathbf{E}) e_j \cdot ds(\mathbf{E}) \\ &= \int_{A_f \cap \partial V(x)} h(\mathbf{E}) n_j ds(\mathbf{E}) \end{aligned} \quad (\text{A3-14})$$

where

- e_j = the unit basis vector in the direction of x_j
- $V(x + \delta e_j)$ = the averaging volume translated in the direction e_j
- $\partial V(x)$ = the surface of the averaging volume
- $\mathbf{n}(\mathbf{E})$ = the unit normal to $\partial V(x)$
- $ds(\mathbf{E})$ = an infinitesimal, oriented segment of $\partial V(x) \cap A_f$
- $ds(\mathbf{E}) = |ds(\mathbf{E})|$

Thus:

$$\nabla \int_{A_f(x)} h(\mathbf{E}) dA = \int_{A_f \cap \partial V(x)} h(\mathbf{E}) \mathbf{n}(\mathbf{E}) ds(\mathbf{E}) \quad (\text{A3-15})$$

An alternative form may be obtained by noting that:

$$\begin{aligned} \int_{A_f \cap \partial V(x)} h(\mathbf{E}) \mathbf{n}(\mathbf{E}) ds(\mathbf{E}) &= \int_{\partial(A_f \cap V(x))} h(\mathbf{E}) ds - \int_{\partial A_f \cap V(x)} h(\mathbf{E}) ds \\ &= \int_{A_f \cap V(x)} \nabla h(\mathbf{E}) dA - \int_{\partial A_f \cap V(x)} h(\mathbf{E}) ds \end{aligned}$$

Similarly, the term $\nabla\eta(\xi)$ in Equation A3-9 can be represented as:

$$\begin{aligned}\nabla\eta(x) &= \int_{A_f(x)} dA \\ &= \int_{A_f \cap \partial V(x)} n(\xi) ds \\ &= \int_{\partial\Omega_f \cap V(x)} ds\end{aligned}\tag{A3-17}$$

Thus the gradient of average head may be expressed in either of two alternative forms, one consisting of line integrals on $\Omega_f \cap \partial V(\omega)$, and the other in terms of a volumetric average of the gradient, i.e. $\langle \nabla h \rangle^f$, and line integrals on $\partial\Omega_f \cap V(\omega)$.

The formulae for estimation of volume-averaged quantities were implemented in a FORTRAN program AVGVOLS. The source and executable code for this program are on file as described in a memo on file regarding quality assurance. The program was verified informally, by using it to postprocess simulations of uniform gradient through sets of throughgoing, orthogonal fractures. Full verification of this software was beyond the scope of the project. In a full verification, a few cases of more complicated fracture geometry should be considered to see if numerical problems arise in estimating the volume-averaged quantities for the more irregular triangular element shapes and range of transmissivities which occur in realistic DFN models.

APPENDIX 4 ESTIMATION OF A 3-D CONDUCTIVITY TENSOR FROM MULTIPLE SIMULATIONS

Block conductivity tensors were estimated for each averaging volume, by analysis of the volume-averaged estimates of gradient ∇h and flux density (velocity) u from all sets of boundary conditions.¹ The idea is to calculate the tensor K with components K_{ij} which minimizes the error:

$$R^2 = \sum_{n=1}^N \epsilon_{(n)} \cdot \epsilon_{(n)} \quad (\text{A4-1})$$

where N is the number of sets of boundary conditions used, and:

$$\epsilon_{(n)} = u_{(n)} + K \nabla h_{(n)} \quad (\text{A4-2})$$

Here $\epsilon_{(n)}$ represents the vector error in the velocity, *i.e.* the vector difference between the measured (simulated) velocity, and the velocity which is predicted for the given head gradient and the fitted conductivity tensor.

In tensor notation, Equation A4-1 may be expanded as:

$$R^2 = \sum_{n=1}^N K_{ij} K_{ik} h_{j(n)} h_{k(n)} + 2 \sum_{n=1}^N K_{ij} h_{j(n)} u_{i(n)} + \sum_{n=1}^N u_{i(n)} u_{i(n)} \quad (\text{A4-3})$$

where Einstein's summation convention is assumed for unparenthesized subscripts, and where h_i denotes $\partial h / \partial x_i$. The error is minimized when:

$$\frac{\partial(R^2)}{\partial K_{ij}} = 2 \sum_{n=1}^N K_{ik} h_{j(n)} h_{k(n)} + 2 \sum_{n=1}^N h_{j(n)} u_{i(n)} = 0 \quad (\text{A4-4})$$

Rearrangement gives:

$$K_{ik} \sum_{n=1}^N h_{j(n)} h_{k(n)} = - \sum_{n=1}^N h_{j(n)} u_{i(n)} \quad (\text{A4-5})$$

Since $K_{ij} = K_{ji}$ (the tensor K is assumed to be symmetric), the expansion of this equation can be written as a matrix equation:

$$HK^T = -U^T \quad (\text{A4-6})$$

Dropping the parentheses on the second index n , so that summation (over $n = 1, 2, \dots, N$) is implied for doubled indices, the elements of the above equation are written explicitly as:

$$K = [K_{11'}, K_{12'}, K_{22'}, K_{23'}, K_{33'}, K_{31}] \quad (\text{A4-8})$$

¹ The notation denoting averaged quantities is suspended in this section for brevity.

A4.2

$$H = \begin{bmatrix} h_{1n} h_{1n} & h_{1n} h_{2n} & 0 & 0 & 0 & h_{1n} h_{3n} \\ h_{2n} h_{1n} & (h_{1n} h_{1n} + h_{2n} h_{2n}) & h_{1n} h_{2n} & h_{1n} h_{3n} & 0 & h_{2n} h_{3n} \\ 0 & h_{1n} h_{2n} & h_{2n} h_{2n} & h_{2n} h_{3n} & 0 & 0 \\ 0 & h_{1n} h_{3n} & h_{2n} h_{3n} & (h_{2n} h_{2n} + h_{3n} h_{3n}) & h_{2n} h_{3n} & h_{1n} h_{2n} \\ 0 & 0 & 0 & h_{2n} h_{3n} & h_{3n} h_{3n} & h_{1n} h_{3n} \\ h_{1n} h_{3n} & h_{2n} h_{3n} & 0 & h_{1n} h_{2n} & h_{1n} h_{3n} & (h_{1n} h_{1n} + h_{3n} h_{3n}) \end{bmatrix} \quad (A4-7)$$

and:

$$U^T = \begin{bmatrix} h_{1n} u_{1n} \\ (h_{1n} u_{2n} + h_{2n} u_{1n}) \\ h_{2n} u_{2n} \\ (h_{2n} u_{3n} + h_{3n} u_{2n}) \\ h_{3n} u_{3n} \\ (h_{3n} u_{1n} + h_{1n} u_{3n}) \end{bmatrix} \quad (A4-9)$$

Solution of this equation for the independent components of K (the vector K) is straightforward. In the present study, assembly and solution of the equations by LU decomposition were performed using a C-language program KFit. The error R^2 is estimated by substitution of the estimated K into Eq. A4-3. The program KFit also calculates the principal components and directions for K . These are given in the demonstration dataset.

A4.1 Tests of Validity for a Conductivity Tensor

To answer the question of whether a fractured rock mass can be described by an effective conductivity tensor, one must first define a measure of the goodness of fit. Long *et al.* (1985) defined a relative measure for a simulated 2-D fractured rock mass, in terms of the differences between measured (simulated) directional conductivities and the directional conductivities which were expected based on the applied gradients and the fitted conductivity tensor. Following Scheidegger (1954), Long *et al.* defined an error measure analogous to R^2 , in terms of the inverse of the the measured and predicted directional conductivities:

$$R_2^2 = \sum_{k=1}^N \left[K_{n(k)}^{-1} - K_{ij}^{-1} n_{i(k)} n_{j(k)} \right]^2 \quad (A4-10)$$

where:

$\mathbf{n}_{(k)}$ = the direction of flow in the k th permeameter simulation

$K_{\mathbf{n}_{(k)}}$ = the directional K measured in direction $\mathbf{n}_{(k)}$

The measure R_1^2 is a somewhat more strict measure of tensor validity than R_2^2 , because it includes the total error of measured (relative to predicted) velocity. R_2^2 , in contrast, includes only the component of error in the direction of the applied head gradient. The fact that R_2^2 fails to account for other components of error was tacitly noted by Long *et al.* (1985), in a discussion of flow components orthogonal to the applied heads. R_1^2 accounts for these orthogonal errors as well as the error in the direction of the applied gradient.

A problem is that both R_1^2 and R_2^2 depend rather strongly on the magnitude of conductivity. For R_2^2 , Long *et al.* proposed the normalized quantity:

$$r_2^2 = R_2^2 K_1 K_2 \quad (\text{A4-11})$$

where:

K_i = the i th principal (2-D) conductivity

as a relative measure, taking $\sqrt{K_1 K_2}$ to be a reasonable estimate of the mean (2-D) conductivity over all directions. This could be generalized to 3-D with an appropriate estimate of the mean conductivity.

Corresponding to R_1^2 , one possible normalized measure is given by:

$$\frac{1}{N} \sum_{n=1}^N \frac{\mathbf{e}_{(n)} \cdot \mathbf{e}_{(n)}}{\|K \nabla h_{(n)}\|^2} \quad (\text{A4-12})$$

For the case of isotropic conductivity K and unit head gradients, it may easily be verified that this reduces to:

$$\frac{1}{NK^2} \sum_{n=1}^N \mathbf{e}_{(n)} \cdot \mathbf{e}_{(n)} = \frac{R_1^2}{NK^2} \quad (\text{A4-13})$$

Therefore a reasonable normalization of R_1^2 for the present study (which uses nominally unit applied gradients) is:

$$r_1^2 = \frac{1}{N} \frac{R_1^2}{(K_1 K_2 K_3)^{2/3}} \quad (\text{A4-14})$$

A4.4

where the denominator of the second term is the geometric mean of the estimated principal conductivities K_i .²

A problem with both r_1^2 and r_2^2 is that they are only *relative* measures of tensor validity. That is, they allow comparisons as to whether one block is better described by a tensor than another, but do not lead to absolute statements as to whether or not a rock mass can be represented by a tensor. What is needed is a definition of what can, for "practical purposes," be regarded as an allowable deviation from a tensor, *i.e.*, to define an acceptable range of values for r_1^2 or r_2^2 .

For lack of a definition of what is "practically" tensor behavior, the present study reports only the relative measure r_1^2 . For the assumption that a given block of rock can be described by a tensor, r_1^2 is roughly the square of the magnitude of the resulting *relative error in flow velocity*, for a unit gradient. Thus these values can be used as a basis for crude estimates of the error in the velocity fields predicted by a multi-block SC model, based on the assumption that every block has an effective conductivity tensor.

² This measure is used for evaluating demonstration runs for the DFN/SC interface, rather than explicitly calculating the quantity in Equation A4-12. This is because the version of KFit used for the demonstration runs produced only summary output, which did not include the quantity in Equation A4-12.

APPENDIX 5 ESTIMATION OF COVARIANCE MATRIX FUNCTION

The covariance matrix function is estimated from a set of measured (simulated) packer-test conductivities, $K_p(x_i)$, and measured (simulated) block-scale conductivity tensors $\mathbf{K}(s, x_i)$, where s indicates the scale on which the conductivity is measured.

To simplify the formulae which follow, define $T: \mathbf{A} \rightarrow A$, for any 3×3 tensor \mathbf{A} (with components a_{ij}) and 6-dimensional vector A (with components A_k), as the rearrangement:

$$A_k = a_{ij}, \quad j \geq i, \quad k = 3(i-1) + (j-i+1) \quad (\text{A5-1})$$

thus giving $a_{11} = A_1$, $a_{12} = A_2$, $a_{13} = A_3$, $a_{22} = A_4$, $a_{23} = A_5$, and $a_{33} = A_6$.

Assuming that there is only one measurement scale s of interest (corresponding to the support scale for the SC), and defining $\mathbf{X}_r(x) = T[\mathbf{K}(s, x)]$, a pair of $K_p(x)$ and $\mathbf{K}(x)$ measurements taken from the same point x constitutes a *complete observation*:

$$\mathbf{X}(x) = [\mathbf{X}_r(x), K_p(x)] \quad (\text{A5-2})$$

The subscripted notation \mathbf{X}_r is used to denote the specific observation at the r th measurement point, i.e. $\mathbf{X}_r = \mathbf{X}(x_r)$.

More generally, for a given point x there may be a $K_p(x)$ but no corresponding measurement $\mathbf{K}(x)$, resulting in an *incomplete observation* of the first type:

$$\mathbf{K}(x) = [\emptyset, \emptyset, \emptyset, \emptyset, \emptyset, \emptyset, K_p(x)] \quad (\text{A5-3})$$

Conversely, there may be a $\mathbf{K}(x)$ without a corresponding $K_p(x)$, giving an incomplete observation of the second type:

$$\mathbf{X}(x) = [\mathbf{X}_r(x), \emptyset] \quad (\text{A5-4})$$

These incomplete observations lead to slight complications in the analysis, as noted below. Generally speaking, DFN model simulations produce a high number of observations of the second type, since the $\mathbf{K}(x)$ can be calculated at an arbitrary number of points for a given simulation, but each $K_p(x)$ measurement requires a separate, transient simulation.

Simpler models can also be considered. For instance, the vector $\mathbf{X}(x)$ could be defined as consisting of two components (e.g., an effective isotropic conductivity K_v and K_p) or four components (e.g. the principal conductivities $\{K_1, K_2, K_3\}$ and K_p , or the directional conductivities $\{K_x, K_y, K_z\}$ and K_p).¹ The discussion which follows is quite general, and applies to any type of p -dimensional

¹ Alternatively, the K_p component could be expanded to include several packer test interpretations at the same point (e.g. K_{Moyes} and K_{GRF} interpretations of the same test). This approach would require some minor changes in the notation used here.

observation vector $X(x)$, except where specific reference is made to the tensor portion $X_T(x)$.²

To utilize the relatively extensive theory which is available for multinormal (multivariate Gaussian) distributions, a transformation $G: X \rightarrow Y$ must be sought which maps the observations onto a vector Y which has a multinormal (multivariate normal) distribution.³ In the case of spatially varying expectation $E[X(x)]$, the trend should be removed by a spatially varying transformation, prior to choosing G .

The choice of G is potentially a time-consuming task. If a simple G cannot be found by inspection, the quickest way to obtain a suitable G may be to fit a discrete (piecewise) transformation to the data. It is essential to keep G simple, so that the inverse G^{-1} may be obtained, for generating the conductivity field in the SC model.

For the demonstration case reported in the present study, only logarithmic transforms were considered, based on the common assumption that conductivities are approximately lognormal. The DFN model was simulated based on spatially uniform statistics, so there was no need to remove a trend in $E[X(x)]$. The demonstration included statistical tests of the hypothesis that the transformed data belonged to a multinormal distribution, but no attempt was made to find a better transformation in the event that this hypothesis was rejected.

A5.1 Logarithmic transformations

The concept of a logarithmic transformation for conductivity tensors requires some discussion. A component-wise transformation:

$$Y_i = a_i + b_i \log X_i \quad (\text{A5-5})$$

where $a_i = E[\log X_i]$ and $b_i = V[\log X_i]^{1/2}$ may work for the simpler cases mentioned above. However, for the case where $X = [X_T, K_p]$, a valid, component-wise transformation may not exist. The off-diagonal components K_{ij} , $i \neq j$, of the conductivity tensor can be less than zero, giving complex-valued $\log K_{ij}$. It is questionable whether *any* component-by-component transformation will give a meaningful estimate of the "average" K tensor, and a meaningful estimate of the variability of K .

A logarithmic transformation which maps a second-order tensor onto another second-order tensor has been suggested by Sven Norman (personal communication, 1991). This "tensor log" operator is defined as follows. For any diagonal tensor D with components:

define the tensor log as $\text{Log } D$, with components:

For any orthogonal matrix A with components a_{ij} , define the tensor log of $B = A^T D A$ as:

² Note that the subscript p is serving a double purpose here, denoting both the dimension of X and the fact that K_p represents a packer test.

³ Note that the problem of estimating a Gaussian transformation is avoided if the DFN model is used to estimate the properties of a nonparametric SC model based on indicator variograms (*cf.* Winberg *et al.*, 1990). The nonparametric approach would need to be extended to handle multicomponent observations, by defining indicator covariograms as well as variograms.

A5.3

$$\begin{aligned} d_{ij} &= 0, & i \neq j \\ d_{ij} &> 0, & i = j \end{aligned} \quad (A5-6)$$

$$\log_{ij} A^T D A = a_{*i} a_{*j} \log_{km} D = A^T (\text{Log } D) A \quad (A5-8)$$

This definition of the tensor log has some desirable properties. Firstly:

$$\text{Log } I = 0 \quad (A5-9)$$

Secondly, it is easily verified that the tensor log is itself a tensor, and transforms according to the same rules as its "tensor exponent" (the inverse operator). The matrix notation **Log B** is used to emphasize this fact. The corresponding tensor notation, $\log_{ij} B$, may be used interchangeably.

This definition is physically sensible for conductivity tensors. If **D** is viewed as the diagonal matrix of eigenvalues for a tensor, then **Log D** defines an ellipsoid with principal axes equal to the logs of the principal axes of the ellipsoid defined by **D**. As the tensor log transforms according to the same laws as the original tensor, taking directional logs is also sensible.

This gives a logarithmic transformation for the tensor portion X_T of X . An additional multivariate transform on this vector is applied as follows:

Define the "tensor" portion of $Y(x)$ as:

$$Y_T(x) = T^{-1}[\text{Log } K(x)] = T^{-1}\{\text{Log } T[X_T(x)]\} \quad (A5-10)$$

and the "packer test" portion as:

$$Y_p(x) = \log K_p \quad (A5-11)$$

The complete, logarithmic transformation is then defined as:

$$Y(x) = G_1[X(x)] \doteq [Y_T(x), Y_p(x)] \quad (A5-12)$$

The subscripted notation $Y_r = G_1[X_r]$ is used to denote the transformed r th observation. The i th component of Y_r is denoted Y_{ri} . For the cases of incomplete observations it is understood that:

$$G_1\{[\emptyset, \emptyset, \emptyset, \emptyset, \emptyset, \emptyset, K_p]\} \doteq [\emptyset, \emptyset, \emptyset, \emptyset, \emptyset, \emptyset, Y_p] \quad (A5-13)$$

and

$$G_1\{[X_T, \emptyset]\} \doteq [Y_T, \emptyset] \quad (\text{A5-14})$$

The sample mean of Y is \bar{Y} , with components:

$$\bar{Y}_i = \frac{\sum_{r=1}^N Y_{ri}}{\sum_{r=1}^N \Lambda(Y_{ri})} \quad (\text{A5-15})$$

where

N = the number of observations (complete or incomplete)

and

$$\Lambda(Y_{ri}) = \begin{cases} 0, & Y_{ri} = \emptyset \\ 1, & Y_{ri} \neq \emptyset \end{cases} \quad (\text{A5-16})$$

The sample covariance matrix S of Y is defined as $S = (s_{ij})$ where the elements s_{ij} are calculated as:

$$s_{ij} = \frac{1}{N_{ij}} \sum_{r=1}^N \Lambda(Y_{ri})(Y_{ri} - \bar{Y}_i) \Lambda(Y_{rj})(Y_{rj} - \bar{Y}_j) = \frac{1}{N_{ij}} \sum_{r=1}^N \Lambda(Y_{ri}) \Lambda(Y_{rj}) Y_{ri} Y_{rj} - \bar{Y}_i \bar{Y}_j \quad (\text{A5-17})$$

where

$$N_{ij} = \sum_{r=1}^N \Lambda(Y_{ri}) \Lambda(Y_{rj}) \quad (\text{A5-18})$$

Denoting the portion of S corresponding to the Y_T portion of Y as S_T , i.e. $S_T = (s_{ij})$, $i, j < p$, a final transformation is applied to give:

$$Z = G_2[Y] \doteq [Z_T, Z_p] \quad (\text{A5-19})$$

where

$$Z_T = S_T^{-1/2} [Y_T - \bar{Y}_T] \quad (\text{A5-20})$$

is the Mahalanobis transform of Y_T (Mardia *et al.*, 1979, p. 14), and

$$Z_p = \frac{Y_p - \bar{Y}_p}{SD[Y_p]} \quad (\text{A5-21})$$

where $SD[]$ denotes the standard deviation of the sample. The effect of this transformation is to separately center and standardize the variance of the tensor component Y_T , and the scalar component Y_p . The Mahalanobis transformation furthermore eliminates the sample correlation between tensor components, so that, in effect, later analysis of correlation between packer test results and block-scale conductivities may be performed using conductivity tensors aligned with a "global" set of principal directions for the local conductivity tensors.

The CMFs are calculated based upon the centered and standardized vectors $Z(x_i)$. The "unbiased" estimate of S_T used to perform the Mahalanobis transformation is included in the univariate statistical summary.

A5.2 Tests of multinormal behavior for transformed data

A "necessary" (but not "sufficient") condition for multivariate data to be considered multinormal, is that each of the components, taken individually, should be normally distributed. This follows from the observation that any projection of a multinormal (multivariate normal) distribution into 1-D space yields a univariate normal distribution (Mardia *et al.*, 1979, p. 60). Therefore a first step in assessing multinormal behavior is to see if the individual components are normally distributed.

In the demonstration case for the present study, this was done using the Kolmogorov-Smirnov (KS) statistic and KS probability, for univariate comparison of the transformed data Z_i with $N(0,1)$. The results are given in the univariate statistical summary for each component of the data vector. The KS statistic D varies from 0 to 1 (100%). High values indicate a poor fit. The KS probability also varies from 0 to 1 (100%). The KS probability as defined here is the significance level (usually $1-\alpha$ in the tables) above which $H_0: Z_i \sim N(0,1)$ would be incorrectly rejected for the given sample size. Higher values indicate a better fit.

More strict assessment of multinormal behavior should be based on truly multivariate tests. Mardia *et al.* (1979) suggest calculating the multivariate skewness $b_{1,p}$ and kurtosis $b_{2,p}$ (defined by Mardia *et al.* p. 20). For large samples of truly multinormal variables, these statistics have the asymptotic distributions (Mardia *et al.*, p. 149):

$$\frac{1}{6}nb_{1,p} \sim \chi_f^2, \quad f = \frac{1}{6}p(p+1)(p+2) \quad (\text{A5-22})$$

and

$$[b_{2,p} - p(p+2)] \sqrt{\frac{n}{8p(p+2)}} \sim N(0,1) \quad (\text{A5-23})$$

where p is the number of components in a data vector. The hypothesis of multinormality is rejected for large values of $b_{1,p}$, and for both large and small values of $b_{2,p}$.

In the demonstration case for the present study, the multivariate skewness and kurtosis measures were calculated only for the transformed tensor:

$$Z = T[Z(s,x)] \quad (\text{A5-24})$$

The skewness and kurtosis values calculated for the component corresponding to K_p component are the ordinary univariate statistics. Due to the high percentage of intervals for which K_p was below the simulation threshold (*i.e.*, non-conductive intervals), it was clear from the outset that $\log K_p$ would *not* be normally distributed.

The existence of measurement thresholds, both for K_p and the components of K , means that future work in this direction should use tests appropriate for truncated multinormal distributions. A univariate test for truncated normal distributions is easily obtained by calculating the CDF:

$$F(x) = \frac{1}{\sqrt{2\pi\sigma^2}} \int_{x_{\min}}^x e^{-\frac{(t-\mu)^2}{2\sigma^2}} dt = \frac{1}{2} + \operatorname{erf}\left(\frac{x_{\min}-\mu}{\sqrt{2}\sigma}\right), \quad x \geq x_{\min} \quad (\text{A5-25})$$

and using this to perform a K-S test for each component. Alternatively a χ^2 test can be performed on each component, by binning together all data at or below the measurement threshold.

A true, multivariate test is not so easily devised. One possibility is χ^2 contingency table analysis, as is commonly used for bivariate data. However, extending this method to multivariate data leads to very low resolution unless the number of data points is very high. For the 7-dimensional observations considered here, in order to have divide the parameter space into just 3 bins for each dimension would give 3^7 bins. For the test to have any meaning the number of data points should be considerably higher than this.

A5.3. Nonparametric estimates of the covariance matrix function

Given a set of observations, which have been transformed to a multinormal sample $Z(x_i)$, the first task in estimation of the CMF is to assemble all *admissible* data pairs $[Z(x_i), Z(x_j)]$. For reasons related to the nested simulation scheme, admissible pairs are restricted to those for which:

$$\|x_j - x_i\| \leq c_n r_{ij} \quad (\text{A5-26})$$

where:

- r_{ij} = the minimum fracture size simulated throughout the smallest block containing both x_i and x_j .
 c_h = an admissibility factor ≥ 2 , and preferably ≥ 5 .

The vector $h_{ij} = x_j - x_i$ is referred to as the lag (separation) vector.

Nonparametric estimates of the CMF are calculated for "lag classes," denoted L_n . For the demonstration case bins corresponding to the L_n were defined in spherical coordinates in the lag space, with logarithmic spacing for the radial coordinate.

The nonparametric estimates of the CMF are calculated from:

$$\Gamma_{k,l}(L_n) = \frac{1}{N_{L_n}} \sum_i \sum_j M[x_i, x_j; L_n, c_h] Z_k(x_j) Z_l(x_i) \quad (\text{A5-27})$$

where:

$$M[x_i, x_j; L_n, c_h] = \left\{ \begin{array}{ll} 1, & x_j - x_i \in L_n \quad \wedge \quad \|x_j - x_i\| \leq c_h r_{ij} \\ 0, & \text{otherwise} \end{array} \right\} \quad (\text{A5-28})$$

is the membership function for admissible members of L_n , and where:

$$N_{L_n} = \sum_i \sum_j M[x_i, x_j; L_n, c_h] \quad (\text{A5-29})$$

is the number of admissible pairs in class L_n .

A5.4 Convergence of the CMF estimates

The issue of convergence is preferably addressed at this point, due to the difficulties inherent to the next step, fitting a CMF. For the demonstration exercise in the present study, no attempt was made to fit a CMF, and the issue of convergence of the CMF estimates was not considered. For future work, this issue of convergence will need to be considered.

A test for convergence, based on the jackknife method (Efron, 1982), is proposed as follows. Let $\Gamma_{k,l(r)}(L_n)$ denote the value of $\gamma_{k,l}(L_n)$ which is obtained by excluding the r th measurement point:

$$\Gamma_{k,l(r)}(L_n) = \frac{1}{N_{L_n(r)}} \sum_{i \neq r} \sum_{j \neq r} M[x_i, x_j; L_n, c_h] Z_k(x_j) Z_l(x_i) \quad (\text{A5-30})$$

where

$$N_{L_n(r)} = \sum_{i \neq r} \sum_{j \neq r} M[x_i, x_j; L_n, c_h] \quad (\text{A5-31})$$

is the number of admissible pairs in L_n , when the r th point is excluded from the dataset. Let:

$$\Gamma_{k,j(\cdot)}(L_n) = \frac{1}{N} \sum_{r=1}^N \Gamma_{k,j(r)}(L_n) \quad (\text{A5-32})$$

Then the *jackknife estimate of standard deviation* for $\gamma_{k,j}(L_n)$ is:

$$\text{SD}_j[\Gamma_{k,j}(L_n)] = \left\{ \frac{N-1}{N} \sum_{r=1}^N [\Gamma_{k,j(r)}(L_n) - \Gamma_{k,j(\cdot)}(L_n)]^2 \right\}^{1/2} \quad (\text{A5-33})$$

This is an estimate of the standard deviation of $\Gamma_{k,j}(L_n)$, for a sample of size N , as an estimate of the $\Gamma_{k,j}(L_n)$ for $N \rightarrow \infty$. Thus this can be related to estimates of the error due to estimation based on finite N .

Convergence may be assumed when the average standard deviation over all non-empty L_n s falls below a specified tolerance α :

$$\frac{1}{N_L} \sum_n \text{SD}_j[\Gamma_{k,j}(L_n)] \leq \alpha \quad (\text{A5-34})$$

where N_L is the number of classes L_n containing at least one admissible pair. Since the $Z(x)$ are centered and standardized, it can be expected that typically $|\Gamma_{k,j}(L_n)| < 1$. Therefore a value of α in the range 0.05 to 0.2 is reasonable, depending of course on the robustness of the CMF-fitting algorithm.

The jackknife estimate of standard deviation, SD_j , falls into the category of "computationally intensive statistics." The CPU time needed to calculate SD_j is roughly N times the CPU time to calculate one set of estimates $\Gamma_{k,j}(L_n)$. As an example, for the demonstration case which had $p = 7$ vector components and 704 lag classes (giving $7 \times 7 \times 704 = 34,496$ possible bins $\Gamma_{k,j}(L_n)$), the calculation time on a PC-AT 386/387, 20MHz compatible was about 2 hours. For large N the calculation of SD_j will obviously require a fast mainframe, and even then the computation may be impractical for large datasets. For such large datasets it may be practical to replace SD_j with a *bootstrap estimate of standard deviation* SD_B (see Efron, p. 28), for which the number of recalculations of values analogous to $\Gamma_{k,j(r)}(L_n)$ is not constrained to equal N .

A5.5 Covariance Matrix Function Fitting

The $p \times p$ matrices of estimators $\mathbf{\Gamma}(L_n) = [\Gamma_{k,l}(L_n)]$ gives a nonparametric estimate of the covariance matrix function $\mathbf{C}(h) = [C_{k,l}(h)]$, where h is the lag vector. The relation of $\mathbf{\Gamma}(L_n)$ to $\mathbf{C}(h)$ is given by:

$$\Gamma(L_n) = \frac{\int_{L_n} C(\mathbf{h}) dV(\mathbf{h})}{\int_{L_n} dV(\mathbf{h})} + \mathbf{E}(L_n) = \frac{1}{|L_n|} \int_{L_n} C(\mathbf{h}) dV(\mathbf{h}) \quad (\text{A5-35})$$

where

$\mathbf{E}(L_n)$ = matrix of residuals (errors) for the class L_n

For compatibility with HYDRASTAR simulation algorithms, it is desirable that $C(\mathbf{h})$ be expressible as a linear combination of covariance functions:

$$C(\mathbf{h}) = \sum_{k=1}^M \mathbf{B}_k C_k(\mathbf{h}) \quad (\text{A5-36})$$

where the M $p \times p$ matrices \mathbf{B}_k are required to be symmetrical and positive-semidefinite, and the $C_k(\mathbf{h})$ are covariance functions based on spherical or exponential models, with geometrical anisotropy.

The problem of fitting a CMF to the $\Gamma(L_n)$ is a matter of finding the set of \mathbf{B}_k and $C_k(\mathbf{h})$ which minimize an error measure such as the sum of the residuals squared:

$$\sum_n \text{tr} \mathbf{E}^T(L_n) \mathbf{E}(L_n) \quad (\text{A5-37})$$

Assuming that only exponential models are considered, the number of parameters in the fitting problem is $6 \times \frac{1}{2}p(p-1) \times M = 126M$ for the full-tensor case. Obviously the problem of finding the optimum fit in a parameter space of such high dimension will be difficult, particularly if the response function (the error measure) is non-smooth and/or has many local minima. For such a function, an optimization algorithm such as the conjugate-gradient algorithm will need to be applied repeatedly for a large number of starting points. A very large number of starting points may be needed to be considered, to give a reasonably good chance of finding the optimum.

However, it is possible that a local minimum which is not the global minimum will still give an acceptable fit, since the very problem of non-uniqueness suggests that there will be multiple sets of \mathbf{B}_k and $C_k(\mathbf{h})$ that combine to give $C(\mathbf{h})$ which are practically identical. Nevertheless, the high dimensionality of the parameter space will make it costly to explore, so it is desirable to keep the trial models as simple as possible (*i.e.*, start by using the smallest M possible).

Geological insight may provide some shortcuts. For example, the fact that the major features at the Finnsjön site fall into three sets, according to orientation, suggests that a preliminary model should include terms $C_k(\mathbf{h})$ with strong geometrical anisotropy, constrained to be approximately aligned parallel to these sets.

A second possibility for simplification is to begin with the case of isotropic conductivity, in which case the number of parameters in the fitting problem is only $12M$. The isotropic-K model could

A5.10

then be extended to the anisotropic- K case, using the isotropic- K model as a starting point. The advantage of this strategy is that, in the process, a CMF is estimated which can be used for simulations of a SC model based on isotropic- K elements. Thus a working model is produced which can be used, if the fitting of the fully anisotropic- K model fails.

**APPENDIX 6 COMPARISON OF DIP DATA AMONG SECTIONS OF BOREHOLES
KFI 06 AND KFI 11**

The tables in this Appendix show the results of a statistical analysis of dip angle distributions from Boreholes KFI 06 and KFI 11. The comparisons were made between intervals in these boreholes, by comparing the distributions in terms of Kolmogorov-Smirnov (KS) and χ^2 statistics. Both statistics were used to test the hypothesis H_0 that the distributions for the two sections being compared are identical. Two values are given for each cell in these tables. The first number is the confidence level at which H_0 is accepted, based on the KS test statistic. The second is the corresponding confidence level for the χ^2 test statistic.

Table A6-1 Comparison of dip angle distributions between intervals from above Zone 2, Borehole KFI 11.

Interval (m)	50-100	100-150	150-200	200-221
0-50	86.2 39.4	74.0 33.4	53.7 25.5	89.3 41.4
50-100	.	73.5 33.3	2.3 3.5	10.9 8.8
100-150	.	.	10.7 8.7	12.9 9.8
150-200	.	.	.	58.8 27.4

Table A6-2 Comparison of dip angle distributions between intervals from within Zone 2, Borehole KFI 11.

Interval (m)	250-300	300-338
221-250	0.1 0.6	49.9 24.0
250-300	.	5.7 5.9

Table A6-3 Comparison of dip angle distributions between intervals from below Zone 2, Borehole KFI 11.

Interval (m)	350-400
338-350	98.4 51.6

A6.2

Table A6-4 Comparison of dip angle distributions between 50 m intervals from different regions, Borehole KFI 11.

Region/ Interval (m)		Zone 2 250-300	Below Zone 2 350-400
Above Zone 2	0-50	39.8 20.5	99.0 53.5
	50-100	51.9 25.0	35.5 18.9
	100-150	87.4 40.3	17.6 11.9
	150-200	1.4 2.6	12.0 8.3
Zone 2 250-300		.	0.2 0.9

Table A6-5 Comparison of dip angle distributions between different regions Borehole KFI 11.

Region Interval (m)	Zone 2 221-338	Below Zone 2 338-400
Above Zone 2 0-221	59.2 27.6	23.8 14.6
Zone 2 221-338	.	6.0 6.2

Table A6-6 Comparison of dip angle distributions between intervals from within Zone 2, Borehole KFI 06.

Interval (m)	253-305
201-253	4.7 5.2

Table A6-7 Comparison of dip angle distributions between intervals from below Zone 2, Borehole KFI 06.

Interval (m)	352-403
305-352	0.0 0.1

A6.3

Table A6-8 Comparison of dip angle distributions between regions, Borehole KFI 06.

Region Interval (m)	Above Zone 2 153-201	Zone 2 201-305
Zone 2 201-305	4.7 5.3	.
Below Zone 2 305-403	61.3 28.4	2.2 3.3

APPENDIX 7 FRACSIZE ANALYSIS ALGORITHM

The fracture size analysis for the present study was performed using a development version of the FracSize tracelength simulation module. The basic algorithm for this version is basically the same as for the FracMan Version $\beta 2.3$ module FracSize as described by Dershowitz *et al.* (1991a). Some minor modifications were made to meet the requirements of the present study.

The main modification was the introduction of probabilistic censoring. The probability of observing a trace of length λ was taken to be:

$$P[\lambda | \lambda_{min}, c_\lambda] = \begin{cases} 0, & \lambda < \lambda_{min} \\ \frac{\lambda/\lambda_{min} - 1}{c_\lambda - 1}, & \lambda_{min} \leq \lambda \leq c_\lambda \lambda_{min} \\ 1, & \lambda > c_\lambda \lambda_{min} \end{cases} \quad (7)$$

where:

$$\begin{aligned} \lambda_{min} &= \text{smallest recorded tracelength} && [L] \\ c_\lambda &= \text{censoring parameter} && [-] \end{aligned}$$

In other words, the probability of observing an existing trace smaller than λ_{min} is taken to be zero. This probability increases linearly between λ_{min} and $c_\lambda \lambda_{min}$. It is assumed that traces larger than $c_\lambda \lambda_{min}$ are always mapped. For a given mapping scale, λ_{min} is the smallest tracelength in the dataset. For the sake of simplicity a single value of c_λ was assumed to apply for all scales. The effective value of c_λ might in fact vary with the mapping scale and methodology, but there is point in generalizing the model further until actual data are available to measure this effect.

A further modification of the algorithm was made to allow efficient simulations of surveys consisting of multiple trace maps of widely varying area and resolution, with varying censoring limits λ_{min} . The revised algorithm is depicted in Figure A7-1.

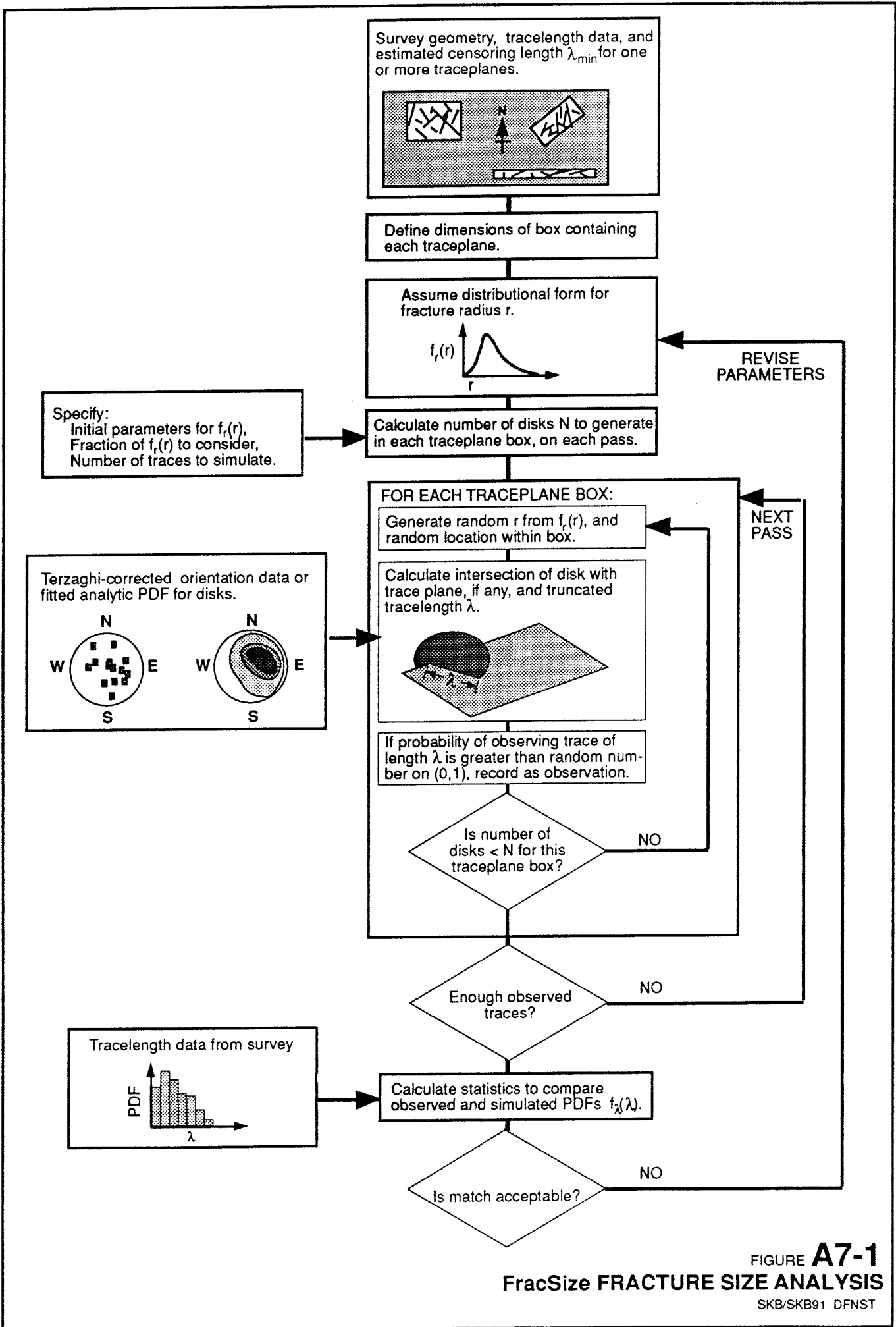


FIGURE A7-1
FracSize FRACTURE SIZE ANALYSIS
 SKB/SKB91 DFNST

APPENDIX 8 ESTIMATION OF NEAREST-NEIGHBOR STATISTIC FROM CORE DATA

This appendix describes methods for estimating Nearest Neighbor (NN) model statistics from core log data. It is emphasized that these methods should be applied only in cases where fracture trace data are inadequate for NN estimation, *e.g.* cases where the trace maps are too small in length and/or breadth to allow identification of the "major" fractures or fracture zone centers. The derivation is as follows.

To obtain a simple estimator of the Nearest neighbor statistic from core data, consider a tabular fracture zone, the normal vector of which makes an angle θ with the axis of a borehole intersecting the zone. Assume:

- All fractures within the zone are approximately parallel to the zone.
- The density of fracture locations can be described by the Nearest Neighbor model, defined with respect to a plane lying within the zone, *i.e.*:

$$f_x(x) \propto x^{-b}, \quad x > 0 \quad (8-1)$$

If $y = x \cos \theta$ is the distance along the borehole from the intersection with the plane of the zone, then for nonintegral b the probable number of intersections with the borehole in the interval $y_1 \leq y < y_1 + \Delta y$ is:

$$\begin{aligned} N &= \int_{y_1}^{y_1 + \Delta y} C y^{-b} \cos^{-b} \theta dy \\ &= C \cos^{-b} \theta \left[(y_1 + \Delta y)^{1-b} - y_1^{1-b} \right] \\ &= C \cos^{-b} \theta y_1^{-b} \left[(1-b) \Delta y + \frac{(1-b)(-b)}{2!} \frac{\Delta y^2}{y} + \dots \right] \end{aligned} \quad (8-2)$$

where C is a constant. For y_1 large relative to Δy , the approximation:

$$\log N \approx \text{const.} - b \log y_1 \quad (8-3)$$

gives a simple estimate of the Nearest Neighbor statistic $b_{NN} = b$, from a log-log plot of borehole distance *vs.* count of fracture intersections.

The assumptions invoked above, particularly the assumption of constant orientation, are quite restrictive. Therefore the above should be viewed as a preliminary estimate.

Simulated borehole sampling (using FracMan) gives a way of checking NN statistics estimated by the above formula, taking into account the effects of arbitrary orientation and size distributions. For the present study, this was done as described in the text, by χ^2 comparison of fracture spacing distributions for simulated and actual fracture populations.

However, this type of test based on fracture spacing is somewhat insensitive, due to the fact that

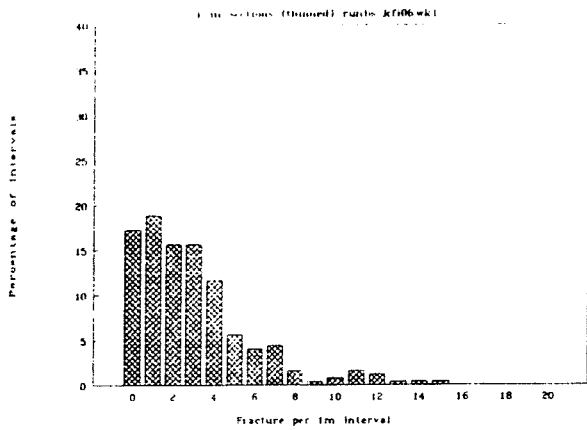
a wide range of fracture location models give approximately exponential spacing distributions. The latter phenomenon has been noted previously (Priest and Hudson, 1976), but evaluation of fracture location models based on fracture spacing is still a common technique in analysis of fractured rock masses. A more discriminating test (Geier and Dershowitz, 1992) is provided by comparison of observed and predicted histograms of fracture frequency.

Figure A8-1 compares a fracture frequency histogram for Borehole KFI 06 with the theoretical histogram for the uniform model, and histograms based on simulated borehole sampling of single realizations of a Nearest Neighbor model for two values of b_{NN} . The value $b_{NN} = 1.8$ is close to the value 1.73 which was used in DFN simulations for the present study. The value $b_{NN} = 0.8$ is closer to the value 0.73 which is estimated from the log-log plot of frequency *vs.* distance in Figure 5-3, by the above approximation formula. The histogram for KFI 06 was produced by thinning the dataset for coated fractures, by random sampling without replacement, to reduce the mean fracture frequency to 3 m⁻¹. The thinning was done in order to simplify this demonstration. The random sampling technique should preserve the main characteristics of fracture location, but it would be preferable to verify this using the entire dataset.

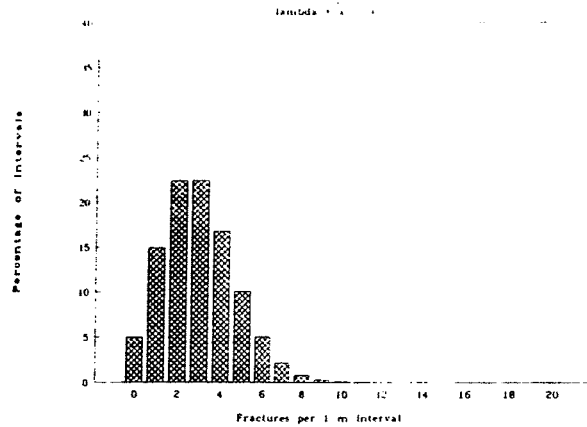
Comparison of the frequency histogram for KFI 06 with the uniform model shows clear differences at both ends of the distribution. The field data contain far too many intervals with no fracture intersections (0 fr/m), and also too many with > 8 fr/m, than can be expected from the uniform location model with the same mean frequency. The long tail of intervals with high frequency is diagnostic of a non-uniform location process.

Comparison with the Nearest Neighbor model, for the case $b_{NN} = 1.8$, gives somewhat better agreement, but there are clearly too many intervals with 0 fr/m, and not enough in the range 1 to 5 fr/m. Thus this model results in excessive differentiation between "good rock" and "fracture zones," relative to the field data.

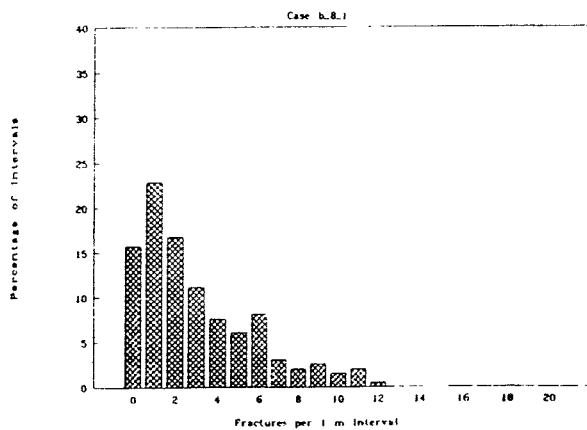
The case $b_{NN} = 0.8$ gives the best match to the data of the cases considered here. Unfortunately, no time was available in the present study to refine the estimate of b_{NN} by statistical comparison with simulated sampling, and incorporate the results in a revised DFN model.



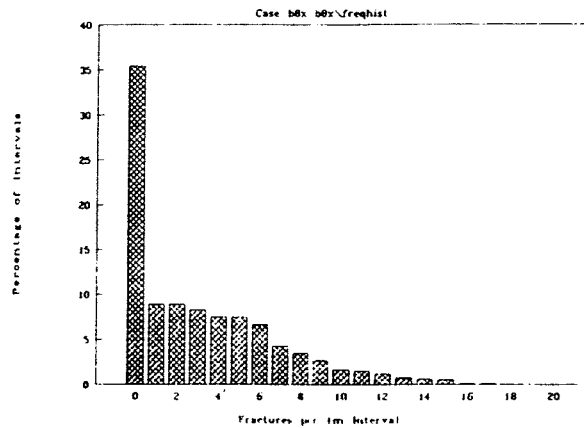
a) Thinned data from KFI 06



b) Uniform Poisson process model



c) Nearest-Neighbor model ($b_{NN} = 0.8$)



d) Nearest-Neighbor model ($b_{NN} = 1.8$)

FIGURE **A8-1**
DEMONSTRATION OF USE OF FRACTURE FREQUENCY
FOR EVALUATION OF LOCATION MODELS

(Reference, 1989)

SKB/SKB91 DFNST

APPENDIX 9 FRACTURE ROUGHNESS PROFILE ANALYSIS

Fracture roughness and/or aperture profiles provide data for estimating the variability of hydrologic properties within a single fracture plane. The profile data are interpreted in terms of a conceptual model for fracture aperture variation to determine input parameters for simulation of variable-aperture fractures.

This appendix describes analysis assumptions, dataset selection and preparation, and results.

A9.1 Analysis Assumptions

A relation between the variogram of aperture and the parameters characterizing a fractal fracture has been developed by Wang, Narasimhan, and Scholz (1988). Briefly, their relationship is based on a fractal model of roughness for the two surfaces of a fracture.

The applicability of a fractal model for fracture surface roughness has been demonstrated by Brown and Scholz (1985). However, data to test this assumption is still limited, and adoption of a fractal model for fracture surface roughness must be viewed as somewhat speculative.

The model of Wang *et al.* assumes two perfectly matched surfaces with fractal dimension D , one of which is displaced by a specified displacement r_c . Wang *et al.* present a mathematical formula which gives the variogram as a function of these two parameters. This model has been incorporated in the program MATCHPT (see Code Description Memorandum on file). The validity of this model has not been fully established. In the present analysis, the applicability of this model will be evaluated by comparison of the observed and theoretical variograms. Full validation of the model would require extensive measurements of aperture, which are at present not available.

A9.2 Fracture Roughness Profile Datasets

Fracture aperture data are not available for the Finnsjön site. Hence data from another site must be used as generic data. The data preferably meet the following three requirements:

- The rock type should be similar to the granitic rocks of the Finnsjön site.
- Fractures should be characterized on a scale comparable to the size of fractures of concern for DFN modelling. A rough guess (based on previous modelling work by GGAB for the Hard Rock Laboratory and the Finnsjön site) is that the minimum scale of concern is about 1 or 2 meters.
- Apertures should be measured *in situ*, if possible, so that the stresses applied to the fracture are relatively undisturbed. The way in which opposing faces of a fracture seat themselves can profoundly affect the aperture distribution, and is difficult to duplicate in the laboratory. This issue is discussed in the text.

One dataset which meets the above requirements is that from the Stripa Channeling Experiment

(SCE) (Abelin *et al.*, 1990, pp. 79-80, 86-93 and Appendix 10). Fracture apertures were estimated from photographs taken in boreholes which were drilled within the planes of individual fractures. The aperture measurements represent averages over 5 cm lengths. Abelin *et al.* give variograms of these measured, averaged apertures in their Appendix 10.

A9.2.1 Dataset Preparation

Variogram data were obtained by digitizing the plots given by Abelin *et al.* (1990). The numbering of the variogram analyses in this report differs from that of Abelin *et al.* The following gives the correspondence of analysis numbers to the plot numbers used in the SCE report:

<u>Analysis Number</u>	<u>SCE Plot Number</u>
1	H3
2	H11
3	H12
4	H9
5	H8
6	H7
7	H1
8	H712
9	H2
10	H4
11	H10
12	H5
13	H6

The digitized data files are archived in the subdirectory DIGITIZD of the QA diskette 91654QA_D04 (see Appendix 17 for listing). The file naming convention is GGABx.ASC, where x is a 1- or 2-digit analysis number. The digitized data files used a special coordinate system as required by the digitizing software that was used, so conversion to the proper scale was required.

The converted data files are given in the directory CONVERTD of the QA diskette. The naming convention for these files is:

<u>Converted File</u>	<u>Corresponding Raw Data File</u>
VARIOx.PRN	GGABx.ASC

where x is the analysis number. Consistency of the converted data with the original plots was checked visually by generating screen plots.

Further data preparation was necessary prior to analysis of these data.

First, there is a difference in significance among the data points along the variograms, due to the finite length of sample. The smallest lag distances represent a large number of independent measurement pairs, but as the lag approaches the length of the sampling line, the number of independent measurements diminishes. Thus there is greater uncertainty in the data for larger

A9.3

lag, and the data must be weighted accordingly. In the present case, data were assigned weights in proportion to the number of independent data pairs, calculated as the total sampling length divided by the lag. For example, for a total sampling length of 2 m, for a lag of 5 cm the weight is $(200 \text{ cm})/(5 \text{ cm}) = 40$, and for a lag of 20 cm the weight is $(200 \text{ cm})/(20 \text{ cm}) = 10$.

Second, the digitizing procedure gave the coordinates of points only at which there is a noticeable change in slope of the variogram plots. Thus the converted files contained sufficient points to reproduce the variogram plots, but do not represent data points that are approximately "in line" with adjacent data points. Thus it was necessary to add points at these intermediate points in cases where they are missing. From the procedure described by Abelin *et al.*, it was known that there should be one data point for each 5 cm increment of lag.

A short C program, APWEIGHT, was used to insert the missing data points and to apply the proper weights to the data. This yielded the final data files used for type-curve analysis. These files are given in the subdirectory WEIGHTED of the QA diskette. The naming convention for these files is:

<u>Weighted File</u>	<u>Corresponding Converted File</u>
VARIOn.WTD	VARIOn.PRN

where x is the analysis number.

A9.3 Results of Type-Curve Matches

The program MatchPoint (Version β -1.0) was used to fit type curves based on the formula of Wang *et al.* (1988) to the weighted variograms. MatchPt calculates the type curves for fractal dimensions from 2.0 to 3.0 (in increments of 0.1), directly from the analytical expression given in Chapter 3, so there is no type-curve data file.

The analysis results were recorded in the MatchPt log file VARIO.LOG, given below, in terms of fracture surface fractal dimension D and shear displacement r_c . A copy of the log file is included on the QA diskette, together with HP Graphics Language (HPGL) files which can be used to reproduce plots of the type-curve matches. Hard-copy plots of the type-curve matches and software application memoranda for each analysis are stored in the project files at GGAB.

A9.4

The following is a printout of the file VARIO.LOG:

MATCHPOINT Version 1.0 Type Curve Analysis Program

(c) Golder Geosystem AB, 1991
 Fractal Analysis of Aperture Variograms
 Analyst: Joel Geier
 Date: Thu Sep 05 10:38:25 1991

Fractal Dimension	Match Point log h	Match Point log $\Gamma(r)$	M	Error	Displacement r_c	Height σ^2	Variance	Data File Name	Plot File Name
2.8	1.7976	0.25148	1	0.024234	62.753	1.7844	VARIO1.WTD	[no plot file]	
2.1	0.63517	0.45996	1	0.027878	4.3169	2.8838	VARIO1.WTD	VARIO1.PGL	
2.9	2.8191	0.060228	1	0.026801	659.31	1.1488	VARIO2.WTD	[no plot file]	
2.3	0.80758	-0.069304	3	0.052139	6.4207	0.8525	VARIO2.WTD	VARIO2.PGL	
2.1	1.0284	0.25728	1	0.0711	10.676	1.8083	VARIO3.WTD	VARIO3.PGL	
2.8	3.1677	0.75961	1	0.071198	1471.5	5.7492	VARIO4.WTD	[no plot file]	
2.2	0.43883	0.12179	3	0.16356	2.7468	1.3237	VARIO4.WTD	VARIO4.PGL	
2.8	2.6473	0.23317	1	0.049514	443.96	1.7107	VARIO5.WTD	[no plot file]	
2.1	0.8291	-0.007745	3	0.1022	6.7468	0.9823	VARIO5.WTD	VARIO5.PGL	
2.2	0.6190	-0.3316	1	0.06567	4.1591	0.4660	VARIO5.WTD	VARIO6.PGL	
2.3	0.5289	-0.2020	1	0.03421	3.3799	0.6281	VARIO5.WTD	VARIO7.PGL	
2.9	2.8590	-0.23081	1	0.031031	722.73	0.58775	VARIO8.WTD	[no plot file]	
2.1	0.4872	-0.16604	3	0.049164	3.0704	0.68227	VARIO8.WTD	VARIO8.PGL	
2.1	0.4388	-0.2668	3	0.08267	2.7466	0.54100	VARIO9.WTD	VARIO9.PGL	
2.9	3.4966	-0.23528	1	0.042513	3137.7	0.58172	VARIO10.WTD	[no plot file]	
2.3	0.46434	-0.55911	3	0.070219	2.913	0.27599	VARIO10.WTD	VARIO10.PGL	
2.1	0.63487	-0.4241	1	0.04841	4.3139	0.37661	VARIO11.WTD	VARIO11.PGL	
2.2	0.7631	-0.14882	1	0.085581	5.7957	0.70988	VARIO12.WTD	VARIO12.PGL	
2.1	0.63487	-0.18066	1	0.052717	4.3139	0.65969	VARIO13.WTD	VARIO13.PGL	

APPENDIX 10 OXFILZ ANALYSIS ALGORITHM

This appendix gives a brief summary of the OxFILZ interpretation method. This is an extension to the OxFILET method (Dershowitz *et al.*, 1991a). The main differences are that the OxFILZ method assumes that:

- Fractures are randomly located according to a compound Poisson process (the finite-probability Nearest Neighbor model), rather than a simple Poisson process (uniformly random location) along the borehole.
- Fracture transmissivity is a function of fracture normal stress, which is assumed to be a simple function of depth. In the OxFILET method, fracture transmissivity is assumed to be independent of depth.
- Fracture transmissivity as measured by a packer test is not necessarily the same as the "average" transmissivity across the fracture. This assumption has also been included in the most recent implementation of the OxFILET method.

The present implementation of the OxFILZ model (OXFILZ Version 1.0) is based on the components as described in the following sections.

A10.1 Major Feature Location

The number of major features (or "fracture zones") intersecting the i th borehole is assumed to be governed by a Poisson process:

$$P(n) = \frac{\exp(-f_m L_i) (f_m L_i)^n}{n!}, \quad n = 0, 1, 2, \dots \quad (\text{A10-1})$$

where

- f_m = major feature frequency, *i.e.* the average number of major features per unit length of borehole
- L_i = length of the borehole.

In the OXFILZ code, f_m is a global variable which is specified by the user.

For each borehole, the number of major features n is determined by generating a random number from the above Poisson distribution. Locations of the features are chosen by choosing n random numbers from the uniform distribution on $[0, L_i]$.

A10.2 Single Fractures

Individual fractures are located according to a finite-probability Nearest Neighbor (FPNN) process, which is related to the major features. The expected number of *conductive* fractures per infinitesimal length of borehole is:

A10.2

$$f_c(s) = A_{NN}(\lambda_{NN} + s)^{-b_{NN}} \quad (A10-2)$$

where

- s = distance to the nearest major feature
- A_{NN} = normalizing factor for Nearest Neighbor model
- b_{NN} = Nearest Neighbor exponent
- λ_{NN} = characteristic length for the FPNN process

The distance s is measured along the borehole, meaning that there is an implicit assumption that the major features are approximately horizontal.

The mean conductive fracture frequency f_c is the average of $f_c(s)$ over an infinite length of borehole. The normalizing constant is related to the other parameters by:

$$A_{NN} = \frac{b_{NN} f_c}{2 f_m} \left[\lambda_{NN}^{-b_{NN}} - (2 f_m)^{b_{NN}} \exp(2 f_m \lambda_{NN}) \Gamma(2 - b_{NN}, 2 f_m \lambda_{NN}) \right] \quad (A10-3)$$

where

$$b = b_{NN} - 1$$

The parameter f_c is viewed as one of four unknowns which are solved for by iterative simulation.

The expected number of fractures \bar{N} in a packer interval of length L_p is calculated by integrating $f_c(s)$ over the length of a section:

$$\bar{N} = \int_{x_1}^{x_1+L_p} f_c(s) dx = \int_{x_1}^{x_1+x_{20}/2+x_{21}/2} f_c(s) dx + \dots + \int_{x_1+x_{2(n-1)}/2+x_{2n}/2}^{x_1+L_p} f_c(s) dx \quad (A10-4)$$

where

- x_{20} = coordinate of first zone above section
- .
- .
- .
- x_{2n} = coordinate of first zone below section

The actual number N of fractures in the interval is chosen from a Poisson distribution:

$$P(N) = \frac{e^{-\bar{N}} \bar{N}^N}{N!}, \quad N = 0, 1, 2, \dots \quad (A10-5)$$

A10.3

Each fracture j has an "average" transmissivity T_j which is drawn from a lognormal distribution. The mean $\mu_{\log T}$ and standard deviation $\sigma_{\log T}$ of $(\log_{10} T_j)$ are viewed as additional unknowns which must be solved for iteratively.

The effective average transmissivity $T_{j,\text{eff}}$ is assumed to be related to the normal stress across the fracture. The value of T_j is assumed to be correct at some reference stress level σ_{N_0} , corresponding to a reference depth z_0 . At other stresses/depths the effective transmissivity is given by:

$$T_{j,\text{eff}} = T_j \left(\frac{\sigma_N}{\sigma_{N_0}} \right)^b = T_j \left(\frac{z}{z_0} \right)^b \quad \text{if } \sigma_N \propto z \quad (\text{A10-6})$$

The exponent b is the fourth unknown parameter which must be solved for iteratively.

Finally, the transmissivity $T_{j,b}$ of a fracture, as it acts at the borehole in a packer test, is assumed to be a random function of the "average" transmissivity $T_{j,\text{eff}}$:

$$\log \left(\frac{T_{j,b}}{T_{j,\text{eff}}} \right) \sim N(\mu_{T_z}, \sigma_{T_z}) \quad (\text{A10-7})$$

where

- $N(\mu, \sigma)$ = normal distribution with mean μ and variance σ^2
- μ_{T_z} = average of $(\log_{10} T_{j,b} - \log_{10} T_{j,\text{eff}})$ as estimated from single-fracture simulations
- σ_{T_z} = standard deviation of $(\log_{10} T_{j,b} - \log_{10} T_{j,\text{eff}})$ as estimated from single-fracture simulations

The total interval transmissivity is calculated as the sum of single fracture transmissivities, as in the original OxFILET method, but the $T_{j,b}$ are used rather than the corresponding T_j . This assumes that the fractures act as parallel, independent conduits.

APPENDIX 11 SIMULATION OF AT-BOREHOLE *vs.* CROSS-FRACTURE FLOW

This appendix describes simulations of single-fracture flow to derive a relationship between at-borehole and cross-fracture transmissivity. Monte Carlo simulations of single-fracture transmissivity variation, and its effect on flow due to fixed boundary conditions, were performed using the `runsim` script, which is a general-purpose driver for Monte Carlo simulations using `MeshMonster`, `EdMesh`, and `MAFIC`.

The output of these simulations was in the form of Moyes' transmissivities for the at-borehole simulations, and effective transmissivities for the steady-state, cross-fracture simulations. The at-borehole simulations also produced transient, packer-test response data suitable for GRF or other transient types of analysis. However, only the Moyes' transmissivities were used in the present study, because these were directly comparable to the available field data.

A11.1 Single Fracture Geometry and Properties

A fixed geometry was used for all single-fracture simulations. A horizontal fracture, centered on the borehole axis, was defined by the fracture geometry file `snglfrac.bab`, which was produced with `FracWorks`. The boundaries of the hexagonal portion of the fracture used for simulation were fixed by the boundary definitions file `snglfrac.hdr`.

Independent, random realizations of the variable transmissivity were generated using an algorithm embedded within the `MeshMonster` code. The algorithm may be summarized as follows:

- The mean (hydraulic) aperture $\bar{\epsilon}_h$ is calculated from the average fracture transmissivity, as defined in the fracture geometry (.bab) file, using the cubic law.
- A fractal dimension D , for the fracture surfaces is generated from a triangular distribution with parameters specified in the `MeshMonster` settings file `mmset`; alternatively a fixed value may be specified in `mmset`.
- Two independent, random surfaces with zero mean height are generated using the recursive polygonal subdivision, fractal interpolation algorithm of Fournier *et al.* (1979). The maximum level of recursive subdivision is determined by a linear relationship with the original log cross-fracture transmissivity, with parameters as specified in `mmset`.
- The hydraulic aperture of each element of the fracture plane is calculated as:

$$\epsilon_{h(i)} = \max\left(0, \bar{\epsilon}_h + \bar{z}_{1(i)} - \bar{z}_{2(i)}\right) \quad (\text{A11-1})$$

A11.2

where $z_{1(i)}$ and $z_{2(i)}$ are the heights of the centroids of the corresponding elements in the upper and lower surfaces. The transmissivity of the element is calculated from $\epsilon_{k(i)}$ according to the cubic law.

The seed value for the random number generator is specified as an argument to the **runsim** script.

A11.2 Boundary Conditions

Each simulation produced four different sets of **MAFIC** output, corresponding to the four different EdMesh script files (*.trbcs).

The file **a.trbcs** imposes a fixed head of 0 m on all segments of the hexagonal outer boundary, an initial head of 0 m throughout the mesh, and a fixed head of 20 m beginning at time 0 s at the inner boundary. This simulates an ideal constant-head test with no wellbore effects, and connection to an infinitely transmissive medium at all points on the fracture perimeter. Whether the latter condition is realistic may be questioned, but the influence of this boundary condition is generally negligible for the combinations of distance to the boundary, test duration, and average fracture transmissivity which were used in the simulations.

The files **x.trbcs**, **y.trbcs**, and **z.trbcs** all simulate steady flow from a given edge of the hexagonal boundary to the opposite boundary. The boundary segments are chosen to apply head gradients in each of three orientations, at mutual 120° angles. A no-flow boundary condition is applied to the inner boundary in each case, essentially producing a small, sealed hole (no-flow inclusion) in the middle of the fracture.

A11.3 Procedure for simulations

The UNIX shell script **runsim** was used to perform the Monte Carlo simulations. The output from the **runsim** script is completely defined by a set of files (see below), which must be present in the UNIX directory from which **runsim** is invoked by typing the command:

```
runsim -q -m -R ...
```

followed by the simulation numbers (e.g., 00 01 02 03, ...). The specific commands used to produce 100 simulations, with random seeds 00 through 99, were:

```
runsim -q -m -R 00 01 02 03 04 05 06 07 08 09
runsim -q -m -R 10 11 12 13 14 15 16 17 18 19
      .
      .
      .
runsim -q -m -R 90 91 92 93 94 95 96 97 98 99
```

The above commands, together with the files listed below (found on the QA diskette 91654QA_D02), give a complete definition of the **runsim** problem.

A11.3

DOS Name	UNIX Name	Purpose
ABSOURCE	babsource	Source directory for input data
AMELIST1	namelist1	Namelist 1 for MAFIC run
AMELIST2	namelist2	Namelist 2 for MAFIC run
BABLIST	bablist	List of .bab files
DESTINY	destiny	Directory for output files
HDRNAME	hdrname	Name of .hdr file
IMESTEPS	timesteps	List of time steps
MMSET	mmset	MeshMonster settings
SEED	seed	Random number seed (not used)
SHSOURCE	mshsource	Directory for mesh files (not used)
SNGLFRAC.BAB	snglfrac.bab	Fracture geometry
SNGLFRAC.HDR	snglfrac.hdr	Boundary geometry
ATR.BCS	a.trbcs	Boundary conditions for simulated packer test
XTR.BCS	x.trbcs	Boundary conditions for cross-fracture flow (x)
YTR.BCS	y.trbcs	Boundary conditions for cross-fracture flow (y)
ZTR.BCS	z.trbcs	Boundary conditions for cross-fracture flow (z)

A11.4 Results of Single-Fracture Simualtions

Output from the simulations was postprocessed using the script **postproc** to produce the following files:

sngla##.2m	Transient response at inner boundary(##=00,01,...)
moyes.prn	At-borehole conductivities based on Moye's formula and assumed steady-state at end of transient test.
xflow.prn	Cross-fracture conductivities (Direction 1, corresponding to x.trbcs)
yflow.prn	Cross-fracture conductivities (Direction 2, corresponding to y.trbcs)
zflow.prn	Cross-fracture conductivities (Direction 3, corresponding to z.trbcs)

The transient response files were not used in the subsequent analysis, but have been archived for possible future investigations of topics such as the relationship between fractal dimension for aperture variation, and the fractional dimension estimated by GRF analysis.

An additional output file, **fractals.prn**, was produced with the UNIX command:

```
grep " D =" *.log* > fractals.prn
```

to extract the fractal dimensions from the **runsim** log files. All log files and intermediate output files were subsequently discarded, since these require considerable storage space and are not needed to reproduce the output. Output files were transferred to the PC for further analysis.

APPENDIX 12 DETAILS OF OXFILZ ANALYSIS

This appendix gives details of the OxFILZ analysis that was performed to simultaneously estimate the conductive fracture frequency, cross-fracture transmissivity distribution, and stress-transmissivity relationship.

A12.1 Input Data for OXFILZ Analysis

The input data for OxFILZ consists of a borehole definition file, and a packer-test result file. The fixed parameters for the OxFILZ analysis are specified interactively and recorded in the log files, as documented below.

A12.1.1 Borehole Definition File

The following is a printout of the borehole definition file FINNSJON.HLS. This was taken directly from the GEOTAB output file KMIN23.LIS, with minor editing to make the format conform to OXFILZ requirements. The column "TOP" is a dummy entry. Inclinations were taken from Andersson *et al.* (1991):

```
Boreholes at Finnsjon Site --
BOREHOLE SECLN START FINISH NUMBER KMINMEAS TOP INCLINATION
NAME      (m)  DATE  DATE  OF SEC  (m/s)  (m)  (degrees)
HF101     2.00 850402 850403 10 5.00E-10 0.0 90.0
BF101     2.00 870304 870324 115 1.00E-10 0.0 90.0
BF102     2.00 880119 880129 42 1.00E-10 0.0 90.0
KF101     2.00 770822 770912 240 2.40E-09 0.0 90.0
KF102     3.00 771005 771019 220 2.00E-09 0.0 50.0
KF103     3.00 771102 771122 223 3.00E-09 0.0 50.0
KF104     3.00 790123 790301 182 1.90E-10 0.0 80.0
KF105     2.00 861201 861205 41 7.50E-10 0.0 50.0
KF105     2.00 870403 870428 69 7.50E-10 0.0 50.0
KF105     3.00 790118 790202 232 1.90E-10 0.0 50.0
KF106     2.00 870121 870128 52 7.50E-10 0.0 90.0
KF106     3.00 790116 790320 207 1.90E-10 0.0 90.0
KF107     2.00 870129 870204 54 7.50E-10 0.0 85.0
KF107     3.00 790122 790301 175 1.90E-10 0.0 85.0
KF108     3.00 800724 801003 140 1.60E-10 0.0 60.0
KF109     2.05 861113 861122 76 1.00E-10 0.0 60.0
KF110     2.00 861123 861130 90 1.00E-10 0.0 50.0
KF111     2.00 861203 870122 75 1.00E-10 0.0 90.0
```

A12.1.2 Packer Test Data File

The following is a printout of the file FINNSJON.TDT. This was produced by minor editing of the GEOTAB output files SHSINJCD.ASC and SHTINJCD.ASC to adjust formats. This file is too lengthy to merit printing out here. This file and FINNSJON.HLS are in electronic format on the accompanying diskette.

A12.2

The listing below gives the beginning and end of the dataset to allow checking against accidental file truncation.

```
BF101      2.00   389.91 870304  1.70E-09
BF101      2.00   391.91 870304  2.20E-09
BF101      2.00   393.91 870304  1.00E-09
BF101      2.00   395.91 870304  2.90E-10
BF101      2.00   397.91 870304  2.40E-10
.
.
.
KF111     20.00   245.93 861105 -9.90E+01
KF111     20.00   265.93 861105 -9.90E+01
KF111     20.00   285.93 861105  2.40E-08
KF111     20.00   305.92 861105  2.90E-10
KF111     20.00   325.92 861105  1.50E-06
KF111     20.00   345.92 861105  4.80E-09
KF111     20.00   365.91 861105  1.80E-10
```

A12.2 OxFILZ Analysis Results

This section describes output files for OxFILZ analyses based on all 2m and 3m packer test data from the Finnsjön site. The interpretations were carried out using the OxFILZ Version β -1.0 code (Appendix 10).

Results of the final runs of OxFILZ may be found on the QA diskette 91654QA_D02. Results of preliminary runs are archived on 91654QA_D05. Four main types of files (*.LOG, *.EPS, and *.PGL) files are contained in these archives:

- *.LOG Records of the analyses, which include fixed parameter values and the path followed by the algorithm to optimize the fitted parameters.
- *.PGL HPGL-language plot files that compare the simulated and actual CDFs of interval transmissivity, for the best model in each run.
- *.EPS PostScript language files created from the *.PGL files.
- *.PRN Printouts of simulated and actual values for each packer interval.

The first part of the filenames give the names of separate runs of the program for different sets of fixed parameters. The points at which the *.PGL and *.PRN files were created are indicated in the corresponding *.LOG files.

The Lotus 1-2-3 worksheet OXPLOTS.WK1 is used to produce plots of the measured and simulated log T profiles, using these *.PRN files.

APPENDIX 13 METHOD FOR TRANSIENT PACKER TEST INTERPRETATION

Constant-pressure packer test data from three boreholes (KFI 11, BFI 01 and BFI 02) at Finnsjön were analysed to estimate hydrologic properties. The data were interpreted in terms of a conceptual model for fractional dimension flow (Barker, 1988; Doe and Geier, 1990), to obtain data which can be used to calibrate and/or validate discrete fracture network models for the SKB 91 Project.

This appendix describes analysis methods, dataset preparation, and results.

A13.1 Analysis Methods

The general theory of fractional dimension packer-test analysis was developed by Barker (1988). A specific application of this theory to constant-pressure test interpretation is given by Doe and Geier (1990). The latter reference gives examples of this analysis, and considerable discussion of the assumptions inherent to the approach.

The GRF model of a packer test is based on the assumption that the cross-sectional area of the conduit being tested varies as:

$$A_c \propto r^{D_f - 1} \quad (\text{A13-1})$$

where r is the distance from the borehole, and D_f is called the fractional dimension. The hydraulic properties of the conduit, conductivity K_c and specific storage S_w , are assumed to be constant along the conduit. As noted by Doe and Geier (1990), for a single-hole test the above case cannot be distinguished from any case in which the product $A_c K_c$ varies according to the same rule.

The dimensionless form of the Laplace-transform solution for a constant-pressure test is given by Doe and Geier as:

$$\bar{Q}_D = \frac{K_{\nu-1}(\sqrt{s})}{\sqrt{s} K_{\nu}(\sqrt{s})} \quad (\text{A13-2})$$

where s is the transform variable and $K_{\nu}(z)$ is the modified Bessel function of the second kind, of order ν . The program FRACDIMQ (*op. cit.*) uses the Stehfest inversion algorithm to calculate dimensionless type curves based on this solution.

The data from a constant-pressure packer test are in the form of flowrate *vs.* time (Q *vs.* t) records. The unknown GRF model parameters D_f , K_c , and S_w can be estimated by matching type curves for different values of D_f to plots of $\log Q$ *vs.* $\log t$, as described by Doe and Geier (1990).

The GGAB program MatchPt performs the type-curve matching semiautomatically, using type-curve data produced by FRACDIMQ. In the present study, type curves were generated for $0.5 \leq D_f \leq 3$, in increments of 0.25. The user interactively shifts the type curve relative to the data curve, to assure a reasonable starting point for the fitting. MatchPt then applies a downhill simplex algorithm to optimize the fit, considering all of the type curves that were supplied as input.

A13.2

This analysis does not consider effects of non-constant pressure during the packer tests. These effects could be considered by applying a multirate correction to the time-pressure data, and analyzing the corrected tests as constant-rate tests (see Doe and Geier, 1990). This was not done in the present case due to the limited scope. The reader is therefore advised to use the individual estimates of GRF parameters with caution. A more thorough analysis is recommended for sensitive applications.

A13.2 Dataset Preparation

The raw packer test data were provided by SKB, directly from the GEOTAB database. Diskettes containing these raw data have been placed in the project files, labelled as:

Raw Packer Test Data from Finnsjön Boreholes
All Transient Data from { BFI01, BFI02, KFI11 }

The raw data were converted to MATCHPT input data using a short program DCONVERT. Version 1.0 of DCONVERT was used to convert the data from BFI 01 and BFI 02. Version 1.1 of DCONVERT was used to convert the data from KFI 11. These program versions are described in a DFN/SC project memorandum on file, "Packer Test Dataset Conversion Program DCONVERT Versions 1.0 and 1.1."

Copies of the converted datasets are to be found on the QA diskette 91654QA_D06. Converted data files were named automatically by the program DCONVERT, according to the following convention:

<u>Converted Files</u>	<u>Borehole</u>
BFI01ddd.2M	BFI 01
BFI02ddd.2M	BFI 02
KFI11ddd.2M	KFI 11

where *ddd* is the nominal depth of the top of the section, in meters.

A13.3 GRF Interpretation Results

Analysis results were obtained in terms of fractional dimension D_f , hydraulic conductivity K_e , and specific storage S_w . These results are recorded in the MatchPt log file, found on the QA diskette 91654QA_D07. This diskette includes HP Graphics Language (HPGL) files which can be used to reproduce plots of the individual type-curve matches. Hard copies of these plots are on file at GGAB. Conversion of these results to generalized transmissivities T_{GRF} and storativities S_{GRF} was done within the LOTUS spreadsheet INTERPS2.WK1 (on diskette 91654QA_D02).

APPENDIX 14 GRF ANALYSIS OF SIMULATED PACKER TESTS

The DFN model was validated by a statistical comparison of simulated packer test results with actual packer test results. The bases for comparison were the distributions of interpreted flow dimension D_f and generalized transmissivity T_{GRF} , estimated by GRF analysis of the simulated and actual packer tests.

This appendix describes the analysis of the simulated tests. The procedure was essentially the same as for the actual tests (Appendix 13), except that the Q vs. t data were extracted from MAFIC simulation results, rather than from data logger records.

A14.1 Dataset preparation

The data for the simulated constant-pressure tests were extracted from the condensed MAFIC output files named:

finn2ann.znnfid

where nn is the simulation number, i is the packer interval number, and d is a code (a, b, c, or d) indicating the effective depth to the block center. The condensed MAFIC output files are stored in the Convex QA files, in the directory Valid/Zones. The script *postproc* (directory Valid/Analysis) was used to extract the transient response data, as well as the Moyes' conductivities, from these files.

The transient data files are named *fsidnn.2m*, where nn , i , and d are as defined above. The originals of these files are in the Convex QA files (Valid/Transients). These were transferred to the PC for MatchPt analysis.

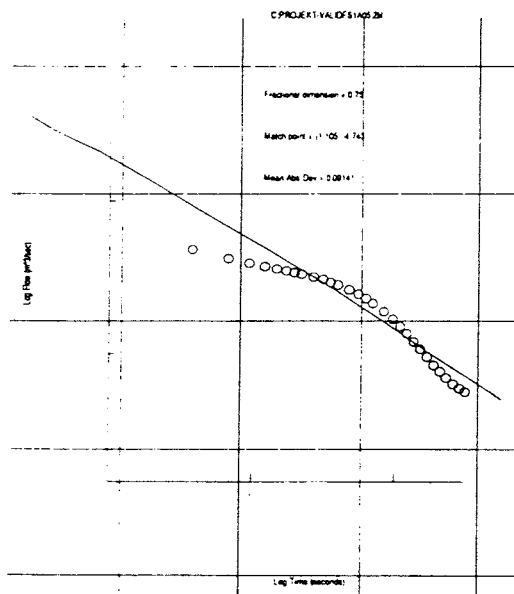
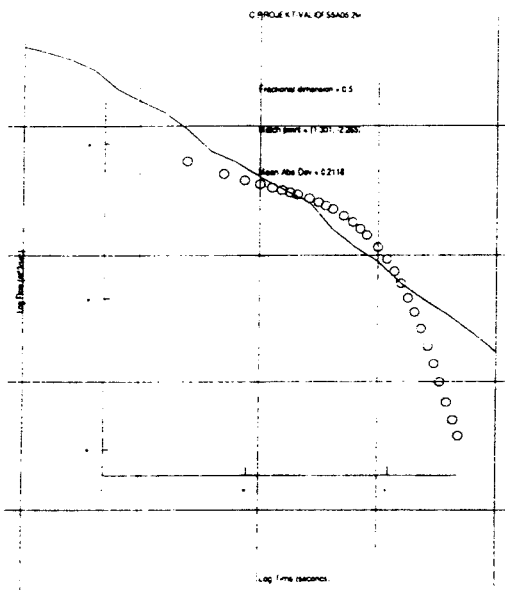
Initially the DOS files were sorted into "flow zones" and "no-flow zones" tests. These and Moyes' estimates are archived on QA diskette 91654QA_D02, (SIMULATN/VALIDATN/CVXOUTPT). Only data from "flow zones" were analyzed, for obvious reasons.

A14.2 GRF Interpretation Results

The analyses of the simulated Q vs. t records using MatchPt was identical to the analyses performed for the actual test data (Appendix 13). The MatchPt log file for the analyses is DFNVALID.LOG. This log file contains several repeated analyses for a few responses which were difficult to fit, so the poorer fits were deleted by manual editing to produce the file DFNVALID.COR. The HPGL plot files for individual type-curve matches are archived on QA diskette 91654QA_D02, in case there is later interest in these plots.

The Lotus 1-2-3 spreadsheet DFNVALID.WK1 was used to calculate generalized transmissivities T_{GRF} and storativities S_{GRF} from the data in DFNVALID.COR, and to produce histograms of D_f and T_{GRF} for comparison with the interpretations of field tests. The spreadsheet VALIDCHI.WK1 was used to carry out the χ^2 tests to compare the distributions from simulated and actual tests.

The following pages give example plots of type-curve matches for the simulated tests.



KEY

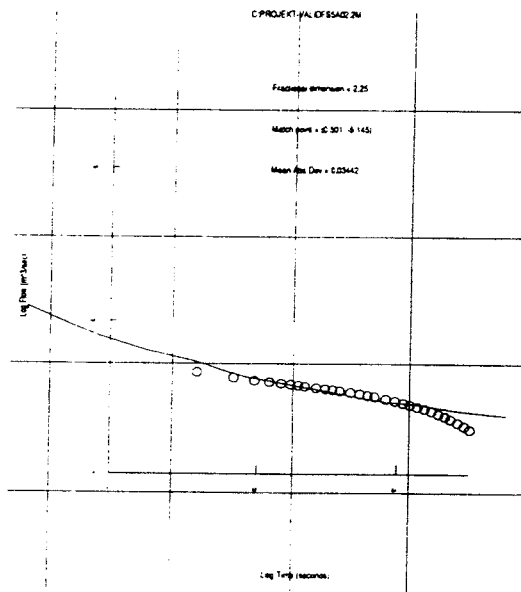
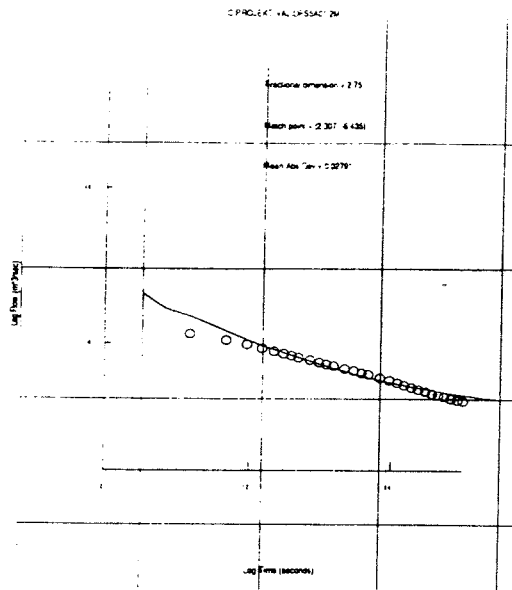
○ Simulated data

— Type curve

Note: Waviness in type curve results from instability in numerical inversion of Laplace transform solution.

FIGURE **A14-1**
EXAMPLES OF GRF TYPE CURVE MATCHES TO SIMULATED PACKER TESTS

SKB/SKB91 DFNST



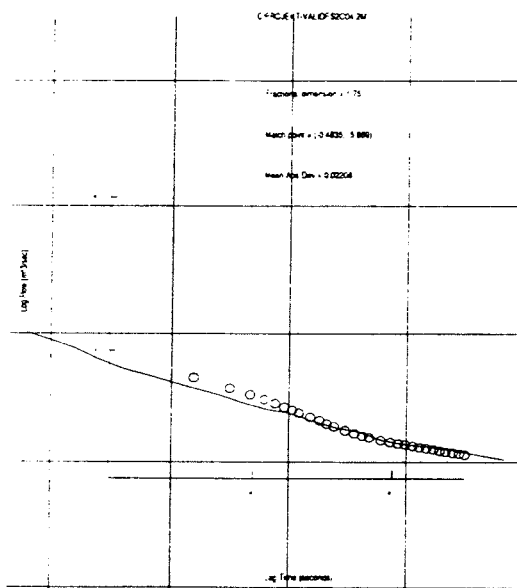
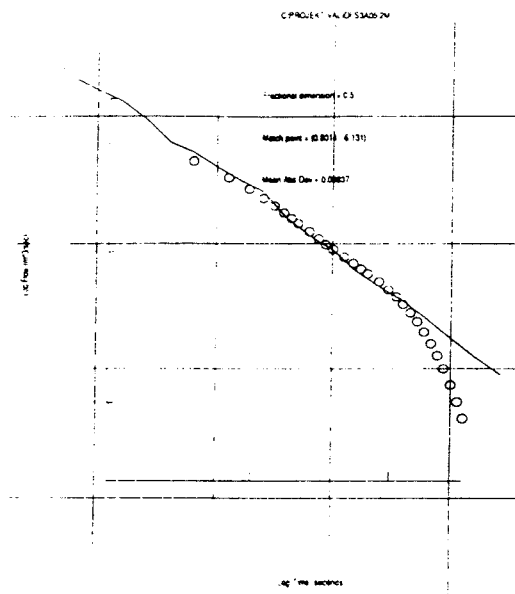
KEY

○ Simulated data
 — Type curve

Note: Waviness in type curve results from instability in numerical inversion of Laplace transform solution.

FIGURE **A14-1** (CTD.)
**EXAMPLES OF GRF TYPE CURVE MATCHES
 TO SIMULATED PACKER TESTS**

SKB/SKB91 DFNST



KEY

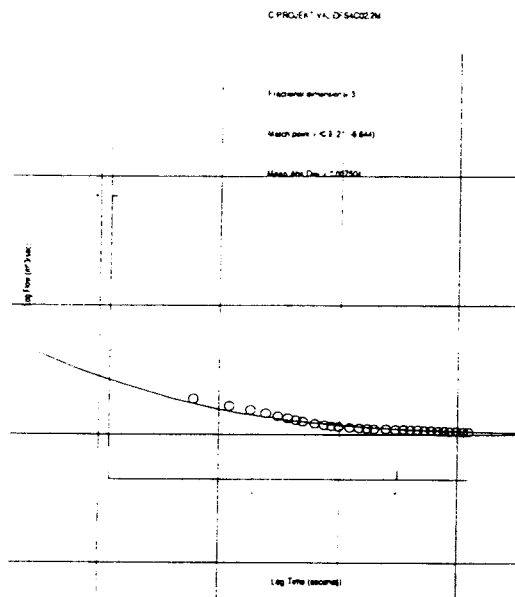
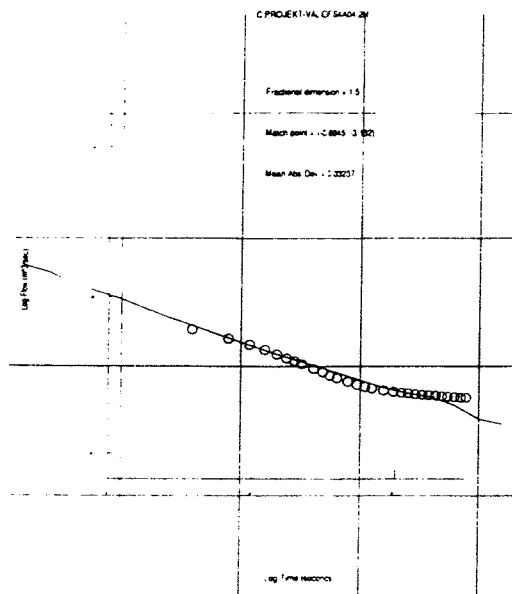
○ Simulated data

— Type curve

Note: Waviness in type curve results from instability in numerical inversion of Laplace transform solution.

FIGURE **A14-1 (CTD.)**
EXAMPLES OF GRF TYPE CURVE MATCHES
TO SIMULATED PACKER TESTS

SKB/SKB91 DFNST



KEY

- Simulated data
- Type curve

Note: Waviness in type curve results from instability in numerical inversion of Laplace transform solution.

FIGURE **A14-1** (CTD.)
**EXAMPLES OF GRF TYPE CURVE MATCHES
 TO SIMULATED PACKER TESTS**

SKB/SKB91 DFNST

APPENDIX 15 PARTIAL DEMONSTRATION OF THE DFN/SC INTERFACE

This appendix gives a partial description of the production of a demonstration dataset for the DFN/SC interface. The demonstration simulations used three different borehole orientations:

- Vertical (57 packer test simulations)
- Inclined 60°N (21 packer test simulations)
- Inclined 60°W (24 packer test simulations)

Each block simulation included three 2m packer test simulations. The reason for the irregular numbers of packer test simulations is that there was no automatic way to change borehole orientation, so this was done by manual intervention in the middle of the batch process. A more systematic approach will require development of a utility program/script to generate random boreholes.

The percentage of nonconductive packer intervals in the demonstration model is much higher than is observed. This means that too many packer intervals will be assigned conductivities equal to the measurement limit. Probably this has the effect of reducing the apparent correlation with block conductivities.

Block-scale flow was simulated with an irregular but well-distributed set of boundary conditions which included 7 sets of constant-head boundary conditions, applying external gradients in the directions:

$\{1,0,0\}$, $\{0,1,0\}$, $\{0,0,1\}$, $\{1,1,1\}$, $\{-1,1,1\}$, $\{-1,-1,1\}$, and $\{1,-1,1\}$,

plus 3 sets of mixed boundary conditions, applying gradients in the directions:

$\{1,0,0\}$, $\{0,1,0\}$, and $\{1,1,1\}$

directions, with no-flow boundaries on the sides of the cubes. This set allows comparisons with the two types of permeameter measurements.

A uniformly distributed distribution of external head gradient would be preferable for theoretical reasons but the above set was more conveniently implemented for the demonstrations. The correlation of the volume-averaged gradients to the externally-applied gradients appears to be rather loose (by inspection), especially for the smaller averaging volumes, so the above set of boundary conditions results in a reasonably random sample of directions for $\nabla\langle h \rangle$. This loose correlation may be characteristic of the DFN model that was used. The velocity heterogeneity can be expected to increase with decreasing averaging volume scale, and this does apparently occur. A quantitative analysis of this heterogeneity would be interesting, but was not possible within the current project.

Estimates of the covariance matrix function were produced for several cases:

- Average conductivity
- Full-tensor block conductivity,
- Full-tensor block conductivity (average conductivity and 6 anisotropy ratios),

A15.2

as defined in the work plan.

A full description of the analysis procedures, programs used, and output files is contained in the quality assurance memorandum for this project.

APPENDIX 16 DATA FROM SIMULATIONS TO ESTIMATE TRANSPORT PROPERTIES

This appendix gives the tables of estimated transport properties, on which the figures in Chapter 8 are based. The following data are provided:

- Histograms of flux-weighted estimates of ϕ_Q
- Histograms of flux-weighted estimates of S_w
- Pairs of flux-weighted estimates of ϕ_Q and S_w for each block-scale simulation with measurable flow.

where:

S_w = flux-weighted specific surface (area per volume of water)

ϕ_Q = flux-weighted porosity

These tables are stored in digital form on the QA diskette 91654QA_D02, in the following files:

QWTDPOR0.PRN	Histograms of ϕ_Q (frequency vs. log ϕ_Q) for each flow direction -- Base Case.
QWTDPOR1.PRN	Histograms of ϕ_Q (frequency vs. log ϕ_Q) for each flow direction -- Breccia Case.
QWTDWET0.PRN	Histograms of S_w (frequency vs. log S_w) for each flow direction -- Base Case.
QWTDWET1.PRN	Histograms of S_w (frequency vs. log S_w) for each flow direction -- Breccia Case.
PORWSCOR.PRN	Data pairs (ϕ_Q , S_w) for all flow directions.

Copies of the above files were previously transmitted to SKB by modem, on January 24, 1992.

All estimates given here are based on 35 m averaging volumes, for 40 m blocks simulated at repository depth (500 m).

A16.1 Flux-Weighted Porosity Estimates - Base Case

File: QWTDPOR0.PRN

CASE:	Base	Base	Base
Flow Dir:	X	Y	Z
Log ϕ_Q	Freq	Freq	Freq
(-)	(%)	(%)	(%)
-7.00	0.00	0.00	0.00
-6.75	0.00	0.00	0.00
-6.50	0.00	0.00	0.00
-6.25	0.00	0.00	0.00
-6.00	0.00	0.00	0.00
-5.75	0.00	0.00	0.00
-5.50	0.00	0.00	0.00
-5.25	50.00	37.50	15.38
-5.00	50.00	62.50	69.23
-4.75	0.00	0.00	15.38
-4.50	0.00	0.00	0.00
-4.25	0.00	0.00	0.00
-4.00	0.00	0.00	0.00
-3.75	0.00	0.00	0.00
-3.50	0.00	0.00	0.00
-3.25	0.00	0.00	0.00
-3.00	0.00	0.00	0.00
-2.75	0.00	0.00	0.00
-2.50	0.00	0.00	0.00
-2.25	0.00	0.00	0.00
-2.00	0.00	0.00	0.00
-1.75	0.00	0.00	0.00
-1.50	0.00	0.00	0.00
-1.25	0.00	0.00	0.00
-1.00	0.00	0.00	0.00
-0.75	0.00	0.00	0.00
-0.50	0.00	0.00	0.00
-0.25	0.00	0.00	0.00
0.00	0.00	0.00	0.00

A16.2 Flux-Weighted Porosity Estimates - Breccia Case

File: QWTDPOR1.PRN

CASE:	Breccia	Breccia	Breccia
Flow Dir:	X	Y	Z
Log ϕ_Q	Freq	Freq	Freq
(-)	(%)	(%)	(%)
-7.00	0.00	0.00	0.00
-6.75	0.00	0.00	0.00
-6.50	0.00	0.00	0.00
-6.25	6.67	0.00	0.00
-6.00	33.33	21.43	40.00
-5.75	13.33	35.71	20.00
-5.50	20.00	14.29	10.00
-5.25	6.67	0.00	0.00
-5.00	6.67	14.29	0.00
-4.75	6.67	7.14	10.00
-4.50	6.67	0.00	20.00
-4.25	0.00	7.14	0.00
-4.00	0.00	0.00	0.00
-3.75	0.00	0.00	0.00
-3.50	0.00	0.00	0.00
-3.25	0.00	0.00	0.00
-3.00	0.00	0.00	0.00
-2.75	0.00	0.00	0.00
-2.50	0.00	0.00	0.00
-2.25	0.00	0.00	0.00
-2.00	0.00	0.00	0.00
-1.75	0.00	0.00	0.00
-1.50	0.00	0.00	0.00
-1.25	0.00	0.00	0.00
-1.00	0.00	0.00	0.00
-0.75	0.00	0.00	0.00
-0.50	0.00	0.00	0.00
-0.25	0.00	0.00	0.00
0.00	0.00	0.00	0.00

A16.3 Flux-Weighted Wetted Surface Estimates - Base Case

File: QWTDWET0.PRN

CASE:	Base	Base	Base
Flow Dir:	X	Y	Z
Log S_w ($m^2/m^3 H_2O$)	Freq (%)	Freq (%)	Freq (%)
0.00	0.00	0.00	0.00
0.25	0.00	0.00	0.00
0.50	0.00	0.00	0.00
0.75	0.00	0.00	0.00
1.00	0.00	0.00	0.00
1.25	0.00	0.00	0.00
1.50	0.00	0.00	0.00
1.75	0.00	0.00	0.00
2.00	0.00	0.00	0.00
2.25	0.00	0.00	0.00
2.50	11.11	25.00	23.08
2.75	88.89	75.00	76.92
3.00	0.00	0.00	0.00
3.25	0.00	0.00	0.00
3.50	0.00	0.00	0.00
3.75	0.00	0.00	0.00
4.00	0.00	0.00	0.00
4.25	0.00	0.00	0.00
4.50	0.00	0.00	0.00
4.75	0.00	0.00	0.00
5.00	0.00	0.00	0.00
5.25	0.00	0.00	0.00
5.50	0.00	0.00	0.00
5.75	0.00	0.00	0.00
6.00	0.00	0.00	0.00
6.25	0.00	0.00	0.00
6.50	0.00	0.00	0.00
6.75	0.00	0.00	0.00

A16.4 Flux-Weighted Wetted Surface Estimates - Breccia Case

File: QWTDWET1.PRN

CASE:	Breccia	Breccia	Breccia
Flow Dir:	X	Y	Z
Log S_w	Freq	Freq	Freq
($m^2/m^3 H_2O$)	(%)	(%)	(%)
Flow Dir:	X	Y	Z
0.00	0.00	0.00	0.00
0.25	0.00	0.00	0.00
0.50	0.00	0.00	0.00
0.75	0.00	0.00	0.00
1.00	0.00	0.00	0.00
1.25	0.00	0.00	0.00
1.50	0.00	0.00	0.00
1.75	0.00	0.00	0.00
2.00	0.00	0.00	0.00
2.25	0.00	0.00	0.00
2.50	0.00	0.00	0.00
2.75	0.00	0.00	0.00
3.00	0.00	0.00	0.00
3.25	0.00	0.00	0.00
3.50	0.00	0.00	0.00
3.75	0.00	0.00	0.00
4.00	0.00	0.00	0.00
4.25	0.00	0.00	0.00
4.50	100.00	100.00	90.00
4.75	0.00	0.00	10.00
5.00	0.00	0.00	0.00
5.25	0.00	0.00	0.00
5.50	0.00	0.00	0.00
5.75	0.00	0.00	0.00
6.00	0.00	0.00	0.00
6.25	0.00	0.00	0.00
6.50	0.00	0.00	0.00
6.75	0.00	0.00	0.00

A16.5 Comparison of Flux-Weighted Porosity and Wetted Surface Estimates - Base Case

File: PORWSCOR.PRN

Porosity ϕ_Q (-)	Wetted Surface S_w (m ² /m ³ H ₂ O)
7.38E-06	322.5579
6.03E-06	348.7943
5.07E-06	334.5234
5.37E-06	357.6375
5.24E-06	274.0520
4.88E-06	425.2076
5.00E-06	347.7399
8.03E-06	328.4098
4.89E-06	388.1472
6.58E-06	403.4656
7.97E-06	364.2799
5.26E-06	395.3179
8.20E-06	267.4215
6.95E-06	332.4128
6.78E-06	335.6038
5.34E-06	376.9199
5.73E-06	386.8240
5.26E-06	390.0996
8.32E-06	310.2217
6.60E-06	326.4409
5.30E-06	340.0611
5.22E-06	264.6253
7.90E-06	412.6743
5.48E-06	371.7965
5.64E-06	346.9282
6.18E-06	333.8509
4.66E-06	468.1590
5.46E-06	404.1808
6.06E-06	361.8232
9.30E-06	322.9977
5.37E-06	402.6603
9.46E-06	235.8346
6.05E-06	285.9954
8.26E-06	360.3376
6.45E-06	372.6505
6.92E-06	326.4215
5.59E-06	328.1563
6.24E-06	409.9551
8.37E-06	313.4786
1.14E-05	329.9824
6.69E-06	422.7918

File: QWTDWET1.PRN (continued)

Porosity ϕ_Q (-)	Wetted Surface S_w (m ² /m ³ H ₂ O)
5.76E-06	333.9116
6.90E-06	360.1966
1.05E-05	255.8773
6.69E-06	383.7002
7.61E-06	437.0270
4.91E-06	289.7978

List of SKB reports

Annual Reports

1977-78

TR 121

KBS Technical Reports 1 – 120

Summaries

Stockholm, May 1979

1979

TR 79-28

The KBS Annual Report 1979

KBS Technical Reports 79-01 – 79-27

Summaries

Stockholm, March 1980

1980

TR 80-26

The KBS Annual Report 1980

KBS Technical Reports 80-01 – 80-25

Summaries

Stockholm, March 1981

1981

TR 81-17

The KBS Annual Report 1981

KBS Technical Reports 81-01 – 81-16

Summaries

Stockholm, April 1982

1982

TR 82-28

The KBS Annual Report 1982

KBS Technical Reports 82-01 – 82-27

Summaries

Stockholm, July 1983

1983

TR 83-77

The KBS Annual Report 1983

KBS Technical Reports 83-01 – 83-76

Summaries

Stockholm, June 1984

1984

TR 85-01

Annual Research and Development Report 1984

Including Summaries of Technical Reports Issued during 1984. (Technical Reports 84-01 – 84-19)

Stockholm, June 1985

1985

TR 85-20

Annual Research and Development Report 1985

Including Summaries of Technical Reports Issued during 1985. (Technical Reports 85-01 – 85-19)

Stockholm, May 1986

1986

TR 86-31

SKB Annual Report 1986

Including Summaries of Technical Reports Issued during 1986

Stockholm, May 1987

1987

TR 87-33

SKB Annual Report 1987

Including Summaries of Technical Reports Issued during 1987

Stockholm, May 1988

1988

TR 88-32

SKB Annual Report 1988

Including Summaries of Technical Reports Issued during 1988

Stockholm, May 1989

1989

TR 89-40

SKB Annual Report 1989

Including Summaries of Technical Reports Issued during 1989

Stockholm, May 1990

1990

TR 90-46

SKB Annual Report 1990

Including Summaries of Technical Reports Issued during 1990

Stockholm, May 1991

1991

TR 91-64

SKB Annual Report 1991

Including Summaries of Technical Reports Issued during 1991

Stockholm, April 1992

Technical Reports

List of SKB Technical Reports 1992

TR 92-01

GEOTAB. Overview

Ebbe Eriksson¹, Bertil Johansson², Margareta Gerlach³, Stefan Magnusson², Ann-Chatrin Nilsson⁴, Stefan Sehlstedt³, Tomas Stark¹

¹SGAB, ²ERGODATA AB, ³MRM Konsult AB

⁴KTH

January 1992

TR 92-02

Sternö study site. Scope of activities and main results

Kaj Ahlbom¹, Jan-Erik Andersson², Rune Nordqvist²,
Christer Ljunggren³, Sven Tirén², Clifford Voss⁴

¹Conterra AB, ²Geosigma AB, ³Renco AB,

⁴U.S. Geological Survey

January 1992

TR 92-03

Numerical groundwater flow calculations at the Finnsjön study site – extended regional area

Björn Lindbom, Anders Boghammar

Kemakta Consultants Co, Stockholm

March 1992

TR 92-04

Low temperature creep of copper intended for nuclear waste containers

P J Henderson, J-O Österberg, B Ivarsson

Swedish Institute for Metals Research, Stockholm

March 1992

TR 92-05

Boyancy flow in fractured rock with a salt gradient in the groundwater – An initial study

Johan Claesson

Department of Building Physics, Lund University,
Sweden

February 1992

TR 92-06

Characterization of nearfield rock – A basis for comparison of repository concepts

Roland Pusch, Harald Hökmark

Clay Technology AB and Lund University of
Technology

December 1991